

EMITTER EROSION IN FLUORESCENT LAMPS

DURING STEADY-STATE OPERATION

I n a u g u r a l d i s s e r t a t i o n

zur

Erlangung des akademischen Grades eines
Doktors der Naturwissenschaften (Dr. rer. nat.)

der

Mathematisch-Naturwissenschaftlichen Fakultät

der

Ernst-Moritz-Arndt-Universität Greifswald

vorgelegt von

Kristian Rackow

geboren am 21. Juni 1980

in Demmin

Greifswald, 22. September 2015

Dekan: Prof. Dr. K. Fesser

1. Gutachter: Prof. Dr. K.-D. Weltmann

2. Gutachter: Prof. Dr. G. Zissis

Tag der Promotion: 21.03.2016

Abstract

Owing to the growing importance of LED technology, the lighting market demands more flexible, high-efficiency fluorescent lamp systems. In particular, the ability to regulate light intensity (the dimmed operation) exerts enormous stress on fluorescent lamps' electrodes, leading to increased electrode erosion and significantly reduced lifetimes.

The thesis describes a new method to determine the actual erosion of fluorescent lamps' electrodes during operation. The method is applied to standard fluorescent lamps to study the standard and dimmed operations of modern electronic ballasts. It has been found that erosion during standard operation occurs primarily due to the evaporation of electrode emitter material at the hot spot that is formed. The lamp current and, more importantly, an additional applied electrode heating current during dimmed operation, significantly affect this erosion process. In contrast, operation frequency exerts only marginal effects on erosion.

The electrode erosion is determined by measuring the amount of evaporated emitter material. Therefore, the absolute density of evaporated barium is measured by laser-induced fluorescence while interrupting the lamp operation for a very short time (approximately 5 ms) to suppress any interaction between the evaporated material and the plasma in the electrode region. The total amount of evaporated material is determined by calculating the total flux by a transport model that uses the measured densities.

To characterize electrode operation and the plasma in the electrode region, additional diagnostic methods are applied. Such electron densities are measured by microwave interferometry, the cathode fall voltage is determined by the capacitive coupled band method, and the electrode temperature is measured by one-dimensional pyrometry.

Table of contents

1	Introduction	1
2	Fluorescent lamps	9
2.1	Configuration, function, type, and operation mode	10
2.2	Electrodes for fluorescent lamps	15
2.2.1	Basic configuration	15
2.2.2	Emitter coating	16
2.2.3	Work function and generation of electrons at the cathode	17
2.3	Electrode erosion	22
2.3.1	Sputtering	22
2.3.2	Chemical reactions	23
2.3.3	Barium evaporation	23
3	Experimental methods	27
3.1	Resistive method for determination of average electrode temperature	27
3.2	Pyrometric electrode temperature determination	28
3.3	Cathode fall estimation with band method	30
3.4	Electron density measurement by microwave interferometry	31
3.5	Determination of absolute particle densities by using LIF	33
3.6	Investigated lamps and operation conditions	35
3.7	Arrangement of the diagnostics	37
4	Method and model for determination of absolute evaporation by the blanking method	39
4.1	Blanking method - basic approach	39
4.2	2D Diffusion model	40
4.3	Solution of the particle balance equation	44
4.4	Application and validation of the model	50

5	Results and discussion	55
5.1	Necessary preliminary investigation - Determination of collisional effects - quenching	55
5.2	Barium production and evaporation in case of a heated electrode	58
5.3	Lamp operation by modern electronic ballast systems at 25 kHz	63
5.3.1	Dynamics of electrode operation	63
5.3.2	Eroded barium in the electrode region	65
5.3.3	Spatial characteristics	67
5.4	Dimmed operation by variation of lamp current	69
5.4.1	Variation of lamp current	70
5.4.2	Influence on additional applied heat current	73
5.5	Frequency variation	77
5.5.1	Anode oscillation during low frequency operation	77
5.5.2	Frequency variation	80
5.5.3	Interpretation of related works at conventional net frequency operation	83
6	Conclusion	87
 Appendix		
A	Experimental methods in detail	93
A.1	Pyrometric electrode temperature determination	93
A.2	Cathode fall estimation with the band method	95
A.3	Electron density measurement by microwave interferometry	102
A.4	Determination of absolute particle densities by using LIF	115
A.5	Model for the correction of saturation effects by the application of LIF	136
B	Additional calculations	147
C	Indices	155
C.1	Bibliography	155
C.2	Glossary	165

1 Introduction

The invention of artificial light provided humanity with the opportunity to use the time after dark for additional activities. The invention of controlled fire 790,000 years ago simultaneously provided the first artificial light source [GOREN-INBAR et al. 2004]. While fire was primarily used for cooking and as a heat source, it also became the social center for meeting in the evening hours. The light generated as a by-product of the fire allowed small tasks such as sewing and the manufacture of tools or weapons to be continued after dark. In addition, fire as a light source transformed dark caves into habitable spaces, providing more protection against the elements. It also increased productivity.

The open fire was enhanced according to the requirement for various applications. As such, specific fireplaces for cooking, baking, heating, and melting metal were developed. However, the melting of metal was only made possible through the discovery of enhanced fuels such as charcoal and coal. For lighting applications, torches were developed as quasi-mobile light sources, the earliest of which consisted of simple wooden staves. Later, the ends of torches were wrapped in fabric and soaked in a flammable substance.

About 10,000 BC, the first simple oil lamps were developed [AMIRAN 1970], comprising hollow stones and a wick made of plant fiber, with animal fat used as fuel. These lamps were easier to control and they delivered continuous light for several hours. In the following centuries, several improvements were made, including the use of plant oil as fuel. In the second century C.E., the first candles were invented.

The next important step in lighting technology was the development of the gas lamp at the beginning of the industrialization period. The original thermo lamp [LEBON 1799] was improved and developed into an advanced light source, later used in streetlights and factories.

In 1800, Humphry Davy invented the first usable electric light source by generating an electric arc between two carbon electrodes. The arc delivers about 10,000 lm, which is 1000 times brighter than a candle. However, the short lifetime of the electrodes (approximately two hours) and poor availability of electrical power prevented the product's wide practical application. In 1857, Heinrich Geissler invented the first gas discharge tube (the GEISSLER tube), which was a glow discharge in a low-pressure tube filled with noble gases.

The electrical revolution of lighting began with the invention of the first commercially practical incandescent lamp by Thomas Edison in 1879 [EDISON 1880]. In contrast to other engineers who tested a glowing wire, Edison used a carbon filament connected to platinum contact wires with lifetimes of several tens of hours. A few months later, Edison and his team developed a carbonized bamboo filament that possessed lifetimes of over 1,200 hours. This was the fundamental cause of the commercial success of electrical lighting. Further

improvements led to the classic incandescent lamp with the glowing metal wire made of a special tungsten alloy.

The practicable application of gas discharge lamps began in 1901 with the invention of the low-pressure mercury vapor lamp by Peter Cooper Hewitt [1901]. Its construction was based on a GEISSLER tube with additional mercury. After ignition, the lamp heats up whereas mercury evaporates. The mercury vapor discharge delivered a quite higher light output than incandescent lamps. The main disadvantage was the poor light quality because light emission at only a small region of the visible light spectra. However, in 1926 Edmund Germer solved this problem by coating the inner wall of the mercury discharge tube with phosphor converting the emitted ultraviolet radiation into visible light. With the development of improved phosphors and durable electrodes, this fluorescent lamp became commercially successful in the early 1940s. At this time, fluorescent lamps had high efficacy in comparison with the other available light sources combined with adequate light quality.

By the end of the 1930s, the high-pressure mercury lamp had been developed. Owing to operation at higher pressure, these lamps had a very strong light output combined with adequate light quality. In the 1960s, a very closely related lamp design called the metal halide lamp was invented. They have a filling of various compounds in an amalgam with mercury, whereas sodium iodide and scandium iodide are commonly in use. These lamps have better light quality and high efficacy. Because of the strong light output, high intense discharge lamps (HID) are used to illuminate halls, as streetlights or in movie projectors. Since the 1990s, new designs with lower light output have been used in vehicle headlamps or video projectors.

In 2010, the white LED entered the market as an alternative means of general lighting. There technical improvements are still in progress [ZISSIS and KITSINELIS 2009]. Today, the efficacy and light quality of LEDs are comparable to fluorescent lamps. The punctual light emission and need for advanced heat dissipation require a complex design and this restriction leads to a limited maximum light output. In addition, the significantly higher prices of LEDs compared with alternative light sources (i.e. compact fluorescent lamps) delay their commercial success.

The social importance of artificial light

Artificial light has increased human productivity. During the industrialization period, gas lamps were used to illuminate factories, enabling the operation of expensive machines around the clock and thus establishing shift work. As electric lighting spread out to customers, homes could be illuminated according to individual requirements and such lighting could be used without limitation during the hours of darkness. Moreover, the invention of streetlights transformed the streets into an additional nocturnal living and social environment.

In contemporary industrialized countries, nighttime has been illuminated and the dark is no longer a limiting factor.

The lighting market

The lighting market is characterized by the intensified growth of green lighting technologies [FROST and SULLIVAN], where green technologies can be summarized as energy efficiency category A & B rated in Europe¹ and equivalent in other regions. This trend is based on increasing energy costs and environmental consciousness as well as on legal regulations that prohibit older inefficient lamps (such as incandescent lamps in the European Union). For the year 2016 the total general lighting market is expected to 71.9 billion Euros [MCKINSEY] whereas the market is divided into the lamp market (16.9 billion Euros), the control gear market (7.3 billion Euros) the fixtures market (43.6 billion Euros) and the market for lighting control systems (4.1 billion Euros). According to the technology a market share of 43 % for fluorescent lamps, 36 % for LED technology 14 % for halogen lamps 5 % for incandescent lamps and 2 % for HID lamps is expected [MCKINSEY]. Thus, even through the imens growing of LED thechnology fluorescent lamps still dominate the market.

Technical evolution of artificial lighting

Throughout its evolution, the development of artificial lighting has been determined by scientific and technological progress. New inventions, especially new materials and manufacturing techniques, allow for the improvement of established light sources or the invention of new ones. As an early example, the discovery of liquid fuel and a wick led to the invention of the oil lamp. Later, the understanding of air circulation and improved fuel (vegetable oil) allowed for the creation of the advanced oil lamp with adjustable light output.

However, the evolution of artificial lighting also led to additional inventions of other technologies. For example, the invention of the gas lamp, and especially its subsequent improvement, led to an understanding of gas burning and the discovery of high-temperature gas burners as useful for melting quartz glass.

Looking at the evolution of electrical light sources, after discovering a new basic principal the main challenge was the construction of light sources that have a sufficient lifetime. As an example, the first carbon arc lamps had lifetimes of two hours. In the case of incandescent lamps, the glowing filament is extremely stressed owing to high temperatures, leading to the rapid erosion of the material. Thus, the main challenge was the development of a durable filament, which was solved by Edison [1880].

After discovering the low-pressure mercury discharge [HEWITT 1901], the technical challenges were the efficient generation of visible light and development of durable and effective electrodes. The generation of visible light was solved by using phosphor, which

¹ A & B rated according the Commission Directive 98/11/EC of 27 January 1998 implementing Council Directive 92/75/EEC with regard to energy labelling of household lamps. A rated corresponds to a relative energy consumption less than 25% and B rated correnponds to a relative energy consumption between 25% and 60% in comparison to a standard incandescent lamps.

converts the emitted ultraviolet radiation and led to the creation of the fluorescent lamp. As this type of lamp possesses a discharge voltage of about 100 V, electrode losses of several tens of volts significantly affect the lamp's efficacy. Thus, development was and remains focused on efficient long-living electrodes.

For high-pressure discharges, the main challenges were manufacturing a transparent, high-pressure, and high-temperature-resistant discharge tube and developing suitable electrodes that can operate at temperatures of more than 3000 K, which occur together with aggressive atmospheres and gas temperatures of up to 6000 K [CHITTKA et al. 1997]. With the invention of metal halide lamps, the optimization of light quality gained importance.

Electrodes of fluorescent lamps

For gas discharge lamps, the electrodes, as the route by which the electric current passes into and out of the plasma, are an essential component that defines the efficacy and lifetime of the lamp. Therefore, research on electrodes for gas discharge lamps and their optimization is of special interest.

As the thesis focuses on fluorescent lamps, they and especially research on electrode erosion should be introduced in more detail. In general, a commercial electrode system for fluorescent lamps consists of a tungsten coil coated with a work function reducing emitter mix of alkali oxides such as BaO, SrO, and CaO. During lamp life, an electrode is damaged by two essential processes. In the case of instant start ballast, the electrode is heated by ion bombardment before transitioning into the arc mode (glow-to-arc-transition) where so-called hot spot builds up. During this time, electrode material such as the emitter material and tungsten is eroded by sputtering. This process limits the number of switching cycles. After transition into the arc mode, during steady-state operation, the emitter material (primarily barium) erodes from the hot spot. In the case of a good adaption of the electrode to the discharge conditions, this erosion is generally in the form of evaporation.

Today, electrode durability is the primary reason for the limited lifetime of fluorescent lamps. In general lighting applications, the maintenance costs of lighting systems are very important and are significantly determined by the replacement of defective lamps. Therefore, there is still an attempt to improve the lifetime and especially the spread in lifetime of such electrode systems.

Research on electrode erosion in fluorescent lamps

Since fluorescent lamps became commercially available in the 1940s [LANKHORST and NIEMANN 2000], their development and research on them have often been affected by industry. Thus, applied oriented and pragmatic approaches have been of particular concern. The first attempts to determine the loss of the emitter material were made in the middle of the twentieth century by optical emission spectroscopy (OES) measurements² in the vicinity

² OES measurements were performed on the Ba atom line at 553.5 nm, the Ba ion line at 455.4 nm, and on the Sr line at 460.1 nm.

of the electrode [HERRMANN 1958; KÜHL 1958; LAKATOS and BITO 1964]. However, the disadvantages³ of OES make the interpretation of the signals quite difficult. For improved investigations, advanced diagnostics are required.

The main trends and aims of electrode research considering the relevance to lamp applications have been summarized by Chittka et al. [1997], who illustrated the special requirements during lamp ignition (glow mode) and stationary operation (arc mode).

Erosion during ignition

Born et al. [2000] investigated lamp ignition in a pulsed low-pressure argon discharge by measuring tungsten erosion directly after the instant start. They applied laser-induced fluorescence (LIF) to determine the absolute densities in the cathode region and compared the spatially and temporally resolved tungsten densities with diffusion model calculations.

Haverlag et al. [2002] showed that coil breakage is caused by tungsten sputtering mainly during the glow-to-arc transition. This assumption was proved by the investigations of Hilscher et al. [2004] on both linear and compact fluorescent lamps by using fast emission spectroscopy and high-speed video observation. In contrast, Hadrath [2007] proved that the sputtering of tungsten is nearly constant during the glow phase by measuring the absolute tungsten density in the vicinity of the electrode using LIF. The high signal during the glow-to-arc transition, observed by emission spectroscopy, occurs because of an increase of electron temperature and electron density, resulting in a significantly more efficient excitation of the sputtered tungsten atoms. The average emitter loss per ignition was quantified by Van den Hoek et al. [2002], who used the emitter material with radioactive Ba133 and determined its deposition on a moveable shield.

A one-dimensional thermal model for an operating fluorescent lamp electrode was developed by Soules et al. [1989], who found semi-quantitative agreement of the calculated temperature distribution with temperature profiles measured by using an optical pyrometer. Another one-dimensional model of the electrode was developed by Golubovskii et al. [2006]. They included self-consistent heating by using the external and discharge currents and found very good experimental agreement with investigations of the diffuse modes, the spot modes, and their transition.

Erosion during stationary operation

Electrode erosion during stationary operation was investigated by Bhattacharya by using the high-sensitivity method of LIF [BHATTACHARYA 1989a, b]. He measured barium density in the electrode region to investigate the loss of barium from the electrode for a fluorescent lamp operating at 60 Hz. High peaks in barium densities occur at a zero current owing to the re-ignition of the lamp. The ionization of neutral barium and collection of the

³ The most important disadvantages of OES in the electrode region are that radiation can only be observed while the lamp is on, radiation occurs only from excited states, and excitation depends on the cathode fall, which dominates the plasma processes in the electrode region.

produced ions by the cathode at low frequency operation were also discussed by Michael [2001]. In 1992, Moskowitz [1992] used LIF to investigate the influence of various lamp parameters (e.g. different lamp ballasts) on the lifetime of lamp electrodes. Additionally, Samir et al. [2007] measured the temporal and spatial distribution of barium atoms in fluorescent lamps by using LIF under 60 Hz operation and showed that the maximum barium is mainly emitted at the hot spot.

The electrode processes and especially the interaction of plasma and electrode for stationary, high-frequency operation were modeled by Garner in 2008 [Garner 2008b]. He concentrated on the characterization of the plasma in the electrode region, which allows for a more detailed representation of the coupling between electrode and plasma. In 2010, Hadrath and Garner [2010] determined the sputtering of barium from the electrode during stationary operation. They observed the resonant line of barium atoms at 553 nm with a Fabry–Perot interferometer to determine barium temperatures. Under certain discharge conditions, they found temperatures significantly higher than the electrode temperatures that could only occur because of sputtering.

In 2009, Rosillo and Chivelet [2009] predicted the lifetime of fluorescent lamps choosing a more empirical approach by measuring certain lamp parameters (such as voltage and coil resistance) during lifetime and correlating these with the achieved lifetime of the lamps. Although this study may seem to be less significant as they used only 34 lamps, it demonstrates the need for a lifetime prediction method. A method to determine the time averaged emitter loss by measuring the maximum heat rate (determination of the heat capacity of the electrode that corresponds to the emitter mass) has been established by Wharmby [WHARMBY 2004]. With his method, Buso et al. [2009; 2012] found a quasi linear loss of emitter with the burn time.

Finally, Kobayashi et al. [2010] modeled emitter loss during lamp life. They focused on an electrode model that predicts temperature profiles during lamp life, illustrating that the proportion of the loss in total barium from the cathode is almost linear with the burn time.

Main goals of this work

This work expands upon the presented related work and it should thus complement the existing knowledge. The main goal is to examine absolute electrode erosion during the stationary operation of commonly used fluorescent lamps. In contrast with other works that determined a time-averaged erosion over several hundred operation hours [BUSO et al. 2009; BUSO et al. 2012; KOBAYASHI et al. 2010; ROSILLO and CHIVELET 2009; WHARMBY 2004], instantaneous erosion and its dependence on operation parameters is determined. The work focuses on commercial T8 lamps at the operating mode of commonly used electronic ballasts with frequencies at several tens of kHz. This operation regime allows the results to be applied to classic tubular lamps as well as to compact lamps.

Initially, erosion under standard conditions at the nominal lamp current is determined. With a view to continuously raising requirements of modern fluorescent lamp systems, dimmed operation (reducing the light output through a reduced lamp current) is investigated. In particular, the focus is on the benefit of an additional heat current for reducing electrode

erosion at reduced lamp currents. To ensure comparability with related works and adaptability to older lamp systems, dependence on operation frequency is also examined.

Methodology

Electrode erosion during stationary operation is characterized by the erosion of barium as the main compound of the electrode. Thus, LIF is used for the sensitive determination of the absolute ground state densities of the released barium in the electrode region. As the determined released barium is affected by the plasma in the electrode region, the determined barium atom and barium ion ground state densities do not represent the absolute loss and thus barium erosion. To overcome this limitation, a new method based on a barium diffusion model (see Chapter 4) is developed in order to determine the absolute barium evaporation from the measured densities.

To characterize the electrode operation for the investigated operation parameters and ensure comparability with related works, additional diagnostics are applied. Electrode temperature as a basic parameter that determines barium evaporation is determined by using pyrometry. The cathode fall voltage as the parameter for electrode operation is estimated by using the commonly used band method. The plasma in the electrode region is then characterized by using microwave interferometry, allowing the determination of electron densities and ionization rates.

Structure of the thesis

The thesis is structured into six chapters. After this introduction, an overview of fluorescent lamps with a focus on electrode processes and erosion is given. The third chapter describes the applied experimental methods and their experimental arrangement. In the fourth chapter, a new method and a model for determining absolute emitter evaporation during lamp operation are presented. The detailed investigation of emitter erosion and its dependence on the operation conditions are presented in Chapter 5. Finally, the thesis ends with a conclusion.

2 Fluorescent lamps

Fluorescent lamps are classical low-pressure discharges designed for converting electrical power into visible light. In 1901 Peter Cooper Hewitt [1901] discovered that a low-pressure discharge through a mixture of mercury vapor at a precise optimum and a rare gas at a somewhat higher pressure was very efficient in converting electrical energy into ultraviolet light [WAYMOUTH 1971]. Up to 70% of the electrical power applied to a discharge with a sufficient long positive column could be converted to a single line of the resonance 6^3P_2 mercury state at 253.7 nm. With the development of a suitable fluorescent phosphor for converting the mercury radiation into visible light and efficient long-lived electrodes (developed in the late 1930s), fluorescent lamps became commercially available in the 1940s [LANKHORST and NIEMANN 2000]. Since then, the basic configuration has not changed. During the next decades, further developments were coupled with the technological improvement of phosphor (enhancement of efficacy) and the improvement of electrodes (enhancement of lifetime).

The tubular construction of fluorescent lamps and the need for external ballasts made fluorescent lamps incompatible with existing lighting systems. Therefore, the first fluorescent lamps were used in industrial applications. In 1981, the efficacy of fluorescent lamps was improved significantly by the introduction of electronically controlled ballasts offered by OSRAM [ROZENBOOM 1983], which allowed the introduction of compact fluorescent lamps in the early 1980s. As these were compatible with the standard socket of incandescent lamps, they became a cost-effective, efficient alternative to the incandescent lamp [PROUD 1983]. Since then, fluorescent lamps became relevant for the consumer market.

Another improvement has been achieved by the introduction of T5 lamps with smaller diameter (T5 = 5/8 inch compared with standard T8 = 8/8 inch) in combination with three-band phosphors. The smaller diameter has many optical advantages for the design of high-performance lamp systems. Today, the efficacies of such lamps can be up to 100 lmW^{-1} compared with approximately 35 lmW^{-1} in 1940 [ABEYWICKRAMA 1997].

All times, discharge lamps have been continuously improved with innovative approaches and the availability of new materials and techniques, whereas the research in the last few years were mainly focused on developing more economical, energy-saving solutions and on ensuring maximum environmental compatibility [OSRAM 2010]. Along with the reduction of energy consumption, the increase of lamp lifetime can improve the environmental compatibility of fluorescent lamps.

For the year 2016, a market share of fluorescent lamps of about 43 % of the global lamp market with revenues of 16.9 billion Euros is expected [MCKINSEY].

2.1 Configuration, function, type, and operation mode

Although huge variations of fluorescent lamps exist, the basic configuration is always the same (see Figure 2-1). The discharge vessel consists of a glass tube, where typically a non-UV-transparent glass is chosen. Depending on the lamp type and the desired power, the total length is between 14 cm and 240 cm and the outer diameter is between 16 mm and 54 mm. The outer diameter defines the typical lamp types: T5 (5/8 inch ~ 16 mm), T8 (8/8 inch ~ 25 mm), and T12 (12/8 inch ~ 38 mm).

The inner wall of the glass tube is covered with phosphor, responsible for converting the UV radiation emitted by mercury to the desired visible light. The chosen phosphors determine the light color and quality (expressed by the color-rendering index⁴ CRI). Today, primary high efficient three-band phosphors (such as Cer-Terbium-Magnesium-Aluminate [RUTSCHER and DEUTSCH 1984]) are used, combining high conversion efficacy and good color rendering. As most of them consist of noble earths, the phosphors are an expensive part of fluorescent lamps.

Electrodes are placed at both ends of the tube, connecting the external electrical circuit with the discharge, and are responsible for driving the current into the plasma. For reduction of electron emission losses, the electrode is coated with a work function lowering emitter. A detailed description of their construction and operation is given in the following section. As fluorescent lamps are typically driven with an AC-current, both electrodes work alternately as cathode and anode.

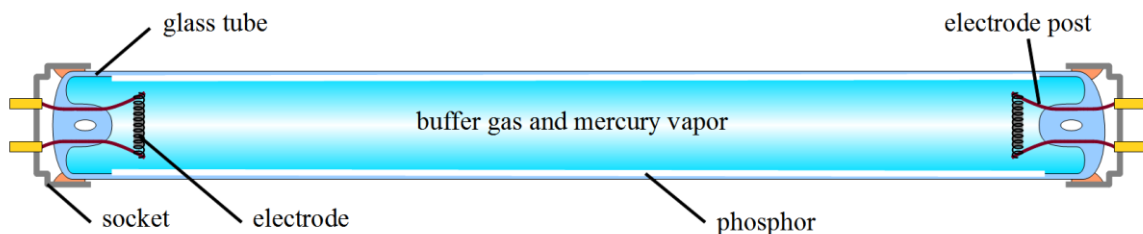


Figure 2-1: Schematic of a tubular fluorescent lamp with stick electrodes

The filling of a fluorescent lamp consists of mercury vapor and buffer gas. During its lifetime, mercury gets lost due to attachment in the phosphor coating. Therefore, more mercury than needed is filled in. Accordingly, the mercury vapor pressure is saturated and defined by the coldest point of the fluorescent lamp, the so-called cold-spot. The vapor pressure and therefore the cold-spot temperature significantly affect the emission of UV-radiation.

⁴ The color-rendering index (CRI) is used to quantify the light quality of a light source. The ability of the light source to reveal colors is related to an ideal natural light source. The higher the value, the better the color of an illuminated object correspond to its natural color. Numerically the highest CRI = 100 is achieved by black body radiation. Typically, fluorescent lamps have a CRI between 70 and 90.

The buffer gas is necessary for reduction of the ignition voltage and especially for reduction of diffusion losses of charged particles to the inner wall. Without buffer gas, a huge amount of electrons would get lost at the inner wall, due to their long free path length. With additional buffer gas (noble gasses) with densities 500 times higher than the density of mercury, the free path length is significantly reduced due to inelastic collision with gas atoms. As the excitation energy of noble gasses (e.g. Argon: 11.55 eV) is significant higher than the desired averaged electron energy (approx. 1 eV), only a small amount of energy is lost due to elastic collision with gas atoms and the discharge is still dominated by mercury. Typically, mixtures of Argon and Krypton with pressures of between 1 mbar and 5 mbar are used. In newer T5-36 W lamps, the mixture consists of about 30% Kr and 70% Ar at a pressure of 2.1 mbar.

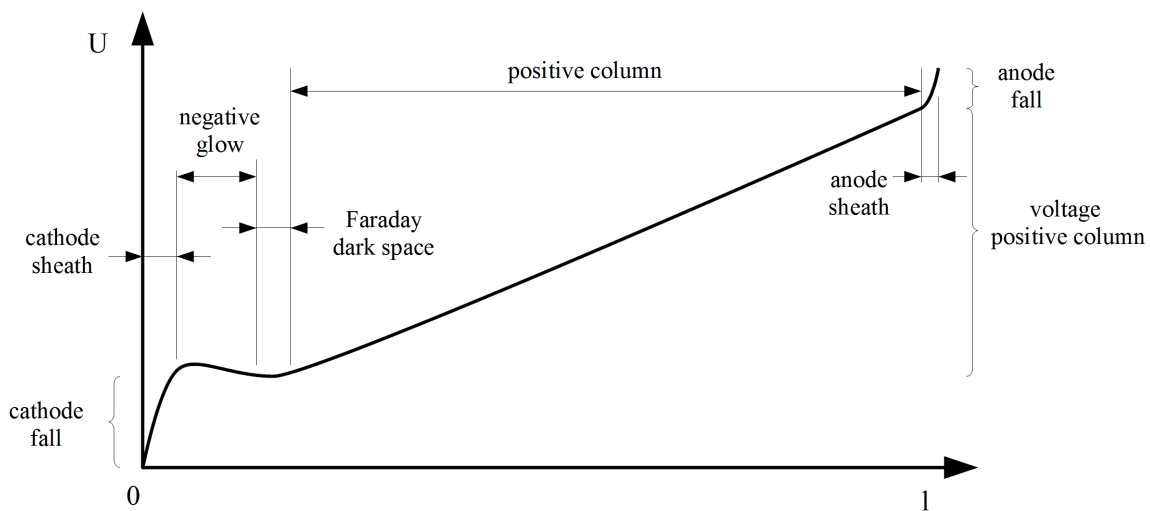


Figure 2-2: Regions and potential from the cathode ($l = 0$) to the anode of fluorescent lamps.

During operation of fluorescent lamps, the typical potential of a low-pressure discharge builds up with the characteristic regions given in Figure 2-2. The longest region is the positive column connected by the anode sheath to the anode and by the cathode sheath, negative glow, and the Faraday dark space to the cathode.

The positive column is determined by an equilibrium of charge carrier production in the plasma and the loss of charge carriers due to ambipolar diffusion to the inner wall where they recombine. Thus, the positive column is very homogeneous and extends over almost the whole length of the discharge. In the positive column, the current is mainly transported by the electrons. The portion of the electron current on the lamp current is approximately 99% [WAYMOUTH 1971]. As typical for low-pressure discharges, the positive column is a low-temperature plasma. In general, the kinetic energy transfer from electrons to heavy particles by elastic collisions is very ineffective due to their great different in mass. At the used pressures, the electron-heavy particle collision rate is too low to achieve the thermodynamic equilibrium. Therefore, the gas temperature (heavy particle temperature,

T_n -neutral particle temperature and T_i -ion temperature) is cold (near to ambient temperature $T_n \approx T_i \approx 300\text{K} \approx 0.026\text{eV}$). In contrast, the electron temperature is quite high. A typical value, suitable for very effective excitation of mercury, is $T_e \approx 1\text{eV}$. The exact value depends on the discharge current and the used buffer gas. In general, a reduction of gas pressure leads to an increase of the ambipolar diffusion coefficient resulting in higher losses of electrons due to recombination at the inner wall. To compensate for the losses, a higher production rate of electrons due to ionization is needed. Due to the lower pressures, the free path length of the electrons increases. Thus, the electrons could accelerate over longer distances leading to higher electron energies (electron temperatures). However, to achieve a higher production rate of electrons per length, the field strength (the voltage along the positive column) has to be increased. The same effects could be observed by the use of different noble gases. In general, the ambipolar diffusion coefficient of gases decreases with an increase of mass. Thus, in the order of the noble gases He, Ne, Ar, Kr and Xe, the diffusion coefficient as well as the electron temperature decreases.

The uv-radiation, later converted by the phosphor to the desired visible light, is produced in the positive column. Due to inelastic collisions with mercury atoms, the electron energy is transferred to excitation processes of mercury, primarily emitting uv-radiation at the resonant lines at 253.7 nm and also at 185 nm. Thus, the electron temperature and the efficacy for converting electrical power into uv-radiation significantly depend on the density (the vapor pressure of mercury), defined by the cold-spot temperature. If the mercury density is too low, there would not be enough mercury atoms for excitation processes and the electron energy would be transferred in excitation processes of the buffer gas. Vice versa, a very high density would lead to intensified self-absorption. An emitted uv-photon is absorbed by a mercury atom in ground state and then again emitted. If these processes dominate (due to too high mercury densities), the probability of radiation-less de-excitation increases and the energy is converted into heat, lowering the uv-emission efficacy. According to the designed power and buffer gas, an optimum vapor pressure could be achieved at a cold spot temperature of about 40°C [RUTSCHER and DEUTSCH 1984] (this corresponds to vapor pressure of approx. 1 Pa).

The positive column is connected via the cathode region, including negative glow and the Faraday dark space to the cathode. At the cathode surface, about 10% of the lamp current is transported by positive ions, 90% by electrons. Thus the negative glow is the transition region between electrode surface and positive column (electron current is about 99%), where the different ion currents are balanced. The ionization rate in the negative glow has to be much higher than in the positive column to produce the needed ion current. To provide the energy necessary for such higher ionization rates, a potential drop between cathode and negative glow builds up. This potential drop is concentrated in a very thin sheath at the electrode surface (cathode sheath). The so-called cathode fall has a typical potential drop of between 5 and 15 V and the cathode sheath size is less than 0.1 mm. In contrast, the negative glow has a typical size of between 1 and 3 cm. Between the negative glow and the positive column, an approximately 1 cm long region with less ionization appears. Analogous to the glow discharge, this darker region is called FARADAY-dark-space [WAYMOUTH 1971].

At the anode, the positive column is connected via the anode sheath to the electrode surface. As the electrode would not emit ions, the anode current is only transported via the electrons collected by the anode. The concrete anode sheath and its anode fall depend on the ratio of discharge current and thermionic emission of electrons. The size of the sheath is approximately 1 mm, whereas the anode fall is between 0 and 2 V. For electrodes with a large surface, the cathode fall could also be negative [WAYMOUTH 1971]. The anode fall builds up during the anode phase. After the cathode phase, there exists a huge amount of electrons (due to high ionization in the negative glow) in the anode region. First, the lamp current (anode current) could be sustained by collecting these electrons without an additional potential drop. However, a low potential drop may occur to recollect thermionically emitted electrons. After a certain time, the electron density in the anode region decreases. Now the anode fall voltage has to build up to collect the electrons necessary to sustain the lamp current. If the anode phase is sufficient short, there is no need for an additional anode fall and the anode losses could be reduced. This effect could be observed for anode phases shorter than 200 μs and is the motivation for the kHz operation mode, commonly used in modern lightening systems.

Types of fluorescent lamps and operation mode

Today, there exists a huge amount of different commercial available fluorescent lamp types; a short overview is given in Figure 2-3. One example is the classical tubular lamp, as well as modifications such as the U-shaped and the circular (no closed loop) lamp. The newer compact lamps, with integrated electronic ballasts, are compatible to the standard socket of incandescent lamps.

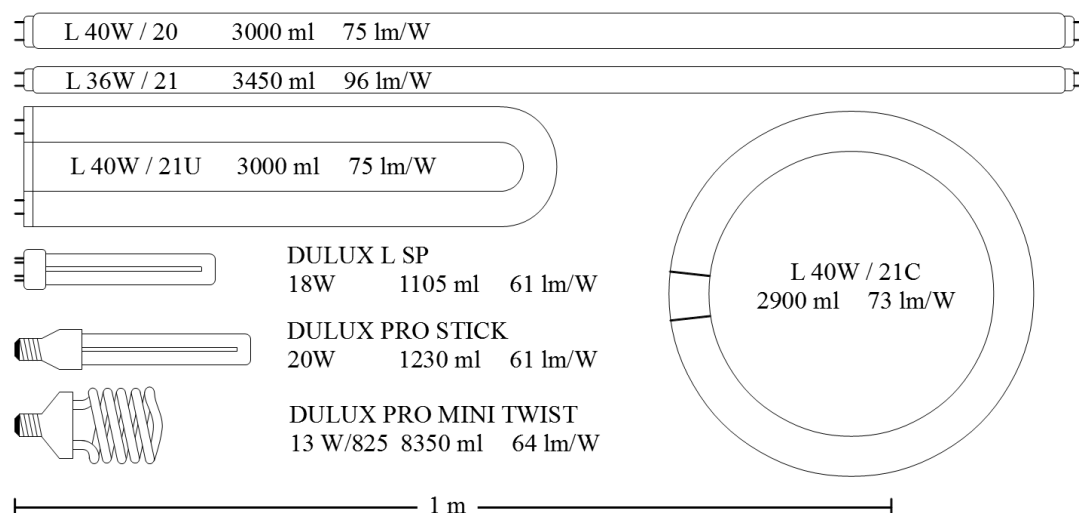


Figure 2-3: Selection of different commercial available fluorescent lamps (FL) such as tubular FL, U-shaped FL, compact FL, compact FL with integrated ballast, and circular FL.

In principal, a fluorescent lamp could be driven by a DC current. As the lamps have a negative differential resistance (at the working point, the voltage will decrease with increasing current) the current has to be limited. Therefore, in DC mode an additional resistance is required which would produce substantial losses. The easiest method to overcome this problem is the use of a choke as inductive ballast, limiting the current. This would allow using the normal net voltage for operation. The European standard circuit for operation with net frequency (see Figure 2-4, left) also includes a starting mechanism. Before ignition of the lamp, the starting switch is closed and the current will flow through the choke and the electrodes. This will heat up the electrodes, which will limit electrode erosion during ignition, a method known as warm start in contrast to instant ignition where electrodes are not heated. After a certain time the starting switch is opened and the current is blocked. The choke will react with a very high voltage, which ignites the lamp. Typical ignition voltages are between 600 and 800 V. The polarity of the discharge changes with every half period. The ambipolar diffusion time is in the region of 1 ms.

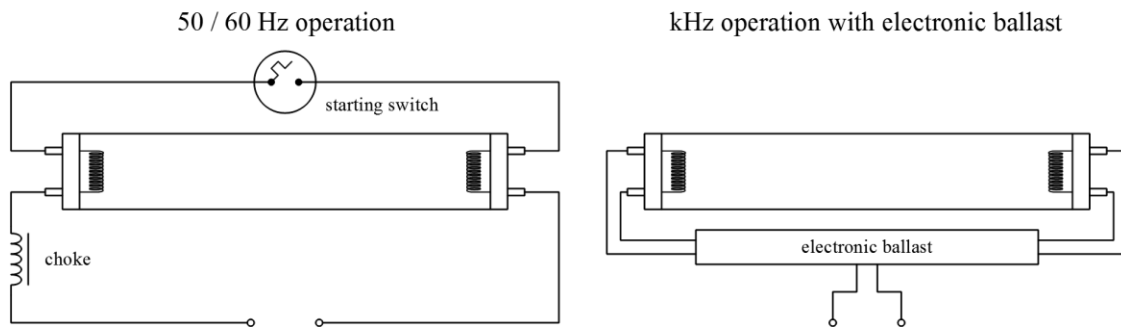


Figure 2-4: Standard circuits for operation of fluorescent lamps with net frequency (left) and with an electronic ballast (right) at a few kHz.

At net frequencies of 50 Hz (Europe) and 60 Hz (US), the discharge regions disappear during change of polarity and have to be built up again in the next half cycle, causing additional losses. By increasing the operational frequency to a value where the period is smaller than the ambipolar diffusion time, these repolarization losses could be avoided. This leads to the invention of electronic ballasts (see Figure 2-4, right) working at frequencies between 5 kHz and 100 kHz. Modern electronic ballasts provide additional advantages such as lower losses in the ballast, reduction of flicker, controlled electrode heating, dimming and the reduction of ballast size and mass [LU et al. 2005; ZISSIS and KITSINELIS 2009]. Very small electronic ballasts allow integration in a standard lamp socket and make compact lamps available. Today, electronic ballasts are state of the art and commonly used.

Therefore, in this work the kHz operation mode of fluorescent lamps is primarily investigated as it allows the results be applied to classic tubular lamps as well as to compact lamps.

2.2 Electrodes for fluorescent lamps

The electrodes of fluorescent lamps, as connections between plasma and the outer electronic circuit, are responsible for driving the current into and out of the plasma. As typical fluorescent lamps are driven in AC-mode, half the time the electrode works as cathode, emitting electrons, and half the time as anode, collecting electrons. The cathode phase is the technologically challenging half of the cycle, because a high electron emission at high temperatures causing low losses is desirable. Thus, the development of electrodes is a compromise of an effective emittance of electrons with low losses and reaching a certain durability, allowing acceptable lifetimes. Up to now, the lifetime of a fluorescent lamp is determined by the lifetime of its electrodes, where typical values between 10,000 and 20,000 hours could be reached.

2.2.1 Basic configuration

For electrodes, the effective electron emission of alkaline earth oxides such as BaO, SrO and CaO is used. The electrode construction has to hold the oxide mixture, especially at the start when the electrode is heated to about 1200 K in a few seconds. Therefore, a tungsten coil, also suitable for additional ohmic heating, is used as a basket.

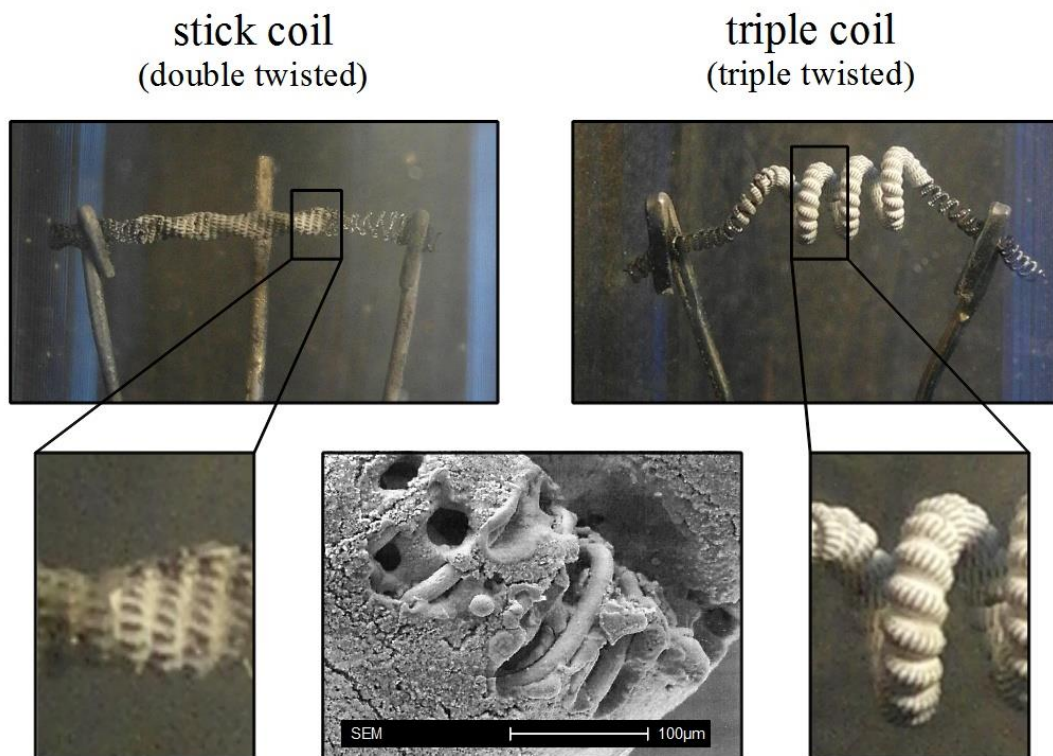


Figure 2-5: Standard electrodes of fluorescent lamps. Left: double-wound stick coil used for T12 and T08 lamps, right: triple coil used for T05 and compact fluorescent lamps, and; middle: SEM of emitter structure (SEM picture is taken from [VAN DEN HOEK 2003]).

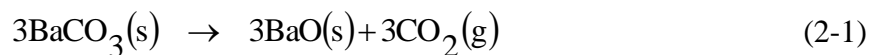
In Figure 2-5 the two standard electrodes for fluorescent lamps are shown. The so-called stick coil (Figure 2-5, left) is used for T12⁵ and T08 lamps. The primary spiral consists of a thin tungsten wire wrapped around a thick wire, known as the primary core, which is needed for mechanical stabilization of the unstable primary spiral. This primary construction is again wrapped tightly to form the stick coil. At both ends, the electrode is connected to the electrode posts by crimp connection. The typical length of the electrode is approx. 10 mm, and the typical diameter is 1 mm. The electrode is coated with approximately 10 mg of emitter, whereas the region 1 mm from the post is free of emitter. For smaller lamp diameters, a stick coil is wrapped again to form a triple coil (see Figure 2-5 right), and these electrodes are primarily used for T05 and compact lamps (T04).

2.2.2 Emitter coating

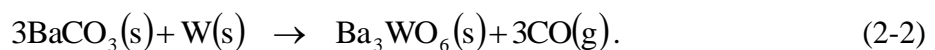
The pre-fabricated electrode system includes the electrode post melted in a glass holder, the tungsten electrode, and the emitter coating. Due to the chemical instability of alkali oxides in air, electrodes are coated with an emission paste that usually contains alkali carbonates, as these are capable of being decomposed by heat to the desired oxides. The emitter mixture consists of barium carbonate with additional alkali carbonate, such as strontium- and calcium-carbonate. The typical particle sizes in the emission paste is about 1 to 5 μm [RUTSCHER and DEUTSCH 1984]. There exist quite a lot of different mixtures, depending on the application and especially on the manufacture, whereas barium carbonate is the main component and is responsible for an efficient emission of electrons. The other carbonates are used to optimize the long-term instant start stability and to increase lifetime. Therefore, the following discussion is focused on barium carbonate, whereas the general processes are similar for the other alkali carbonates.

Activation of emitter

The decomposition of barium carbonate by heat to the desired barium oxides is achieved during lamp production under absence of oxygen at high temperatures. For this so-called activation, the electrodes are heated up to about 1300 K and the gases produced are pumped out. The two most significant reactions are the wanted thermal decomposition of barium carbonate to the desired barium oxide by production of CO_2 :



and the unwanted oxidation of tungsten by carbon oxide by production of CO at the boundary layer of tungsten and barium carbonate:



⁵ The term “T12” describes a tubular lamp with a diameter of 12-eighths of an inch.

Figure 2-6 (left) illustrates these main processes. At typical activation temperatures (about 1300 K), the unwanted reaction (2-2) is thermodynamically highly favored [RUTLEDGE and RITTNER 1957]. Thus, barium carbonate is wasted by production of Ba_3WO_6 forming a layer between tungsten and barium carbonate. Further production of Ba_3WO_6 is limited by the diffusion of barium carbonate through this layer.

To reduce the loss of barium according to reaction (2-2), a special temporal temperature profile is used during activation, optimizing the amount of barium oxide. In general, a high temperature of the electrode should be reached very quickly and kept constant for a certain time. The process could be controlled by measuring the gases produced.

The produced BaO forms a porous structure as indicated in Figure 2-5 (bottom, middle), and Figure 2-6 (right) illustrates a scanning electron microscope (SEM) image of the cross section of an activated electrode. Around the small tungsten wires a more or less irregular layer of Ba_3WO_6 is formed. All barium carbonate is converted to porous BaO.

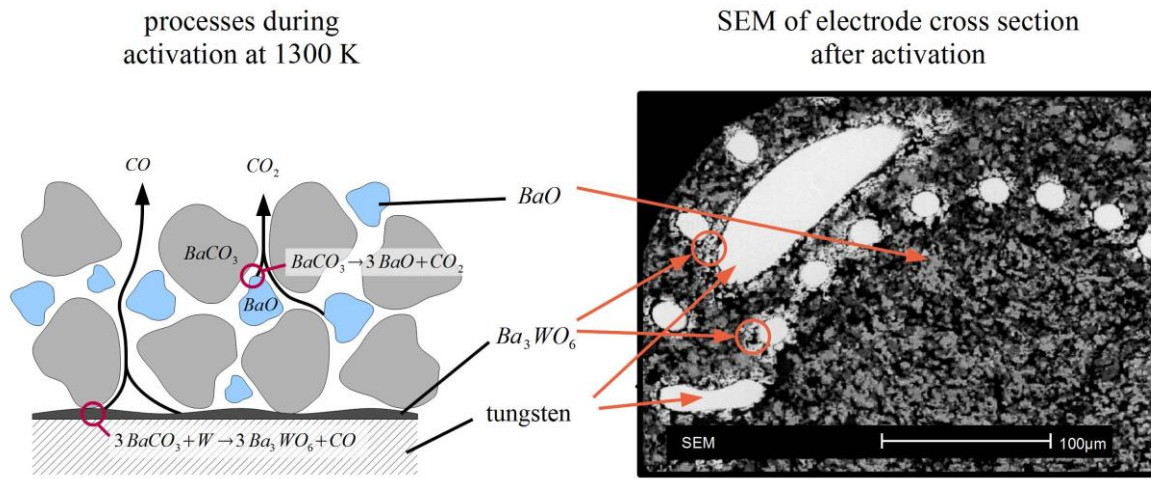


Figure 2-6: Left: processes during activation converting $BaCO_3$ to the desired BaO . A Ba_3WO_6 layer is formed at the boundary layer of tungsten and $BaCO_3$. Right: scanning electron microscope (SEM) image of cross section of an electrode after activation. The SEM picture is taken from [VAN DEN HOEK 2003].

2.2.3 Work function and generation of electrons at the cathode

The key feature of the cathode is the efficient emission of electrons. In order to leave a solid body, the energy of an electron has to be at least as high as the potential barrier keeping it in the solid. For metals, the electron energy distribution (EED) is given by the Fermi-Dirac-distribution:

$$W(E) = \frac{1}{e^{\frac{E-E_F}{k_B T}} + 1}, \quad (2-3)$$

where $W(E)$ denotes the average number of electron in the state with the energy E , E_F the Fermi energy, k_B the Boltzmann constant, and T the temperature. At a temperature of absolute zero, there is no electron at energies higher than the Fermi energy. The potential

difference between this Fermi energy and the outer surface is defined as the work function Φ_0 (see Figure 2-7a) [JENKINS 1969]. The work function depends on the material, the surface structure and the surface coating. Therefore, it is strongly influenced by impurities and additional surface layers such as oxide coating or barium tungstate. For pure tungsten the work function is about 4.5 eV [CHITKA et al. 1997], whereas for tungsten with an atomic layer of barium it is less than 2 eV [MISHRA et al. 2004]. A further lower work function of 1.36 eV is reached by barium layer on barium oxide [MISHRA et al. 2004]. Thus, the used barium oxide emitter is well suited to lower the work function significantly. However, every electron that leaves the electrode has to overcome the work function. Depending on the operation mode of a fluorescent lamp, two different mechanisms dominate.

During the glow phase (approx. the first second) of instant start circuits, the electron emission is due to secondary emission by bombardment of positive ions. For this so-called γ -process, a high cathode fall voltage is needed to provide enough energy for the ions. Due to this high energy, the ions also destroy the electrode by sputtering [HADRATH 2007]. During the glow phase, the electrode is heated up until a certain temperature is reached and transits to the arc mode (glow-to-arc transition).

Thermionic emission of electrons

During steady-state operation the electrode works in the so called arc-mode (arc discharge [RAIZER 1991]), characterized by the thermionic emission of electrons from a hot electrode. The formation of a hot-spot occurs, having a typical temperature of between 1100 and 1400 K and a typical width of 0.5 mm.

At such high temperatures, the electron energy distribution function (2-3) of the electrons in the metal has a significant amount of electrons above the work function that are able to leave the solid body. Accordingly, electrons are emitted at the hot surface. The number of electrons emitted per time and surface area, also written as current density J , is described by the RICHARDSON-equation [RICHARDSON 1965]:

$$J = A \cdot T^2 \cdot e^{-\frac{\Phi}{k_B T}}, \quad (2-4)$$

where T is the temperature of the metal, Φ the work function, k_B the Boltzmann constant, and A the RICHARDSON constant [MELISSINOS 1966]. As could be seen easily from the equation, the current density strongly depends on the surface temperature as well as on the work function. Due to balancing heating and cooling mechanisms, a temperature of the hot-spot will arise so that the discharge current during the cathode phase could be delivered by thermionic emission. The main heating mechanisms are the heating due to the collected electron in the anode phase (electron heating), heating by ions accelerated in the cathode fall during the cathode phase (ion heating), and ohmic heating by the discharge current in the thin tungsten wire. The main cooling mechanisms are the emission of electrons during the cathode phase (providing the work function), heat radiation and heat conductance along the electrode and through the buffer gas [RUTSCHER and DEUTSCH 1984].

Reduction of work function by electric fields

In the presence of an electric field at the surface, as it is produced by the cathode fall voltage, the thermionic emission could be increased by the reduction of the work function in equation (2-3). In case of the alkali oxide electrodes used in fluorescent lamps, two effects that must be considered are the SCHOTTKY- and the patch-effect [GARNER 2008b]. Both are lowering the work function in presence of an electric field and allowing a fast temporal modulation of the electrode emission. This is needed for AC driven fluorescent lamps, as the temperature stays more or less constant during one period.

The SCHOTTKY-effect is also known as enhanced thermionic emission. An electron, escaping from the surface ($r = 0$) of a conductor, induces a mirror charge and therefore sees a potential in the form:

$$E(r) = -\frac{e^2}{4\pi\epsilon_0 r^2}, \quad (2-5)$$

(e electron charge, ϵ_0 vacuum permittivity) outside the surface. Together with the potential produced by the outer electric field $-eEr$, the effective potential barrier, and therefore the work function, is lowered (see Figure 2-7). The resulting effective work function Φ could be written as the difference of the original work function Φ_0 and the drop of the potential barrier $\Delta\Phi$ depending on the electric field:

$$\begin{aligned} \Phi &= \Phi_0 - \Delta\Phi \\ \Delta\Phi &= \sqrt{\frac{e^3 E}{4\pi\epsilon_0}}. \end{aligned} \quad (2-6)$$

(e electron charge, E electric field, ϵ_0 vacuum permittivity).

The patch-effect depends on local variations of the work function. As the work function of alkali oxide electrodes depends on the density of free barium, it could vary strongly between neighbored crystals [WAYMOUTH 1971]. Assume neighbored surfaces with different work functions Φ_1 and Φ_2 have the same size. For an infinity checkerboard pattern of these two surfaces, it has been shown [BECKER 1935; NOTTINGHAM 1936] that in the absence of an electric field the effective work function is given by the averaged work function $\bar{\Phi} = (\Phi_2 + \Phi_1)/2$, as illustrated in Figure 2-7b. In the presence of a moderate electric field, the effective work function is reduced to a value below $\tilde{\Phi} < \bar{\Phi}$ (see Figure 2-7c). For an even stronger electric field, the effective work function is equal to the lower work function Φ_1 (see Figure 2-7d). Thus, the electric field allows the effective work function to be varied by an amount of $\Delta\Phi = (\Phi_1 - \Phi_2)/2$. To give an example, a difference between work functions of about 1 eV at an electric field in the range of 10,000 V/cm leads to an increase of the thermionic emission by a factor of $e^5 \approx 100$ [WAYMOUTH 1971].

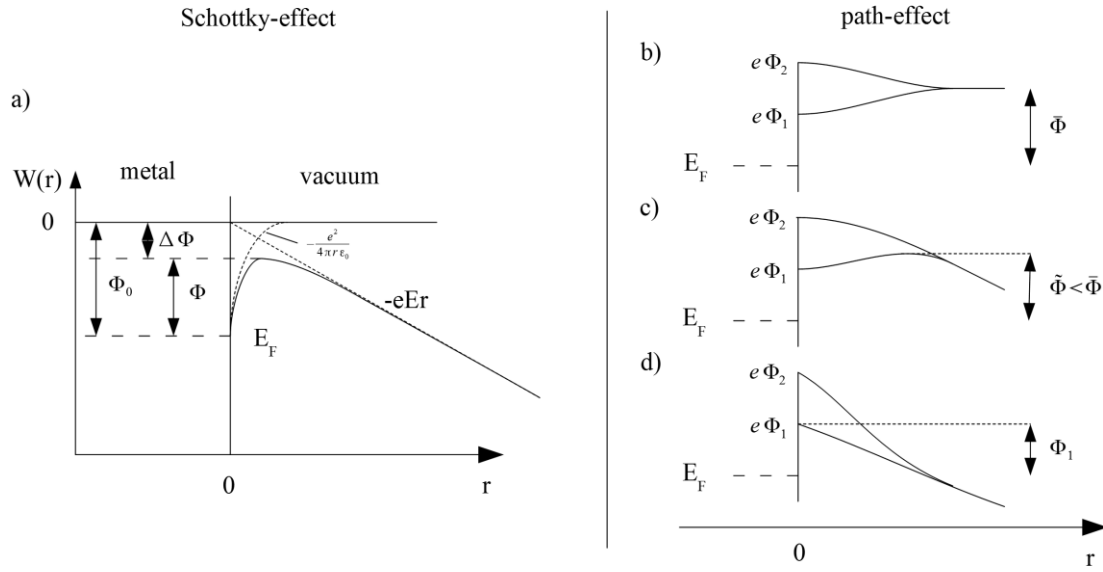


Figure 2-7: Reduction of work function by electric fields in case of the SCHOTTKY-effect (left) and the path-effect (right).

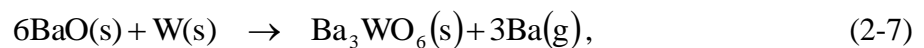
Need to lower the work function with presence of free barium

As mentioned before, a low work function due to the presence of free barium is essential for this kind of high efficient electrode. The need to lower the work function could be illustrated by two calculations according equation (2-4). To reach the same electron emission of pure tungsten (work function 4.5 eV [CHITTKA et al. 1997]) at 2500 K, tungsten with an atomic layer of barium (work function 2 eV [MISHRA et al. 2004]) would only need a temperature of 1196 K. Thus, the presence of barium reduces the energy needed for electron emission (electrical electrode loss) and significantly lowers the electrode temperature to a level that allows for the long-term operation of tungsten filaments.

The sensitive coupling of work function and hot-spot temperature should be illustrated by another calculation. It can be assumed that a typical hot-spot temperature is 1250 K and a work function is 2 eV for barium on tungsten [MISHRA et al. 2004]. An increase of the work function of 0.1 eV, e.g. by the reduced production of barium would therefore lead to an increase of the hot-spot temperature of 56 K to 1306 K. Thus, even a minor increase of the work function leads to a significant increase of the electrode temperature and therefore to increased electrode erosion.

Production of barium during operation

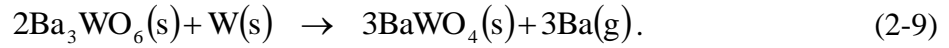
The free barium is continuously produced during operation. After activation, the emitter consists of barium oxide. In hot-spot operation mode, the barium is provided from reduction of the oxide by tungsten:



whereas, the corresponding vapor pressure of free barium is given, according to Rutledge and Rittner [1957], by:

$$p_{Ba(g)} = 133.3 \text{ Pa} \cdot 10^{\frac{8.02 - \frac{16400 \text{ K}}{T}}{}}. \quad (2-8)$$

The reaction appears only at the tungsten surface and is limited by the temperature (see equation (2-8)), the loss of the produced barium and the presence of barium oxide at the surface. The produced barium tungstate Ba_3WO_6 forms a layer at the tungsten surface limiting further transport of barium oxide to the surface as well as the diffusion of the free barium produced (see Figure 2-8). However, Rutledge and Rittner [1957] have shown that reaction (2-7) does not represent the end point in the reduction of barium oxide. The produced tungstate Ba_3WO_6 is capable of further reduction with tungsten:



For this reaction the corresponding vapor pressure of free barium is given by:

$$p_{Ba(g)} = 133.3 \text{ Pa} \cdot 10^{\frac{8.02 - \frac{16860 \text{ K}}{T}}{}}. \quad (2-10)$$

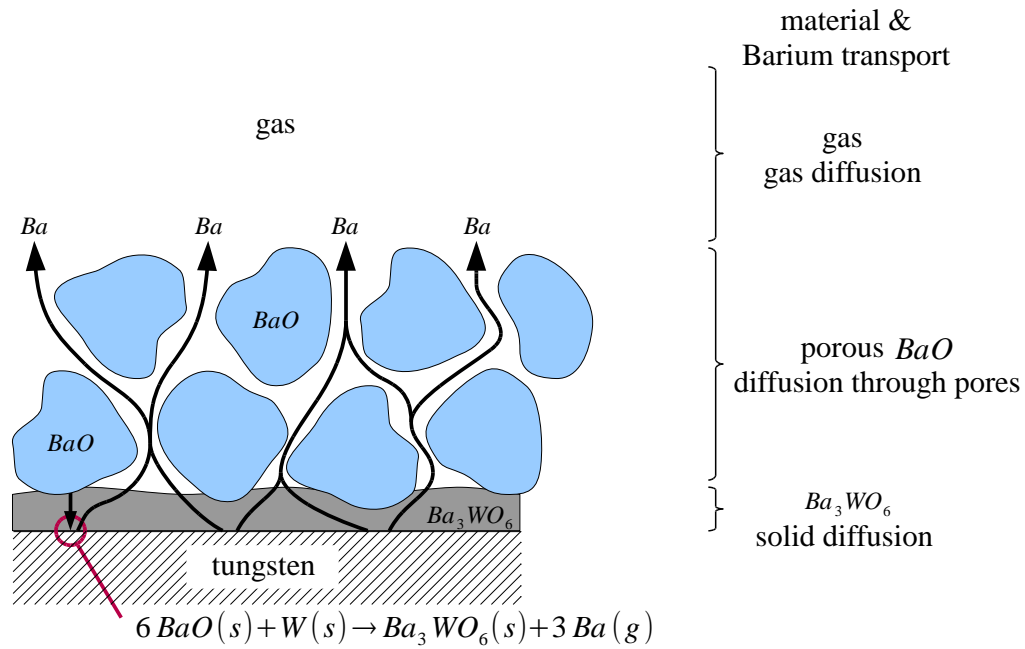


Figure 2-8: Production of free barium at the surface of tungsten wires during operation in spot mode at temperatures of about 1250 K. The loss of the produced barium is determined by the diffusion through the Ba_3WO_6 layer (solid diffusion), diffusion through the porous emitter (primary BaO), and diffusion through the buffer gas to the inner wall.

As the vapor pressure of free barium produced by reaction (2-9) at 1250 K is about half of the pressure produced by reaction (2-7), it could be concluded that reaction (2-7) is dominant. Through experimental studies, Rutledge and Rittner [1957] determined that

normal electron emission occurs as long as barium is generated by reaction (2-7) and that emission fails when reaction (2-9) takes over as the source of free barium, causing the end of the electrode's life.

2.3 Electrode erosion

The lifetime of a fluorescent lamp is determined by the lifetime of its electrodes. Thus, long living, robust electrodes are essential for durable fluorescent lamps. During live time, the electrode and its emitter are consumed. Thus, the investigation and understanding of the erosion process is of special interest.

The electrode operation strongly depends on the presence of free barium, produced by reduction of barium oxide. If the amount of free barium is not sufficient to reach the thermionic emission necessary, the lamp would not ignite or would stay in the glow mode, causing rapid destruction of the electrode. Finally, the electrode's lifetime depends on the remaining reservoir of the emitter, primarily barium oxide. Considering this, the term electrode erosion is equivalent to the term emitter erosion. In a broader definition, all processes lowering the lifetime of the electrode during operation could be understood as electrode erosion. There are three essential processes: sputtering (removing electrode material), chemical reaction (consuming barium or reducing further barium production), and the evaporation of barium (consuming the barium emitter), which will be discussed in more detail.

2.3.1 Sputtering

If ions with a certain amount of kinetic energy hit the electrode surface, the emitter material is released by sputtering. In case of the alkali oxide electrode, sputtering occurs for ion energies above 15 eV [GARNER 2008b; WAYMOUTH 1971]. The amount of sputtering increases exponentially as the kinetic energy of the incident ion increases above this sputter threshold [STUART and WEHNER 1962]. As the kinetic ion energy at the electrode surface is determined by the cathode fall voltage (the potential drop of the (approx.) 0.1 mm thin cathode sheath at the surface), even a small increase of the cathode fall can drastically increase sputtering.

In particular, sputtering occurs during instant start (cold start). The lamp ignites in glow-mode (glow discharge) where cathode fall voltages up to 100 V [WAYMOUTH 1971] may appear, causing a significant amount of sputtering. It has been proved by [HADRATH 2007], that the kinetic energy of the ions is sufficient enough to sputter the emitter material and also the tungsten. After a certain time in the glow mode, the electrode is heated by ion bombardment and transits into the arc-mode (glow-to-arc-transition). In the arc-mode, thermionic emission dominates and the cathode fall voltage is below the sputter threshold.

The instant start limits the number of switching cycles and reduces the electrode lifetime. To reduce sputtering during ignition, the electrode could be heated before ignition, the so called warm-start [GOUD and DORLEIJN 2002]. This delayed ignition is the standard

procedure of modern electronic ballasts and leads to a significantly increased electrode ignition durability.

During operation, sputtering always appears if thermionic emission is not sufficient. The electrode is designed for one optimal discharge current by using a tungsten filament producing enough ohmic heating for reaching the desired hot-spot temperature. During dimmed operation, a lower discharge current is applied and a sufficient hot-spot temperature could not be reached. This will result in a higher work function causing higher cathode fall voltages and therefore causing sputtering. To reduce sputtering in dimmed operation, the electrode could be heated by an additional heat current through the electrode [GOUD and DORLEIJN 2002].

Finally, sputtering will occur before end of life. If the emitter is consumed or chemical reactions making it ineffective, the work function will increase and, accordingly, the cathode fall voltage will exceed the sputter threshold. Thus, at its end of life the electrode is destroyed by sputtering.

2.3.2 Chemical reactions

Electrode erosion due to chemical reactions summarizes all chemical reactions that lower electrode life. There are two main categories of possible reactions, reactions consuming emitter material (especially barium or barium oxide) and reactions reducing or preventing the production of free barium, resulting in insufficient thermionic emission and therefore increasing the cathode fall voltage above the sputter threshold. Usually, these reactions are caused by impurities during the lamp's production, such as water. Another typical process is the sputtering itself. During instant start, a certain amount of tungsten is sputtered and attached inordinately on the cold electrode. This could lead to an increase of work function, resulting in lower thermionic emission leading to higher electrode temperatures [WAYMOUTH 1971]. After 10 to 60 minutes, the effect will disappear and the electrode returns to normal operation.

2.3.3 Barium evaporation

During steady-state operation, the electrode operation depends on the presence of free barium on the electrode's surface. Due to the high hot-spot temperatures, the free barium inevitably evaporates. Such loss has to be compensated by continuously delivering free barium by reduction of the barium oxide according to reaction (2-7). As the amount of barium oxide is limited, its consumption due to barium evaporation determines the electrode's lifetime. To illustrate the consumption, in Figure 2-9 SEM images of a new electrode (left) and an electrode at about 75% of its lifetime (right) are presented. First, the hot-spot is attached at the right side of the electrode at the intersection of coated and uncoated electrode. During lamp life, the hot-spot moves along the electrode (to the left), consuming the local barium oxide and producing a rough surface of consumed emitter and barium tungstate Ba_3WO_6 [VAN DEN HOEK 2003].

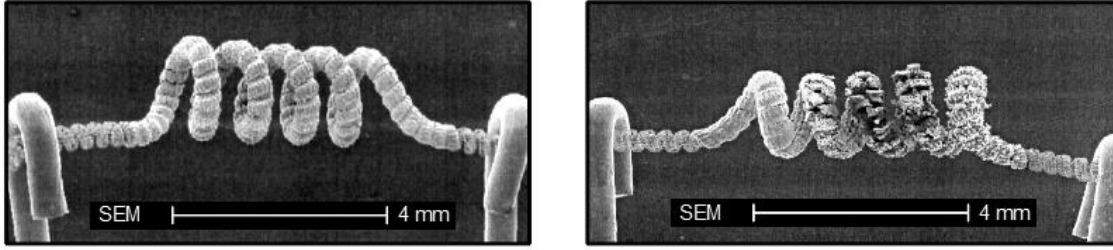


Figure 2-9: SEM image of triple coils: a new electrode (left), and an electrode at about 75% of its lifetime (right). During lifetime, the hot-spot moves from the right side along the electrode and consumes the BaO emitter by production of free Ba and Ba_3WO_6 remaining as porous coating at the electrode. Pictures are taken from van den Hoek [2003].

If the supply of barium oxide is not limited at the hot-spot, reaction (2-7) is in thermodynamic equilibrium and free barium with a density according to the hot-spot temperature (see equation (2-8)) is produced at the tungsten surface. In that case, the overall barium production rate is equal to the loss rate of barium, as lost barium will be delivered in addition by the reaction to sustain the vapor pressure at the tungsten surface. Thus, the emitter consumption is proportional to the loss rate of the free barium.

The loss rate is determined by the diffusion of barium from the tungsten surface through the barium tungstate Ba_3WO_6 (solid diffusion), through the porous emitter (KNUDSEN diffusion [RUTLEDGE and RITTNER 1957; STECKELMACHER 1986; WAYMOUTH 2003]), and finally through the buffer gas (gas diffusion) towards the inner wall, as illustrated in Figure 2-8. The solid diffusion through the barium tungstate Ba_3WO_6 depends on the thickness and permeability of the layer that may change during time and is characterized by the history of the electrode. The diffusion through the emitter depends on its porosity determined by the particle size, the emitter mixture, and the activation process. The diffusion through the buffer gas could be described by the diffusion equation:

$$\frac{\partial}{\partial t} n_{\text{Ba}}(t, \vec{r}) = -\vec{\nabla} \cdot \Gamma_{\text{Ba}} = \vec{\nabla} \cdot (D_{\text{Ba}} \vec{\nabla} n_{\text{Ba}}(t, \vec{r})), \quad (2-11)$$

where $n_{\text{Ba}}(t, \vec{r})$ is the temporal and space dependent barium density, Γ_{Ba} is the barium flux and D_{Ba} the barium diffusion coefficient in the buffer gas. As the barium flux Γ_{Ba} , and, accordingly, the barium loss directly depend on the diffusion coefficient, the obvious approach for reducing the losses is to keep the diffusion coefficient as small as possible. This could be done by either increasing the buffer gas pressure or choosing a noble gas with higher mass. It has been shown by Waymouth [1971], that an increase of argon pressure from 1 Torr up to 2.5 Torr would reduce the barium loss by the same factor of about 2.5. However, the range of choosing a buffer gas to reduce barium losses is small, as the efficacy of UV emission strongly depends on it and has a higher priority in lamp design.

Not all of the evaporated barium is directly lost, since a minor amount is transported back to a cold region of the electrode, either as barium atoms or as barium ions. In contrast to production by reduction of BaO, the vapor pressure of pure barium, is quite higher [RITTNER et al. 1957]:

$$p_{Ba(g)} = 133.3 \text{ Pa} \cdot 10^{7.83 - \frac{9730 \text{ K}}{T}}, \quad (2-12)$$

For typical hot-spot temperatures (at 1250 K, $p_{Ba(g)} = 148 \text{ Pa}$), back transported barium would completely evaporate as the hot-spot would be formed close by. Thus, back transported barium is not available for lowering the work function in the presence of the hot-spot and is effectively lost for further electrode operation.

Beside higher gas pressure and the usage of high-mass noble gases, the barium loss could be reduced by the addition of SrCO_3 and CaCO_3 to the basic emitter mixture. It has been shown by Rutledge and Rittner [1957] that a mixture of barium and strontium oxide could significantly reduce the barium vapor pressure according to equation (2-8).

However, the total barium evaporation is very difficult to calculate. Whereas the diffusion through the buffer gas is more or less well defined, the diffusion of barium oxide and the produced barium through the barium tungstate Ba_3WO_6 layer at the tungsten surface depends of several aspects as the structure of the layer and the electrode history. In addition, consideration must be given to the KNUDSEN diffusion through the porous emitter. Accordingly, research for determining evaporation focuses on diffusion through the buffer gas. At typical electrode life times of 20.000 hours, the evaporation rate and the densities of the evaporated barium are quite low and very difficult to determine. Thus, the research on barium evaporation was limited by the actual technical capabilities, whereas the evaporation has been determined indirectly and not during operation. Therefore, there are still attempts to determine the real barium evaporation directly and during operation.

3 Experimental methods

In this study, the absolute densities of the eroded barium are measured by laser-induced fluorescence (LIF), and to understand the electrode operation in detail, additional methods are applied. The electrode temperature as a key parameter for evaporation is measured by an optimized pyrometric measurement system. The electrode operation itself is characterized by its local work function determining the electrode sheath plasma. Thus, the cathode fall voltage is determined by the capacitive coupled band method and the electron densities in the electrode region are measured by microwave interferometry.

To increase readability of the thesis, in the following an overview of the applied methods is given. A more detailed description including the characterization of the applied setup, optimization techniques, and error discussion can be found in Appendix A, in order to provide readers focused on the results and discussions with an overview and to provide readers interested in experimental methods with details. Afterwards, the investigated lamps and precondition parameters are described.

3.1 Resistive method for determination of average electrode temperature

For investigations of electrode material evaporation of a heated electrode and for calibration of the pyrometric electrode temperature measurement, the resistive method for determination of average electrode temperature is applied. In general, the electrode resistance during heating by a constant DC-current is related to its cold resistance measured at known temperature and allowing the determination of an average electrode temperature. Due to its practicable application it has been established as a standard method for commercial fluorescent lamps [DORLEIJN and GOUD 2002; LIDE 2001; MYOJO 2010; WHARMBY 2004].

The electrodes of fluorescent lamps consist of a coiled construction of tungsten wire filled with an emitter, whereas the relative amount of emitter may vary according to the manufacture and the lamp type [DORLEIJN and GOUD 2002]. By applying a DC current through the electrode, the current is transported only by the tungsten wire. At high temperatures and without impurities, the electric resistance of such a tungsten wire depends only on its temperature. This effect can be used to derive the temperature from the ratio of the resistance at high temperatures R_h divided by the resistance at room temperature (cold) R_c . For the temperature range, interesting for fluorescent lamp electrodes (up to 1400 K), the following relationship has been established [DORLEIJN and GOUD 2002; LIDE 2001; MYOJO 2010; WHARMBY 2004]:

$$T_h = T_c \cdot \left(\frac{R_h}{R_c} \right)^{0.814}, \quad (3-1)$$

where T_h is the unknown high temperature during heating and T_c is the known cold reference temperature (normally room temperature at $25^\circ\text{C} = 298.15\text{ K}$) at which R_c has been measured.

The cold electrode resistant (R_c is in the range of 1 to 3 Ohm) is measured at a low DC current of about 1 mA to prevent heating during resistance measuring. To ensure a precise measurement and minimizing effects of the contact resistance, the four-wire sensing according to Figure 3-1b is applied. The voltage is measured by KEITHLEY 2001-Multimeter and the current is provided and measured by the high precision current source KEITHLEY 238-Current.

For increased accuracy, the contact surfaces of inner electrode posts and outer contact are soldered. Before each measurement, the setup is calibrated with a reference that consists of an original lamp socket with shortened electrode (see Figure 3-1).

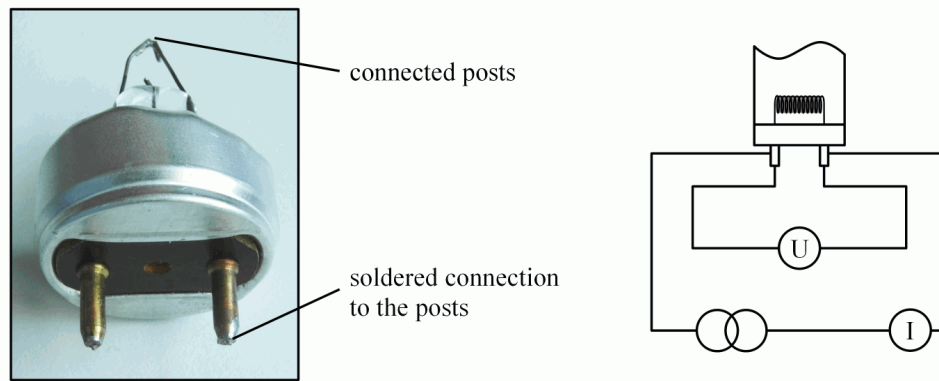


Figure 3-1: Setup for heating and determination of the average electrode temperature by the resistive method. Electrical setup for heating the electrode and high precision electrode resistance measurement by four-wire sensing (right), and original lamp socket with shortened electrode used as calibration reference (left). The contact surfaces of inner electrode posts and outer contact are soldered.

With this setup and the applied calibration, an absolute accuracy of the average electrode temperature of about 1% has been achieved at the interesting temperature range of 1000 K to 1400 K. The systematic error due to variation in contact-circuit resistance of different lamps determines the main error (see Appendix B.4 for details).

3.2 Pyrometric electrode temperature determination

To measure the electrode temperature during operation as a key parameter characterizing thermionic emission and emitter evaporation, a pyrometric system [GARNER 1998] provided by the OSRAM AG, is used.

In general, the electrode is imaged on an infrared detection array and the intensity is measured (see Figure 3-2). According to PLANCK's law (see equation (A-1)), the infrared intensity could be used to calculate the temperature. Such a one-dimensional temperature profile along the electrode could be determined. The applied system depicts the electrode via an infrared transparent lens on an InGaAs detector array, which has 128 pixels and a

spectral response range between 900 nm and 1700 nm. To avoid unwanted emission of plasma in the electrode region, an optical bandpass filter (maximum transmission at 1500 nm) is placed in front of the detector array.

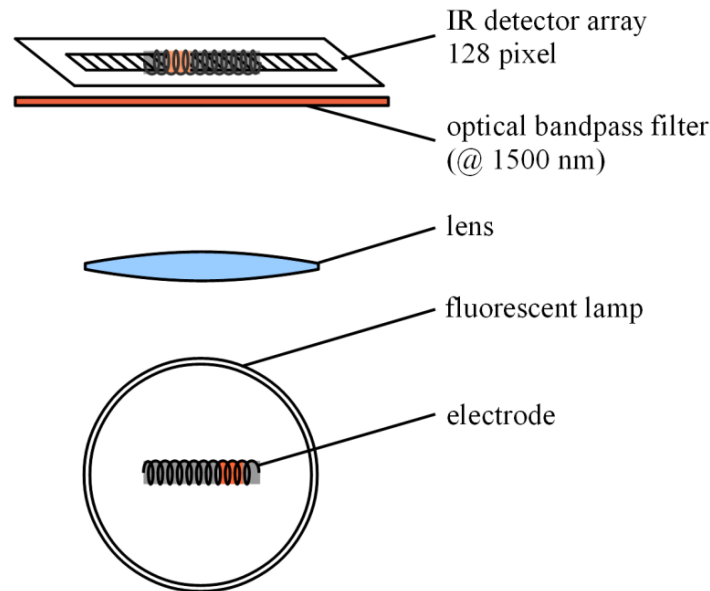


Figure 3-2: Basic configuration of the spatially resolved electrode temperature measuring system.

In principal, PLANCK's law allows the calculation of the temperature from the measured infrared intensity by a proper calibration of the system. For calculation, the emissivity of the electrode surface, which is defined by the surface material and structure, has to be known. In contrast to other materials, alkali earth oxides show a huge variation of the emissivity according to the temperature. In addition, the emissivity is affected by impurity of the surface and disposal of barium and tungsten. Therefore, the emissivity of the emitter material varies widely with the temperature and during lifetime. To overcome this problem, a special calibration method has been developed.

For every measurement, alignment of the electrode takes place first. Next, the electrode is heated by several DC currents (also called heat current) while the lamp is off and the intensities of the detector array are stored. Simultaneously, the electrode resistance is measured and the average electrode temperature is determined according to the resistive method (see Section 3.1). As such, for each pixel the measured intensities could be assigned to a certain temperature used as calibration. For measurements during operation, for each pixel the actual intensity is used to interpolate the temperature from the intensity – temperature calibration for the corresponding pixel. Such a calibrated electrode temperature profile could be determined with a temporal resolution of about 5 ms. The method allows the determination of electrode temperatures for nearly every type of electrode and electrode material without knowledge of its emissivity. Mainly, the accuracy is determined by the calibration, which leads to an error of about 1.7%.

Details on the method, setup, and calibration are given in Appendix A.1

3.3 Cathode fall estimation with band method

The band method is applied to estimate the cathode fall voltage that characterizes the electrode operation. The cathode fall voltage depends on the formed hot-spot, the resulting effective work function, the discharge current, the buffer gas and the amount of mercury vapor. It directly determines the plasma in the electrode region. For optimal electrode operation, the cathode fall voltage has to be below a certain level (typically 15 V) to prevent electrode erosion due to sputtering (see Section 2.3.1). Thus, measuring the cathode fall voltage provides essential information about electrode operation and plasma conditions. The Band diagnostic method, illustrated in Figure 3-3, is based on placing metallic foil around the outer surface of the glass tube at the electrode region and measuring the potential between electrode and foil. The metallic foil is capacitive coupled to the inner wall sheath. Therefore, the method can only be applied to AC driven lamps. Due to its simplicity, the band diagnostic has been established as a standard method for fluorescent lamps [HAMMER 1989, 1995; NACHTRIEB et al. 2005]. Other methods such as an internal probe [CHEN and LABORATORY 1964], a movable electrode [ARNDT 1976; MISONO 1992], or actinometry⁶ [HADRATH et al. 2007] need a modified lamp or deliver much less information.

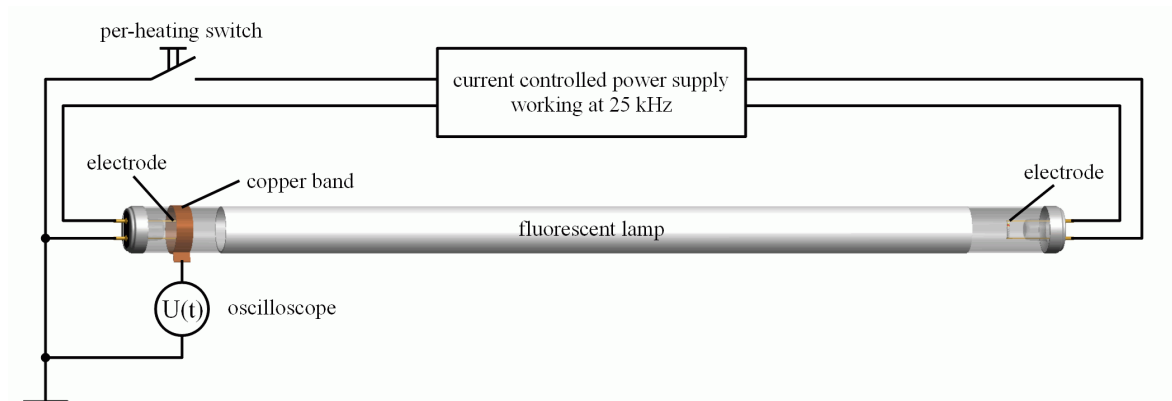


Figure 3-3: Experimental setup for the band diagnostic method. A metallic foil is placed around the outer surface of the glass tube and the potential between electrode and foil is measured.

The simplicity of the setup is accompanied by several limitations on the interpretation of the measured potential. Although the measured signal is related to cathode fall voltage, it involves effects by the discharge, e.g. the plasma-wall sheath at the inner surface, and effects of the external measurement circuit. The potential difference between the inner wall sheath and the boundary between bulk plasma and electrode sheath produces an additional unknown shift. Nevertheless, Rich Garner [2008c] significantly improved the understanding of the method and interpretation of the signals. For detailed understanding of

⁶ Actinometry, a non-invasive method, determines if the cathode fall voltage exceeds certain thresholds by observing certain emission lines of Argon.

the method, an equivalent circuit representation of the band diagnostic is discussed in Appendix A.2. It includes the electrode sheath potential (the quantity of interest), the potential between the electrode sheath-plasma boundary and inner wall sheath-plasma boundary, the potential drop through the inner wall sheath, and the potential across the glass.

For the measurements in this work, the applied band probe consists of a 0.15 mm thick and 24 mm wide copper foil. The band is wound completely around the outer surface of the glass tube and is centered to the electrode. The band is connected to the voltage probe LeCroy PP005 (voltage divider 10:1, 10M Ω , 11pF), which is connected to the digital storage oscilloscope LeCroy WavePro 7300. For measurement, the signal is averaged 100 times, whereas the oscilloscope is triggered by zero crossing of the discharge current.

To allow comparison of different lamps and discharge conditions and especially to open the opportunity to compare the results with other work, a new calibration method for the external circuit (including the formed capacitor C_b between inner wall sheath and outer band probe, the voltage probe and the oscilloscope) has been applied. It is based on a comparison of the potential along the positive column with the potential measured with a second band probe at the other electrode. With the calibration, a scaling factor of about $c_{\text{band}} \approx 1.145$ has been determined for the applied setup. It varies for different lamps in a smaller range of about 5%.

However, a detailed discussion of the method of the equivalent circuit representation and the calibration method is given in Appendix A.2.

3.4 Electron density measurement by microwave interferometry

In order to characterize the plasma in the electrode region by its electron density, the non-invasive method of microwave interferometry is applied. In contrast to other invasive methods, such as internal probe⁷ measurements or the STARK broadening of H_β -line⁸, microwave interferometry is best suited for application on commercial fluorescent lamps.

Microwave interferometry measures the phase shift of electromagnetic waves by propagation through a plasma. Under the investigated condition, the wave number k describing the propagation of electromagnetic waves depends on the electron density n_e :

⁷ For internal probe measurements, a thin electric conductor is inserted in the active plasma and its voltage-current characteristic is measured [CHEN and LABORATORY 1964; MOTT-SMITH and LANGMUIR 1926]. The method requires a modification of the discharge by inserting the internal probe, which also disturbs the discharge itself.

⁸ To determine electron densities by broadening of H_β -lines [TORRES et al. 2007], the STARK broadening due to the electric fields, depending on the electron density, is measured. This method could be applied for electron densities above 10^{20} m^{-3} and needs the presence of hydrogen. For application in fluorescent lamps, hydrogen has to be added to the gas filling.

$$k = \frac{\omega}{c} \sqrt{1 - \frac{n_e^2}{n_c^2}}$$

with

$$n_c = \frac{\epsilon_0 m_e}{e^2} \cdot \omega^2$$
(3-2)

where ω is the angular frequency, c is the speed of light, n_c is critical electron density, m_e is the electron mass, ϵ_0 is the vacuum permittivity and e is the electron charge. The detailed discussion as well as the concluded assumptions are given in Appendix A.3.1.

For electron densities smaller than the critical density $n_e < n_c$, the phase of electromagnetic wave is shifted [RACKOW et al. 2011]. By measuring these phase shifts, the path average electron density could be determined. To ensure applicability of the method, the frequency of the electromagnetic wave has to be chosen carefully. On the one hand it should be very high to achieve a sufficient spatial resolution (determined by the resulting wavelength), whilst on the other hand the increasing frequency results in a smaller phase shift, and as such the detection limit is lower.

As a compromise, a customized 150 GHz system from Millitech Inc. has been applied. The interferometer operates as a heterodyne detector, whereas the operational frequency $f_{\text{HF}} = 150 \text{ GHz}$ is mixed with a second frequency $f_{\text{LO}} = 150.1 \text{ GHz}$ of a local oscillator to an intermediate frequency $f_{\text{ZF}} = 100 \text{ MHz}$ used for phase detection. The resulting 150 GHz beam is focussed via a dielectric lens made of REXOLITE to the region of interest. A second lense and corrugated horn antenna are used for detection. By measuring the beam path, it has been proven that a spatial resolution of about 4 mm could be realized.

For phase detection, the measure-signal and the reference-signal at 100 MHz are sampled with PC-AD-card (Gage Cobra GS21G8) at 500 MS/s and analyzed via an optimized algorithm. The algorithm for analyzing the sampled signal allows for the adaptation of the temporal resolution whereas a higher temporal resolution results in a lower-phase resolution. For typical measurements, a temporal resolution of 256 ns is applied. The resulting error in the determined path average electron density $\langle n_e \rangle_{\text{path}}$ is $2.4 \cdot 10^{16} \text{ m}^{-3}$ for a single shot measurement and $2.4 \cdot 10^{15} \text{ m}^{-3}$ for a 100 time averaged standard measurement.

In order to overcome the restrictions of these method a new technique was developed to determine the phase shift caused by the plasma. During measurement, the lamp is rapidly switched off by an IGBT⁹-shorting circuit, and thus the phase when the plasma is on and the reference phase when the plasma is off are determined during one measurement with a duration of about 10 ms.

A detailed discussion of the method, the applied setup, the phase detection algorithm, and the resulting error are given in Appendix A.3.

⁹ A **insulated gate bipolar transistor** (IGBT) is a three-terminal power semiconductor device, used for fast switching. It consist of an isolated gate field-effect transistor for the control input and of a bipolar power transistor for switch the load.

3.5 Determination of absolute particle densities by using LIF

For determination of eroded barium and barium ions in the electrode region (during lamp operation), LIF is applied. In contrast to other non-invasive methods such as laser absorption, LIF is more sensitive and allows a better spatial resolution necessary for measurements of the low densities and strong gradients that occur.

The method based in exciting a state of an atom (or a molecule) of interest by laser and observing fluorescent emission due to the natural decay of the excited state. The emitted fluorescent radiation is proportional to the density of the state excited. The method could be described by a system of rate equations that include the absorption of the laser photon and the decay of the excited state by emission of fluorescent photons. The absorption and emission of photons are wavelength selective and characteristic for each atom and molecule. Thus, by choosing proper laser-wavelength and observing the fluorescent wavelength, the density of a selected state of the species of interest could be measured. Typically, a state system with different excitation and fluorescent wavelengths is chosen to separate laser and fluorescent photons. The theoretical fundamentals of the LIF-spectroscopy are discussed in detail in several textbooks such as [DEMTRÖDER 2007], as well as in a few theses such as [KRAMES 2000; NIEMI 2003; SCHNABEL 1999]. A short summary of the fundamentals necessary for this work is presented in Appendix A.4.

For the applied setup, a pulsed solid-state Nd:YAG laser QUANTA RAY PRO-230 (from SPECTRA PHYSICS) is used to pump the dye laser PRECISIONSCAN - D1800 (from SIRAH) [SIRAH-GMBH 1998] with a double grating resonator (each with 1800 grooves/mm) in LITTMANN configuration. In case of exciting the barium ground state, the laser frequency is double by a KDP¹⁰ crystal. The typical line width is 1.34 pm (value given for 350 nm). For beam quality optimisation, a spatial filter is used resulting in a GAUSSIAN beam profile with a full wide at half maximum (FWHM) of approximately 0.72 mm. Antireflective-coated prisms are used to direct the laser beam through the electrode region of a fluorescent lamp. The fluorescent radiation is observed perpendicular to the laser beam (see Figure 3-4a).

The region of interest is imaged by a system of two lenses to the entrance slit of a 0.5 m monochromator (ACTON RESEARCH – SPECTRA PRO-500I) used as a wavelength separator to suppress scattering laser light as well as background light emitted by the plasma in the lamp. The resulting observation volume has a size of $0.67 \times 0.67 \times 1 = 0.44 \text{ mm}^3$.

For light detection, a gated photomultiplier (PMT, HAMAMATSU D1477-06) is mounted behind the exit slit. The signal of the multiplier is detected by a digital storage oscilloscope (LeCroy WavePro 7300) triggered by a synchronization signal of the Nd:YAG laser. For further analyses, the waveforms are transferred to a personal computer (PC).

To improve sensitivity, the temporal shape of the fluorescent signal is analyzed. The detected fluorescent pulse has a length of about 10 ns, which corresponds to the natural

¹⁰ Potassium Dihydrogen Phosphate (KDP) is a tetragonal, negative uniaxial crystal that could be used for frequency doubling of lasers. For successful frequency doubling, the optical axis of the crystal must be oriented in the right angle (depending on the wave length) to the incident light.

lifetime of the excited state. For background corrections, the signal before and after the pulse is used (see Appendix A.4.3). In case of measuring barium atom ground state, a detection limit of $n_{\text{Ba, lower limit}} \approx 1.5 \cdot 10^{13} \text{ m}^{-3}$ has been realized.

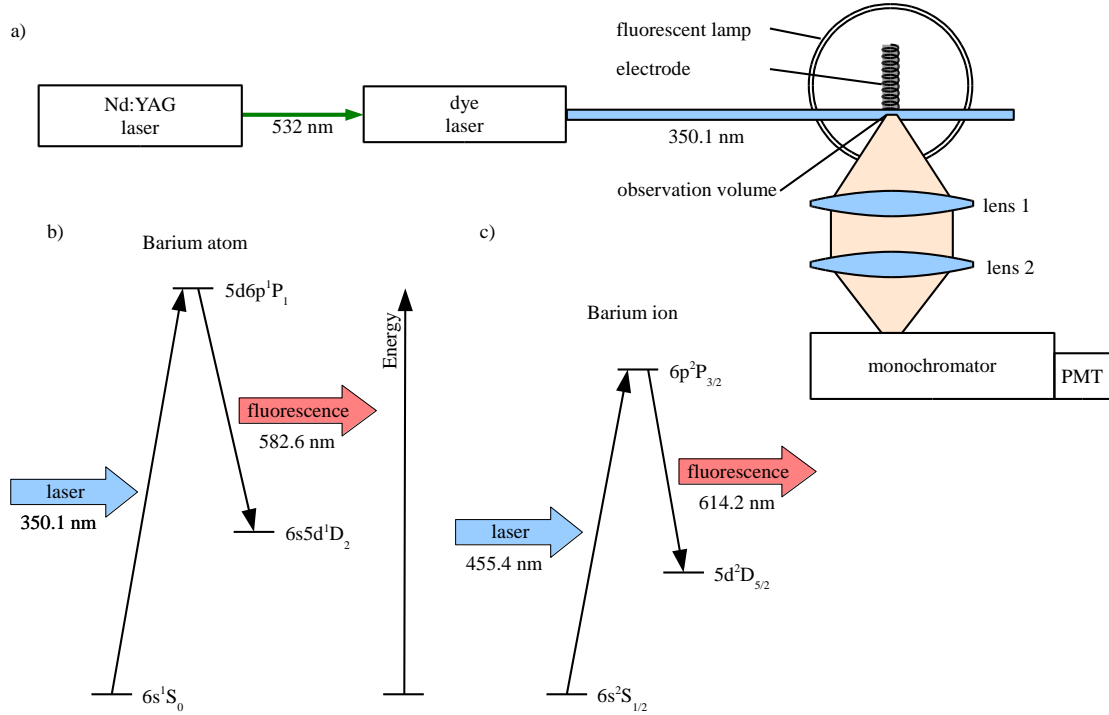


Figure 3-4: Absolute particle densities determination of eroded barium by LIF

- Experimental arrangement of the LIF experiment. The beam of a Nd:YAG pumped dye laser is used to excite barium or barium ions in front of the electrode of a fluorescent lamp. The fluorescent radiation is imaged to a monochromator and detected by a photomultiplier (PMT).
- Part of the barium atom level diagram with transitions used for the experiment
- Part of the barium ion level diagram with transitions used for the experiment

For absolute density measurements the laser beam excitation cross section, the exact observation volume and the observation system have to be calibrated. Thus, for this work a Rayleigh-scattering calibration is applied (see Appendix A.4.4).

In order to measure barium atoms, the ground state is excited (350.1 nm) to the barium level $\text{Ba}(5d6p^1P_1)$ and the fluorescent radiation at 582.6 is measured (see Figure 3-4b). When measuring barium ions, the ground state is excited (455.4 nm) to the level $\text{Ba}^+(6p^2P_{3/2})$ and the fluorescent radiation at 614.2 is measured (see Figure 3-4c).

According to the applied laser power of approximately 8 μJ , the excited states should be saturated (in equilibrium according to their statistical weights) and there should be no dependence of the fluorescent radiation on the laser power. However, a nonlinear increasing fluorescent signal by increasing laser power has been found. To solve this problem, a model solving the temporal and spatial rate equations system has been developed (see Appendix A.5). It has been found that the increasing fluorescent radiation results from spatial power broadening. By increasing laser power, the region where the

excited system is saturated expands. Thus, the effective laser excitation cross section also expands and has to be considered for absolute density calibration. In the experiment, the obtained saturation characteristic is used for correction and absolute calibration. It is also used for correction of laser power fluctuations during measurements.

Further details on the method, the setup, characterization of the setup, the calibration, and the saturation correction model are given in Appendix A.4.4 and A.4.5.

3.6 Investigated lamps and operation conditions

For investigation, fluorescent lamps identical to commercial T8–36 W (L36W/765) lamps are used. The tube diameter is 25.4 mm and the nominal length is 120 cm. The lamp contains mercury and a mixture of 75% argon and 25% krypton at a pressure p of 2.10 mbar.

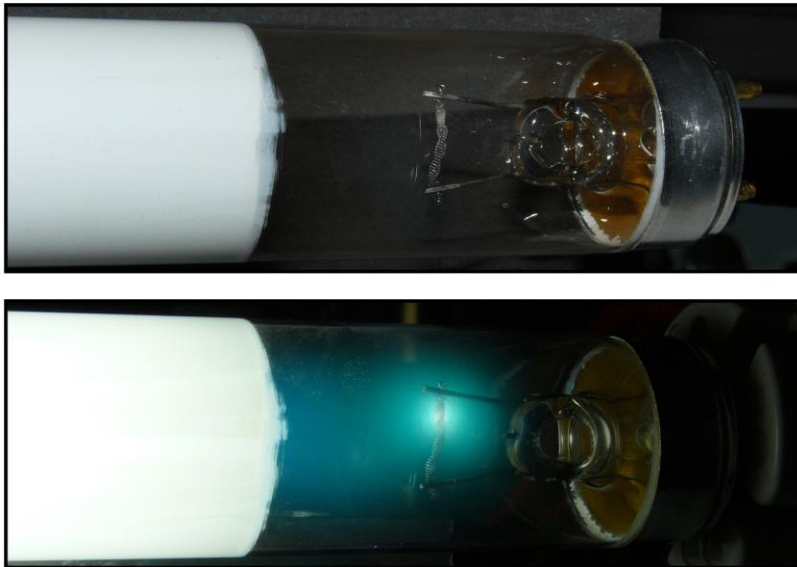


Figure 3-5: Photos of the electrode region of the investigated T8-lamps. In contrast to commercial lamps, the ends have been cleared of phosphor to allow LIF and temperature diagnostics.

As electrode, so-called stick coils with a nominal rms lamp current of 320 mA are used. The electrode is carried by two holders (posts) positioned at a distance of about 10 mm. A total of 10 mg of standard OSRAM emitter (about 70% BaCO_3 and 30% SrCO_3) are used. To enable transmission for LIF and temperature diagnostics, the ends have been cleared of phosphor. Photos of the electrode region with the typical visual observation of the electrode region are shown in Figure 3-5.

To be as close as possible to commercial lamps, the lamps have been produced on the original assembly line of OSRAM-AUGSBURG. To clear phosphor from the ends, the glass tubes have been taken from the assembly line, the phosphor at the ends have been wiped out, and the lamps have been placed back on the assembly line. The emitter has been activated according the original OSRAM standard.

Before investigation, the lamps are burned-in for 100 hours. This preconditioning leads to an activation of the electrode processes and builds up a stable hot-spot.

Lamp operation

For lamp operation, a special current-controlled power supply provided by the OSRAM AG has been used. It is quartz-oscillator stabilized and operates at 25 kHz. The frequency stabilization is necessary for synchronization of the laser system. As is typical in other experimental setups, a combination of power amplifier and transformer are used. These setups produce a disturbed current curve during zero crossing¹¹. With the applied power supply the effect could be eliminated, which is important for investigations related to commercial ballast systems.

Figure 3-6 depicts the electrical setup, where each electrode is connected with two wires to the power supply. The second wire is used for pre-heating the electrode before lamp ignition (warm start), after which the current flows primarily to one of the two wires (full lines in Figure 3-6). To ensure stability and reproducibility of the formed hot-spot, the primary current wire is always connected to the same connection pin (marked).

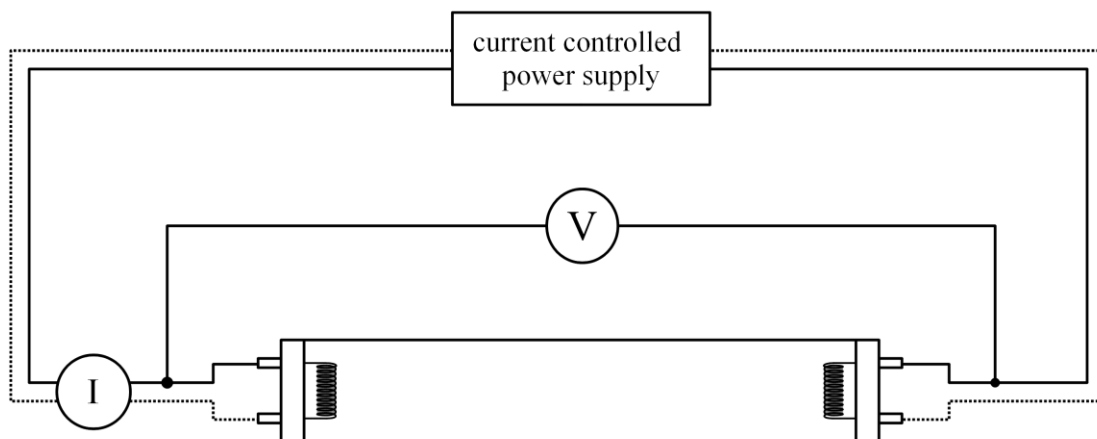


Figure 3-6: Standard Electrical setup.

The lamp voltage is measured with the high voltage differential probe LeCroy ADP300 (bandwidth DC up to 20 MHz) connected to the oscilloscope LeCroy WavePro 7300. For current measuring, the high frequency AC/DC current probe LEM-PR50 (bandwidth DC up to 50 MHz) is used and connected to the oscilloscope. The current signals is also used for triggering the delay generator STANFORD RESEARCH DG535 synchronizing the laser

¹¹ In general, the combination of power amplifier and transformer leads to a voltage controlled power supply. Thus, the applied voltage determines the current through the lamp. During zero crossing the polarity of the lamp changes whereas, the operation mode of the electrodes changes from cathode to anode or vice versa. For the cathode phase, the cathode fall has to build up. Before reaching the cathode fall voltage, no lamp current will flow. Thus, after each zero crossing of the lamp current a short period of zero current follows.

system to the lamp. By adjusting the delay time, the time between zero crossing of lamp current and laser pulse could be varied. The trigger signal is also used to trigger the interferometer.

Preconditioning before measuring

Before measuring, the lamp is preconditioned to ensure stable and reproducible conditions. The lamp is started pre-heated (warm start). Therefore, the electrodes are heated up by a current (about the nominal lamp current) through the electrodes. After 4 seconds, the lamp is ignited. Afterwards, the lamp burns for 30 minutes before measurements are taken. During this time, the lamp temperature increases and reaches a stable level. This is very important as the mercury vapor pressure strongly depends on the wall temperature. For practical reasons this time is used for adjustment of the lamp and the measurement system. After every change of lamp current, the lamp is again burned for 30 minutes before measurements.

3.7 Arrangement of the diagnostics

Due to lack of space, the LIF diagnostic and the interferometry could not be applied simultaneously. To ensure comparable lamp operations for both diagnostics, the time between both measurements has to be as short as possible. Therefore, the lamp is mounted on a motorized positioning system (see Figure 3-7) and could be moved in an automated fashion in x and z directions (for movement in y direction a manual stage is used). Thus after the LIF measurement, the lamp is moved to the interferometry measurement position. This allows both diagnostics to be applied in quick succession without switching the lamp off. In addition, the motorized positioning system allows fine spatial resolved scanning (spatial resolution of about 20 μm) of the electrode region for both diagnostics.

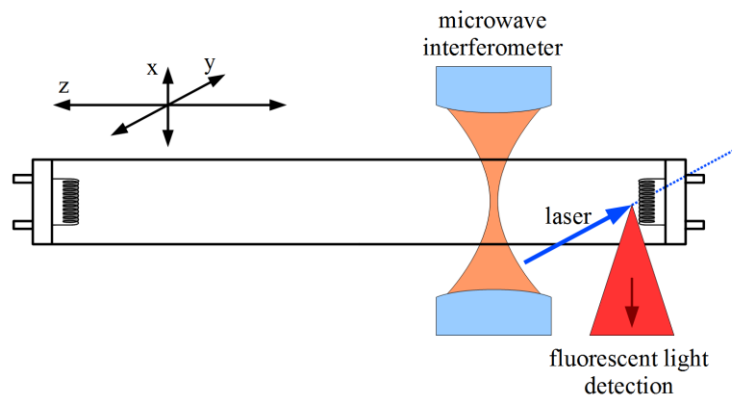


Figure 3-7: Experimental arrangement of the LIF and interferometry experiment. The lamp is mounted on a motorized positioning system (x and z-direction). Thus, it could be moved between both diagnostic positions (LIF and microwave interferometry). In addition, the positioning system is used for fine adjustment of the lamp position.

For the LIF diagnostics, an accurate adjustment of the electrode position is essential. For alignment of the electrode to the excitation laser beam, the electrode is moved through the beam by moving the lamp in z direction and the transmitted beam intensity is detected by a photodiode. The electrode position could be obtained from the measured intensity (see Figure 3-8), whereas the electrode edge is located where the transmitted beam intensity reaches a value of $(\text{maximum} + \text{minimum}) / 2$. Thus, the electrode could be positioned with an accuracy of about 0.05 mm for the LIF measurements. The normal LIF measurement position is 0.5 mm in front of the electrode so that the excitation beam does not hit the electrode surface.

As the distance between LIF position and interferometry position is known, the determined electrode position is also used for positioning the lamp for the interferometry measurement.

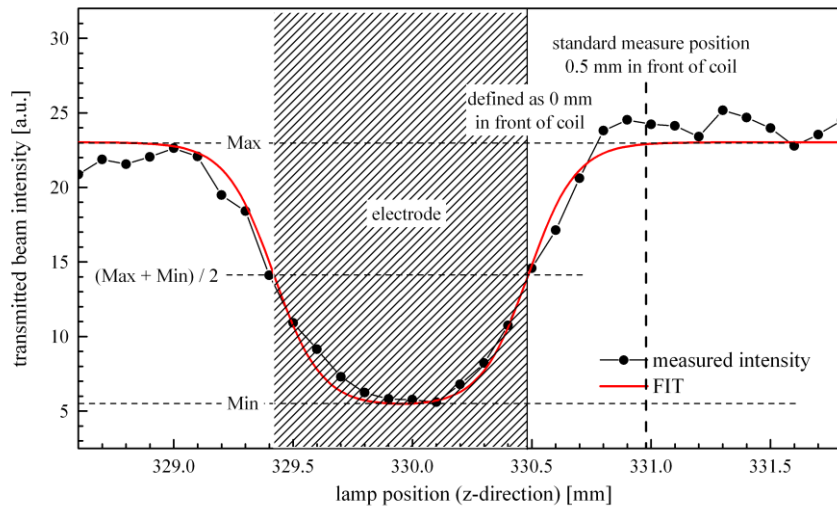


Figure 3-8: Positioning of the electrode for the LIF experiment. The electrode is moved through the excitation laser beam whereas the transmitted beam intensity is detected by a photodiode. If the beam hits the electrode, the laser beam is shadowed and the transmitted intensity decreases. From the slope, the position of the electrode edge could be obtained.

For temperature diagnostics, the electrode temperature diagnostic system replaces the interferometer setup. This allows direct determination of the electrode temperature after the LIF measurement. For this series of experiments, the interferometry is applied later.

4 Method and model for determination of absolute evaporation by the blanking method

During operation, the plasma in the electrode region affects the eroded electrode material. As such, a direct quantification of the absolute amount of electrode erosion is not possible without detailed knowledge of the plasma.

In the following, a new method for determining the absolute evaporation is introduced. First, the basic approach by quickly switching off the lamp is explained. Afterwards, the model for deducting the absolute evaporation from measured densities is introduced and validated.

4.1 Blanking method - basic approach

Once defused through the emitter, the evaporated barium is transported through the plasma in the electrode region. With the applied LIF, only the absolute barium atom ground state density could be measured. Hence, every process that influences the ground state densities also influences the measured LIF signal. In addition, the ground state density does not represent the total barium density. A fraction of barium is in an excited state or ionized particularly in the plasma in the electrode region. For determination of the total density of barium, these excited and ionized states have to be taken into account. In addition, the absolute density is of minor interest. The erosion of the electrode is characterized by the loss of the emitter, and thus the amount of lost barium and its transportation through the electrode region has to be determined. In general, the transport of the evaporated barium is described by its particle balance equation:

$$\frac{\partial}{\partial t} n_{\text{Ba}}(t, \vec{r}) = -\vec{\nabla} \cdot \Gamma_{\text{Ba}} - \nu_{\text{Ba}}^{\text{io}} n_{\text{Ba}}(t, \vec{r}) - \sum_i \nu_{\text{Ba}}^{0 \rightarrow i} \cdot n_{\text{Ba}}(t, \vec{r}) + \sum_i [\nu_{i \rightarrow 0} \cdot n_i(t, \vec{r})]. \quad (4-1)$$

The equation includes the time- and spatial-dependent densities $n_{\text{Ba}}(t, \vec{r})$ of the barium atom ground state and $n_i(t, \vec{r})$ of the excited levels, the time and spatial dependent ionization frequency $\nu_{\text{Ba}}^{\text{io}}$ and excitation frequency $\nu_{\text{Ba}}^{0 \rightarrow i}$ from the ground state to the excited level i and the de-excitation frequency $\nu_{i \rightarrow 0}$, describing the de-excitation from an excited level i to the ground state. The atom flux Γ_{Ba} is determined by the diffusion coefficient D_{Ba} of barium atoms:

$$\Gamma_{\text{Ba}} = -D_{\text{Ba}} \vec{\nabla} n_{\text{Ba}}(\vec{r}). \quad (4-2)$$

The diffusion coefficient D_{Ba} has been experimentally determined in argon [NAMIOTKA et al. 1996; WALKER et al. 1987].

For determination of the desired barium flux from the measured barium atom ground state density, the transport equation has to be solved. The general problem by solving the particle balance equation is the determination of the temporal and spatial depending ionization- and excitation-frequencies $\nu_{\text{Ba}}^{\text{io}}$, $\nu_{\text{Ba}}^{0 \rightarrow \text{i}}$. In [SIGENEGER et al. 2010] we determined the ionization frequency in case of a 25 kHz Ar/Kr discharge by solving the spherical BOLTZMANN equation. This approach has several limitations such as the accurate determination of the time depending cathode fall. In addition, the found solution is only valid for the special discharge condition. Therefore, comparisons of different operating conditions such as lamp current, additional heating through the electrode, lamp frequency, as well as the gas filling and pressure are not possible.

To avoid solving the full particle balance equation (4-1), the continuous lamp operation is disturbed by switching off the lamp for a certain period of time and simultaneous observance of the evaporation. This so called blanking-method was also used by Garner for measurement of electron densities in the electrode region [GARNER 2008a]. He showed that after switching off the lamp, the electron density in the electrode region decays in a time scale of 100 μs . As the cathode fall decreases as soon as the lamp is switched off, the high energetic electrons relax in a μs timescale resulting in significant lower electron energy distribution. As a result, the ionization and excitation frequencies also relax in a μs timescale.

By investigating the diffusion process after switching off the lamp in a microsecond timescale, the ionization and excitation processes in equation (4-1) could be neglected. Thus, the particle balance equation after switching off the lamp could be simplified to:

$$\frac{\partial}{\partial t} n_{\text{Ba}}(t, \vec{r}) = -\vec{\nabla} \cdot \Gamma_{\text{Ba}} = \vec{\nabla} \cdot (D_{\text{Ba}} \vec{\nabla} n_{\text{Ba}}(t, \vec{r})). \quad (4-3)$$

This simplified particle balance equation is more generally valid as it is not connected to special discharge conditions and could be solved with moderate effort [RACKOW et al. 2010]. In the following, a two-dimensional model solving the balance equation is presented.

4.2 2D Diffusion model

In order to describe the barium transport in the electrode region after switching off the lamp, the simplified particle balance equation (4-3) has to be solved both spatially and time dependent. As a three-dimensional model is too complex, a rotation symmetric two-dimensional model is applied in order to solve the equation. Hence, the electrode geometry has to be simplified.

Geometry and boundary conditions

Figure 4-1 shows the used geometry and the generated triangular mesh grid. The z-axis is the rotation axis and represents the center axis of the lamp. Thus, the normal barium flux is set to zero by the corresponding NEUMANN boundary condition. During operation, the eroded barium is deposited at the inner wall which corresponds to the boundary at

$r = 12.7$ mm (inner lamp radius of a T8-lamp). The wall temperature is set to the room temperature, and because the vapor pressure of barium at room temperature is very low, a barium density equal to zero is assumed at this boundary. Hence, a corresponding DIRICHLET boundary condition is chosen.

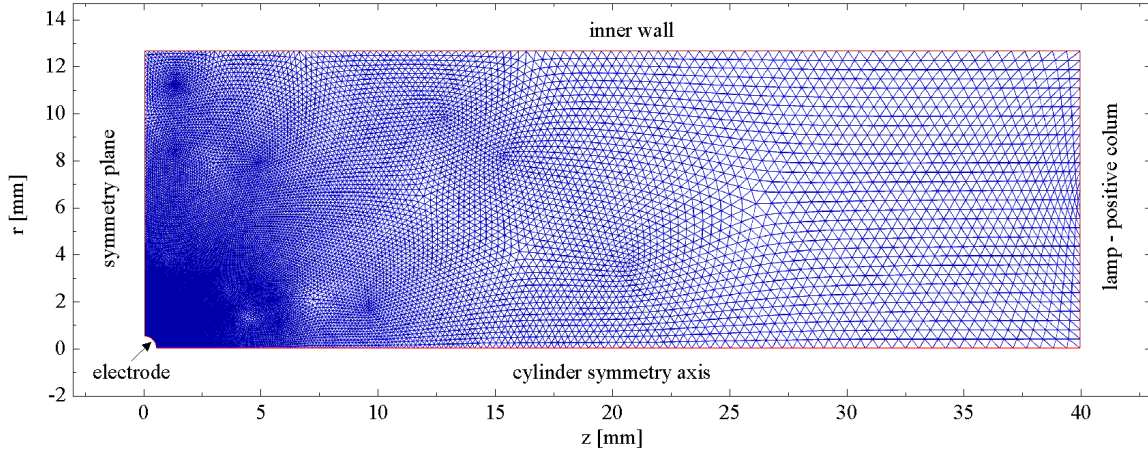


Figure 4-1: Geometry and triangular mesh grid of the used rotational symmetric two-dimensional model.

During steady-state operation, the investigated barium is produced in the hot-spot. Thus, the electrode is reduced to the spot by assuming a sphere with the radius $R_{\text{electrode}} = 0.5$ mm (corresponding to the radius of a stick electrode) at $r = z = 0$. In order to solve the transport equation, an appropriate boundary condition has to be found. An accurate representation of the barium atom flux generally requires a detailed description of the barium production and its diffusion through the emitter. Due to the insufficiency of existing models and limited knowledge of corresponding data, two different assumptions are made. As the electrode has a certain heat capacity, its temperature and therefore the barium evaporation process could be assumed to be constant during short periods (5 ms) of switching off the lamp. Thus, for the first assumption a constant flux of barium atoms is set at the electrode surface (NEUMANN boundary condition). For the second assumption, a constant barium atom density at the electrode surface is set (DIRICHLET boundary condition).

To save computation resources, only the region for $z > 0$ is considered, as the region for $z < 0$ is mirror symmetric. Therefore, the normal flux at the symmetry plane ($z = 0$) is set to zero by a corresponding NEUMANN boundary condition.

The connection to the positive column is represented by the boundary at $z = 40$ mm. At normal conditions, the evaporated barium is deposited at the inner wall near to the electrode and the amount of barium transported to the positive column could be neglected. Thus, the normal barium flux is set to zero (NEUMANN boundary condition) at this boundary.

In order to generate the rectangular grid, the mesh generator implemented in the commercially available software MatLab [MATHWORKS 2011] is used. As higher gradients of the barium densities appear near the electrode, the spatial resolution is set higher at this region. The generated mesh has about 30,000 mesh points, whereas the spatial resolution varies from 0.007 mm at the electrode to 0.6 mm at the boundary to the positive column.

Numerical solution of the particle balance equation

By application of a rotational symmetric model, the particle balance equation (4-3) has to be formulated in cylindrical symmetry:

$$\frac{\partial}{\partial t} n_{\text{Ba}}(t, r, z) = \frac{1}{2\pi r} \vec{\nabla} \cdot (2\pi r \cdot D_{\text{Ba}} \vec{\nabla} n_{\text{Ba}}(t, r, z)). \quad (4-4)$$

In order to solve this equation, the “parabolic” solver implemented in MatLab [MATHWORKS 2011], is used.

The solution of the equation strongly depends on the temperature and pressure-dependent barium diffusion coefficient D_{Ba} , which could be calculated according to [NAMIOTKA et al. 1996]:

$$D_{\text{Ba}}(T, p) = D_{\text{Ba},0} \cdot \left(\frac{p_0}{p} \right) \cdot \left(\frac{T}{T_0} \right)^{3/2}, \quad (4-5)$$

where T_0 is the standard temperature of 273 K and p_0 is the standard pressure of 1 bar.

The standard diffusion coefficients $D_{\text{Ba},0}$ of barium ground state atoms in argon $D_{\text{Ba},0,\text{Ar}} = 0.118 \text{ cm}^2/\text{s}$ and krypton $D_{\text{Ba},0,\text{Kr}} = 0.0839 \text{ cm}^2/\text{s}$ were experimentally determined by Namiotka et al. [1996] and Walker et al. [1987]. For a mixture of two gases, the resulting diffusion coefficient could be calculated according to BLANK’s law:

$$D_{\text{Ar, Kr}} = \frac{1}{\frac{\chi_{\text{Ar}}}{D_{\text{Ar}}} + \frac{\chi_{\text{Kr}}}{D_{\text{Kr}}}}, \quad (4-6)$$

where χ denotes the mole fraction of the gas.

The strong temperature gradient in the electrode region (about 1200 K at the electrode and room temperature at the wall) leads to a spatially dependent barium diffusion coefficient that has to be considered. Thus, before solving the particle balance equation, first the temperature has to be calculated.

For solution of the whole problem, a three-step model is used as illustrated in Figure 4-2. In the first step, an appropriate mesh of the geometry is generated, and in the second step, the spatial temperature distribution in the electrode region is computed. As the thermal conductivity κ of a gas depends on the temperature, an iterative process is applied. The thermal conductivity is derived from the actual temperature and is used to calculate the temperature again until a stable solution is found. Finally, the barium transport equation is solved by using the barium diffusion coefficient derived from the spatial temperature computed in the previous step.

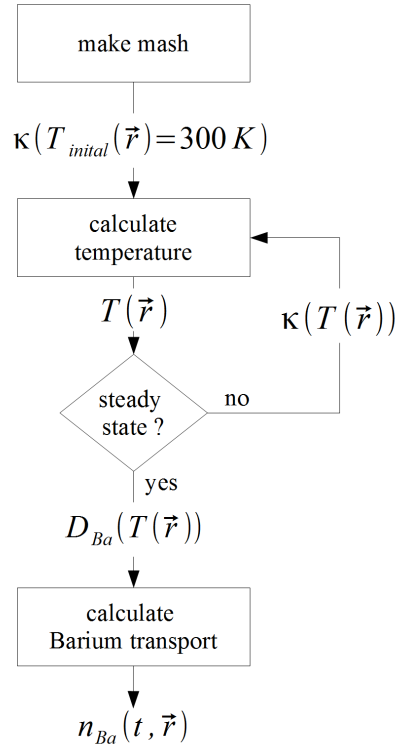


Figure 4-2: Schematic of the model. In order to solve the barium particle balance equation, first an appropriate mesh of the geometry is generated. Next, the temperature in the electrode region is computed in an iterative process. Finally, the barium particle balance equation is solved.

Calculation of the temperature in the electrode region

A good estimation of the temperature in the electrode region of a low pressure lamp can be obtained by solving the stationary heat balance equation as demonstrated by Winter et al. [2008] in case of a DC glow discharge. They also demonstrated that in the first approximation convection could be neglected. The stationary heat balance equation in cylindrical symmetry is given by:

$$\frac{1}{2\pi r} \bar{\nabla} \cdot (2\pi r \cdot \kappa(T(r, z)) \cdot \bar{\nabla} T(r, z)) = 0, \quad (4-7)$$

where $\kappa(T(r, z))$ is the temperature dependent thermal conductivity. In order to compute the temperature, this heat balance equation is solved by the use of the “*asempde*”-solver implemented in MatLab [MATHWORKS 2011]. The thermal conductivity is calculated according to Younglove and Hanley [1986] by an empirically found formula for Argon (described in detail in Appendix B.2). As the thermal conductivity κ depends on the temperature, an iterative process is applied. The thermal conductivity is calculated according the temperature of the previous iteration until a stable solution is found.

At the electrode surface, a constant gas temperature is set by assuming the gas temperature is equal to the electrode/hot-spot temperature ($T_{\text{hot-spot}}$). Typical hot-spot temperatures of

the used lamps are in the range of 1200 K. To study the dependence of the solution of the model on this temperature, several electrode temperatures are tested. At the inner lamp wall a constant temperature of $T_{\text{wall}} = 300\text{K}$ is set. As an initial condition, a constant temperature of 300 K is set to the whole electrode region.

In Figure 4-3 the calculated temperature distribution by assuming a gas temperature of 1200 K at the electrode surface is given. In addition, the plot shows the temperature profile along the z-axis ($r = 0$). In the first approximation, the temperature profile looks like the solution by assuming spherical symmetry $T \propto 1/r$. The deviance to this solution is caused by considering the temperature-dependent thermal conductivity and by the application of a more realistic rotational symmetric model of the electrode region. In the plot (Figure 4-3), the resulting normalized barium diffusion coefficient (according to equation (4-5)), used to solve the particle balance equation, is also given. Due to the high temperature, the diffusion coefficient is nine times higher near to the electrode. Thus, consideration of the temperature dependence is essential for solving the particle balance equation.

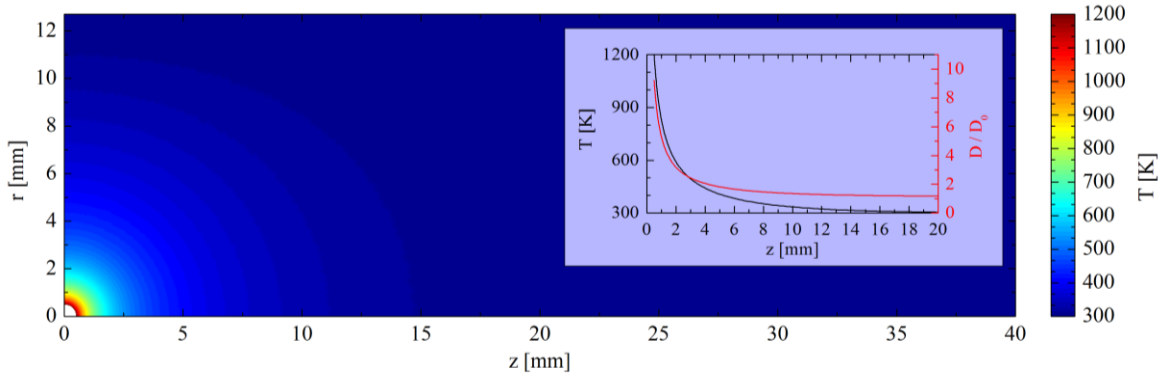


Figure 4-3: Temperature distribution computed by the applied model by assuming a gas temperature of 1200 K at the electrode surface. The graph shows the temperature profile in z-direction for $r = 0$ and the resulting normalized diffusion coefficient used for solving the particle balance equation of barium.

4.3 Solution of the particle balance equation

Solving the particle balance equation starts with $t = 0$, when the lamp is assumed to be switched off. The barium densities occurring during normal operation are significantly smaller than the densities observed during the process of switching off the lamp. Hence, as an initial condition, the barium density is assumed to be zero all over the electrode region $n_{\text{Ba}}(t = 0, \vec{r}) = 0$. Proof of this assumption is provided in Section 0.

In Figure 4-4, the time and spatially-dependent solution of the particle balance is presented. The buffer gas is assumed to be Argon at 3 mbar, leading to a diffusion coefficient of $D(T = 273\text{K}) = 40\text{cm}^2/\text{s}$. The electrode temperature is set to 1200 K and the temperature distribution shown in Figure 4-3 is applied. At the electrode, a constant barium flux of 10^{12}atoms/s (surface integrated) is set. The computation starts at $t = 0$ when the lamp is assumed to be switched off. The density builds up instantaneously and, depending on the

position, the density goes into saturation after a certain time. With increasing distance from the electrode surface, the equilibrium density decreases and it takes longer to reach this saturation.

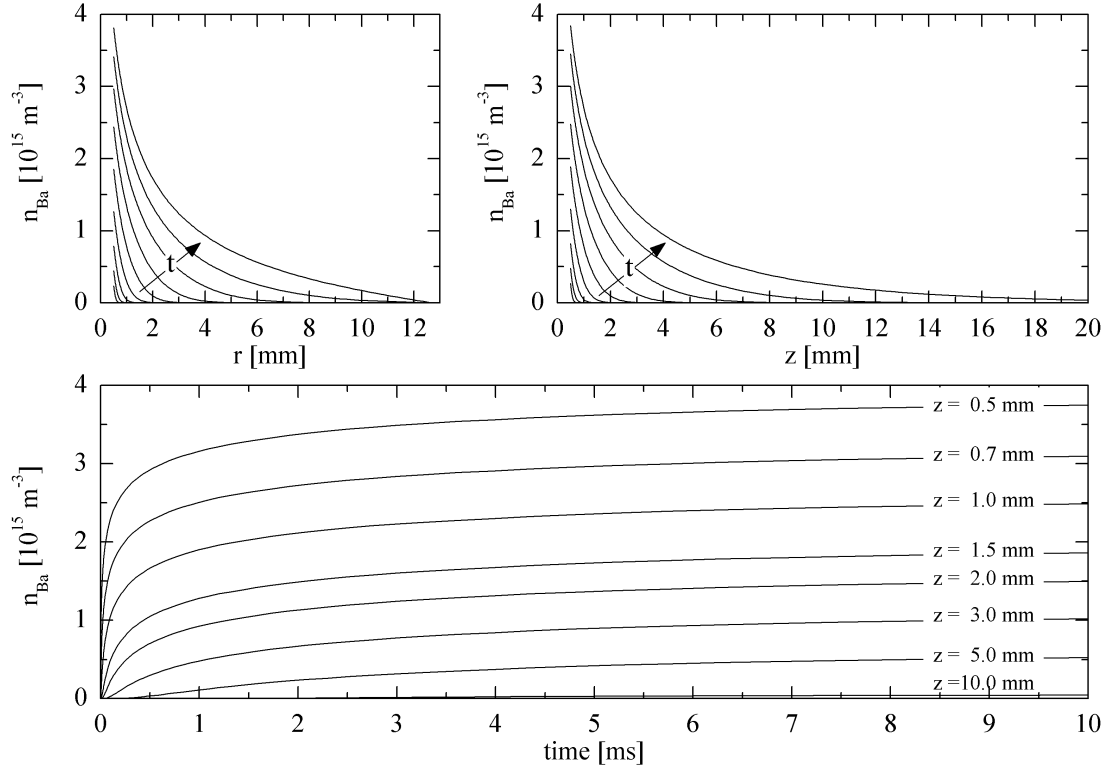


Figure 4-4: Spatial and time-dependent evolution of barium densities computed by solving the particle balance equation for barium atoms. The electrode temperature is set to 1200 K, the gas is argon at 3 mbar, and at the electrode a constant barium flux of 10^{12} atoms/s (surface integrated) is set.

- Barium densities' profiles for different times in r -direction ($z = 0$).
- Barium densities' profiles for different times in z -direction ($r = 0$).
- Time-dependent barium densities at different z -positions ($r = 0$) in front of the electrode.

Influence on the temperature distribution

To discern the importance of considering the temperature distribution in the electrode region, Figure 4-5 depicts the solution of the model for assuming different hot-spot temperatures (1200 K, 800 K and 300 K). Again, a constant barium flux of 10^{12} atoms/s (surface integrated) is set at the electrode. In Figure 4-5a, the computed temperature distribution in z -direction ($r = 0$) is given for the three hot-spot temperatures. The resulting normalized barium diffusion coefficient (according to equation (4-5)) is given in Figure 4-5b. In contrast to the assumption of a constant temperature (room temperature of 300 K) in the electrode region, higher electrode temperature significantly increases the diffusion coefficient. This effect is particularly strong near to the electrode surface such that the diffusion coefficient is up to nine times higher for hot-spot temperatures of about 1200 K. Hence, the distribution of the densities of the eroded barium strongly depends on the

temperature. By reaching stationary erosion (see Figure 4-5c, for $t \rightarrow \infty$), the densities in case of 300 K electrode temperature are four times higher than for an electrode temperature of 1200 K. In order to reach the same flux, the lower diffusion coefficient at 300 K has to be compensated by a higher gradient of the density (see equation (4-2)), leading to higher densities. The effect also appears shortly after switching off the lamp as illustrated in Figure 4-5d for $t = 0.23$ ms.

The temporal evolution in front of the electrode is given in Figure 4-5e for $z = 1$ mm and in Figure 4-5f for $z = 5$ mm ($r = 0$ mm). Whereas the underlying temporal characteristic is nearly similar for the different hot-spot temperatures, the absolute densities differ. In general, the evolution is slower and the difference in the relative values is much smaller when far away from the electrode (Figure 4-5f for $z = 5$ mm). Thus, near to the electrode ($z = 5$ mm) the absolute densities vary in a range of about 250% value (at a certain time) whereas far away from the electrode ($z = 5$ mm) the densities vary in a range of about 25% for the three different hot-spot temperatures. Thus, by determining the absolute barium flux by comparing model and measurements, the densities far away (about 5 mm) from the electrode should be considered to minimize the error due to the insufficient knowledge about the hot-spot temperature and the resulting temperature distribution in the electrode region.

Influence on the electrode boundary condition

In addition to different hot-spot temperatures, two different boundary conditions at the electrode surface are tested. Besides the previously discussed constant flux, a constant density is also assumed. In Figure 4-6, the spatially resolved solution (in z -direction) as well as the temporal evolution of the resulting densities are given, whereas an electrode temperature of 1200 K is assumed. Again, the constant flux at the electrode surface is set to 10^{12} atoms/s (surface integrated). For the constant boundary condition the density, identical to the stationary density in case of a constant flux (for $t \rightarrow \infty$) of $n_{\text{Ba,surface}} = 0.37 \cdot 10^{14} \text{ m}^{-3}$, is set to ensure comparability. In general, the assumption of a constant density leads to a faster evolution of the densities, whereas the effect is particularly strong near to the electrode.

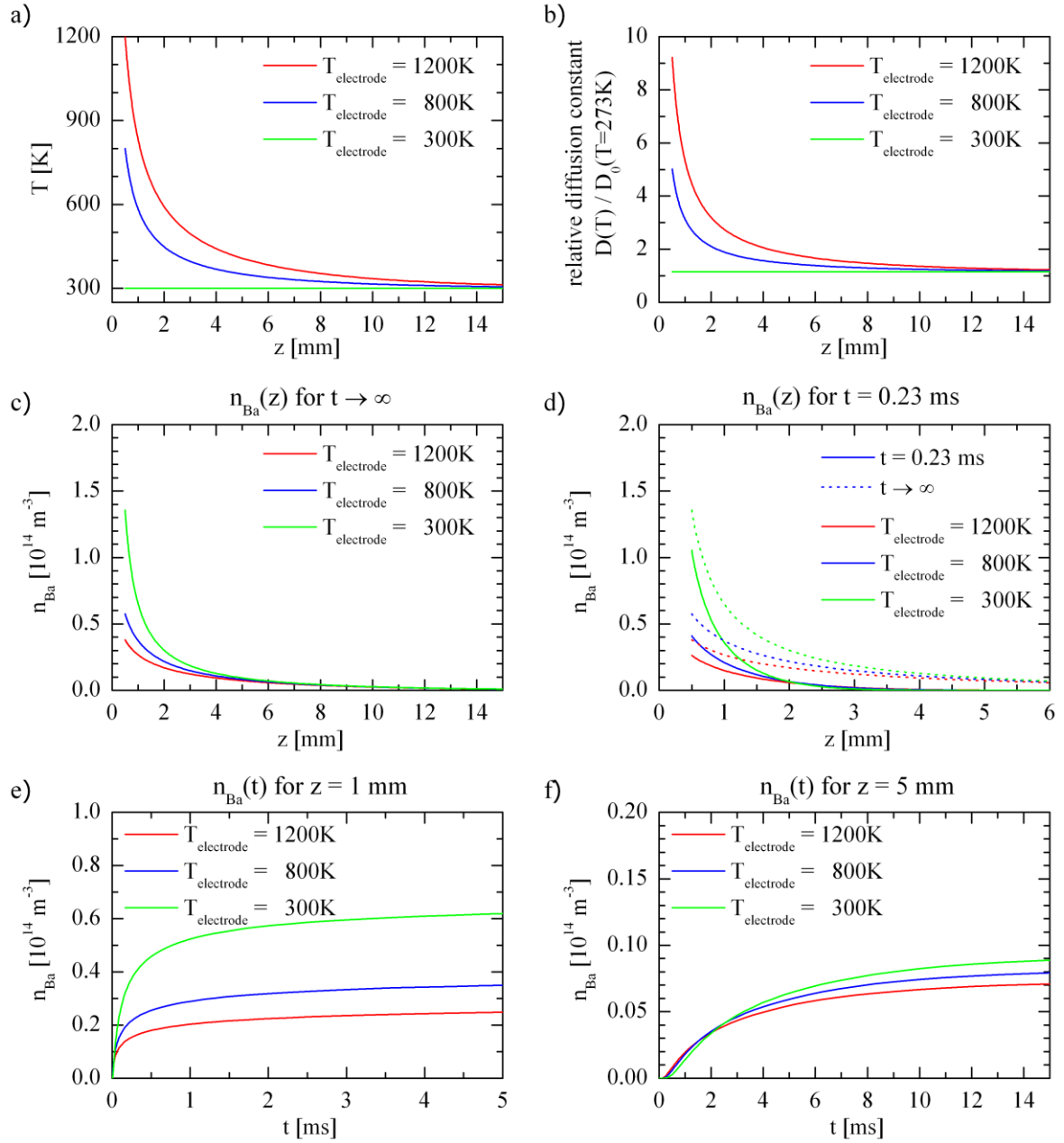


Figure 4-5: Temperature dependence of the solution of the barium transport model. At the electrode, a constant barium flux of 10^{12} atoms/s (surface integrated) is set.

- Computed temperature profile in z -direction ($r = 0$) of three different electrode temperatures (300 K, 800 K and 1200 K).
- Corresponding profile of the barium diffusion coefficient applied to the barium transport model.
- Resulting barium density profile in z -direction for $t \rightarrow \infty$.
- Resulting barium density profile in z -direction for $t = 0.23$ ms and $t \rightarrow \infty$ (dotted line).
- Temporal barium density evolution for $z = 1$ mm (0.5 mm in front of the electrode surface) and $r = 0$.
- Temporal barium density evolution for $z = 5$ mm (4.5 mm in front of the electrode surface) and $r = 0$.

In case of a constant flux, the density at the electrode has to build up gradually over time. In contrast, in case of a constant density at the electrode surface, the high density at the

electrode is present immediately. Such, a strong gradient of the barium density leading to higher barium fluxes (see equation (4-2)) exists, particularly in the period after switching off the lamp. Thus in the beginning, the assumption of a constant density leads to higher fluxes and therefore to a faster evolution of the barium densities. The flux is time dependent whereas initially a very high flux appears which converges to the constant flux assumed by reaching the stationary densities for $t \rightarrow \infty$. The very high fluxes at the beginning of the computation are not realistic. On the one hand, barium continues to remain in front of the electrode before switching off the lamp. Thus, the density gradient defining the flux is limited. On the other hand, the electrode cannot deliver the huge flux that occurs in the model. By taking further into account the fact that barium production is determined by the temperature and that transportation through the emitter is limited, the assumption of a constant flux at the electrode surface seems to be more realistic. However, in order to prove the model both assumptions are compared with the measurements in the following subsection.

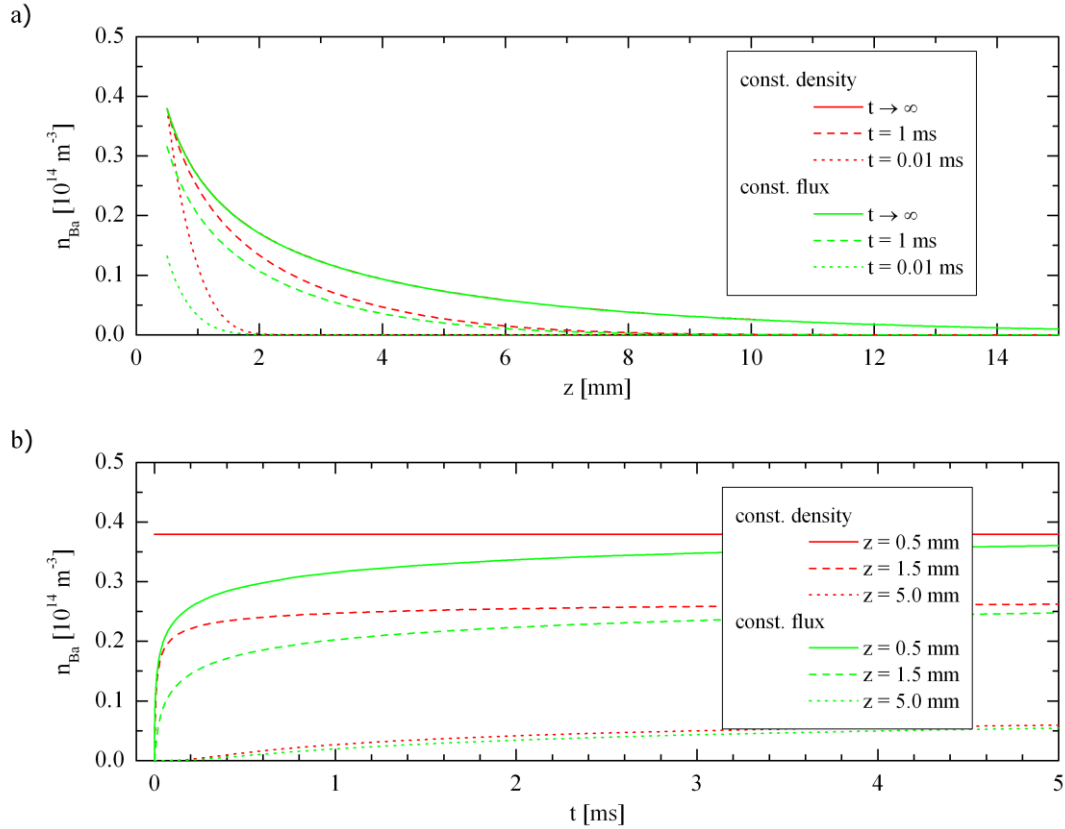


Figure 4-6: Comparison of two different boundary conditions at the electrode surface. In case of a constant flux, the barium flux is set to 10^{12} atoms/s (surface integrated). For the assumption of a constant density, the density at the electrode surface is set to $n_{Ba, \text{surface}} = 0.37 \cdot 10^{14} \text{ m}^{-3}$. The electrode temperature is set to 1200 K and the gas is argon at 3 mbar.

a) Barium densities' profiles for different times in z -direction ($r = 0$).

b) Time-dependent barium densities at different positions (z -positions) in front of the electrode for $r = 0$.

In general, both tested boundary conditions and all assumed electrode temperatures lead to a similar characteristic of the evolution of the barium densities. The underlying difference between these assumptions is the time span until the stationary density distribution is reached. To illustrate these temporal characteristics, the rise time $t_{0.5}$ of the density is given in Figure 4-7, spatially resolved for each assumption. The rise time $t_{0.5}$ is defined as the duration until the density reaches half of the stationary density $n_{\text{Ba}}(t \rightarrow \infty)$:

$$n_{\text{Ba}}(r, z, t_{0.5}) = \frac{1}{2} n_{\text{Ba}}(r, z, t \rightarrow \infty). \quad (4-8)$$

As mentioned before, the rise time increases with the distance from the electrode surface (z-position) resulting in slower evolution of the local densities. More relevant for practical application of the model in order to determine absolute fluxes is the relative variation of the local rise time for different assumptions. Thus, the relative variation for different electrode temperatures is about factor 3 at $z = 1$ mm (by assuming a constant density at the electrode surface), in contrast to about a factor 0.3 at $z = 5$ mm. Hence, comparing experiment and model near to the electrode leads to higher errors (due to the insufficient knowledge about the hot-spot temperature and the corresponding temperature distribution in the electrode region) as measurements far away (5 mm).

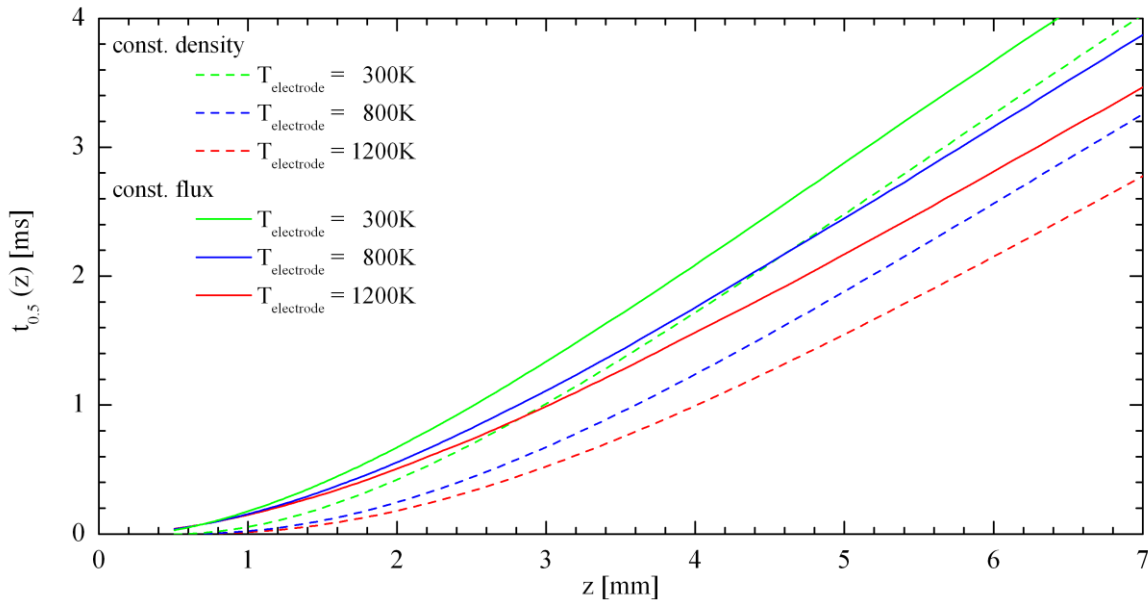


Figure 4-7: Spatially resolved (z-direction) rise time of the densities for the investigated assumptions of hot-spot temperature and electrode surface boundary condition. The rise time $t_{0.5}$ is defined as the duration until the local density reaches half of the stationary density $n_{\text{Ba}}(t \rightarrow \infty)$.

4.4 Application and validation of the model

In order to validate the model, its outcomes are compared with measurements on fluorescent lamps. Therefore, the lamps are switched off for about 5 ms whereas evaporation and transport of barium is measured by LIF. For lamp operation, the electrical setup also used for electron density determination by microwave interferometry is applied (see Figure A-12).

For measurements, a T8-36W lamp is used, operating at 25 kHz with a lamp current of 320 mA. In Figure 4-8, the temporal characteristics during switching off (blanking) the lamp are given. At $t = 0$ ms the lamp is switched off for 5 ms with the IGBT⁹-shorting circuit placed parallel to the lamp. The switching off is synchronized with the operational frequency and starts after the cathode phase (at zero crossing of the current). During the first 100 μ s of shorting, a minimal current of about 10 mA remains. This is caused by the used IGBT's (IXEH 40N120) that have a emitter-gate threshold voltage of 0.95 V. Thus, also a small remaining lamp voltage could be measured. However, the cathode fall decreases immediately after switching off the lamp and there are no longer high energetic electrons (the so-called beam electrons) present in the electrode region. The remaining electrons relax in a timescale of about 100 μ s due to ambipolar diffusion.

Whilst switching off the lamp, the barium ground state density is measured 3 mm in front of the electrode surface (in comparison with the model $z = 3.5$ mm). At this position, the barium ground state densities during normal operation are near to the detection limit.

After starting the switching-off procedure, the density increases in a millisecond-timescale and seems to become saturated after approximate 4 ms. Thus, the evolution of the barium density corresponds to the model. Although the densities are measured in a distance of 3 mm from the electrode surface, it is four times higher than densities measured during continuous operation close to the electrode surface in a distance of 0.5 mm. As the densities accrued during the switching-off procedure are orders of magnitudes higher than during normal operation (before switching off), the assumption of the starting condition $n_{\text{Ba}}(t = 0, \vec{r}) = 0$ for the model seems to be adequate.

Obtaining the barium flux from measurements

For determination of the total barium evaporation flux, the results of the barium transport model $n_{\text{model}}(t, z)$ are fitted to the measured barium density $n_{\text{Ba, measured}}(t, z)$ (see Figure 4-8 dashed lines). This is achieved by simultaneous scaling of the model outcome in the amplitude by a factor A and in time by a factor B according to:

$$n_{\text{Ba, measured}}(t, z) = A \cdot n_{\text{model}}(B \cdot t, z). \quad (4-9)$$

With factor B a deviation of the diffusion coefficient could be compensated, whereas the amplitude A corresponds to the discrepancy of the flux between measurement and model. The method of least squares [HELMERT 1907] implemented in MatLab is used for fitting.

From the determined factors, the absolute flux Γ_{Ba} whilst switching off the lamp as well as the diffusion coefficient $D_{\text{Ba}, 273\text{K}}$ could be calculated:

$$\begin{aligned}\Gamma_{\text{Ba}} &= A \cdot \Gamma_{\text{model}} \\ D_{\text{Ba}, 273\text{K}} &= \frac{D_{\text{model}, 273\text{K}}}{B},\end{aligned}\tag{4-10}$$

where Γ_{model} is the flux of barium atoms assumed in the model and $D_{\text{model}, 273\text{K}}$ is the assumed diffusion coefficient.

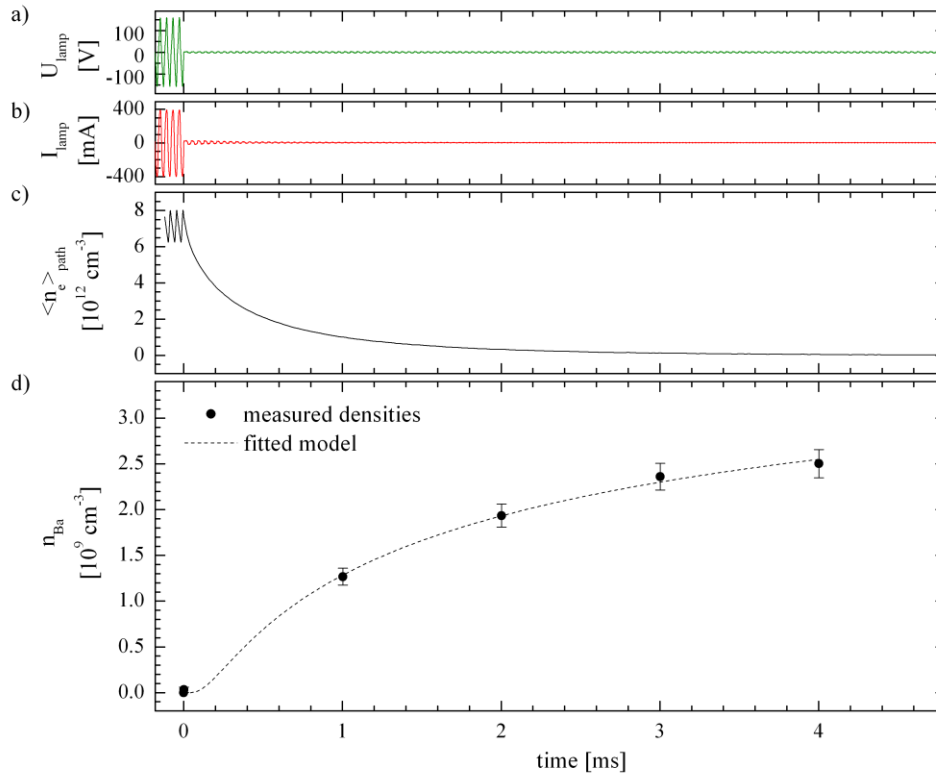


Figure 4-8: Measurements while blanking (switching off) the lamp. The lamp is operated with a current of 300 mA (rms) at 25 kHz. At $t = 0$ ms, the lamp is switched off by shorting with the TTL¹²-triggered IGBTs placed parallel to the lamp.

- a) lamp voltage
- b) lamp current
- c) path average electron densities
- d) Barium atom ground state densities at a distance of 3 mm from the electrode surface ($z = 3.5$ mm). The dashed lines are a fit of the outcome of the barium transport model to the measured densities.

For the measured barium densities, this procedure leads to a total barium flux from the electrode of $9.5 \cdot 10^{11} \pm 0.52 \cdot 10^{11}$ atoms/s. The obtained barium diffusion coefficient is

¹² transistor–transistor logic compatible level (TTL)

$D_{\text{Ba}, 273\text{K}} = 32 \pm 7 \text{ cm}^2/\text{s}$, which is in good agreement with $32.7 \text{ cm}^2/\text{s}$ for the mixture of 75% Argon and 25% Krypton at 3 mbar (see equation (4-6)). The given errors are an output of the fitting algorithm. The good agreements of model and measurements prove the assumption made in the model. Therefore, the chosen approach seems to be adequate for the desired determination of absolute fluxes.

For a further detailed validation, an additional experiment with a modified lamp having the possibility to vary the gas filling has been applied. Thus, the gas pressure and therefore the barium diffusion coefficient could be varied. Gas fillings of Argon at 3 mbar, 6 mbar, and 10 mbar are investigated. Due to the limitation of the pumping station, only mercury-free gas fillings could be tested. Thus, the other discharge parameters such as lamp voltage are not comparable with normal fluorescent lamps. As an example, the barium densities during blanking are given in Figure 4-9 for a gas pressure of 6 mbar and for different positions in front of the electrode.

In comparison with the previous measurement (Figure 4-8), the increase of the density (at $z = 3.5 \text{ mm}$) is significantly slower due to the halved diffusion coefficient. However, the fitted model data are in good agreement to the measured densities.

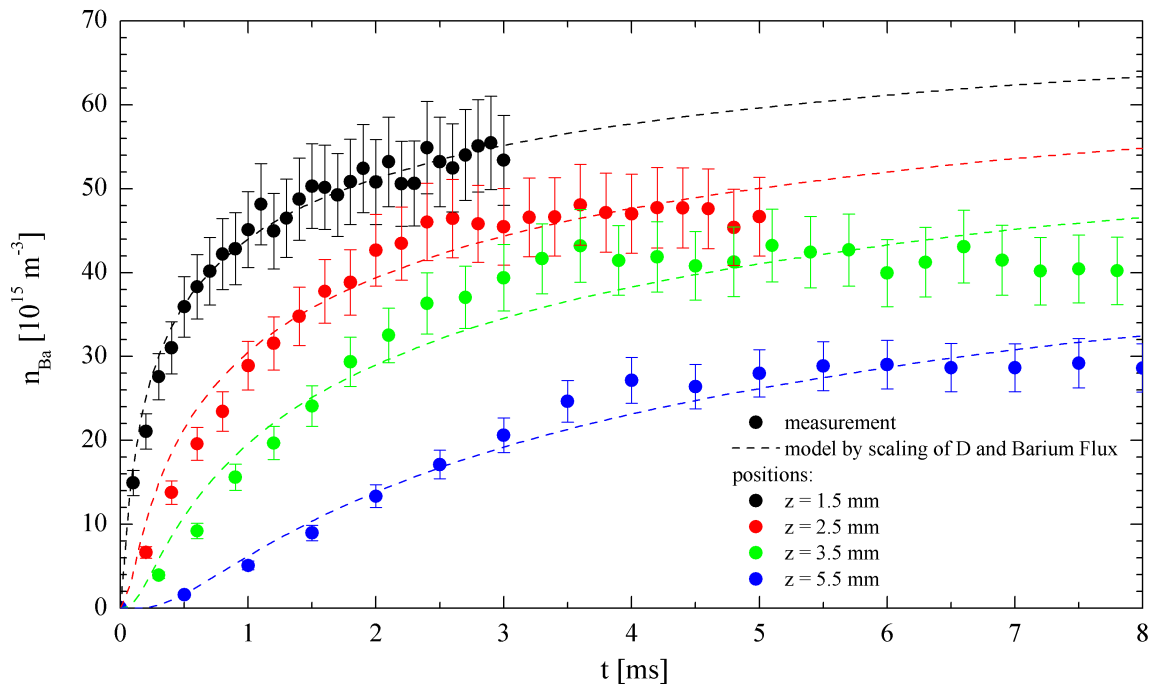


Figure 4-9: Barium density whilst switching off the lamp. The buffer gas is Argon at a pressure of 6 mbar. The density is measured at different positions in front of the electrode. The dashed lines are a fit of the outcome of the barium transport model to the measured densities.

The same measurements have been performed for the other tested gas pressures. Analogously, the diffusion coefficient has been determined by fitting the outcome of the model to the measured densities. To evaluate the different assumptions of the model (the gas temperature computed for different electrode temperatures of 300 K, 800 K and 1200 K as well as the electrode boundary condition of a constant flux and a constant density), the

various outcomes of the model have been used for fitting. As such, for every tested pressure six different diffusion coefficients have been obtained, given in Figure 4-10 as functions of the pressure. By assuming a higher electrode temperature in the model (leading to higher gas temperature), the obtained diffusion coefficients decrease. The higher diffusion coefficients in the model $D_{\text{model}}(r) = D_{\text{model}, 273\text{K}} \cdot (T(r)/273\text{K})^{3/2}$ lead to a faster increase of the densities. Thus, in order to reach the measured increase of the densities, a lower diffusion coefficient is sufficient. The same effect accrues for different boundary conditions. As already discussed, the assumption of a constant density at the electrode surface leads to a faster evolution of the densities (see Figure 4-7). Hence, by fitting the measurements to these data, one obtains again a lower diffusion coefficient.

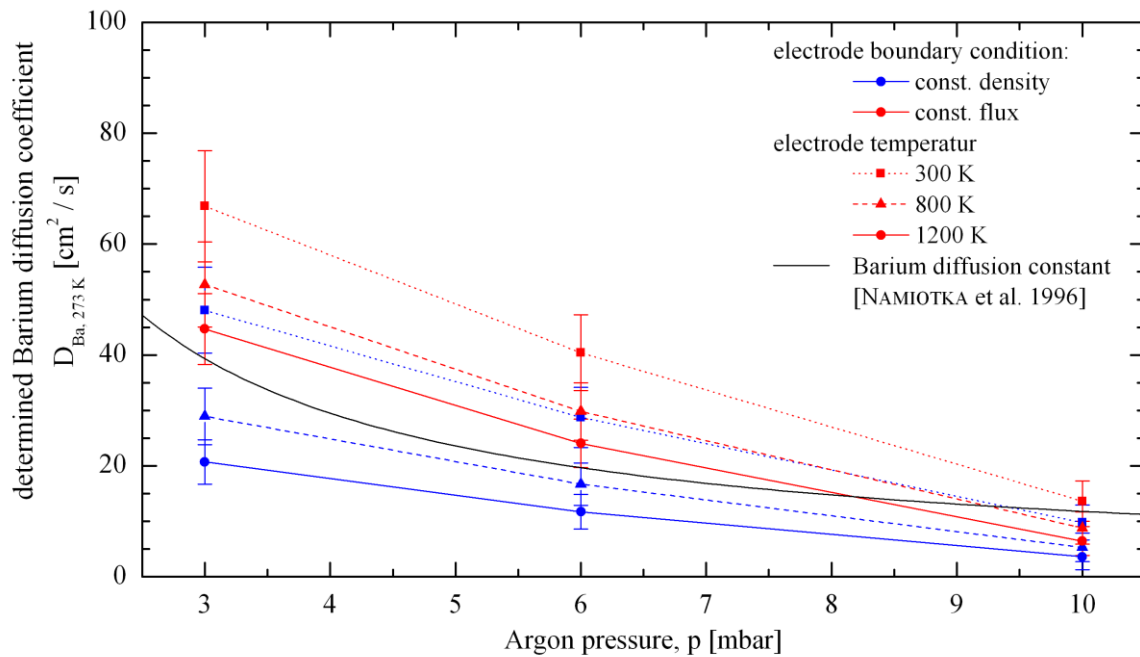


Figure 4-10: Determined barium diffusion coefficient at 273 K for different Argon pressures. The obtained diffusion coefficient depends on the assumption of the transport model. Three different assumptions of the electrode temperatures and two different boundary conditions at the electrode surface are tested (blue, constant barium density; red, constant barium flux). The black line denotes the diffusion coefficient taken from the literature [NAMIOTKA et al. 1996].

In comparison with the obtained diffusion coefficients, the experimentally determined coefficients [NAMIOTKA et al. 1996] are also given in Figure 4-8 (black line). However, the best agreement occurs if an electrode temperature of 1200 K and a constant flux at the electrode surface are assumed. By assuming a constant density at the electrode surface, the obtained diffusion coefficients are too low. In general, a constant density at the electrode surface is unlikely, as it would lead to very high fluxes immediately after switching off the lamp. The evaporated barium is produced at the interaction layer of tungsten and barium oxide and has to diffuse through the porous emitter, which limits the flux. Thus, a constant flux is more likely and corresponds to the obtained diffusion coefficients.

However, consideration of the high temperatures in the electrode region seems to be very important. Without considering the temperature distribution (assume a constant temperature of 300 K), the obtained diffusion coefficients are a factor 1.5 up to 2 above the coefficient from the literature. As would be expected, the best agreement with the previous literature was found by assuming an electrode temperature of 1200 K, typical for fluorescent lamps. The investigation concluded that the best agreement of model and measurement could be found by assuming an electrode temperature of 1200 K and a constant flux at the electrode surface for the model. Thus, in the following these assumptions are applied for determination of barium fluxes by the blanking method.

5 Results and discussion

This chapter presents the investigations and discussions on electrode operation and electrode erosion. To ensure practical relevance of the investigations, they were performed on fluorescent lamps as close as possible to commercial lamps (see Section 3.6). Thus, the range of parameter variation and especially gas and pressure variation is limited.

To ensure the applicability of the LIF and the validity of its absolute calibration, first the effect of collisional depopulation (quenching) of excited levels is presented. Afterward, the fundamental processes of emitter erosion by barium evaporation is investigated in case of a heated electrode.

Subsequently, the operation and emitter erosion during lamp operation is presented. First, the operation mode of modern ballast systems with frequencies of several tens of kHz is investigated. This is followed by investigations of the dimmed operation mode, which becomes increasingly important for practical application of modern lighting systems. In addition, the reduction of electrode erosion by application of an additional heating current is presented. Finally, the chapter investigates the dependency on the operational frequency, including the operation at net frequency.

5.1 Necessary preliminary investigation - Determination of collisional effects - quenching

The lifetimes of excited levels are determined by their natural lifetime and additional depopulation processes such as induced emission and quenching collisions. Both processes shorten the lifetime, whereas induced emission occurs in LIF experiments normally only during the laser excitation. Quenching collisions lead to radiationless depopulation of the excited state, which in turn lowers the amount of fluorescent photons (see equation (A-42)) as well as the lifetime of the excited state.

Often quenching by rare gases has been supposed to be negligible, but for certain atomic levels [HANNAFORD and LOWE 1983] found significant collision effects in the regime of gases and pressures relevant, whereas the strongest effect is produced by heavy rare gases such as Xenon. Thus, for absolute density determination, quenching has to be investigated. For determination of quenching rate coefficients, the lifetime of the excited barium Ba(5d6p¹P₁) has been measured in a hollow cathode lamp for different rare gases and pressures. In the first approximation, the effective lifetime τ_i^* of the excited state i depends on the relation [NIEMI 2003]

$$\frac{1}{\tau_i^*} = \frac{1}{\tau_i} + Q_i = \frac{1}{\tau_i} + \sum_q k_q^i n_q, \quad (5-1)$$

where τ_i denotes the natural lifetime (see equation (A-31)). The effective quenching rate Q_i is the sum over the products of the quenching rate coefficients k_q^i of the excited state and the quenching partner q and its density n_q (see equation (A-33)). By increasing the pressure, the quenching rate coefficient increases whereas the effective lifetime decreases.

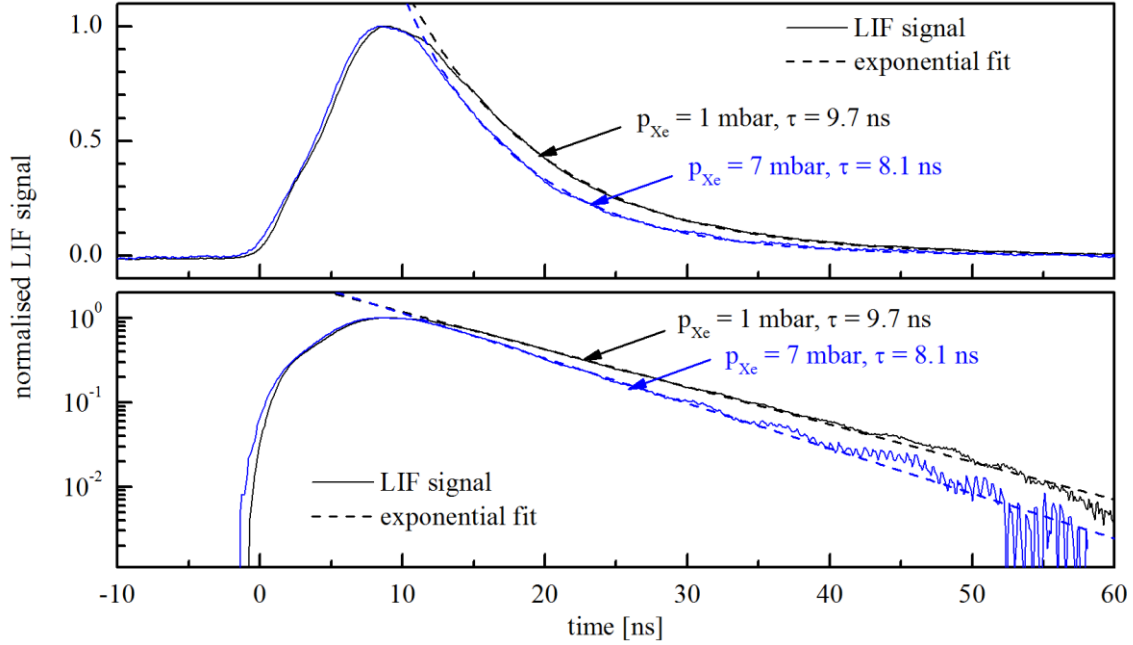


Figure 5-1: Time-resolved fluorescent signal of the excited barium $\text{Ba}(5d6p^1P_1)$ level for two different pressures of the rare gas Xenon in a hollow cathode lamp at 20 mA discharge current. By increasing the pressure from 1 mbar to 7 mbar, the time constant of the exponential decay decreases.

In the experiment, the investigated level is excited and the time-dependent fluorescent signal is measured. By fitting an exponential function on the decay of the signal (see Figure 5-1), the effective lifetime is determined¹³. By plotting the reciprocal lifetime as a function of the partial pressure of the quenching partner in a so-called STERN-VOLMER-plot [STERN and VOLMER 1919] (see Figure 5-2), the quenching rate coefficients could derive from the slope. The extrapolation to zero pressure denotes the reciprocal natural lifetime.

¹³ For extraction of the effective lifetime from such measurements, two important facts have to be considered. The maximum of the fluorescent signal occurs before the end of the excitation and the detection system has a limited response time of approx. 6 ns. Therefore, for fitting of an exponential function the data 10 ns after the maximum are used. This method is independent on laser intensity and saturation effects as only the decay of the excited level after excitation is analyzed. As long as there is no self-quenching, this method is independent on the density of the investigated species.

The determined quenching rates in Argon and in a mixture of 50% Argon and 50% Krypton are inside the error intervals of the measurement and the linear regression¹⁴. For these gas fillings quenching could be neglected. The determined natural lifetime corresponds well to the literature of $\tau_0 = 12.17 \text{ ns}$ [CURRY 2004; NIGGLI and HUBER 1987]. By increasing the Xenon pressure from 1 to 5 mbar, the reciprocal lifetime increases by approximately 10%. Thus, for gas fillings with Xenon collisional depopulation has to be considered for absolute density measurements and for comparison of measurements in different pressures.

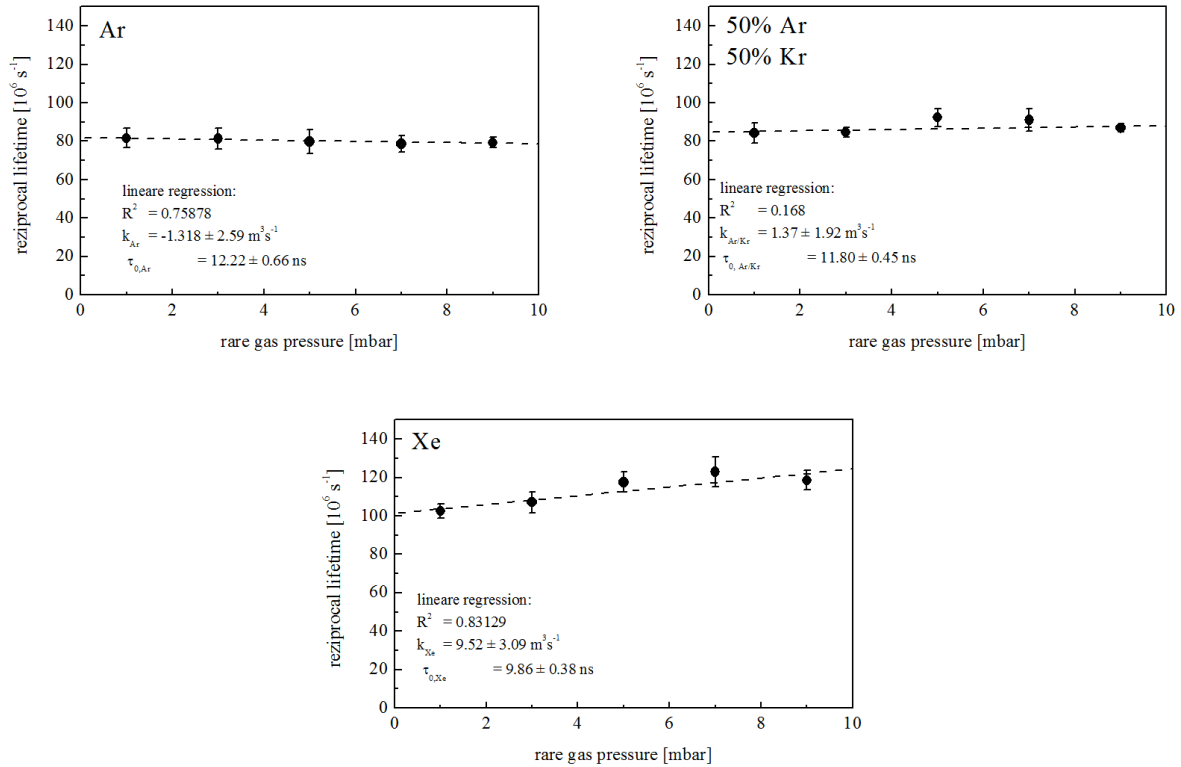


Figure 5-2: Determination of quenching rates by Stern-Volmer-plots. The reciprocal lifetime is derivate from the exponential decay of the fluorescent emission of the excited barium level $\text{Ba}(5d6p^1P_1)$ in a hollow cathode lamp at a discharge current of 20 mA.

¹⁴ The natural lifetime of the investigated barium level $\text{Ba}(5d6p^1P_1)$ is 12.17 ns [CURRY 2004; NIGGLI and HUBER 1987], whereas the response time of the detection system is approx. 6 ns. Hence, only effective quenching rate reducing the lifetime from 12 ns to 6 ns could be recognized. As the quenching rate depends on the reciprocal lifetime, the error increase to higher quenching rates in the range of $1/6 \text{ ns} \approx 166 \cdot 10^6 \text{ s}^{-1}$.

5.2 Barium production and evaporation in case of a heated electrode

The production of barium and its evaporation is studied by investigation of a heated electrode. Thus, distortions by plasma can be ignored.

For investigations, the electrode of a 36W T8 lamp is heated by applied DC currents and the absolute barium ground state density in the center in front of the electrode is measured by LIF. To be representative, an about 5000-hour-aged lamp is used. Thus, a porous emitter has already been formed and the production of barium has stabilized.

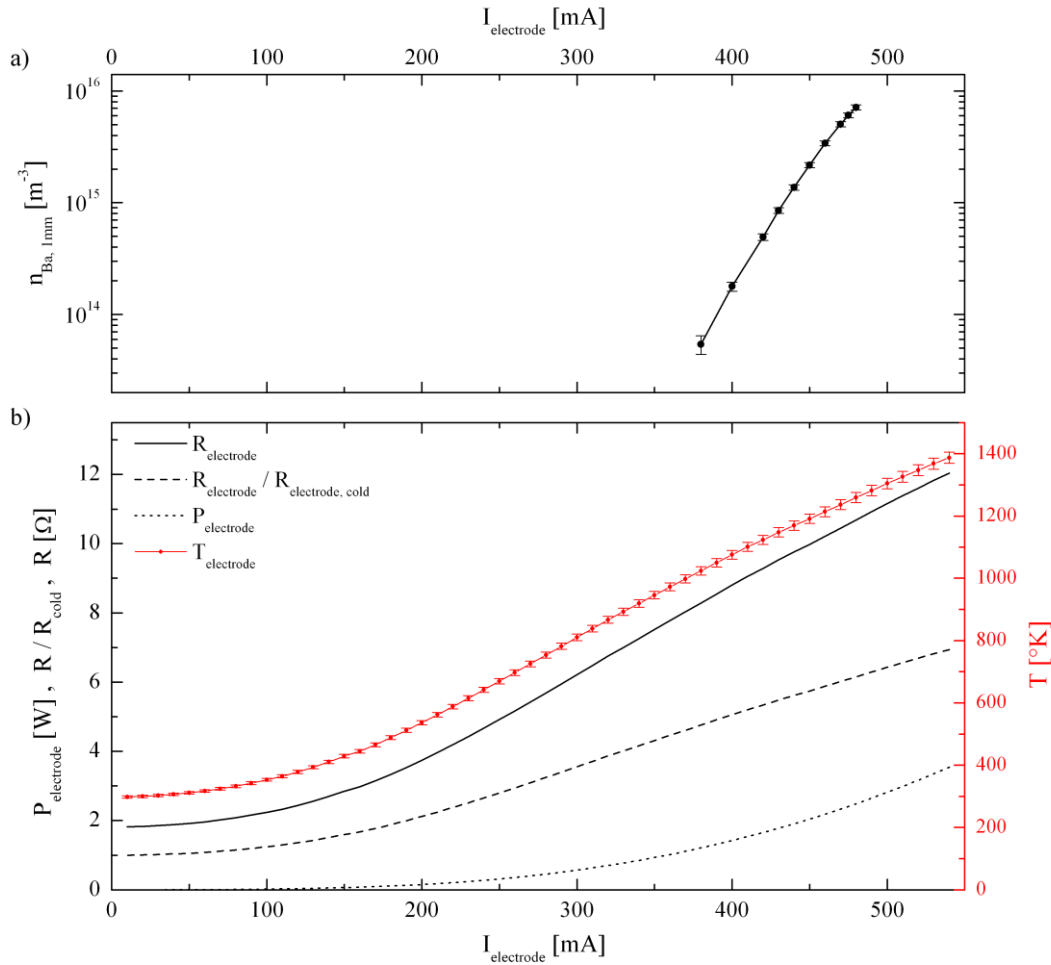


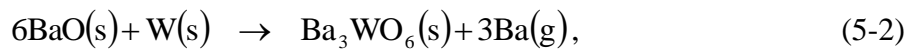
Figure 5-3: Barium evaporation of a heated electrode.

- a) absolute density of evaporated barium, measured 1 mm in front of the surface of a heated electrode, as function of the applied heat current
- b) resistance of the electrode, $R_{\text{hot}}/R_{\text{cold}}$ - ratio, applied power, and the temperature deduced from the $R_{\text{hot}}/R_{\text{cold}}$ - ratio

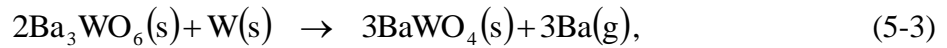
Figure 5-3 shows the obtained absolute barium density (1 mm in front of the electrode surface) during heating as a function of the applied DC current. In addition, the measured electrode resistance, the electrode temperature and the heating power are also shown. During heating with a DC current, the electrode temperature could be interpreted as

homogeneous along the electrode. Hence, the temperature has been determined by the ratio of the resistance at high temperature R_h divided by the resistance at room temperature (cold) R_c (see Section 3.1). Due to the detection limit of the LIF, barium densities could only be detected for heat currents above 380 mA, which correspond to an averaged electrode temperature of about 1030 K and barium densities of $n_{Ba} = 3 \cdot 10^{13} \text{ m}^{-3}$. By further increasing the heat current to 480 mA, the barium densities increase by about two orders of magnitude, whereas the temperature increases by about 140 K.

The barium evaporation characteristic could be obtained by plotting the barium density as function of the determined electrode temperature as given in Figure 5-4. For comparison, the equilibrium vapor pressure¹⁵ of free barium is given for the reduction of the oxide by tungsten [RUTLEDGE and RITTNER 1957]:



for the reduction of the produced tungstate [RUTLEDGE and RITTNER 1957]:



and the thermal reduction of barium [BLEWETT et al. 1939; CLAASSEN and VEENEMANS 1932]:



For low temperatures $T < 1100 \text{ K}$, the measured barium atom densities correspond to the vapor pressure of the reduction of the barium oxide (equation (5-2)) and the connected reduction of the tungstate (equation (5-3)). Thus, it could be concluded that for this temperature range, free barium is produced by these reactions at the boundary layer of barium oxide and tungsten. Furthermore, the produced barium could diffuse unobstructed from the boundary layer through the tungstate and the porous emitter to the electrode surface.

For higher temperatures, the measured densities increase but are lower than the barium vapor pressure of the considered barium-producing reactions, whereas the discrepancy increases with increasing temperature. Hence, for the highest investigated temperature, the measured density is about one order of magnitude below the expected vapor pressure. However, the observed densities are higher than the vapor pressure of the thermal reduction of barium (equation (5-4)). Thus, this reaction could be excluded as relevant barium production process. The discrepancy at higher temperatures, between the measured densities and the vapor pressure resulting from the reduction of barium oxide, could be caused by two effects. On the one hand, the diffusion of the produced barium through the emitter as well as through the tungstate layer is obstructed. Thus, by diffusion through the emitter the resulting gradients lead to lower densities at the electrode surface. This effect becomes more relevant for higher fluxes or higher densities. On the other hand, the reaction

¹⁵ The corresponding vapor pressures are given in Section 2.2.3.

rate for the reduction of barium oxide (according equation (5-2) and (5-3)) is limited by the size of the boundary layer and by the concentration of the reacting agents. Therefore, for higher temperatures, the reaction rates are limited by the diffusion of barium oxide through the tungstate layer to the boundary layer.

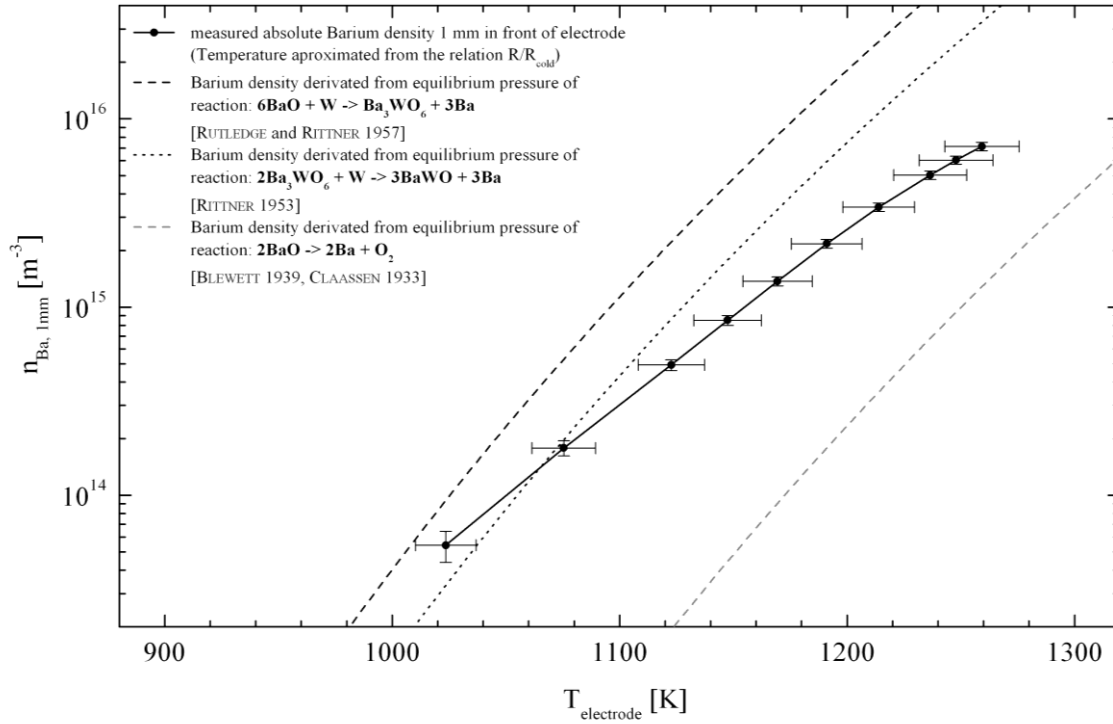


Figure 5-4: Absolute density of the evaporated barium 1 mm in front of the electrode as function on the average electrode temperature estimated by the relation $R_{\text{hot}}/R_{\text{cold}}$.

However, both effects are caused by a reduced transport through the electrode layers. The diffusion of barium through the emitter is determined by its local thickness and porosity. A higher porosity leads to longer free path lengths, which in turn leads to an increased flux. The diffusion of barium oxide through the tungstate layer depends on its local thickness. Thus, the local barium evaporation depends on the local electrode-emitter configuration, which varies in time. Therefore, the total evaporation depends on the initial electrode-emitter configuration as well as on the electrode history and is lower than the evaporation according to the barium vapor pressure of the involved reaction.

From the electrode surface, the produced free barium diffuses through the electrode region. Finally, it is deposited at the inner walls. In case of the heated electrode, the measured barium densities are given in Figure 5-5 as functions of the distance from the electrode surface for three different electrode temperatures. As expected, the densities decay the further they are from the surface, whereas the decay could be well approximated by an exponential decay according to:

$$n_{\text{Ba}}(z) = n_{\text{Ba}, z=0} \cdot e^{-\frac{z}{z_0}}. \quad (5-5)$$

In the formula, $n_{\text{Ba}, z=0}$ denotes the density at the electrode surface ($z=0$) and z_0 the spatial decay length. By fitting the equation to the measured densities (see in Figure 5-5), spatial decay lengths of about 10 mm have been found. The relatively high values in comparison with the model (see Section 4) accrue due to the fact that the whole electrode is heated. In the first approximation the heated electrode could be assumed as a long cylinder leading to radial diffusion. In contrast, diffusion from a small hot-spot is a three-dimensional problem (spherical diffusion) leading to shorter decay lengths.

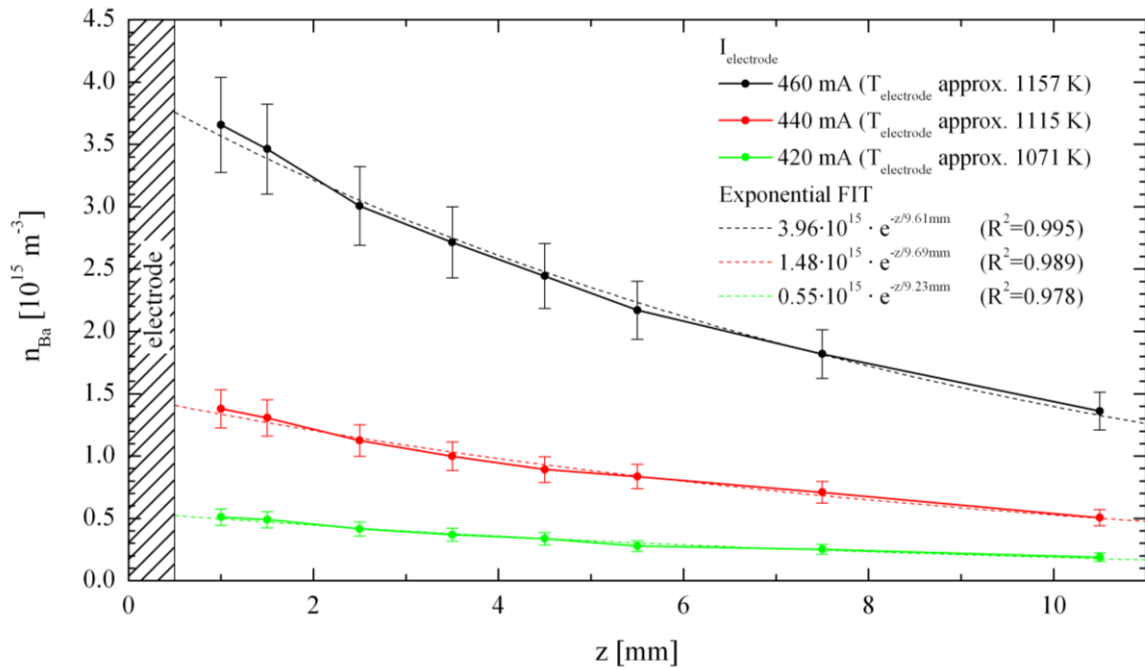


Figure 5-5: Barium densities decay in front of the electrode as a result of the diffusion of the evaporated barium. The densities are plotted as functions of the distance from the electrode z for different heat currents resulting in different electrode temperatures.

Heat loss due to thermal radiation

Additional information concerning the heat balance of the heated electrode could be obtained by plotting the applied heat power as a function of the temperature (see Figure 5-6). The measurement is taken under stationary condition so that the temperature is

constant. Thus, the power needed to heat the electrode is identical to the power lost due to thermal transport and thermal radiation. For high temperatures the relation:

$$P(T) \propto T^{3.45} \quad (5-6)$$

between electrode temperature T and heating power P (identical to the power loss) has been found. The exponent of 3.45 corresponds to the STEFAN–BOLTZMANN law:

$$P(T) = A\varepsilon\sigma \cdot T^4 \quad (5-7)$$

describing the total power radiated from a black body. In the equation, A is the surface area, σ is the STEFAN–BOLTZMANN constant, and ε is the emissivity. Thus, for high electrode temperatures ($T > 800K$) the main heat loss mechanism is thermal radiation. The discrepancy of the exponents (found 3.45 and 4 according to the STEFAN–BOLTZMANN law) could be caused by the temperature and wavelength depending emissivity of the emitter $\varepsilon = \varepsilon(T, \lambda)$.

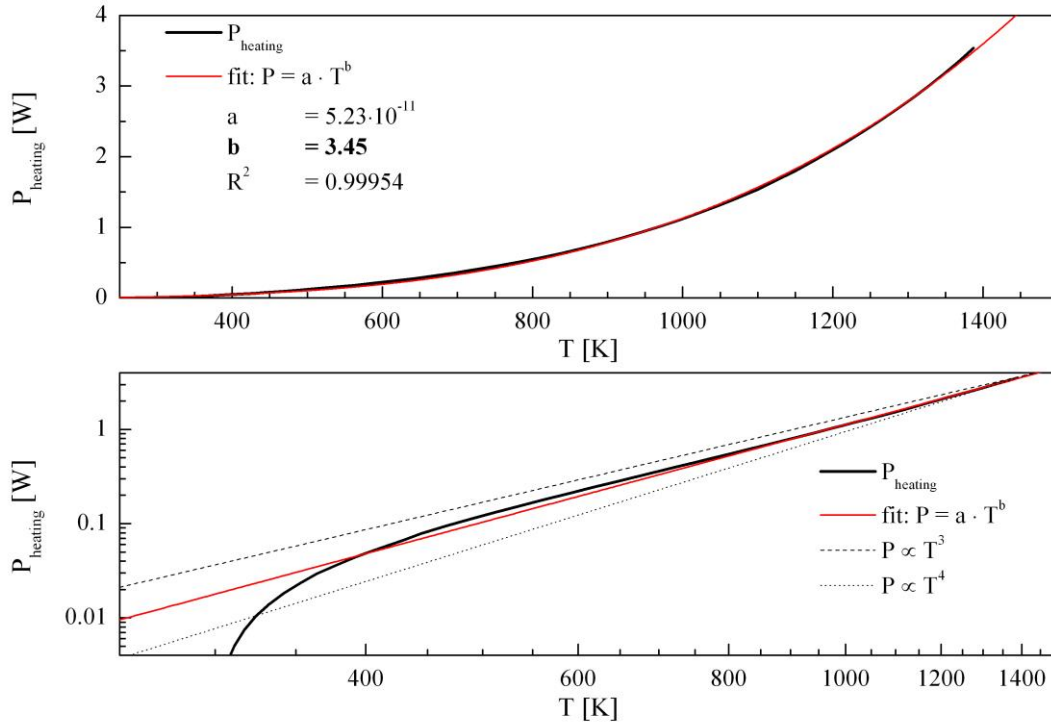


Figure 5-6: Heating power-temperature characteristic by heating an electrode with an applied DC current. The measurement is taken under stationary conditions, so that the applied heat power is equivalent to the heat losses. The average electrode temperature is estimated by the relation $R_{\text{hot}}/R_{\text{cold}}$. For high temperatures, the heat losses correspond to $P(T) \propto T^{3.45}$, which indicates the dominance of thermal radiation according to the STEFAN–BOLTZMANN law.

5.3 Lamp operation by modern electronic ballast systems at 25 kHz

The steady-state lamp operation is investigated in case of lamp operation by a modern electronic ballast system. Therefore the setup according to Figure 3-6 is used, whereas the lamp is driven by a current-controlled power supply working at 25 kHz. A T8-36W lamp, containing mercury and a mixture of 75% Argon and 25% Krypton at a pressure p of 2.10 mbar, is used for the investigation.

5.3.1 Dynamics of electrode operation

In Figure 5-7, the electrode operation is summarized for a lamp current of 320 mA, whereas the temporal lamp current, voltage, cathode fall voltage, electrode densities in the electrode region, and its deviation are given. As the effective spatial resolution of the applied microwave interferometer is about 4 mm, the measured densities are spatially averaged electron densities in front of the electrode.

The application of a current-controlled power supply leads to a nearly sinusoidal current profile. In contrast to voltage-controlled supplies, the electrode current is well defined whereas the lamp voltage arises as a result of the electrode processes. Thus, the voltage profile shows deviance from a sinusoidal function, especially during the transitions between cathode and anode phases.

During the cathode phase, the electrode has to sustain the lamp current by emitting electrons. Due to thermionic emission a certain amount of electrons is emitted continuously, the so-called *zero field current*. This emission depends on the temperature of the hot spot as well as on the effective emitting area. In general, the thermionic emission of electrons does not deliver the full lamp current during the cathode phase. Hence, the additional amount of electrons is emitted by the electric field emission according to the SCHOTTKY- and the patch effect (see Section 2.2.3). When the thermionic emission of electrons is no longer able to sustain the whole lamp current the electric field emission starts. Therefore, the cathode fall (a thin plasma sheet with a strong potential drop) builds up at the electrode surface. For the investigated discharge conditions, this can be observed approximately 2 μ s after the start of the cathode phase (Figure 5-7c). After a short peak, discussed in detail by Garner [2008b], the cathode fall stays at a constant level, with typical values in the range of 10 to 15 V. The emitted electrons pass the sheath and gain energy equivalent to the cathode fall. As they have significantly more energy, they are called beam electrons in contrast to the surrounding low energetic electrons in the electrode region, the so-called plasma electrons. During the cathode phase, secondary electrons are produced by ionization of mercury or rare gas atoms due to collisions with the high energetic beam electrons. Accordingly, the electron density increases (Figure 5-7d). The production of the secondary electrons depends on the energy of the beam electrons, determined by the cathode fall and the amount of beam electrons, and the actual lamp current.

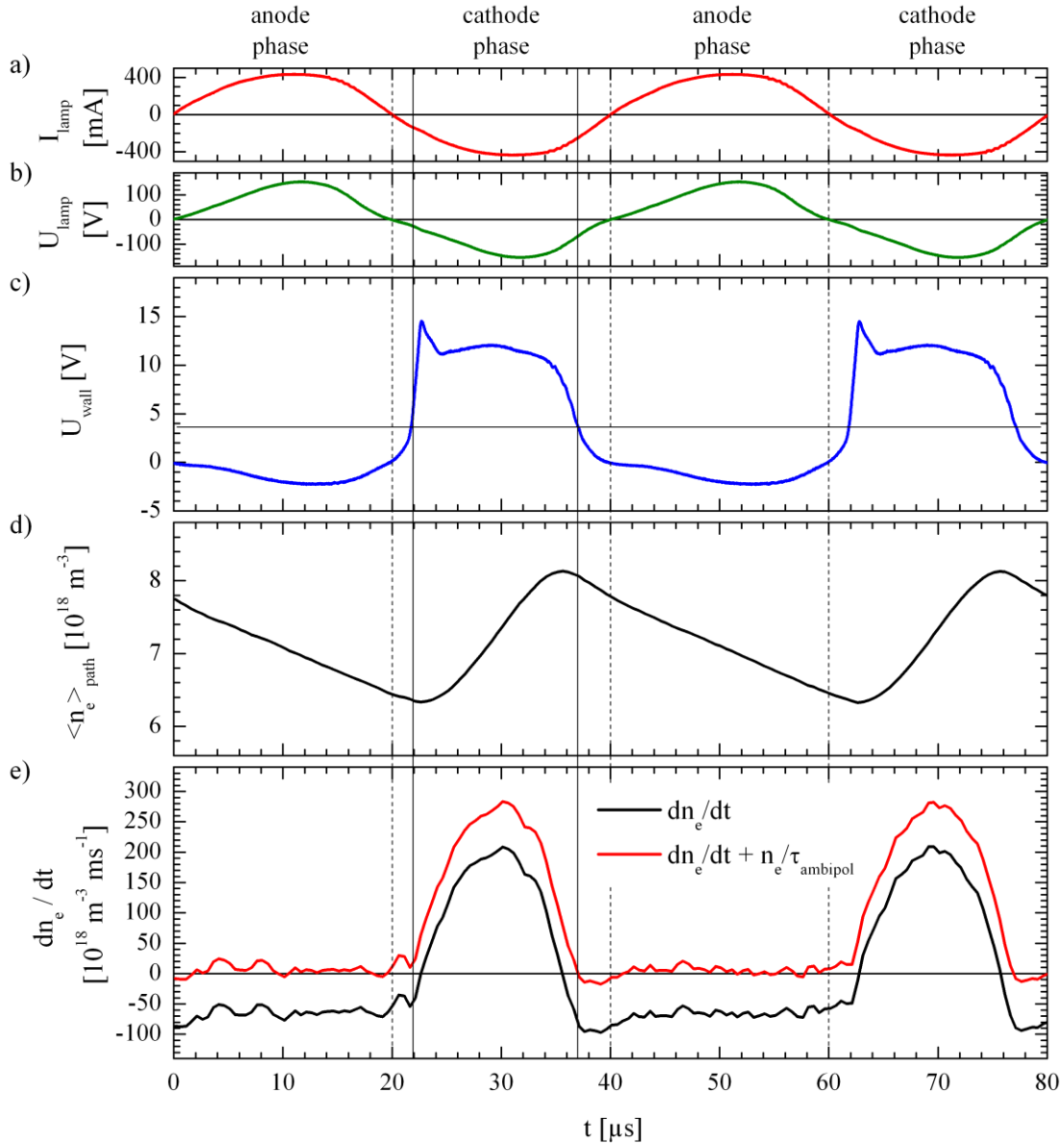


Figure 5-7: The 25 kHz operation mode. A T8-36W lamp with a gas mixture of Argon and Krypton at 2.1 mbar is operated at a current of 320 mA (rms value).

- a) lamp current
- b) lamp voltage
- c) cathode fall voltage measured by the capacitive band method
- d) path-averaged electron density
- e) deviation of the electron density (black) and derived electron production rate (red)

Towards the end of the cathode phase, the decreasing lamp current reaches the level of thermionic emission of electrons. The electric field emission of electrons is no longer needed and the cathode fall collapses, approximately 3 μs before the end of the cathode phase (see Figure 5-7c).

During the anode phase, the electrode has to collect the electrons. To prevent the thermionic emission of electrons and to collect the amount needed to sustain the lamp

current, an anode fall builds up with a typical potential between 0 V and 2 V [WAYMOUTH 1971]. Thus, the electron density decreases nearly constant by ambipolar diffusion, and field driven flux to the electrode. This could be seen directly in the deviation of the electron density given in Figure 5-7e. During the whole anode phase, the deviation is nearly constant and independent on the lamp current. This prompts the conclusion that the main loss of electrons during the anode phase accrues due to ambipolar diffusion. Thus, the corresponding ambipolar diffusion time constant could be estimated by:

$$\tau_{ambipol} \approx \frac{n_e}{\frac{d n_e}{d t}} \quad (5-8)$$

$$\approx 100\mu s$$

By correction of the losses due to ambipolar diffusion (red curve in Figure 5-7e), the electron production rate, (in the first approximation identical to the ionization rate), during the cathode phase could be determined. In correspondence to the cathode fall, the production of secondary electrons starts with the presence of beam electrons 2 μs after the beginning of the cathode phase and ends 3 μs before the end of the cathode phase.

The average electron density depends on the balance of production of electrons during the cathode phase and the loss of electrons during the anode phase. In contrast to low frequency operation, the electron density does not decrease completely during the anode phase.

5.3.2 Eroded barium in the electrode region

At the electrode, a stable hot-spot is established. The temperature of the spot is defined by the energy and the heat balance. However, the complex interaction of several mechanisms such as the thermionic emission, electric field emission and the corresponding cathode fall define the stable equilibrium. The resulting hot-spot temperature defines the production of free barium. As the lamp is driven with 25 kHz, the hot-spot temperature is constant during the period. Thus, the barium erosion as a result of evaporation is constant.

The evaporated barium is transported through the electrode region while interacting with the surrounding plasma. As a result, a pronounced modulation of the barium ground state densities could be observed, as depicted in Figure 5-8d. With increasing cathode fall, the high energetic beam electrons excite and ionize the evaporated barium atoms. Hence, the measured barium atom ground state density decreases with the increasing cathode fall voltage. The density of the high energetic beam electrons decreases immediately with the decrease of the cathode fall voltage at the end of the cathode phase. Thus, the excitation and ionization of the evaporating barium atoms also decreases. As a result, the density of the ground state starts to increase due to the evaporation and relaxation of excited levels, whereas continuous evaporation is the dominant effect. During the whole anode phase, the excitation and ionization is at a quite lower level so that the ground state density could increase.

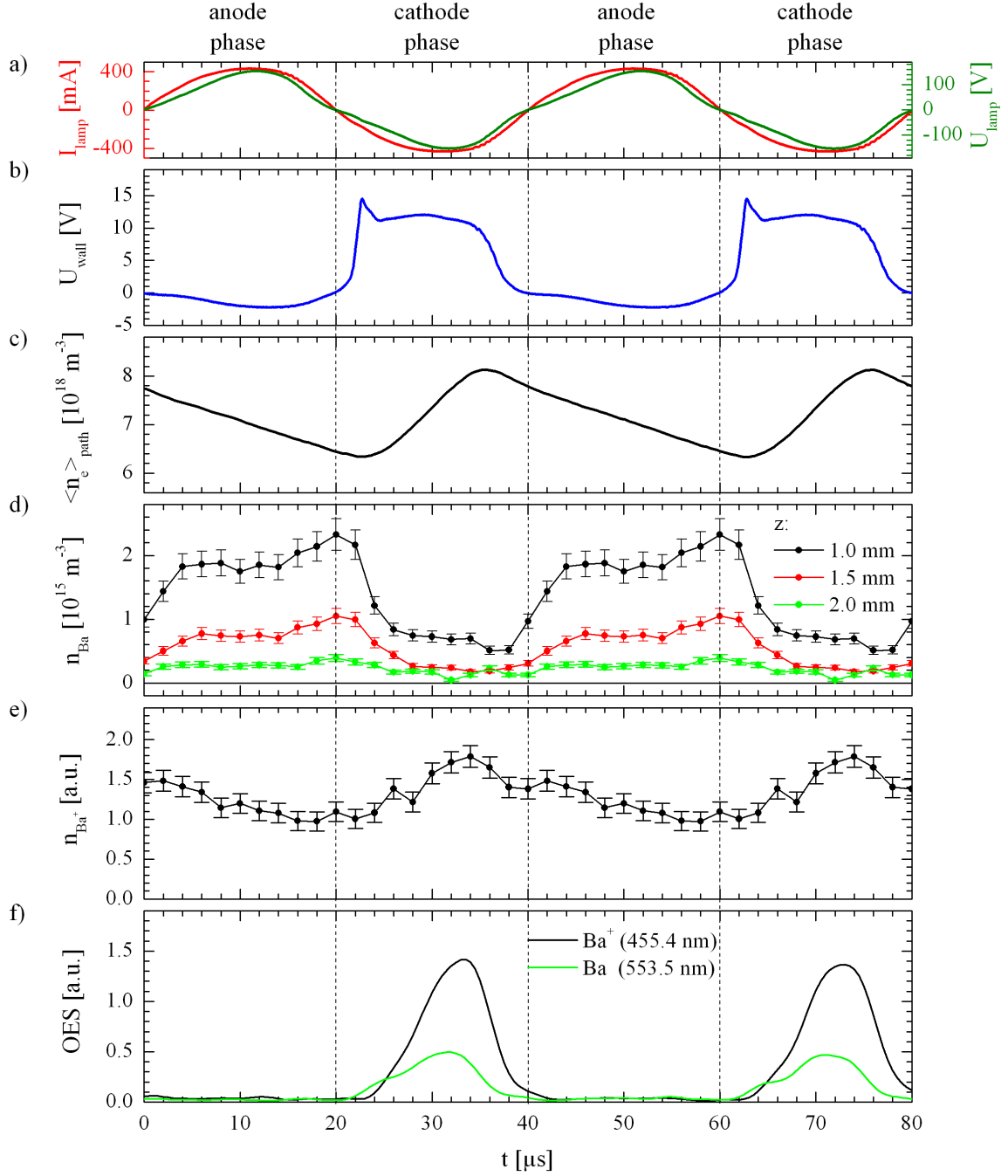


Figure 5-8: Typical results for the 25 kHz operation mode for a lamp current of 320 mA (rms value).
a) lamp current and lamp voltage
b) cathode fall voltage measured by the capacitive band method
c) path-averaged electron density
d) absolute barium atom ground state density at $z = 1, 1.5$ and 2 mm, measured by LIF
e) relative barium ion ground state density at $z = 1$ mm, measured by LIF
f) optical emission of the resonant barium ion line (455.4 nm) and the resonant barium atom line (553.5 nm) measured by OES

Due to the plasma effects, the measured densities show a strong spatial dependence. By increasing the measure position from $z = 1\text{ mm}$ to $z = 1.5\text{ mm}$ (equivalent to 0.5 mm to 1 mm distance from the electrode surface), the density increases by a factor of approximately 2.5. Going further away, the density reaches the detection limit of the system.

The relative barium ion ground state density, measured by LIF, is given in Figure 5-8e. During the cathode phase, the barium ion ground state density increases due to production of barium ions by ionization of barium atoms. This corresponds to the decay of the atom ground state density. During the anode phase, there is no production of additional barium ions. Thus, the ions produced in the cathode phase are transported through the electrode region and its density decreases. As the transport is driven by electric fields, it is very complex to describe the process in detail. In [SIGENEGER et al. 2010] we presented an approach to determine the electric field and the barium ion transport for one selected discharge condition of a 25 kHz Argon/Krypton discharge. However, the measured ion density shows only a moderate modulation.

In addition, the temporal-dependent optical emission¹⁶ of the resonant barium ion line at 455.4 nm and the resonant barium atom line at 553.5 nm are presented in Figure 5-8f. The optical emission depend on the temporal-dependent electron energy distribution.

Thus, optical emission can only be observed during the cathode phase, when high energetic beam electrons are present. The fact, that there is no emission of the resonant barium atom line (553.5 nm) during the anode phase, even though the highest atom ground state densities exist, allows the conclusion that excitation of barium atoms during the anode phase is very low and could be neglected. In general, the resonant barium ion line at 455.4 nm is significantly more intensive. Therefore, this line is often used in the literature to measure barium in the electrode region, although the correlation to the eroded barium is indirect. The intensity of the line depends on the erosion of barium, on its ionization, on the electric field-driven transport and finally on the excitation of the ions, whereas the ionization and excitation are very sensitive to the actual cathode fall voltage.

5.3.3 Spatial characteristics

The spatial dependence of the measured parameters is detailed in Figure 5-9. The temperature profile in Figure 5-9b is measured with the spatially-resolved pyrometric measurement system, provided by the OSRAM AG (see Section 6A.1) along the electrode axis. The temperature profile has a maximum of approximately 1100 K and a width of about 1 mm. In agreement, the width of the barium ground state density profile in front of the electrode at $z = 1\text{ mm}$ (0.5 mm in front of the electrode surface) has been found to be about 1 mm (see Figure 5-9c).

¹⁶ For measurement of the optical emission, the LIF setup is used. The monochromator is used to scan over the transition wavelength, whereas the temporal signal of the photomultiplier is measured.

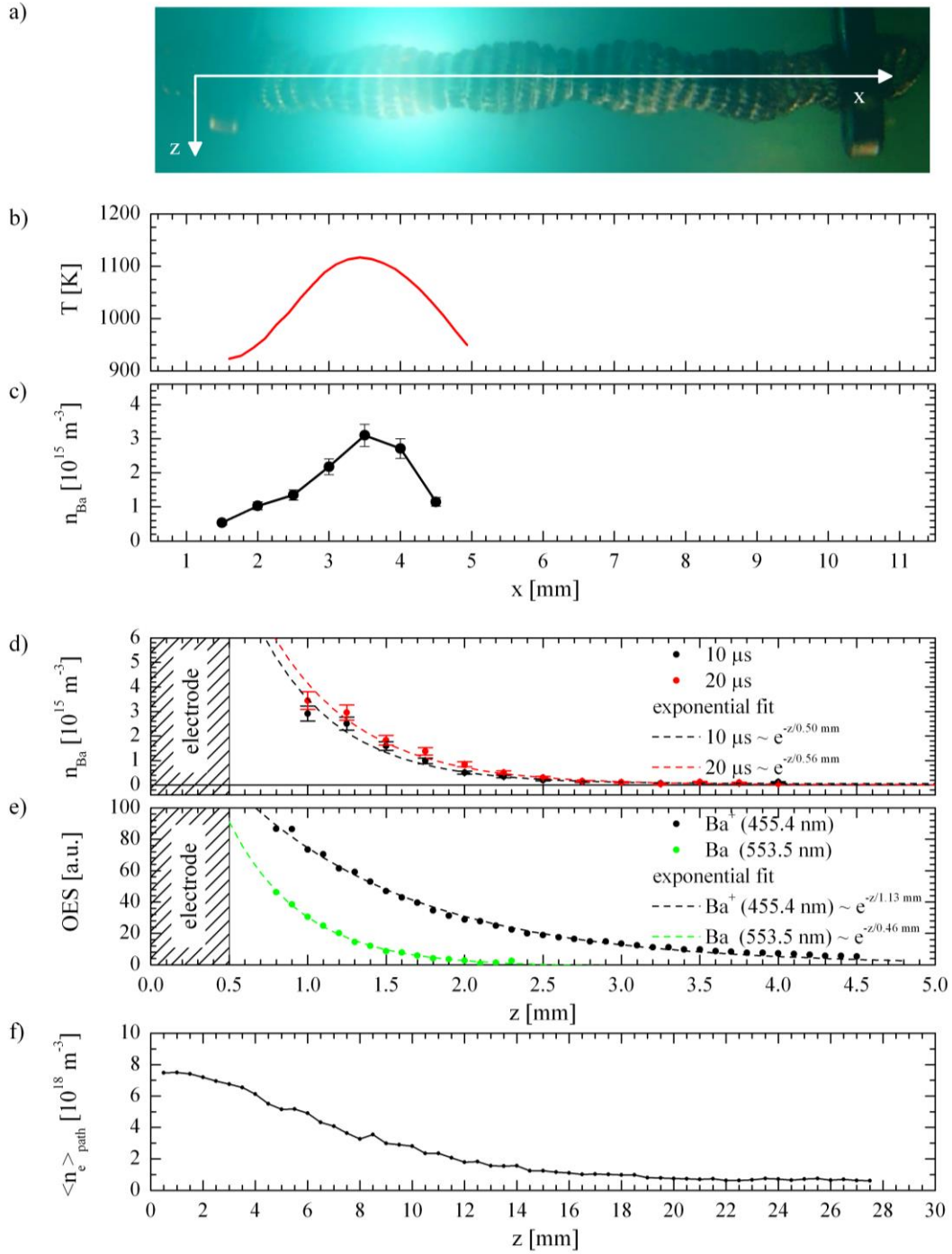


Figure 5-9: Spatial dependents of the measured quantities for the 25 kHz operation mode for a lamp current of 320 mA (rms value).

- a) photograph of the electrode including the coordinate system
- b) temperature along the electrode ($z = 0$ mm)
- c) barium ground state density at $t = 20 \mu\text{s}$ and $z = 1$ mm
- d) barium ground state density in z -direction at $t = 10 \mu\text{s}$ and $t = 20 \mu\text{s}$ ($x = 3.6$ mm)
- e) Time-averaged optical emission in z -direction ($x = 3.6$ mm)
- f) Time- and path-averaged electron density in z -direction

In z-direction, the barium ground state density decays exponentially (see Figure 5-9d). The decay length is in the range of 0.5 mm. In detail, a decay length of 0.5 mm has been found during the anode phase (at $t = 10 \mu\text{s}$) and of 0.56 mm at the end of the anode phase (at $t = 20 \mu\text{s}$). During the cathode phase the decay length could not be determined due to the low density.

For the time-averaged optical emission of the resonant barium atom line at 553.5 nm (see Figure 5-9e), a corresponding decay length of about 0.46 mm has been found. In contrast, for the resonant barium ion line at 455.4, a significantly longer decay length of 1.13 mm has been determined. This indicates that excited barium ions still exist at greater distances from the electrode. However, the detected optical emission is line of sight integrated and depends on the excitation processes. Thus, the measurements are not directly connected to the corresponding densities.

In case of the electron densities, a much longer decay length of about 8 mm has been found (see Figure 5-9f). The density decays from about $\langle n_e \rangle_{\text{path}} = 8 \cdot 10^{18} \text{ m}^{-3}$ at the electrode to a tenth at the positive column.

5.4 Dimmed operation by variation of lamp current

Modern lighting systems provide the opportunity to adjust the light output. Furthermore, by combining fluorescent lamps with different light colors, the color can be adjusted to the requirements or preferences of the user. Thus, in the daytime a higher color temperature could be set, whereas in the evening a warmer light with lower color temperatures could be set. Technically, the variation of the light output of a fluorescent lamp is solved by varying the lamp current, also called dimming.

In general, an electrode is designed according to the discharge conditions such as lamp current, gas and pressure. In case of a dimmable lamp, the electrode has to operate within a certain current range without significant reduction of the lifetime.

In case of high lamp current, the energy balance of the electrode shifts to higher hot-spot temperatures, which lead to higher thermionic emissions of electrons, which in turn lead to lower cathode fall voltage (typical characteristics of an arc discharge). In case of electrode erosion, the higher hot-spot temperatures lead to significant higher barium evaporation (see Figure 5-4), thus reducing the electrode's lifetime.

In contrast, for low lamp currents, the hot-spot temperature decreases. Thus, the thermionic emission of electrons decreases disproportionately, which in turn leads to an increase of the cathode fall voltage. If the cathode fall voltage exceeds a certain level, the energy of the ions is sufficient to sputter electrode material, which also reduces the electrode's lifetime. The sputter threshold of the cathode fall voltage has been found to be about 15 V [GARNER 2008b; WAYMOUTH 1971] and could be exceeded for low lamp currents.

By further decreasing lamp currents, the discharge transits to the glow mode with further increased cathode fall voltages in the order of about 100 V. Due to the high sputter rates that occur, the electrode is destroyed in a few hours in this mode.

To reach a sufficient electrode lifetime during dimmed operation for low lamp currents, an additional heat current I_{heat} is applied through the electrode. The additional current

represents an additional heating mechanism, increasing the hot-spot temperature. By applying a proper heat current, the hot-spot temperature could be adjusted to a level where the thermionic emission is sufficient to reduce the cathode fall voltage below the sputter threshold. The efficacy of the additional heating depends on choosing the optimal heat current for the desired lamp current. To ensure compatibility of different fluorescent lamps of various manufactures with different electronic ballast systems, the relevant currents and heat currents are specified in standard *EN 60901*.

To deliver reliable data of barium erosion during dimmed operation, in the following lamp operation is investigated by varying the lamp current and the additional applied heat current.

5.4.1 Variation of lamp current

For the purposes of investigation, the same lamp and setup were used as those of the previous. The lamp is driven at 25 kHz with different discharge currents. The electrode temperature profile, measured in the center of the electrode along the axis with the pyrometric measurement system provided by the OSRAM AG (see Section 6A.1), for the different discharge currents is given in Figure 5-10.

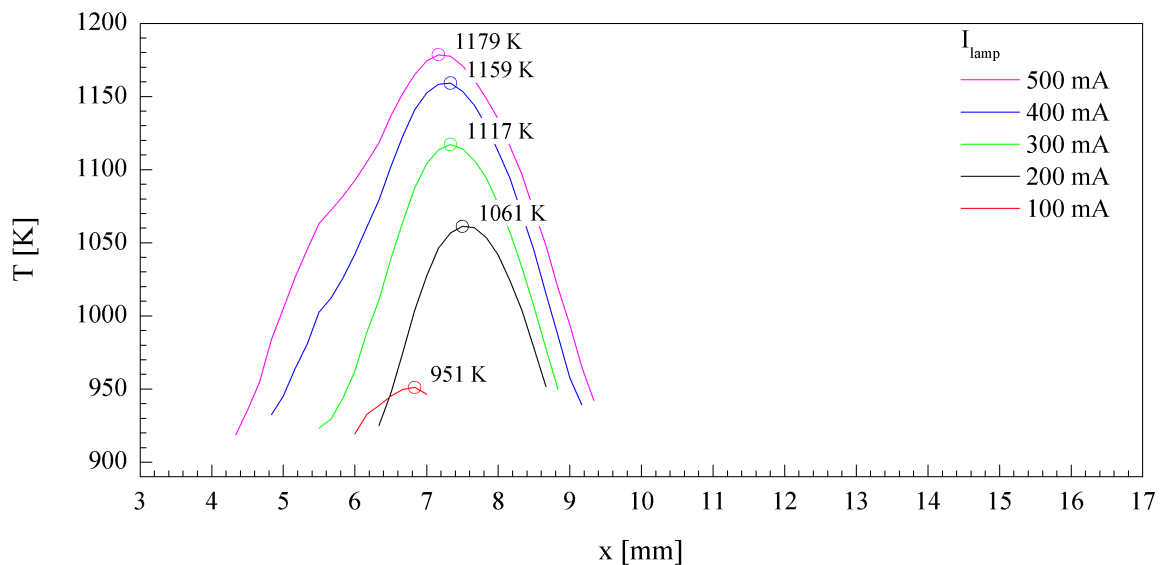


Figure 5-10: Temperature profile of the electrode for different lamp currents of a T08-36W lamp operating at 25 kHz. The temperature is measured along the electrode ($z = 0$ mm) with the pyrometric measurement system, provided by the OSRAM AG.

For the lowest discharge current investigated, a very low hot-spot temperature of about 951 K has been found. For higher discharge currents, the maximum electrode temperature increases to about 1179 K for 500 mA. Simultaneously, the profile positions shift in a range of about 0.5 mm and broaden for the highest discharge current. This broadening at 500 mA indicates that the heat input due to ohmic heating is too high and the electrode is working at

a current significantly higher than its nominal current. Thus, a significant increase of barium evaporation has to be expected.

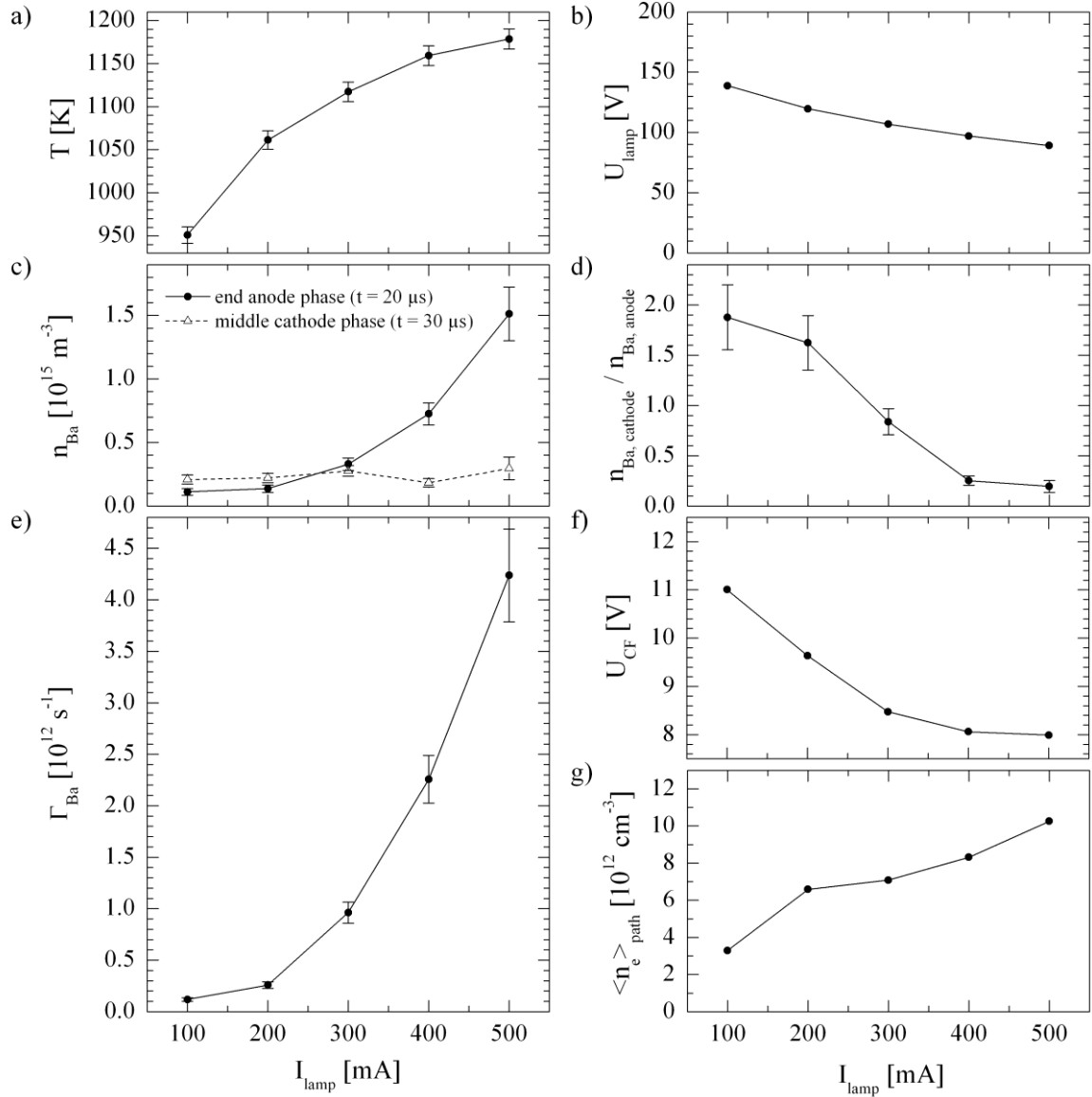


Figure 5-11: Variation of lamp current by operating at 25 kHz.

- a) maximum of the electrode temperature
- b) lamp voltage (rms value)
- c) absolute population density of the barium ground state measured 0.5 mm in front of electrode surface ($z = 1 \text{ mm}$) at the end of the anode phase (at $t = 20 \mu\text{s}$) and in the middle of the cathode phase (at $t = 30 \mu\text{s}$)
- d) ratio of the barium density during cathode phase (at $t = 20 \mu\text{s}$) and at the end of the anode phase (at $t = 30 \mu\text{s}$), indicating sputtering effects
- e) absolute flux of evaporated barium determined by the blanking method
- f) cathode fall voltage measured with the band method (voltage at the middle of the cathode phase)
- g) path- and time-averaged electron density in the electrode region

For a more detailed discussion, the measured parameters are summarized in Figure 5-11. As hot-spot temperatures, the maximum of the corresponding temperature profiles are given in Figure 5-11a. As typical of the arc-discharges, the lamp voltage (Figure 5-11b) decreases with increasing lamp current caused by changes of the electrode operation and in the positive column.

With the increasing lamp current, the energy balance of the electrode shifts to higher hot-spot temperatures due to increased ohmic heating. The higher spot temperatures lead to higher thermionic emission of electrons, which in turn leads to lower cathode fall voltage (typical characteristics of an arc discharge) and finally to a reduced lamp voltage. The same process affects the observed path-averaged electron density given in Figure 5-11g. In the first approximation, one would expect a linear dependence of the electron density on the lamp current as the lamp current defines the number of beam electrons. Nevertheless, the reduction of the cathode fall voltage for higher lamp currents leads to lower energies of the emitted beam electrons. Thus, the production rate of secondary electrons per beam electron (due to ionization of mercury or buffer gas atoms) is reduced.

All the electrode processes affect the barium erosion. In Figure 5-11e, the absolute barium evaporation flux, determined by the blanking method, is given. For low lamp currents of 100 mA and 200 mA, the barium evaporation flux is in the range of $1.5 \cdot 10^{11} \text{ s}^{-1}$, which is very low and below the level one would expect for an electrode lifetime of 20,000 hours of $\Gamma_{\text{Ba}, 20000\text{h}} = 3.2 \cdot 10^{11} \text{ s}^{-1}$ (see Appendix B.3). For discharge currents above 200 mA, the barium fluxes increase disproportionately. Thus, for 500 mA the barium flux is very high and about a factor of 13 above the value one would expect for the lifetime of a typical lamp. Hence, this discharge current is too high for the electrode and significantly affects its lifetime. However, the measured fluxes correspond to the measured temperatures.

Additional information could be obtained by analyzing the barium densities during operation, 0.5 mm in front of the hot-spot (Figure 5-11c). Although the densities do not allow a direct determination of the barium fluxes (the measured ground state densities are affected by ionization and excitation processes during the cathode phase, see Section 5.3.2), the densities at the end of the anode phase correspond to the fluxes determined by the blanking method. In addition, an abnormality for the both lowest investigated lamp currents has been found. For these currents, the densities at the end of the anode ($t = 20 \mu\text{s}$, solid line in Figure 5-11c) are lower than the densities during the cathode phase ($t = 30 \mu\text{s}$, dashed line in Figure 5-11c). Usually, the barium ground state densities during the cathode phase are significantly lower, as they are excited and ionized by the high energetic beam electrons present in the cathode phase (see Figure 5-8d). Thus, the higher densities during the cathode phase could only be caused by additional barium atom production. As the evaporation rate could be assumed constant, the additional production could only be explained by sputtering of barium. This assumption is in agreement with the observed lower hot-spot temperatures and the resulting higher cathode fall voltages (Figure 5-11f).

As an indicator for this effect, the ratio of barium ground state density during the cathode phase and the density at the end of the anode phase 0.5 mm in front of the electrode surface could be used (see Figure 5-11d):

$$a = \frac{n_{\text{Ba},0.5\text{mm,cathode}}}{n_{\text{Ba},0.5\text{mm,anode}}} = \frac{n_{\text{Ba},0.5\text{mm}}(t = 30\mu\text{s})}{n_{\text{Ba},0.5\text{mm}}(t = 20\mu\text{s})} \quad (5-9)$$

For normal (no sputtering) operation, the ratio is significantly smaller than 1. Thus, for the highest investigated currents (400 mA and 500 mA) the ratio is below 0.2. For the lowest currents (100 mA and 200 mA) the ratio is above 1 (about 1.8), indicating sputtering as discussed. However, the ratio could be used as an indicator, but does not deliver quantitative values. During the cathode phase, the sputtered atoms are also excited and ionized. Thus, without detailed knowledge of the corresponding excitation and ionization rates, depending on the electron energy distribution, it is not possible to determine the absolute amount of sputtered barium. However, the fact that the ratio is above one, it can be concluded that a significant amount of barium erosion is caused by sputtering. To reduce the erosion, these operation conditions should be avoided.

5.4.2 Influence on additional applied heat current

To reduce sputtering of electrode material at low lamp currents, an additional heating current typically is applied through the electrode. Thus, the electrode temperature and therefore the thermionic emission of electrons increases, whereas the sputtering causing cathode fall voltage decreases. In the following experiment, the same lamp and discharge conditions as in the previous section are investigated. The additional DC heat current I_{heat} is applied through the electrode by connecting the current source (KEITHLEY 238) to the two outer electrode contacts (see Figure 5-12). To ensure heating by a DC current, an additional choke with 2.5 mH is placed in line with the current source. Thus, higher frequencies and especially the operational frequency of 25 kHz is blocked.

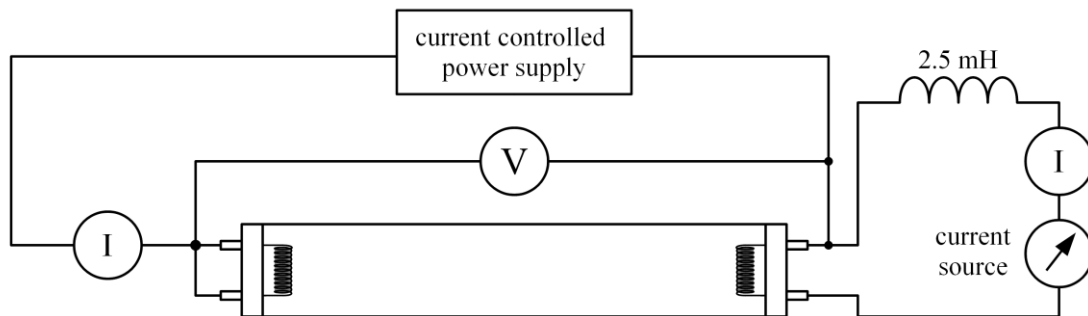


Figure 5-12: Applied electrical setup for variation of lamp and heat currents. For heating the current source, KEITHLEY 238 is used. To ensure a DC heat current, a choke with 2.5 mH is placed in line to block higher frequencies.

The change of the electrode temperature profile by application of additional heat currents is given in Figure 5-13 for the standard lamp current of 300 mA. For heat currents of 100 mA and 200 mA, the temperature profile changes only slightly in comparison to the profile without additional heating. The temperature increases about 5 K and the temperature profile slightly broadens. For a heat current of 300 mA, a significant broadening and an increase of the temperature of about 12 K could be observed. By further increasing the heat current, the maximum of the hot-spot is shifted about 1.5 mm towards the edge of the electrode. In addition, the temperature of the whole electrode increases. Thus, for heat currents above $I_{\text{heat}} \geq 400$ mA, no local hot-spot could be found as the whole electrode has temperatures allowing thermionic emission of electrons.

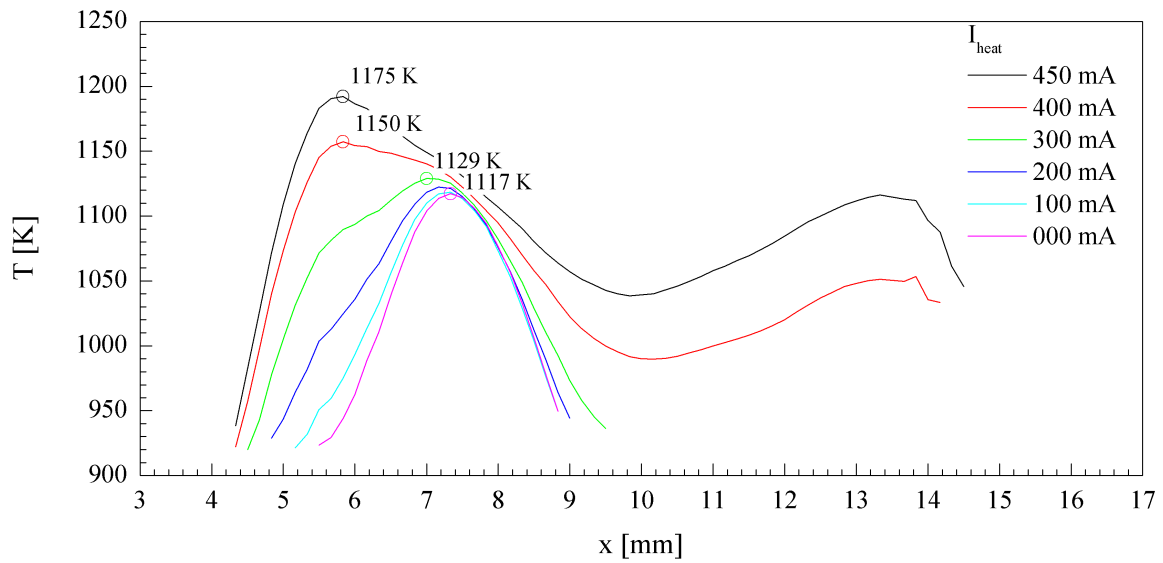


Figure 5-13: Electrode temperature profiles by application of additional heat currents. The T08-36W lamp is operating at 25 kHz with a lamp current of 300 mA (rms). The temperature is measured along the electrode ($z = 0$ mm) with the pyrometric measurement system, provided by the OSRAM AG.

The dependence of the other investigated parameters, especially the resulting barium evaporation, are summarized in Figure 5-14 for all investigated lamp currents. Again, the maximum of the electrode temperature profile (as indicated in Figure 5-13 by the circles) is given in Figure 5-14a. First, the maximum electrode temperatures only slightly increase with increasing heat current (as already discussed for 300 mA lamp current). By reaching a certain threshold, the maximum electrode temperature starts to increase strongly. This threshold seems to depend on the lamp current whereas a higher lamp current leads to a lower threshold. As such, the stronger increase for a lamp current of 500 mA starts at a heat current of about 250 mA and for a lamp current of 200 mA it starts at a heat current of about 400 mA. In agreement with the measured electrode temperatures, the absolute fluxes of evaporated barium (determine by the blanking method) increase. As the values range over more than two orders of magnitude, a logarithmic plot has been chosen for use in Figure 5-14c. Especially for high heating currents (400 mA and 450 mA), a stronger increase of the evaporation could be found. This could be explained by the increased

maximum temperature and in particular by the additional broadening (see Figure 5-13) of the hot spot, leading to an enlarged evaporation surface. Although the densities measured at the end of the anode phase (at $t = 20 \mu\text{s}$, given in Figure 5-14d) are a result of the evaporation of barium and its transport through the plasma in the electrode region, they have the same tendency.

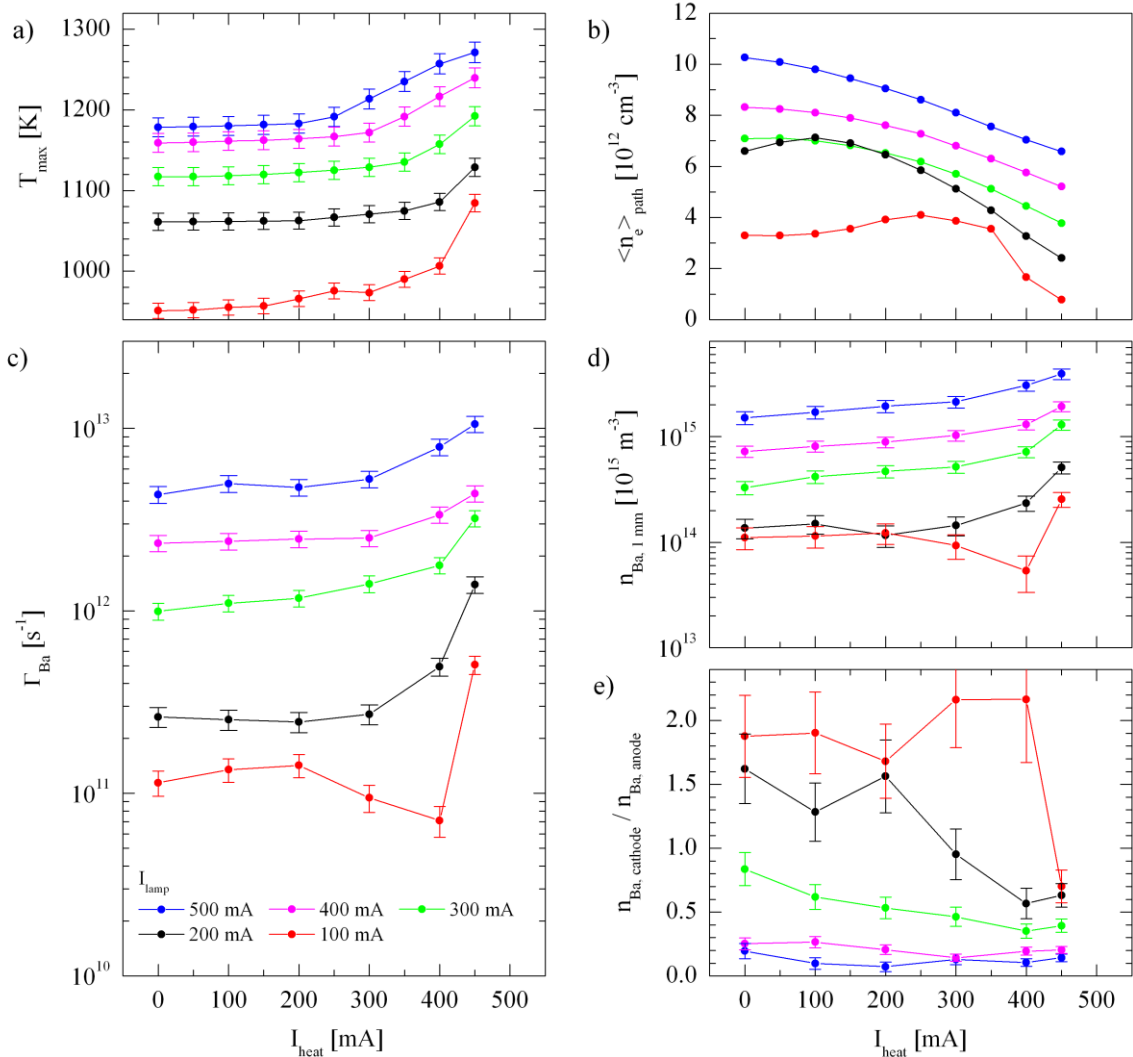


Figure 5-14: Influence of additional applied heat currents on electrode processes of different lamp currents.

- a) maximum of the electrode temperature
- b) path- and time-averaged electron densities in the electrode region
- c) evaporated barium determined by the blanking method
- d) absolute population density of the barium ground state measured 0.5 mm in front of electrode surface ($z = 1 \text{ mm}$) at the end of the anode phase at $t = 20 \mu\text{s}$
- e) ratio of the barium density during cathode phase (at $t = 20 \mu\text{s}$) and at the end of the anode phase (at $t = 20 \mu\text{s}$), indicating sputtering effects

A more detailed understanding of the electrode operation by application of an additional heat current could be derived from the measured electron densities given in Figure 5-14b.

For heat currents of $I_{\text{heat}} \geq 300 \text{ mA}$, the path-averaged electron densities in the electrode region decrease with increasing heat current. As the thermionic emission increases with temperature for higher heat currents, the cathode fall voltage and therefore the production of secondary electrons by the beam electron would be reduced. Finally, this leads to the observed reduction of the electron densities. For the two lowest investigated lamp currents, a different behavior has been found. Here, first the path-averaged electron densities grow with increasing heat current until a certain maximum is reached. By further increasing heat current, the electron densities decreases as observed for the higher lamp currents. Thus, for a lamp current of $I_{\text{lamp}} = 200 \text{ mA}$ the maximum could be found for a heat current of $I_{\text{heat}} = 100 \text{ mA}$, whereas for the lowest lamp current of $I_{\text{lamp}} = 100 \text{ mA}$ the maximum shifts to a higher heat current of $I_{\text{heat}} = 300 \text{ mA}$.

In addition to the abnormal increase of the electron densities, a change of the sputter indication ratio of barium ground state density during the cathode phase and at the end of the anode phase can be found (according equation (5-9); see Figure 5-14e). For a certain heat current, the ratio drops below the threshold value of one, indicating a significant reduction of sputtering. For a lamp current of $I_{\text{lamp}} = 200 \text{ mA}$, this heat current is about $I_{\text{heat}} = 300 \text{ mA}$ and for $I_{\text{lamp}} = 100 \text{ mA}$ it is about $I_{\text{heat}} = 450 \text{ mA}$. Evaporation starts to increase at these heat currents (Figure 5-14c), so we can conclude that the electrode operates in the normal thermionic mode with reduced sputtering. However, the discovered heat currents for reduction of sputtering are about 150 mA higher than the heat currents of the maximum electron densities. Up until now, the effect of the appearance of this maximum in the electron density for low lamp currents is not completely understood, but perhaps it could be used as a simple method for adapting the heat current according to the lamp to reduce sputtering. In contrast to temperature determination and LIF, for determination of electron densities the ends of the lamps need not to be cleared of phosphor. As such, the method could be applied to non-modified commercial lamps.

For the dimmed operation, it can be concluded that for low lamp currents an additional applied heat current could reduce sputtering. In the case of investigated lamps for a lamp current of $I_{\text{lamp}} = 200 \text{ mA}$, the heat current should be about $I_{\text{heat}} = 300 \text{ mA}$ and for $I_{\text{lamp}} = 100 \text{ mA}$ it is about $I_{\text{heat}} = 450 \text{ mA}$. By applying these currents, the barium evaporation would increase and reach a level comparable to the normal operation at about 320 mA. Thus, if sputtering could be avoided completely (which is not absolutely guaranteed by the measured data), the lifetime of the electrode would not be reduced even during dimmed operation. An additional heating for lamp currents higher than 300 mA is not necessary and would significantly increase the barium evaporation. For these lamp currents, an increased evaporation has been found. Thus, for a lamp current of 400 mA the evaporation is increased by a factor of about 2 in comparison to 300 mA, and for a lamp current of 500 mA by a factor of about 4. This in turn would reduce the electrode lifetime by the same factors.

5.5 Frequency variation

Until the introduction of electronically controlled ballasts, fluorescent lamps were operated at the net frequency (Europe: 50 Hz; US: 60 Hz). In the early 1980s, electronically controlled ballasts facilitated operation at higher frequencies of a few kHz, thus improving the efficacy [ROZENBOOM 1983]. In the following, the dependence of the electrode erosion on the operating frequency is investigated in a range from 50 Hz up to 5 kHz for different lamp currents.

To vary the frequency in the desired range, a special lamp operation setup is applied (Figure 5-15). Two high voltage sources are used to generate a negative and a corresponding positive voltage, whereas one electrode is connected to the shared potential. For lamp operation, the positive and negative voltages are alternately switched to the other electrode. For switching, TTL¹² triggered IGBT⁹s (insulated-gate bipolar transistors) are used. Thus, the operational frequency could be varied by variation of the control signals of the IGBTs. To achieve a current controlled operation, a 220 Ω resistor is placed in series to the lamp. To protect the voltage sources against shorting, each is protected by a 110 Ω resistor. In contrast to normal lamp operation with a sinusoidal voltage or current, the setup leads to a rectangular current profile. These characteristic needed, as it leads to constant current during the anode phase and subsequent cathode phase, and allows a direct comparison of the different frequencies under the same discharge conditions.

For investigation, the same T8-36W lamp (mixture of 75% Argon and 25% Krypton at a pressure of 2.10 mbar) as in the previous sections is used.

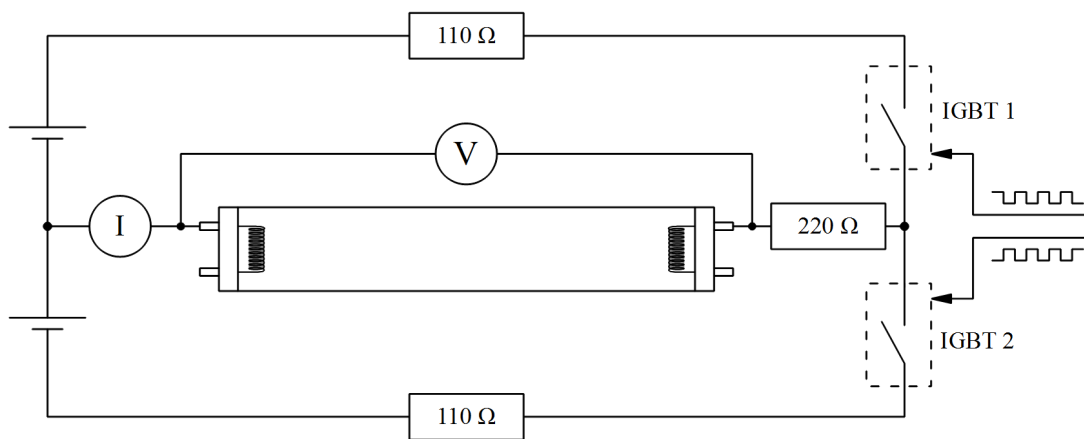


Figure 5-15: Electrical setup used for frequency variation. Two TTL-controlled IGBT-switches are used for alternating switch one electrode to a positive and a negative potential generated with two high voltage sources FUG MCA 750-1500. The operational frequency could be varied by changing the TTL-signals.

5.5.1 Anode oscillation during low frequency operation

As the dependence of the electrode operation on the operational frequency is dominated by anode effects, first the anode phase should be investigated for low frequencies.

During the cathode phase, a high electron density builds up in the electrode region due to secondary electrons produced by the beam electrons. Thus, each anode phase starts with high electron densities. During the anode phase, the electrode collects the electrons, and therefore a certain anode fall voltage is needed. Due to the reservoir of electrons in the electrode region at the beginning of the anode phase, initially there is no need for a high anode fall. Under certain conditions (electron excess in the electrode region) even a negative anode fall voltage could appear [WAYMOUTH 1971]. However, during the anode phase, the electron density in the electrode region decreases due to field driven drift, collection of electrons by the anode, and ambipolar diffusion. The time constant of the decay is about one millisecond and therefore in the order of the ambipolar diffusion. After certain duration of the anode phase, the electron density in the electrode region reaches a level where an increased anode fall voltage is needed to sustain the electron current. Approximately, this density level corresponds to the electron density in the positive column [WAYMOUTH 1971]. By further increasing the electron density, the anode fall voltage also increases until it reaches the level where the energy gain of the electrons is sufficient to ionize mercury atoms. Thus, additional secondary electrons are generated leading to an abrupt rise of the electron density. This in turn leads to the decrease of the anode fall voltage, as it is no longer needed to sustain the lamp current. After a certain time, the decreasing electron density reaches a critical level and the anode fall voltage rises again. Finally, it ends up with an oscillation of the electron density and anode fall voltage. These so-called anode oscillations are typical for anode phases longer than about one millisecond. For a current controlled lamp operation, the oscillations could be observed in the lamp voltage.

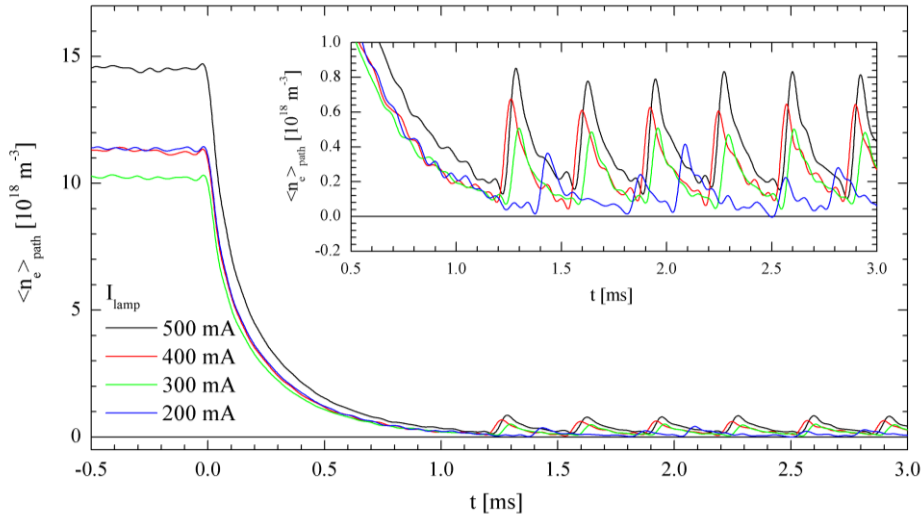


Figure 5-16: Anode oscillation illustrated by the path-averaged electron densities in the electrode region. The T8-36W lamp is operated with a rectangular-shaped current profile at 50 Hz. At $t = 0$ ms, the anode phase starts.

In Figure 5-16, the appearance of anode oscillations are plotted by the path-averaged electron density for different lamp currents. The T8-36W lamp is operated by a rectangular-shaped AC current at 50 Hz. The anode phase starts at $t = 0$ ms. At about 1.2 ms the

electron density is decreased to a level that causes the anode fall voltage to increase. Thus, the first anode oscillation starts. Remarkably, the starting time is the same for all investigated currents except the lowest (200 mA). Even the frequency of the oscillation is the same (about 3 kHz) for these currents. For the lowest lamp current, the oscillations start about 0.2 ms delayed and seem to be unstable. The minimal remaining electron density and the height of the electron density fluctuation increase with increasing lamp current.

It could be concluded that for anode phases shorter than 1.2 ms (this corresponds to an operational frequency of 420 Hz), the appearance of anode oscillations and therefore additional anode fall voltage could be avoided. A substantial part of the increase of lamp efficacy at kHz-operation is caused by avoiding anode oscillations.

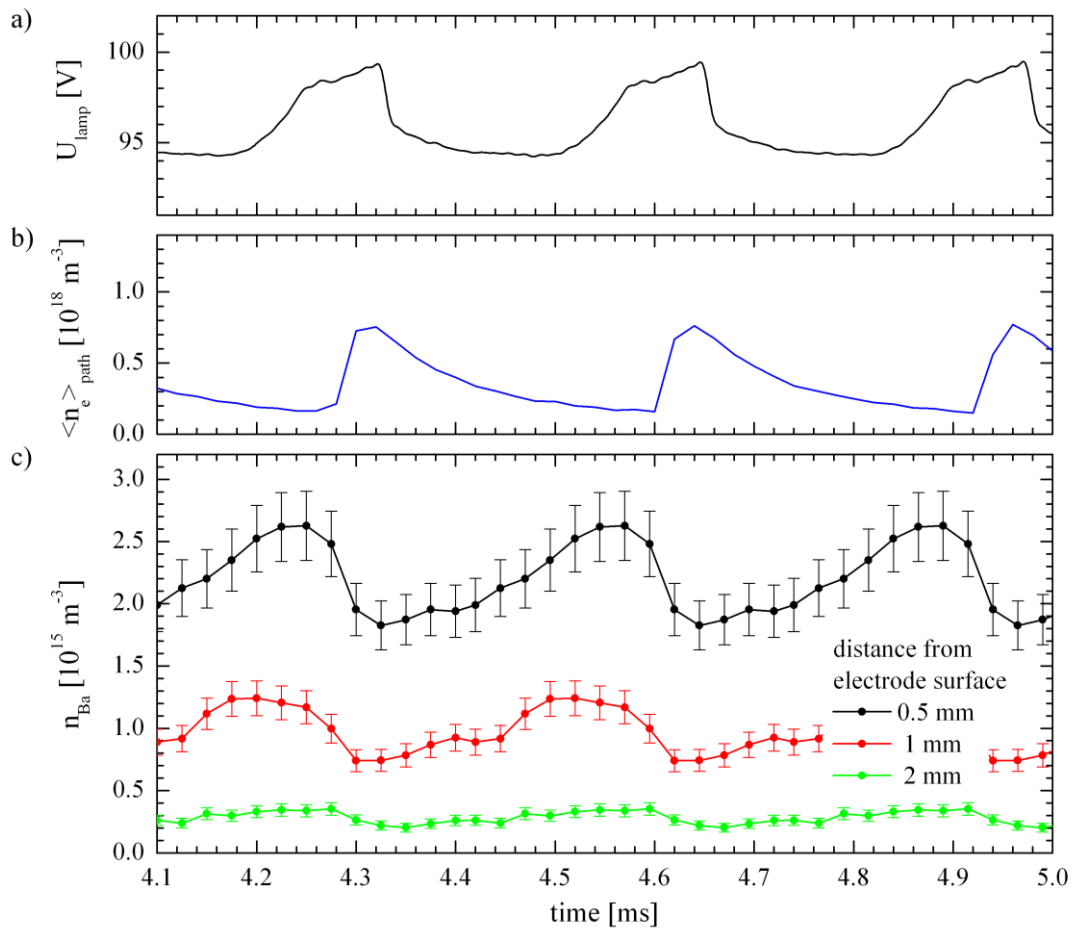


Figure 5-17: Modulation of the barium ground state density due to anode oscillations. The T8-36W lamp is operated with a rectangular-shaped current profile at 50 Hz and 500 mA. The anode phase begins at $t = 0$ ms.

- a) lamp voltage
- b) path-averaged electron density in the electrode region
- c) barium ground state density at different positions in front of the electrode surface

Anode oscillations lead to an abrupt increase of the electron energy, and subsequently a modification of the electron-energy distribution function. Besides the already discussed increase of the electron density, the higher electron energy affects all particles in the

electrode region. Thus, the ground state density of the evaporated barium atoms is also modulated, as shown in Figure 5-17 for a lamp current of 500 mA. The anode oscillations correspond to an increase of the lamp voltage of about 5 V. Shortly before reaching the maximum voltage (anode fall voltage), the ionization (generation secondary electrons) starts and the electrode density increases. Simultaneously, the barium ground state density in front of the electrode decreases due to the higher electron energy leading to additional excitation and ionization. As the electron energy should be greater than the mercury ionization energy, the ionization of barium atoms is a minor process. From the given data it could be concluded that the duration of the intense excitation is shorter than 40 μ s.

However, near to the electrode (0.5 mm from the electrode surface) anode oscillation leads to a modulation of the barium ground state density of about 30%. Even at a distance of 2 mm, where only a tenth of the density is measured, the modulation could be observed. The effect has important consequences for interpretation of measured densities during the anode phase. For low frequency operation (if anode oscillations appear), the measured densities are modulated by the anode oscillation. Thus, the additional error in the measured densities (about 30% at a distance of 0.5 mm from the electrode surface) has to be considered.

5.5.2 Frequency variation

An overview of the discharge characteristics by varying the operational frequency is given in Figure 5-18 for a lamp current of 300 mA. The lamp current shows the desired rectangular characteristics, whereas for low frequencies a low modulation due to anode oscillation could be observed. The modulation could also be found in the lamp voltage (see Figure 5-18b). The fundamental impact of the operational frequency could be derived from the path-averaged electron density given in Figure 5-18c. As already discussed, with the beginning of the anode phase ($t = 0$) the electron densities start to decrease. As the lamp is driven by a rectangular AC current, the decrease is the same for all operational frequencies. However, after about 1.2 ms the electron densities reach the level where anode oscillations start (also discussed in Section 5.5.1). For frequencies with anode phases shorter than this time (operational frequencies above 420 Hz), no anode oscillations appear. During the cathode phases, the path-averaged electron densities increase to a level of about $12 \cdot 10^{18} \text{ m}^{-3}$, whereas the level is reached after about one millisecond. For operational frequencies above 1 kHz, the cathode phase is too short, so that this value will not be reached. Accordingly, the electron densities at the beginning of the anode phase are lower. However, the electron density and especially its fluctuation are determined by the durations of both half cycles. By operation with a sinusoidal current, the electron densities would also be affected by the temporal current fluctuations, leading to slightly modified temporal density characteristics.

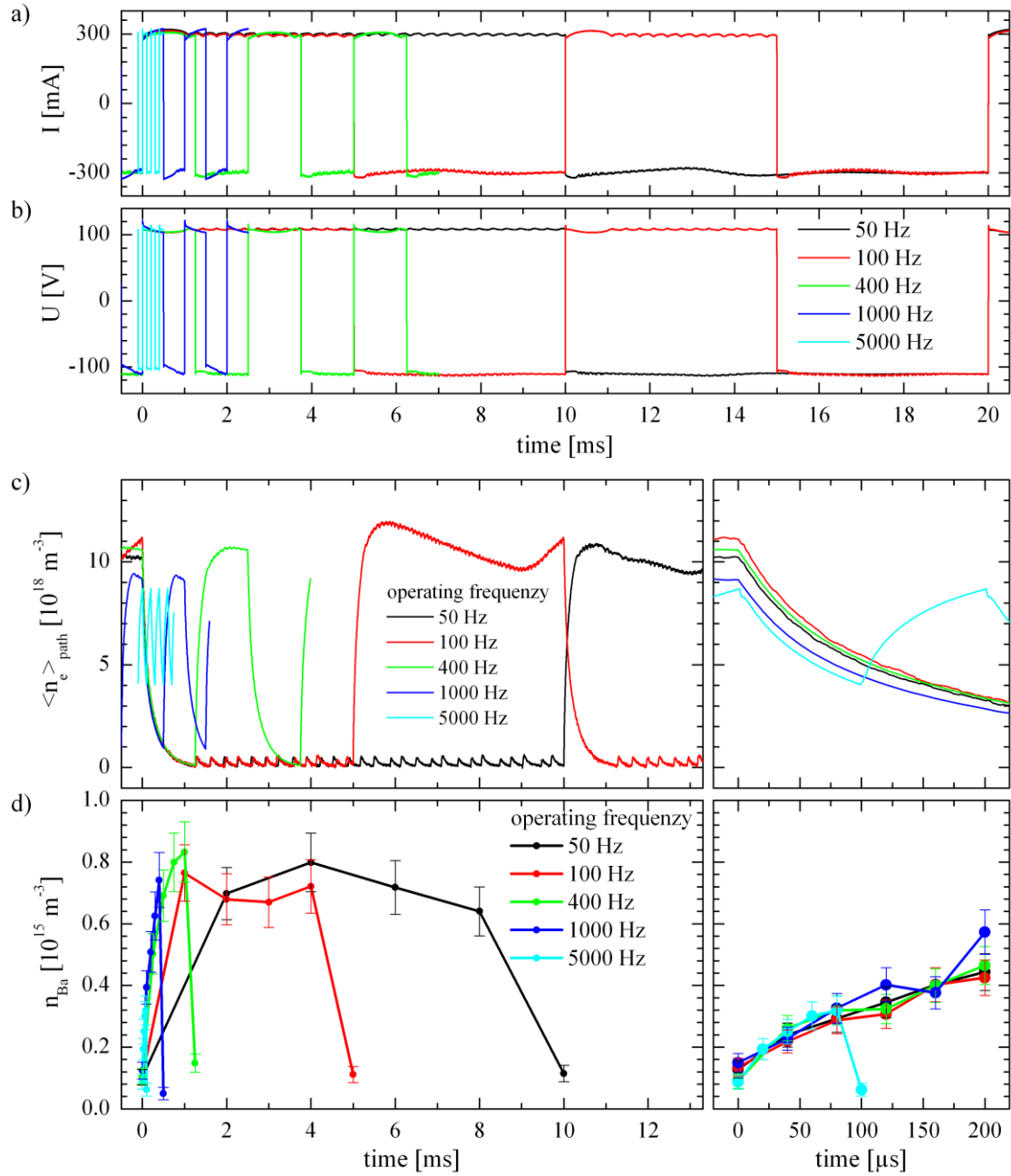


Figure 5-18: Time-dependent behavior by variation of the operational frequency for a lamp current of 300 mA. For clear representation, only a few periods of the measured parameters are given for each frequency.

- a) lamp current
- b) lamp voltage
- c) path-averaged electron density in the electrode region,
- d) barium ground state density measured 0.5 mm in front of electrode surface ($z = 1 \text{ mm}$) during the anode phase

In addition, the temporal barium ground state densities, measured 0.5 mm in front of the electrode surface ($z = 1 \text{ mm}$), are given in Figure 5-18d. As already discussed, with the beginning of the anode phase the densities start to increase. This increase is the same for all

investigated frequencies, so we can conclude that the evaporation of barium is independent of the operational frequencies. With the appearance of the anode oscillations, the measured densities reach a saturated level of about $0.8 \cdot 10^{15} \text{ m}^{-3}$. The generation of additional barium atoms in ground state is in equilibrium with the excitation and ionization of the ground state. However, the densities are not constant as they are modulated by the anode oscillations (see Figure 5-17). The measurement of the densities in Figure 5-18d is not synchronized to the anode oscillations. Thus, for $t > 1.2$ they are randomly affected by anode oscillation modulation in the range of about $\pm 15\%$ of the average density during the anode phase.

For anode phases shorter than 1 ms, the densities would not reach the saturated level. With the beginning of the cathode phase, the high energetic beam electrons lead to an instantaneous decrease of the barium ground state densities. As the densities stay at a very low value (near to the detection limit) during the whole cathode phase, for clear representation only the first value is given in Figure 5-18d. However, during the anode phase the barium ground state densities are affected by anode effects such as anode oscillations. Thus, comparing evaporation processes is very complex. If the current could be kept constant, the slope of the increasing densities at the beginning of the anode phase could be used as indicator. Hence, for detailed comparison the blanking method is applied.

In Figure 5-19 the dependence on the operational frequency is summarized for different lamp currents (200 mA up to 500 mA). In case of the electron densities (Figure 5-19a) the maximum path-averaged densities during the cathode phase and the minimum densities during the anode phase (dashed line) are given. In correspondence with the already discussed characteristics at 300 mA lamp current, for frequencies above 400 Hz the electron densities do not completely decay during the anode phase and anode oscillation does not appear. The behavior seems to be independent of the chosen lamp current. For frequencies above 400 Hz, a decrease of the lamp voltage could also be observed for all currents except the lowest current of 200 mA. Primarily, the decrease is caused by the suppressing of discharge losses due to anode oscillations at these frequencies.

However, by changing the discharge conditions by varying the frequency, the barium evaporation determined by the blanking method is not affected. Thus, it could be concluded that for the investigated frequency range, the barium erosion due to evaporation does not significantly depend on the operational frequency. This fact implies that the temperature of the hot-spot and therefore the electrode energy balance is also not significantly affected.

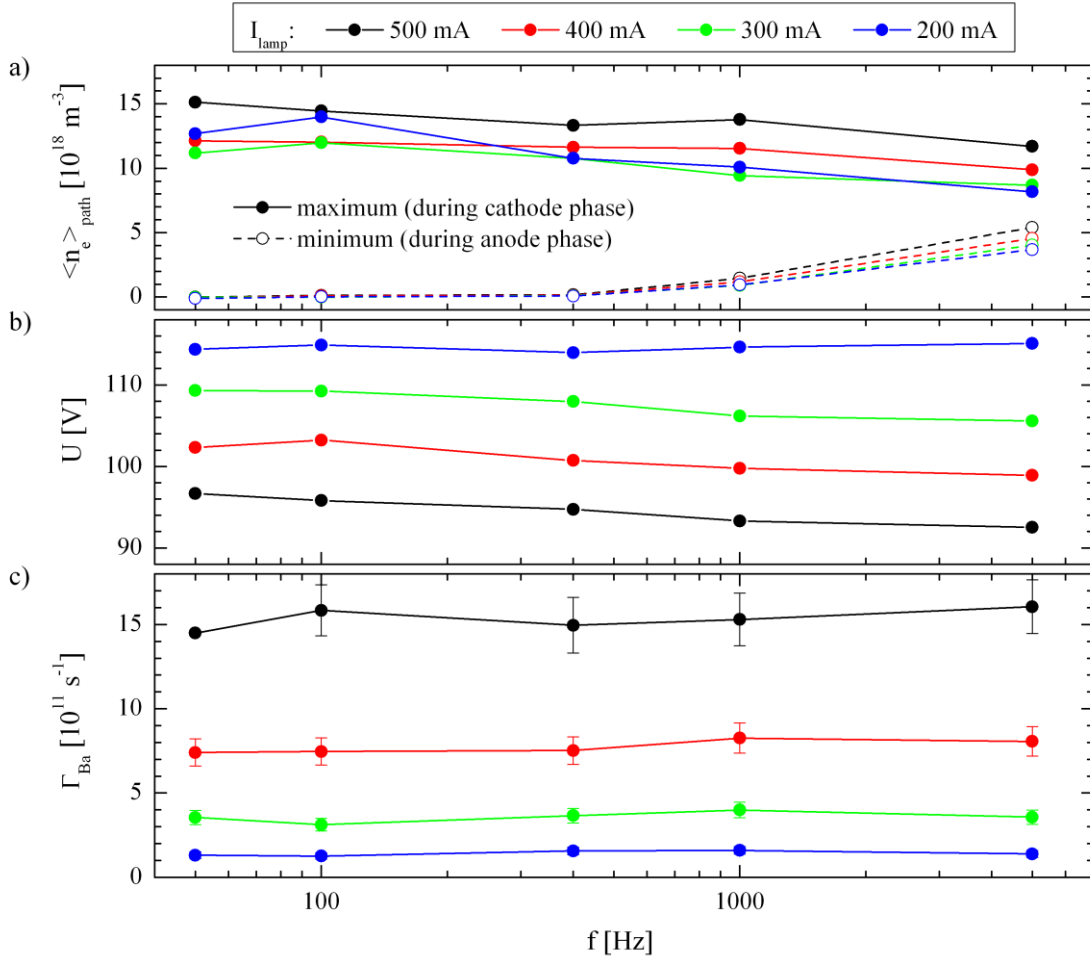


Figure 5-19: Dependence on the operational frequency. The T8-36W lamp is driven with various rectangular-shaped AC currents.

- a) minimum (dashed line) and maximum (solid line) of the path-averaged electron density in the electrode region
- b) lamp voltage (rms)
- c) absolute barium flux from the electrode determined by blanking method

5.5.3 Interpretation of related works at conventional net frequency operation

Former works investigated the electrode erosion during net frequency operation by either determination of optical emission or density measurements (LIF) of the released barium atoms and ions. In Section 5.5.2, it was shown that the barium density is modulated by the different plasma conditions during anode and cathode phases. Thus, in former works the measured quantities always result from the interaction of the released barium with the plasma in the electrode region. In particular, by application of optical emission spectroscopy, this effect has to be considered, as the plasma in the electrode region is responsible for excitation of the investigated levels.

The characteristic behavior of a T5 lamp at conventional net frequency operation is shown in Figure 5-20. For operation, the standard European setup is applied (see Figure 2-4 left), with its current limiting choke in series with the lamp.

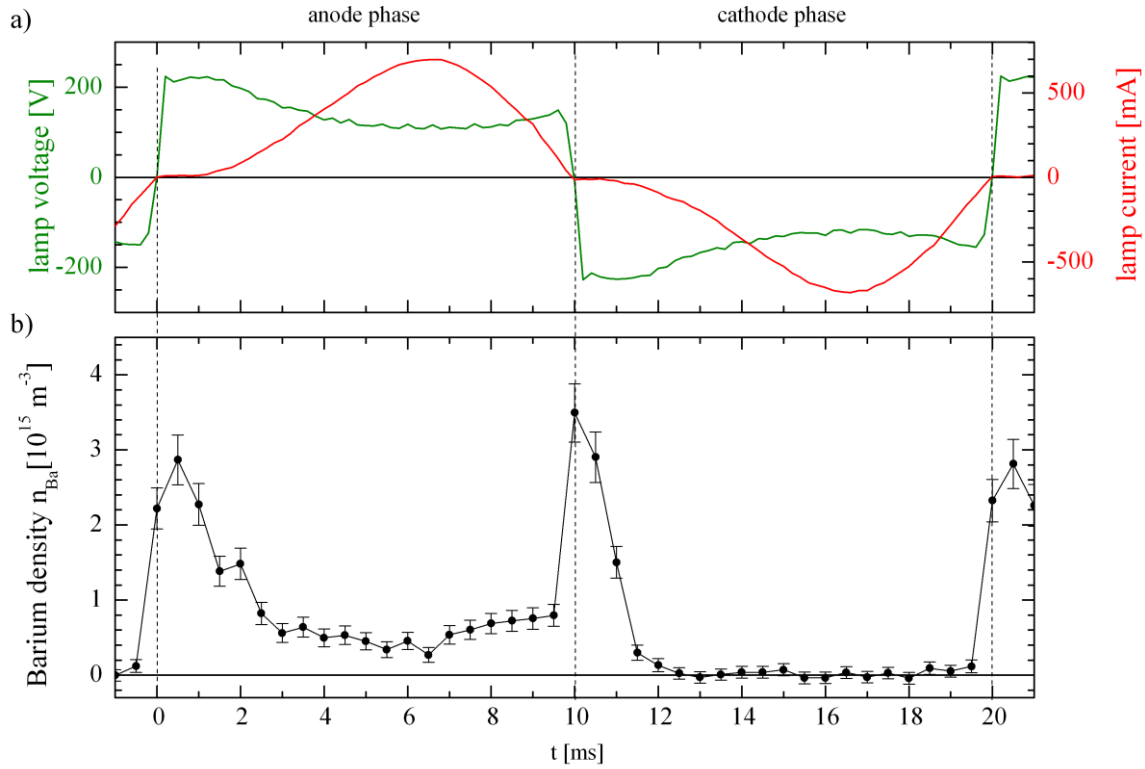


Figure 5-20: Characteristic behavior at conventional net frequency operation. The T5 lamp is operated with a choke in series at net frequency of 50 Hz.

- a) lamp voltage and current
- b) density of the barium ground state density measured by LIF 1 mm in front of the electrode surface

Different barium densities during anode and cathode phase

The barium ground state density during the cathode phase is significantly lower than during the anode phase. Several works [BHATTACHARYA 1989b; MANABE et al. 2007; SAMIR et al. 2007; SAMIR et al. 2005] interpreted this characteristic as different loss during the anode and cathode phases. They supposed the loss of neutral barium from the emitter occurred mainly in the anode half cycle due to additional heating of the electrode in the anode phase and cooling in the cathode phase by thermionic cooling. However, we found no variation of electrode temperature during one full period (at 60 Hz), whereas Samir et al. assumed a rapid increasing temperature of a very thin surface layer.

Our research shows that there is a decreased barium ground state density during the cathode phase due to excitation and ionization by the presence of high energetic beam electrons. During the anode phase, the barium atom ground state density saturates at a higher level

after approximately 1 ms (see Figure 5-18). Furthermore, the density is affected by anode oscillations for lower frequencies (see Figure 5-17).

Barium density peaks at net frequency operation

At the transitions between anode and cathode phase where the current is minimal, a short increase of the barium ground state density could be observed (see Figure 5-20). Bhattacharya [1989b] interpreted these peaks as an increased loss due to ion bombardment enhanced by the high lamp ignition voltage at the beginning of the next cycle. Samir et al. [2007; 2005] supposed an increase barium evaporation was due to a rapid temperature change of a very thin surface layer of the hot spot.

For a better understanding, additional investigations of these peaks have been made as part of this work. It has been found that these density peaks depend on the duration and current of the transitions between the anode and cathode phases. During the transition, there is a certain time with minimal to no current. Thus, there is no need for a cathode fall voltage or anode fall voltage to sustain this minimal lamp current. Accordingly, in the electrode region there are no high energetic electrons present and no barium atoms are ionized or excited. Thus, the barium transport processes correspond to the processes by application of the developed blanking method. In contrast to blanking, the duration and the current during transition is not controlled and depends on the external circuit as well as on the individual lamp and electrode characteristics. As this varies for different lamps, the peaks observable by these uncontrolled blanking are not applicable for determination of erosion.

To illustrate this behavior, an experiment with controlled transitions between anode and cathode phase has been realized. The lamp is driven by a rectangular AC-current (setup according Figure 5-15), whereas the lamp voltage is shortened for various time during transitions (see Figure 5-21a). Thus, during transitions the observed barium ground state densities increase, whereas the height of the peaks depends on the duration of the blanking (see Figure 5-21d, e).

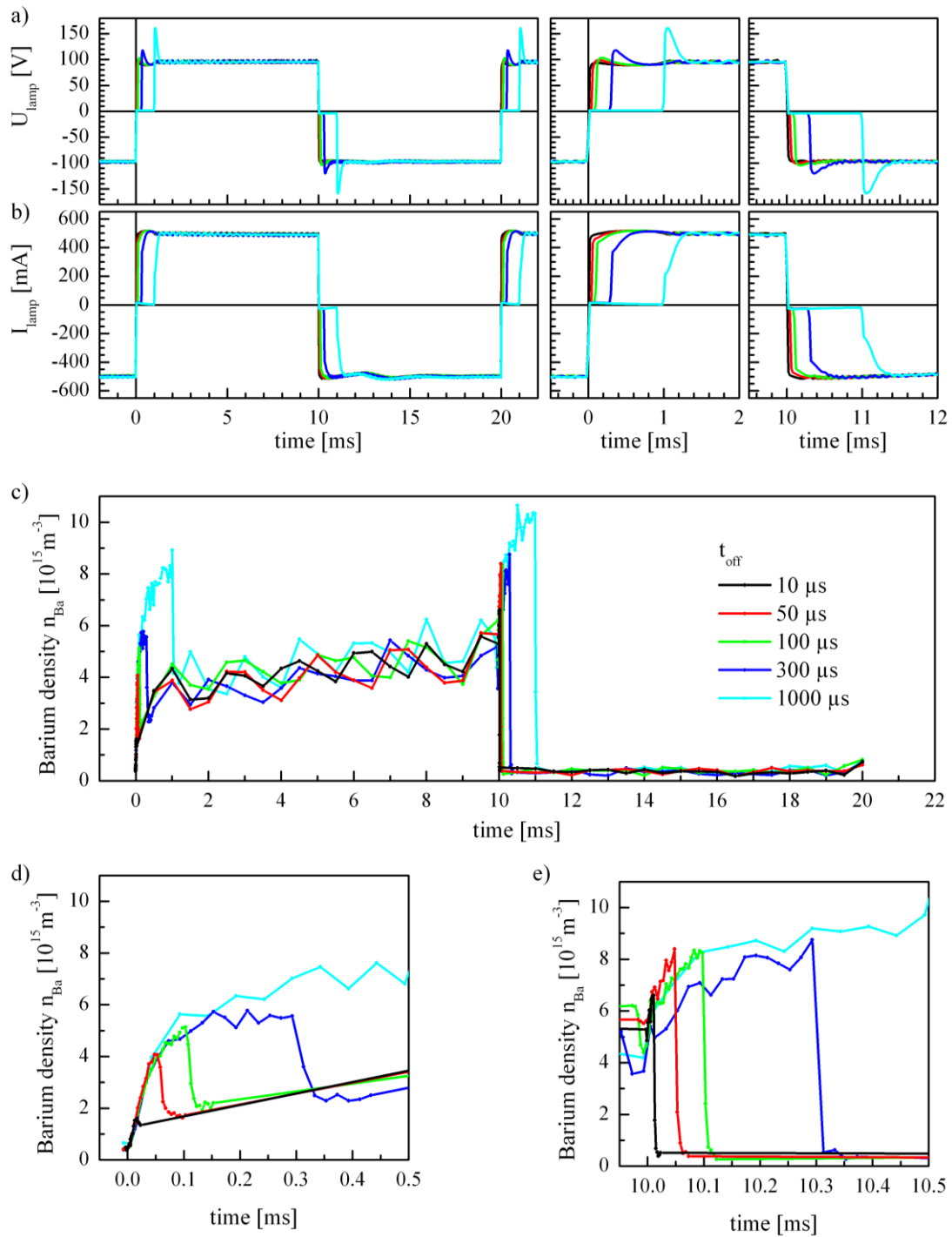


Figure 5-21: Modified net frequency operation with defined off-times during transitions between anode and cathode phases. The T5 lamp is driven with rectangular current, whereas it is shortened by an IGBT-shortening circuit for various times during transitions between anode and cathode phases. For cleanliness, error bars are not plotted.

- a) lamp voltage and current
- b) lamp current and current
- c) barium atom ground state density measured 1 mm in front of the electrode surface
- d) barium atom ground state at transition from cathode to anode phase
- e) barium atom ground state at transition from anode to cathode phase

6 Conclusion

The durability of fluorescent lamps is determined by the durability of their electrodes. Therefore, electrode erosion during continuous operation with modern electronic ballast systems (at several tens of kHz) is of special interest for lamp manufacturers and this has been investigated in the present work. For the first time, absolute particle fluxes from the electrode to the plasma instead of particle densities (determined in former works) have been determined during operation.

In this work, electrode erosion was characterized by the determination of the released barium as the essential emitter component responsible for electrode operation. The released barium was measured during operation by using LIF, whereas additional diagnostics were applied to characterize electrode operation. The investigations were performed on commercial T8 fluorescent lamps with cleared out ends.

The following are the achieved results:

- In a preliminary investigation, the applicability of using LIF for the determination of absolute barium densities in fluorescent lamps was proven by measurements on a model lamp. It was shown that collisional depopulation (quenching) occurs only for Xenon at pressures above 5 mbar and thus this could be neglected for the investigations on fluorescent lamps. For the absolute calibration of LIF, a RAYLEIGH scattering calibration was applied. For further improvements to the determination of absolute density, a saturation correction was performed. Therefore, a model that considers both temporal and spatial saturation effects was developed and applied for the purpose of this research. It was found that spatial saturation broadening requires particular consideration.
- The chemical emitter processes that generate barium were investigated in an electrode heating experiment. For electrode temperatures below approximately 1100 K, the barium densities in the electrode region correspond to the equilibrium pressure produced by the reduction of the barium oxide by tungsten and the further reduction of the produced tungstate. For higher electrode temperatures, the barium densities in the electrode region are lower than these equilibrium pressures, indicating a reduced reaction rate. These reduced reaction rates could be caused either by the reduced diffusion of the reactant (primarily barium oxide) or by reduced barium transport through the porous emitter. However, these results prove that barium evaporation, even under simplified conditions, depends on the temperature and the emitter structure that varies during electrode lifetime.

- For the first time, absolute barium ground state densities during operation at 25 kHz could be measured because of the high sensitivity of the applied system. The densities show pronounced modulation because of the plasma in the electrode region. During the cathode phase, beam electrons (electrons emitted by the electrode) gain energies of approximately 10 to 15 eV because of the cathode fall (estimated by using the band method). These high energetic electrons generate secondary electrons by ionization of gas and mercury atoms (detected by an increase of the electron density by using microwave interferometry). Furthermore, these electrons excite and ionize the barium atoms observed by using LIF. Thus, the absolute determination of electrode erosion by the release of barium is not possible without detailed knowledge of the local plasma parameter. Even a relative comparison of different operation conditions is not possible, as the plasma, and therefore the amount of barium atoms in the ground state, varies.
- To determine the absolute emitter evaporation (evaporation of barium) during operation, the blanking method was developed and established. During operation, the lamp was switched off for approximately 5 ms in order to measure the undisturbed barium evaporation. These new methods allow to compare various operation and discharge conditions without knowledge on the detailed plasma parameter.
- For the interpretation of the blanking method, a new barium diffusion model for the electrode was developed and validated in the course of this research. In the initial step, the one-dimensional models of the electrode region computed the temperature distribution used to calculate the spatial- and temperature-dependent diffusion coefficient. In the second step, the temporal barium diffusion was calculated. By adapting the computed results on measured barium densities by application of the blanking method, the absolute barium evaporation (barium flux) and barium diffusion coefficient as a control parameter were determined. The model was validated by taking measurements at different lamp pressures. The detected evaporation rates were of the order of $\Gamma_{\text{Ba}} \approx 10^{12} \text{ s}^{-1}$ and corresponded to typical electrode lifetimes of approximately 10,000 hours.
- Dimmed operation was studied at an operation frequency of 25 kHz. It was found that lamp currents above the nominal lamp current lead to a drastic increase in emitter evaporation. An increase in the lamp current from 300 mA to 500 mA leads to an increase in emitter evaporation by a factor of five, whereas the maximum hot-spot temperature increases from 1120 K to 1170 K. By decreasing lamp currents to 100 mA, very low evaporation could be observed (reduced by a factor of seven) at a hot-spot temperature of 950 K. For these low lamp currents, an anomalous temporal barium density characteristic was found. Whereas under normal conditions the barium ground state density during the anode phase was significantly higher than during the cathode phase (owing to the ionization and excitation of the barium ground state by high energetic electrons present during the cathode phase), for low

lamp currents higher densities during the cathode phase could be found. These higher densities could only be caused by the additional production of barium during the cathode phase by sputtering. Thus, the proportion of barium ground state density during the cathode and anode phases could be used as an indicator of sputtering. However, the total amount of sputtering could not be determined; indeed, it may be higher than the evaporation level at these lower lamp currents.

- The investigations of dimmed operation with additional heat currents showed that they are useful for lower lamp currents. As such, for a lamp current of 100 mA, an additional heat current of 400 mA could reduce sputtering, indicating the proportion of barium ground state density during the cathode and anode phases. For a lamp current of 200 mA, an additional heat current of 300 mA seems to be optimal. The found optimal heat currents correspond to minimal electron density. Until now, this characteristic has not been fully understood, but it could be used as an indicator of the optimal operation conditions for electrodes.
- The investigations of frequency dependence show no significant dependence on emitter evaporation. For frequencies below 400 Hz, anode oscillation occurs, which reduces lamp efficacy but does not affect electrode evaporation. However, with the applied microwave interferometry, it was possible to measure the fluctuations in electron densities caused by anode oscillation. It could also be shown that anode oscillation affects the barium ground state densities. As such, for the interpretation of OES or other absolute detection techniques, these effects have to be considered for lower operation frequencies.
- The comparison of the obtained results with those of former works leads to an improved understanding of older measures. Thus, the lower barium ground state densities during the cathode phase observed [Bhattacharya 1989b; Samir et al. 2007; Samir et al. 2005] could now be explained by the increased ionization and excitation of the barium ground state because of the high energetic beam electrons present during the cathode phase. In addition, it was found that the peaks observed by Bhattacharya [1989b] during transitions between the anode and cathode phases are caused by uncontrolled reduced currents during the transitions. Thus, the peaks are unsuitable for comparing the barium erosion of different lamps, as they depend on the external circuit as well as the individual electrode and lamp characteristics.

Outlook

This work focused on commercial T8 fluorescent lamps with stick coil electrodes. Thus, in future works the developed flux determination by using the blanking method should be applied to smaller T5 and T4 lamps, typically used as compact lamps. As these lamps have a triple coil electrode, the main challenge will be the adaption of LIF measurements on the

three-dimensional structure of the electrode. In addition, the electrode structure has to be considered by the model applied in order to interpret the blanking method.

Another improvement would be the substitution of the complex and expensive LIF by other more robust methods such as laser absorption. Parallel to this work, approaches to determining fluxes by using such methods in combination with a complex plasma model of the electrode region have been investigated [LIEBERER et al. 2011; SIGENEGER et al. 2010].

The investigations of dimmed operation indicate sputtering at lower lamp currents. As sputtering causes early lamp failures, investigations that are more detailed should be performed. Hadrath and Garner [2010] showed that it is possible to differentiate between evaporated and sputtered barium atoms by using OES coupled with a FABRY-PEROT interferometer. Hence, future work should concentrate on determining the absolute amount of sputtered electrode components.

Appendix

A Experimental methods in detail

In this work, the absolute densities of the eroded barium are measured by laser-induced fluorescence (LIF). To understand electrode operation in detail, additional methods are applied. The electrode temperature as a key parameter for evaporation is measured by an optimized pyrometric measurement system. The electrode operation itself is characterized by its local work function determining the electrode sheath plasma. Thus, the cathode fall voltage is determined by the capacitively coupled band method and the electron densities in the electrode region are measured by microwave interferometry.

In the following, the applied methods are described and the setups characterized. Afterwards, the investigated lamps and precondition parameters are described.

A.1 Pyrometric electrode temperature determination

Max Planck was the first to describe the radiation emitted by a black body in thermal equilibrium. He invented the formula commonly known as PLANCK's law. As a modification, the temperature-dependent spectral radiance $L(\lambda, T)$ of a real surface can be formulated in the wavelength form as:

$$L(\lambda, T) = \varepsilon(\lambda, T) \cdot \frac{2hc^2}{\lambda^5} \cdot \frac{1}{e^{\frac{hc}{\lambda k_B T}} - 1}. \quad (\text{A-1})$$

Here, ε is the emissivity, k_B is the BOLTZMANN constant, T is the absolute temperature, h is the PLANCK constant, c is the speed of light and λ is the wavelength. The emissivity is a correction term for non-ideal black bodies and is the relation between the radiation of a real surface and the radiation of an ideal black body. By the determination of the spectral radiance of the electrode, its temperature can be calculated according to this formula. At typical hot-spot temperatures of 1200 K, the maximum radiance is in the infrared range at about $\lambda_{\max} \approx 2 \mu\text{m}$.

For the measurements in this work, a pyrometric system [GARNER 1998], provided by OSRAM AG, is used. The basic configuration is given in figure A-1. The electrode is imaged via an infrared transparent lens on an InGaAs detector array. The detector array has 128 pixels and a spectral response range between 900 nm and 1700 nm. To avoid the unwanted emission of the plasma in the electrode region, an optical bandpass filter (maximum transmission at 1500 nm) is placed in front of the detector array. The detector is connected

to a PC and the data are analyzed with the commercially available Software LabView. The electrode is aligned in such a way that its length (approximately 1 cm) fills nearly the whole length of the detector array (typically 90 pixels) and the measured intensity corresponds to the center axis of the electrode.

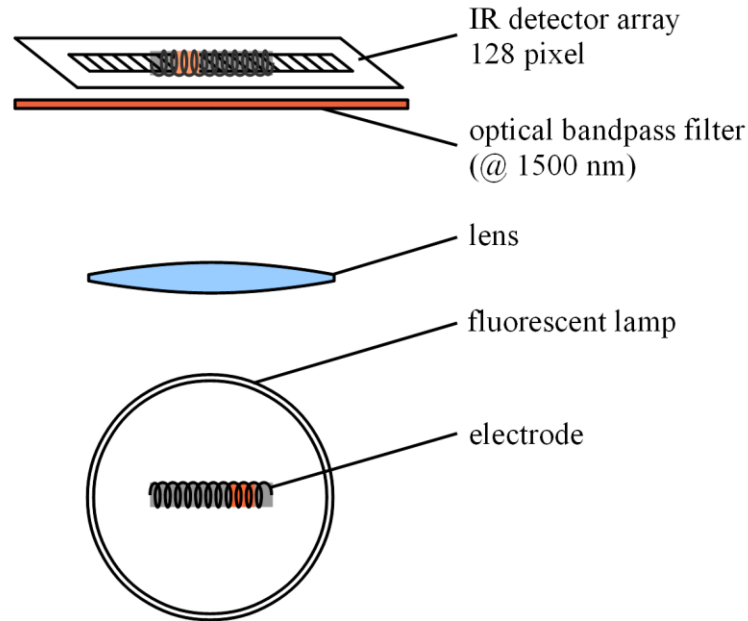


Figure A-1: Basic configuration of the spatially resolved electrode temperature measuring system.

For the calculation of the temperature according to equation (A-1), the emissivity of the electrode has to be known. This is defined by the surface material and structure. Unfortunately, the emissivity varies with the surface temperature and the emission wavelength. Commonly, a constant emissivity is assumed for a small temperature and wavelength range. Corresponding values can be found tabulated for certain materials and temperatures. In contrast to other materials, alkali earth oxides show a huge variation of the emissivity according to the temperature. In addition, the emissivity is affected by the impurity of the surface and disposal of barium and tungsten. Therefore, the emissivity of the emitter material varies over a wide temperature range and during lifetime. To overcome this problem, a special calibration method is applied.

For every measurement, the electrode is first aligned. In the second step, the electrode is heated up by several DC currents (also called heat currents) while the lamp is off and the intensities of the detector array are stored (see Figure A-2a). By the simultaneous measurement of the electrode resistance, for each pixel the stored intensities can be assigned to a certain temperature (see Section 3.1 for details), as illustrated in Figure A-2b. For the measurement of the hot-spot temperature during operation, for each pixel the actual intensity is used to interpolate the temperature from the intensity – temperature calibration for the corresponding pixel (see Figure A-2b). Finally, an intensity profile (red curve in

Figure A-2a) can be transferred into the desired temperature profile (Figure A-2c). Temperatures below 950 K are clipped, as the detected intensities are too low.

This method allows determining electrode temperatures for nearly every type of electrode and electrode material. Accuracy is determined by the calibration, whereas the determination of the averaged electrode temperature from the ratio of the hot-to-cold resistance produces an essential error of about 1.7% (see Appendix B.4). To ensure the correctness of the calibration during several measurements, a second calibration is carried out afterwards and compared with the first one.

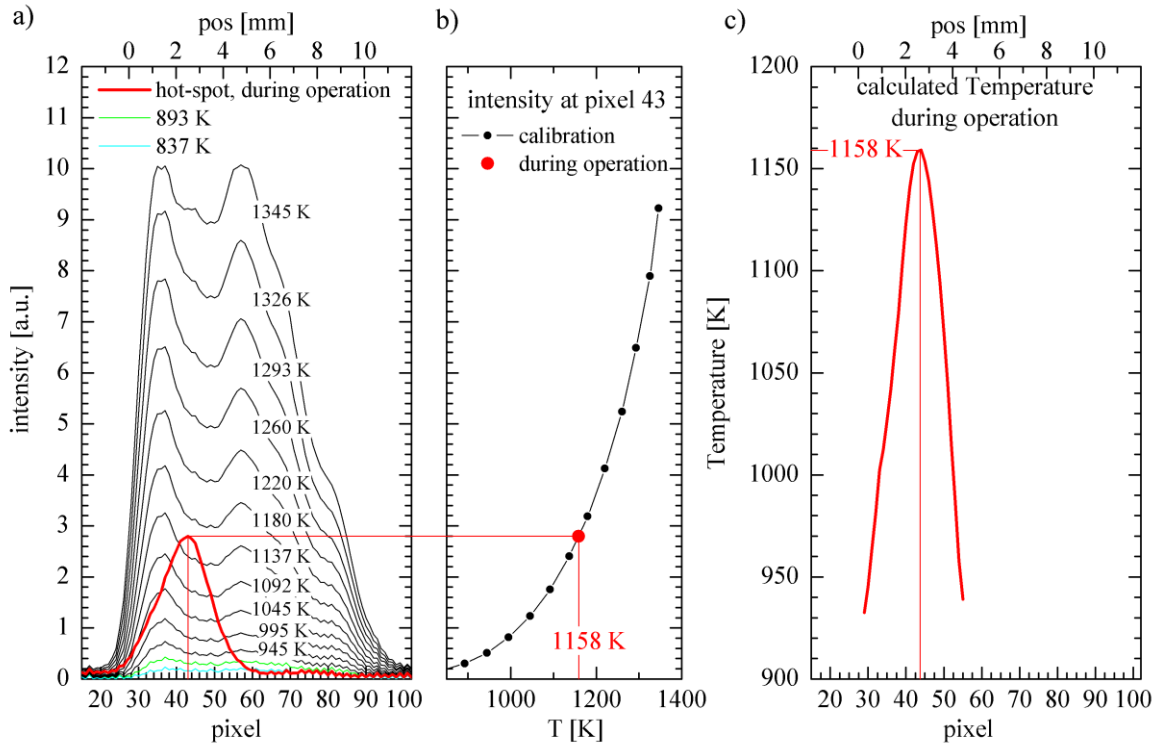


Figure A-2: Calibration of the online electrode temperature measuring system and calculation of the hot-spot temperature during operation.

- measured intensity of the heated electrode for certain temperatures (calibration measurements) and intensity of the hot-spot during operation (red curve),
- intensity – temperature dependence used for the calibration of pixel 43 and interpolation of the local hot-spot temperature (red),
- calculated temperature profile of the hot-spot

A.2 Cathode fall estimation with the band method

The cathode fall voltage is a significant parameter characterizing electrode operation. It depends on the formed hot-spot, the resulting effective work function, the discharge current, the buffer gas and the amount of mercury vapor, and it directly determines the plasma in the electrode region. Electrons emitted at the hot-spot gain energy in the order of the cathode fall voltage while passing the cathode sheath. Therefore, the electron energy distribution strongly depends on the cathode fall voltage, which again affects electrode

operation (discussed in detail in Section 2.1). For optimal electrode operation, the cathode fall voltage has to be below a certain level (typically 15 V) to prevent electrode erosion due to sputtering (discussed in detail in Section 2.3.1). Thus, measuring the cathode fall voltage provides essential information about electrode operation and plasma conditions.

For the determination of the cathode fall voltage, several methods exist. The most direct methods are the measurement of the plasma potential with an internal probe [CHEN and LABORATORY 1964] and the use of a movable electrode [ARNDT 1976; MISONO 1992]. Both methods allow the determination of the potential along the discharge and, with some limitations, the determination of the cathode fall voltage. However, they cannot be applied to commercial lamps, as specially constructed lamps have to be used. Of non-invasive methods, actinometry can be used to determine if the cathode fall voltage exceeds certain thresholds by observing certain emission lines of Argon [HADRATH et al. 2007]. Information that is more detailed can be obtained with the popular band diagnostic method [HAMMER 1989, 1995; NACHTRIEB et al. 2005]. As this method can be applied on commercial lamps, it has been established as a standard approach in the lamp industry. Therefore, it is used in this work.

Band diagnostic method

The band diagnostic method, illustrated in Figure A-3, is based on placing metallic foil around the outer surface of the glass tube in the electrode region and measuring the potential between the electrode and foil. The metallic foil is capacitively coupled to the inner wall sheath. Therefore, the method can only be applied to AC-driven lamps. The simplicity of the setup is accompanied by several limitations on the interpretation of the measured potential.

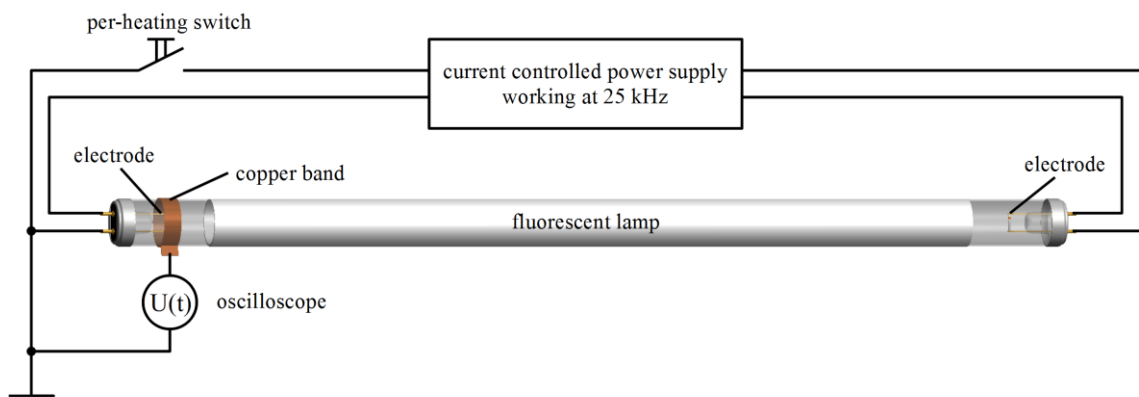


Figure A-3: Experimental setup for the band diagnostic method. Metallic foil is placed around the outer surface of the glass tube and the potential difference between the electrode and foil is measured.

Although the measured signal is related to the cathode fall voltage, it involves effects of the discharge (e.g. the plasma-wall sheath at the inner surface) and effects of the external measurement circuit. The capacitive AC coupling suppresses the constant component of the potential difference and leads to an unknown shift of the signal. An attempt to overcome

this issue has been made by Nachtrieb et al. [2005] with additional diagnostics and modeling. The potential difference between the inner wall sheath and the boundary between bulk plasma and electrode sheath produces an additional unknown shift. Nevertheless, Rich Garner [2008c] significantly improved the understanding of the method and interpretation of the signals.

Lumped parameter model

For a detailed understanding of this method, an equivalent circuit representation of the band diagnostic method (Figure A-4, right), deduced from the cross section of the electrode region (Figure A-4, left), can be used. The measured quantity is the voltage $U(t)$ between the electrode post and the capacitively coupled band. The voltage is the sum of the electrode sheath potential $V_{CF}(t)$ (the quantity of interest), the potential difference between the electrode sheath–plasma boundary and inner wall sheath–plasma boundary $\Delta V_p(t)$, the potential drop through the inner wall sheath $\Delta V_w(t)$ and the potential across the glass (of the formed capacitor C_b between the inner wall sheath and outer band probe). To measure the voltage, a probe connected to the band probe and the oscilloscope is used. This external circuit has to be considered and it is specified by the resistance R_0 and the capacitance C_0 . As the oscilloscope is connected to the ground, the measure post is also connected to the ground.

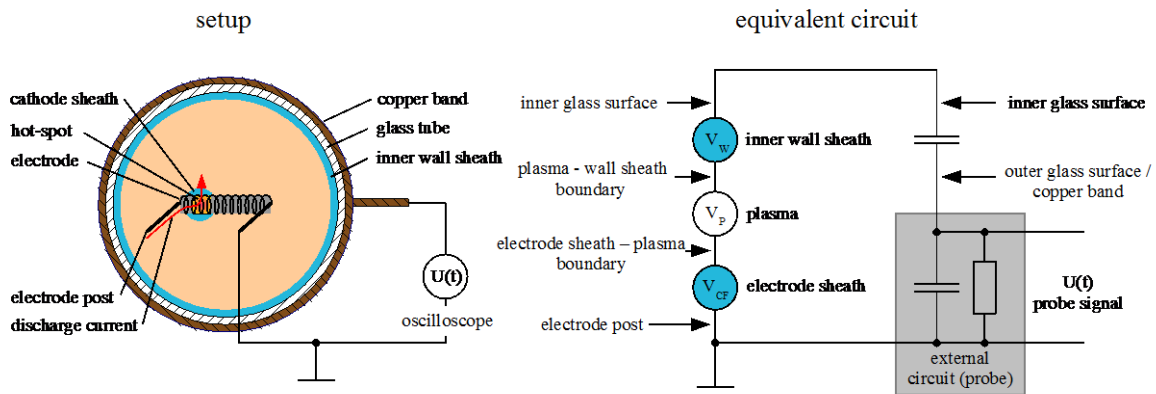


Figure A-4: Cross section of the lamp in the electrode region by the application of the band method (left) and lumped parameter model of the method (right).

For an absolute determination of the cathode fall voltage, additional knowledge of the different sheaths, either through modeling or through other diagnostics, is necessary. The plasma potential drop $\Delta V_p(t)$ is related to the ambipolar potential drop from the hot-spot (the cathode fall sheath) to the inner wall sheath. This depends on the radial plasma density profile and the electron temperature in the bulk plasma, which both vary over time for AC operation. The inner wall sheath is determined by the ion, electron and sheath displacement currents, and this can be expressed in terms of a nonlinear sheath capacitance [GARNER 2008c].

However, the lack of knowledge of the temporal-dependent plasma potential drop $\Delta V_p(t)$ and inner wall sheath potential drop $\Delta V_w(t)$ does not allow an accurate quantitative determination of the cathode fall voltage, the method suitable for a good estimation. The time response is essentially determined by the cathode fall sheath and, in contrast to an internal probe, it is generally much faster [GARNER 2008c].

Setup

For the measurements in this work, the setup shown in Figure A-3 is used. The applied band probe consists of a 0.15 mm thick and 24 mm wide copper foil. The band is wound completely around the outer surface of the glass tube and is centered on the electrode. It is then connected to the voltage probe LeCroy PP005 (voltage divider 10:1, 10M Ω , 11pF), which is connected to the digital storage oscilloscope LeCroy WavePro 7300. To prevent the coupling of stray radiation, the ground of the voltage probe is directly connected to the grounded electrode post. The other electrode post is connected to the current-controlled power supply. During starting the lamp, the electrode is preheated by a DC current. To do so, the preheating switch (see Figure A-3) is closed. After lamp ignition, the switch is opened to ensure that the discharge current goes through the non-grounded post and that there is no current through the grounded/measure post. Therefore, the voltage drop of the ohmic resistance of the electrode can be eliminated in the measure circuit. For measurement, the signal is averaged 100 times, whereas the oscilloscope is triggered by the zero crossing of the discharge current. In Figure A-5b, a typical signal is given (green curve).

Calibration of the external circuit

The formed capacitor C_b between the inner wall sheath and outer band probe and the voltage probe (with the resistance R_0 and the capacitance C_0) represents a capacitive voltage divider with high pass characteristics. The measured voltage $U(f)$ is related to the inner wall potential $V_w(f)$ according to the transfer function:

$$U(f) = \frac{i2\pi \cdot C_b R_0}{1 + i2\pi \cdot (C_b + C_0) R_0} \cdot V_w(f) \quad (A-2)$$

The characteristic cutoff frequency is given by:

$$f_c = \frac{1}{2\pi \cdot (C_b + C_0) R_0} \quad (A-3)$$

With a band capacitance of about $C_b \approx 100\text{pF}$ (see the Appendix B.8 for details) and the values of the applied voltage probe $C_0 = 11\text{pF}$, $R_0 = 10\text{M}\Omega$, the cutoff frequency is about $f_c \approx 150\text{Hz}$. For frequencies smaller than the cutoff frequency, the measured voltage is significantly damped and 90° phase shifted. In contrast, for frequencies significantly higher than the cutoff frequency (such as the standard operation frequency of 25 kHz), the

measured voltage is proportional to the inner wall potential $V_w(t)$, whereas the proportional factor $1/c_{\text{band}}$ is determined by the capacitive voltage divider:

$$\begin{aligned} \text{for } f \gg f_c \approx 150\text{Hz} \\ U(t) &\approx \frac{C_b}{C_b + C_0} \cdot V_w(t) . \\ &\approx \frac{1}{c_{\text{band}}} \cdot V_w(t) \end{aligned} \quad (\text{A-4})$$

With an estimated value of the band capacitance of about $C_b \approx 100\text{pF}$ and the voltage probe capacitance of $C_0 = 1\text{pF}$, the proportional constant should be about $c_{\text{band}} \approx 1.11$. For the determination of the wall potential, the measured voltage has to be multiplied by this factor. This correction factor directly depends on the band capacitance, which relies on the wall thickness, the width of the band probe and the inner wall sheath.

To increase the accuracy of the band method, especially for comparing different lamps and discharge conditions, a calibration method for the determination of the correction factor c_{band} is applied. The basic idea is to move the band to the second electrode (to the other end of the fluorescent lamp) and compare the measured band voltage $U_{\text{band-end}}$ with the measured lamp voltage. The band coupling capacitance C_b at the second electrode is identical to that at the first electrode (electrode of interest). In the first approximation, the inner wall potential at the second electrode $V_{w-\text{end}}$ can be assumed to be about the lamp voltage $V_{w-\text{end}} \approx U_{\text{lamp}}$. For this assumption, the correction factor c_{band} can be calculated according to:

$$c_{\text{band}} \approx \frac{U_{\text{lamp}}}{U_{\text{band-end}}} . \quad (\text{A-5})$$

In Figure A-5c, the measured band voltage at the second electrode $U_{\text{band-end}}$ (black curve) is given. The corresponding time-dependent correction factor c_{band} is given in Figure A-5d (black curve). During the cathode phase, the relation $U_{\text{lamp}}/U_{\text{band-end}}$ is almost constant, whereas in the anode phase, the ratio is in general greater and decreases over time. The fluctuations in the near zero crossing of the lamp voltage are caused by dividing through a measured, noisy voltage near to zero.

The error of the ratio during the anode phase results from not considering the potential difference between the second electrode and the wall potential at the second electrode V_{w-end} . During the cathode phase of the second electrode (the anode phase of the electrode under investigation), this unconsidered potential difference is about 11 V. A good approximation to consider the potential difference is to assume the potential difference between the second electrode and the wall potential at the second electrode (during its cathode/anode phase), which is identical to the potential difference between the first electrode and the wall potential at the first electrode (during its cathode/anode phase):

$$\begin{aligned} U_{lamp} - V_{w-end} &\approx -V_w(t - 20\mu s) \\ U_{lamp} - c_{band} U_{band-end} &\approx -c_{band} U_{band}(t - 20\mu s) \end{aligned} \quad (A-6)$$

This leads to the correction term in (A-5):

$$c_{band} \approx \frac{U_{lamp}}{U_{band-end} - U_{band}(t - 20\mu s)} \quad (A-7)$$

The corrected voltage $U_{band-end} - U_{band}(t - 20\mu s)$ is given in Figure A-5c (red curve). The corresponding time-dependent correction factor c_{band} is given in Figure A-5d (red curve). In contrast to the simpler method, the corrected approach leads to a constant relation of about $c_{band} \approx 1.145$ during almost the whole cathode and anode phase. To obtain the wall potential of the electrode under investigation $V_w(t)$, the band probe voltage U_{band} is multiplied by this experimentally determined correction factor c_{band} . In addition, an offset correction is carried out by assuming the wall potential $V_w(t)$ to be zero after the anode phase (at $t = 0$). This offset correction is a simplification as there should be a small potential drop at the hot-spot of about ± 1 V at the end of the anode phase. The exact value can be negative or positive depending on the discharge conditions [GARNER 2008c; WAYMOUTH 1971]. Therefore, the chosen approach should be adequate for the comparison of identical discharge conditions.

The described calibration method is applied for every lamp, whereas the obtained correction factors c_{band} vary in a small range of about 5%.

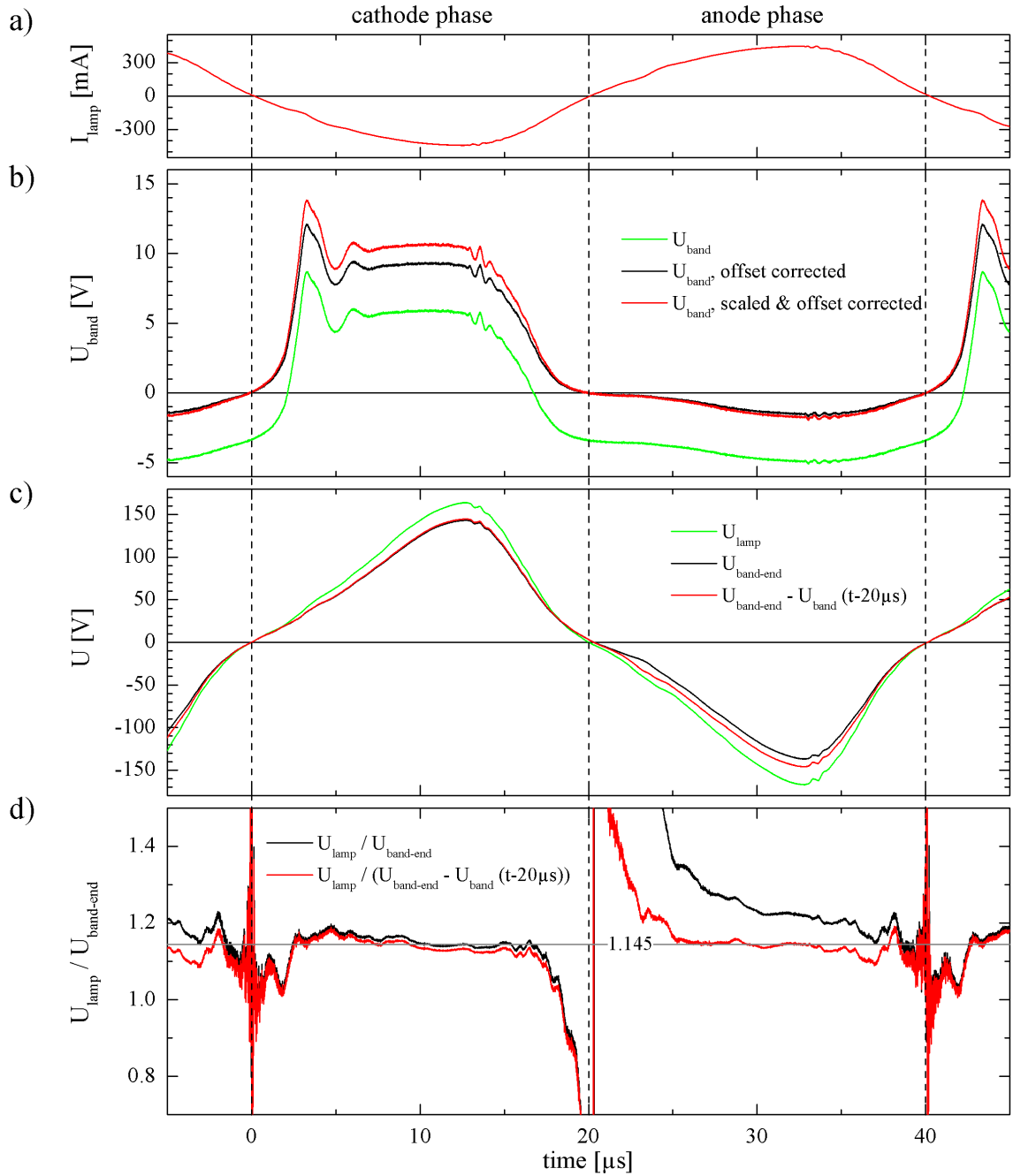


Figure A-5: Typical signals and calibration of the external circuit by the application of the band method.

- Current of a lamp driven by the standard rms current of 320 mA at 25 kHz,
- Signal of the band probe (U_{band} - green), offset corrected signal of (U_{band} , offset corrected - black) and scaled and offset corrected signal (U_{band} , scaled&offset corrected - red);
- Lamp voltage (U_{lamp} - green), band probe signal by moving the band to the end of the lamp to the second electrode ($U_{\text{band-end}}$ - black) and the band probe signal at the second electrode minus the one half period shifted band probe signal of the first electrode $U_{\text{band-end}} - U_{\text{band}}(t-20\mu\text{s})$ (red);
- Calibration factor of the external circuit determined by dividing the lamp voltage through $U_{\text{band-end}}$ (black) and through $U_{\text{band-end}} - U_{\text{band}}(t-20\mu\text{s})$ (red).

A.3 Electron density measurement by microwave interferometry

The propagation of high frequency electromagnetic waves through a plasma depends on its electron density. With microwave interferometry, this effect is used for the determination of the electron density. In general, the propagation through the plasma or the reflection of an electromagnetic wave is measured. In contrast to other methods, such as internal probe¹⁷ measurements or the STARK broadening of the H_{β} - line¹⁸, microwave interferometry is a non-invasive method and therefore best suited for application on commercial fluorescent lamps.

A.3.1 Propagation of high frequency electromagnetic waves through non-magnetized plasma

The propagation of a plane electromagnetic wave is described by:

$$\vec{E}(\vec{r}, t) = \vec{E}_0 \cdot e^{i(\vec{k}\vec{r} - \omega t)}, \quad (\text{A-8})$$

where \vec{E} is the spatial- and temporal-dependent electric field vector, \vec{E}_0 the initial electric field vector, \vec{k} the wave vector and ω the angular frequency. All propagation characteristics are described by the frequency-dependent wave vector $\vec{k}(\omega)$. The interrelation of the wave vector and its frequency are described by the dispersion relation. The dispersion relation of a plasma can be obtained by solving the MAXWELL equations and the equations of the motion of electrons in a plasma simultaneously [BITTENCOURT 2004; GOLDSTON and RUTHERFORD 1995; RAZER 1991]. Therefore, here only the result and interpretation, necessary for microwave interferometry in non-magnetized plasmas, are presented.

For homogeneous, non-magnetized plasma, the dispersion relation of a plane electromagnetic wave is given by:

$$(\omega^2 - c^2 k^2) \cdot \left(1 + i \frac{\nu_m}{\omega}\right) - \omega_p^2 = 0, \quad (\text{A-9})$$

¹⁷ For internal probe measurements, a thin electric conductor is inserted into the active plasma and its voltage current characteristic is measured [CHEN and LABORATORY 1964; MOTT-SMITH and LANGMUIR 1926]. This method requires a modification of the discharge by inserting an internal probe, which also disturbs the discharge itself.

¹⁸ To determine electron densities by broadening of H_{β} - lines [TORRES et al. 2007], the STARK broadening due to the electric fields, depending on the electron density, is measured. This method can be applied for electron densities above 10^{20} m^{-3} and it needs the presence of hydrogen. For application in fluorescent lamps, hydrogen has to be added to the gas filling.

rearranged to the wave number k :

$$k = \frac{\omega}{c} \sqrt{1 - \frac{\omega_p^2}{\omega^2} \cdot \frac{1}{1 + i \frac{\nu_m}{\omega}}} . \quad (\text{A-10})$$

Here, c is the speed of light, ν_m is the effective electron collision frequency for momentum transfer and ω_p is the plasma frequency introduced by [TONKS and LANGMUIR 1929]:

$$\omega_p = \sqrt{\frac{e^2 n_e}{\epsilon_0 m_e}} , \quad (\text{A-11})$$

with e as the electron charge, n_e the electron density, ϵ_0 the vacuum permittivity and m_e the electron mass.

In contrast to standard problems, the wave number k of plasmas (A-10) is a complex number. Whereas the real part of the wave number k describes the spatial-dependent phase of the wave (see equation (A-8)), the imaginary part describes the spatial-dependent damping of the amplitude. The square root term in equation (A-10) can also be interpreted as the relative permittivity ϵ_r , which is also a complex number. Important to remark is the fact that the relative permittivity of plasma for high frequency electromagnetic waves is less than one¹⁹. Instead of the smaller wavelength in normal dielectrics, the wavelength of high frequency electromagnetic waves in plasmas increases.

The collision frequency for momentum transfer ν_m in equation (A-10) describes the average collision rate of an electron with an atom or ion leading to momentum transfer. Thus, these collisions cause energy transfer from electrons to atoms or ions. Finally, this leads to the absorption of the electromagnetic wave and is responsible for the imaginary component of the wave vector (A-10). The magnitude of this effect depends on the ratio of collision frequency ν_m and on the angular frequency of the electromagnetic field ω . For the plasma conditions investigated in this work, the collision frequency is much smaller than the angular frequency $\nu_m \ll \omega$ (see Appendix B.5), which simplifies equation (A-10) significantly to:

$$k = \frac{\omega}{c} \sqrt{1 - \frac{\omega_p^2}{\omega^2}} . \quad (\text{A-12})$$

¹⁹ In contrast to atoms and molecules where all electrons are bounded, in plasmas there exist free electrons. By movement without collisions, these electrons oscillate in phase with the electric field. They shift away from the center of the equilibrium against the direction of the electric force. As they have a negative charge, they induce a negative polarizability, leading to $\epsilon_r < 1$. In contrast, bounded electrons feel an elastic restoring force in response to displacement. Therefore, the displacement is directed against the electric field, forcing a positive polarizability $\epsilon_r > 1$ [RAIZER 1991].

The resulting dispersion relation is illustrated in Figure A-6. The term below the square root can be positive or negative. If the angular frequency is greater than the plasma frequency $\omega > \omega_p$, the term is positive and the wave vector is real, indicating the normal propagation of an electromagnetic wave. For an angular frequency lower than the plasma frequency $\omega < \omega_p$, the term is negative and the wave vector is imaginary. An electromagnetic wave will be reflected, whereas the amplitude is exponentially damped in the plasma and there will be no propagation.

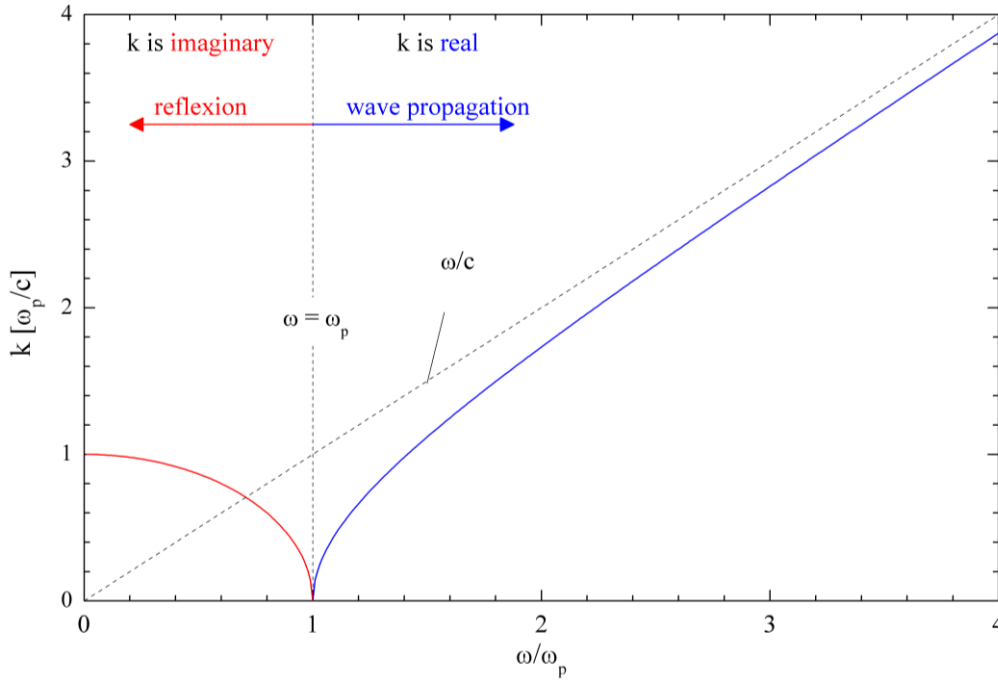


Figure A-6: Dispersion relation of high frequency electromagnetic waves in non-magnetized plasmas.

For the critical point $\omega = \omega_p$, the critical electron density (also called the cutoff density) can be derived as:

$$n_c = \frac{\epsilon_0 m_e}{e^2} \cdot \omega^2. \quad (\text{A-13})$$

This also allows reformulating equation (A-12) into a more practicable form:

$$k = \frac{\omega}{c} \sqrt{1 - \frac{n_e^2}{n_c^2}}. \quad (\text{A-14})$$

For the experimental determination of the electron densities, two different approaches are possible. Reflectometry can be applied for electron densities higher than the critical density $n_e > n_c$. The electromagnetic wave is reflected at the position where $n_e = n_c$ and the reflection is detected. By the variation of the frequency of the electromagnetic wave

(equivalent to a variation of the critical density n_c), spatial electron density profiles can be obtained. This method is typically used for high temperature and fusion plasmas.

For electron densities smaller than the critical density $n_e < n_c$, interferometry can be applied. An electromagnetic wave propagates through a plasma, whereas its phase is shifted. From the phase difference $\Delta\varphi$ of the shifted phase and the phase because of the absence of the plasma, the electron density can be calculated. This method is applicable for low temperature plasmas and thus it is used in this work. The phase difference $\Delta\varphi$ produced by a plasma can be derived from equations (A-8) and (A-14):

$$\begin{aligned}\Delta\varphi &= \varphi(n_e(r) = 0) - \varphi(n_e(r)) \\ &= \frac{\omega}{c} \cdot \left(r - \int 1 - \frac{1}{2} \cdot \frac{n_e(r)}{n_c} dr \right).\end{aligned}\tag{A-15}$$

Hence, the phase difference depends on the integral electron density. Thus, only an integral density can be determined. By assuming an electron density much smaller than the critical density $n_e \ll n_c$, the integral in equation (A-15) can be simplified by the TAYLOR expansion. This allows the determination of a path-averaged electron density:

$$\langle n_e \rangle_{\text{path}} = 2 \cdot \frac{c}{\omega} \cdot n_c \cdot \frac{\Delta\varphi}{l},\tag{A-16}$$

where l is the length of the path or the length of the plasma²⁰.

The limitation of measuring only a path-averaged electron density can be overcome if the electron density profile along the path is known or can be assumed (see Appendix B.6).

Choosing a proper frequency

To design the microwave interferometry setup, the operation frequency should be chosen with special diligence. In general, the chosen frequency has to be higher than the angular plasma frequency or in other words, the electron density has to be lower than the corresponding critical density $n_e < n_c$. According to equation (A-12), the change in the wave vector, and therefore the measured phase difference $\Delta\varphi$, is higher for lower frequencies (see Figure 6-7). Thus, lower frequencies increase the detection limit (the minimal detectable electron density) and decrease the noise. However, if the chosen frequency is too low, the TAYLOR expansion of equation (A-15) is not possible and the linear dependency of the measured phase difference and electron density will be lost. As a good estimation, the chosen frequency should be one order of magnitude higher than the plasma frequency.

²⁰ The described path-averaged electron density $\langle n_e \rangle_{\text{path}}$ corresponds to an observed plasma with a constant density n_e along its length l .

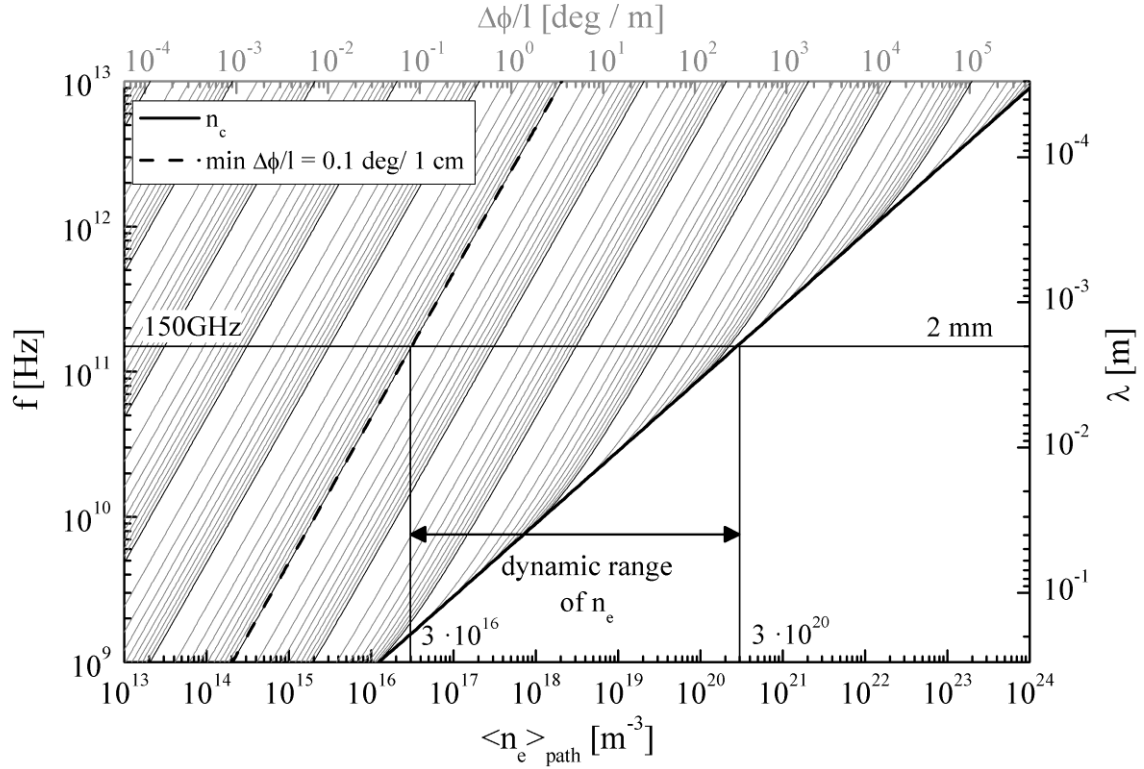


Figure 6-7: Dependence of the measured phase difference $\Delta\phi$ on the path-averaged electron density $\langle n_e \rangle_{\text{path}}$ and the operation frequency of the applied interferometer. The black line indicates the critical density n_c . For a fixed frequency, only electron densities to the left-hand side of the line can be detected. Similarly, to measure a certain density, a frequency above the line has to be used. By following the gray lines from the crossing point of a certain electron density and a frequency (wavelength) to the top of the diagram, the corresponding phase difference $\Delta\phi$, normalized to a one meter path (plasma) length, can be obtained. The dashed line indicates the typical detection limit of 0.1 degrees for a path length of 1 cm (typical for this work).

Although higher frequencies decrease the change in the wave vector (by limiting the maximum detectable electron density), they are often sought as the wavelength decreases. Typically, a focused beam is used for microwave interferometry. With a good forming of the beam, a focus diameter of twice the wavelength can be achieved. Thus, the spatial resolution is limited to twice the wavelength. In particular, for small plasmas or plasmas with strong electron density gradients, high frequencies with small wavelengths are sought. A more practical aspect is the availability of oscillators, amplifiers and detectors. Whereas a frequency range up to 50 GHz ($\lambda = 6\text{mm}$) is commercially available²¹ with quite good phase detection limits, the range between 200 GHz and 2 THz is only available with considerable difficulties. For frequencies above 2 THz, laser-based THz systems are available, which offer only moderate phase detection limits.

²¹ A Vector Network Analyzer such as the ZVA50 from Rohde & Schwarz operates up to 50 GHz and reaches a phase accuracy of about 0.03 degrees [ANDRASCH et al. 2014; EHLBECK et al. 2011].

In conclusion, the microwave frequency has to be chosen according to the investigated plasma by taking into account the minima and maxima electron density, the needed spatial resolution and the availability of the microwave components.

A.3.2 Interferometer setup

For the application of microwave interferometry on fluorescent lamps, the used wavelength should be significantly lower than the lamp diameter of about 25.4 mm. By taking into account the other important aspects²², a customized 150 GHz system from Millitech Inc. is chosen.

The interferometer (see Figure A-8) operates as a heterodyne detector, whereas the operation frequency $f_{\text{HF}} = 150$ GHz is mixed with a second frequency $f_{\text{LO}} = 150.1$ GHz of a local oscillator to an intermediate frequency $f_{\text{ZF}} = 100$ MHz used for phase detection. This commonly used technique transfers high frequency signals to lower frequencies where they can be analyzed more accurately.

The operation frequency f_{HF} is generated by frequency doubling the signal of a 75 GHz stabilized gun diode. By using a directional coupler, the signal is split into two, one for a reference path and the other for a test path. All components are connected by rectangular waveguides operating in the single mode regime at the H_{10} mode, ensuring stable phase transition. A corrugated horn antenna is used to form a divergent Gaussian beam. The beam is focused via a dielectric lens made of REXOLITE. A second pair of lenses and a corrugated horn antenna are used for detection. The fluorescent lamp is placed between both lenses (as illustrated in Figure A-8) in the focused beam with a minimum beam waist of about 4 mm, which is approx. twice the wavelength.

The detected signal is mixed by using a second harmonic mixer with the signal of a second stabilized gun diode operating at $f_{\text{LO}} = 75.05$ GHz to the intermediate frequency $f_{\text{ZF}} = 100$ MHz:

$$f_{\text{ZF}} = |f_{\text{HF}} \pm 2f_{\text{LO}}|. \quad (\text{A-17})$$

The intermediate test signal is connected by a coaxial cable. In principle, the sum frequency of 300.1 GHz is also present in the test signal. As this high frequency component is damped by the coaxial cable, a low pass filter is not required (indeed, the cable is used as a low pass filter). For the phase analysis, a second signal at the intermediate frequency is needed. This reference signal is generated by mixing the signal of the reference path with that of the second gun diode.

²² The most important aspects are the availability of microwave components at the desired frequency and an adequate temporal resolution (about 1 μs) by simultaneously achieving a sufficient phase detection limit (better than 0.5 deg).

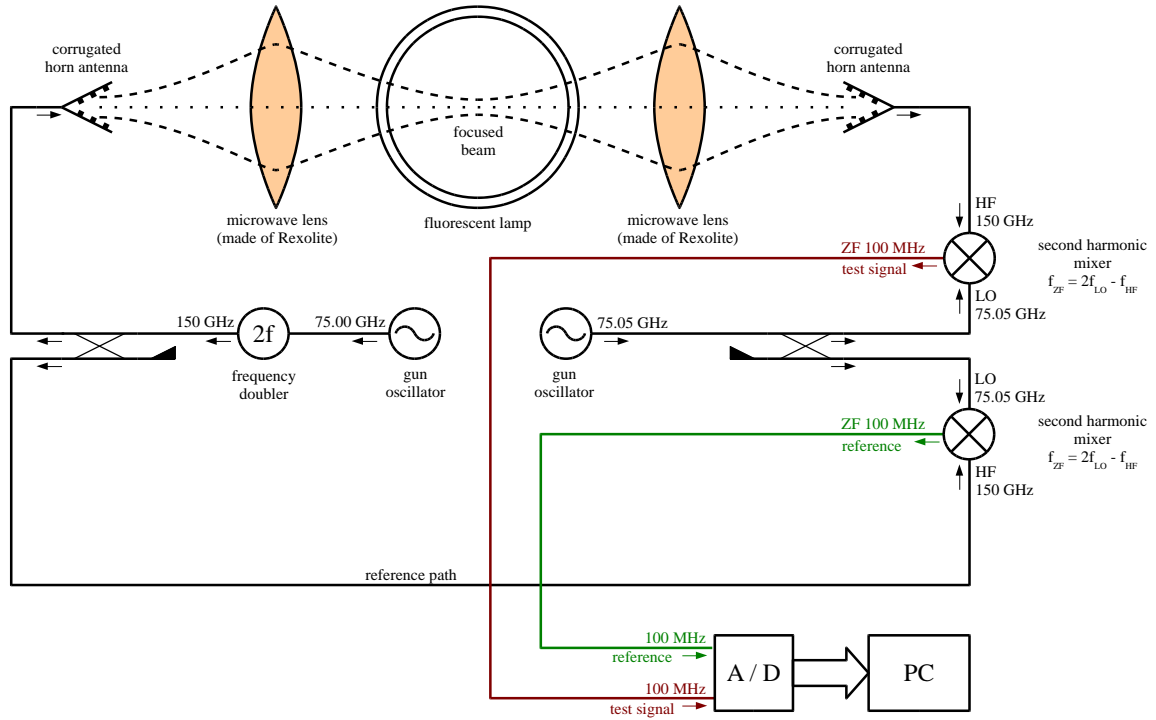


Figure A-8: Configuration of the 150 GHz heterodyne microwave interferometer: The 150 GHz signal is generated by frequency doubling a 75 GHz stabilized gun diode. For the phase analyses, a second stabilized gun diode generates 75.05 GHz used to mix down the signals to 100 MHz with a second harmonic mixer.

A special advanced analysis system is used to determine the phase. A comparable heterodyne interferometer, such as that used by Greenberg and Hebner [1993], simply multiplies the test and reference signals. The resulting down-mixed signal contains the cosine of the phase differences as well as the amplitudes of both signals. By determining the phase from such a signal, additional phase noise occurs due to the amplitude noise of both signals and the nonlinear dependence on the phase.

For the applied setup, additional noise is avoided by analyzing both signals separately. Therefore, the reference and test signals are sampled with a PC-AD card (Gage Cobra GS21G8) at 500 MS/s. For the analyses, self-written software based on LabView is used. The sampled signals are divided into separate blocks, and each block is analyzed separately as illustrated in Figure A-9. The typical block size is 128 samples (that corresponds to a duration of the block of 512 ns). In the first step, the actual intermediate frequency f_{ZF} is determined by using the BUNEMAN frequency estimation [DWIVEDI and SINGH 2010; NATIONAL 2012]. In a second step, a sine function with the amplitude A and a cosine function with the amplitude B of the determined frequency is fitted on both signals via the linear fitting algorithm provided by LabView:

$$U(t) = A \cdot \sin(2\pi f_{ZF} \cdot t) + B \cdot \cos(2\pi f_{ZF} \cdot t). \quad (\text{A-18})$$

The phase of the signals can be obtained by:

$$\varphi_{\text{signal}} = \text{atan2}(B, A). \quad (\text{A-19})$$

This algorithm is chosen, as it is significantly faster than fitting in a single step frequency, amplitude and phase.

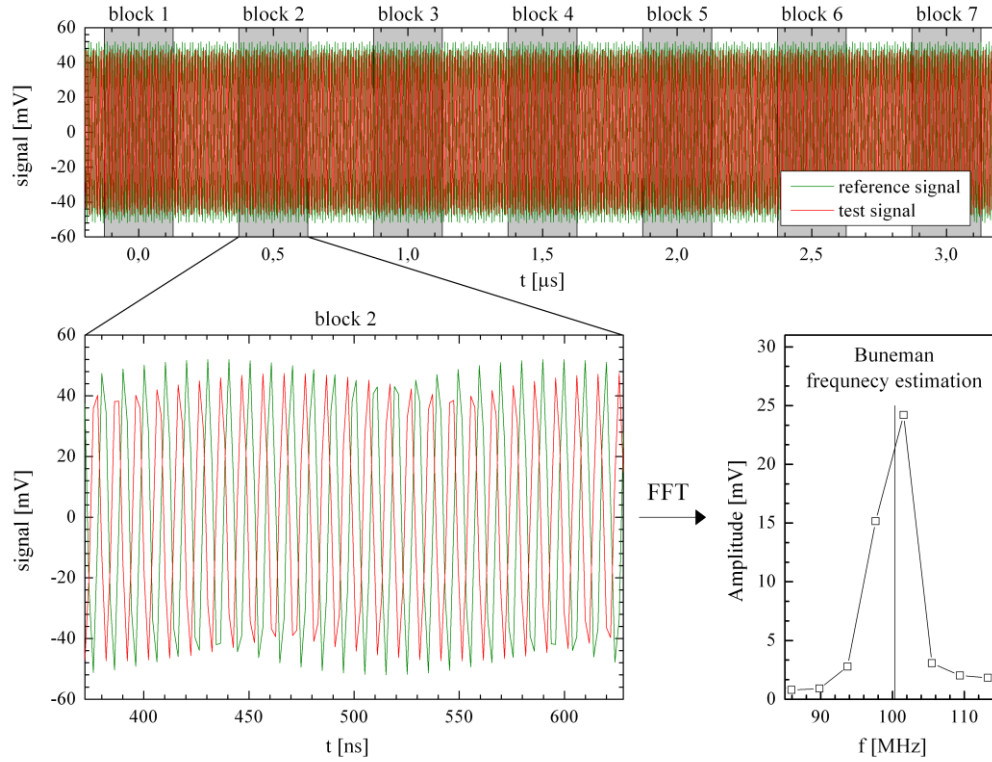


Figure A-9: Numerical method for the phase detection of the sampled reference and test signals. The signals are divided into separate blocks. For each block, the actual frequency is determined by using the BUNEMAN frequency estimation.

Finally, the phase is obtained by simply subtracting the phase of the reference signal from that of the test signal:

$$\varphi = \varphi_{\text{test signal}} - \varphi_{\text{reference signal}}. \quad (\text{A-20})$$

The algorithm is applied to each block, with one phase point generated for each, representing the averaged phase of the block. Hence, the temporal resolution is limited by the block size, while a block should contain several periods of the intermediate signals. In this way, an effective temporal resolution of 50 ns (block size of 25) can be obtained. In general, a higher temporal resolution (smaller block size) yields a higher phase noise. With a typical block size of 128 points (256 ns), a single shot phase resolution of 0.2 degrees can be realized.

Characterizing the interferometer

As microwave interferometry is an integral measurement along the observed path, it is essential to know the exact path. This could be done by characterizing the microwave beam. For application on fluorescent lamps, spatial resolutions significantly smaller than the lamp diameter are required. Therefore, a focused microwave beam is used with a focus diameter of the order of the wavelength. Such a beam can be described according to the GAUSSIAN beam optic, which is a solution of the paraxial HELMHOLTZ equation. Here, only a basic description will be given, as the GAUSSIAN beam optic is discussed in several textbooks in detail [HODGSON and WEBER 1992]. The electric field of such a beam propagating in the z direction is given by:

$$E(x, y, z) = E_0 \cdot \frac{w_0}{w(z)} \cdot \exp\left(-\frac{x^2 + y^2}{w^2(z)} - ikz - ik \frac{x^2 + y^2}{2R(z)} + i\zeta(z)\right). \quad (\text{A-21})$$

Here, w_0 is the waist radius in the focus, $w(z)$ is the waist radius locale, k is the wave number, $R(z)$ is the radius of the curvature of the beam's wave fronts and $\zeta(z)$ is the GOUY phase shift.

To generate such a beam, corrugated feed horn antennas in combination with dielectric lenses are used. However, corrugated feed horn antennas do not produce an ideal beam [QIN and GUO 1998; SINGAL et al. 2005; WYLDE and MARTIN 1993]. In addition, misalignment leads to the deformation of the ideal beam. Such a deformed beam can be decomposed into a superposition of the HERMITE-GAUSSIAN beam modes [MARTIN and BOWEN 1993; WYLDE 1984]:

$$E_{deformed}(x, y, z) = \sum_{m,n} A_{nm} \cdot H_m\left(\sqrt{2} \frac{x}{w_0}\right) \cdot H_n\left(\sqrt{2} \frac{y}{w_0}\right) \cdot E(x, y, z), \quad (\text{A-22})$$

where A_{nm} is the relative amplitude of designated the TEM_{mn} mode, with m and n being the horizontal and vertical orders (x and y direction), and H_k is the k^{th} physicist's HERMITE polynomial.

For the characterization of the focused beam of the interferometer, a metallic aperture with a diameter of 2 mm is driven through the beam and the amplitude of the reference and test signals is measured. The ratio of these signals directly depends on the transmission and allows determining the beam profile. After the adjustment of the antennas, the determined beam profile in focus is given in Figure A-10. The beam waist and the occurring modes are obtained from the profiles in the x and y directions by fitting equation (A-22) with MatLab to the measured profiles. In both directions, the fundamental H_0 mode dominates. The amplitudes of the next highest modes are about one order of magnitude smaller. The beam in the y direction (FWHM of 4.1 mm) is a bit wider than that in the x direction (FWHM of 3.82 mm). This could be caused by the misalignment of the antennas or the corrugated feed horn antennas themselves, which might not produce a perfectly cylindrical symmetric

beam²³. However, even though the produced beam is a bit deformed, the fundamental mode dominates. The achieved beam diameter of about 4 mm (FWHM) is significantly smaller than the lamp diameter and thus it is suitable for measurements of fluorescent lamps.

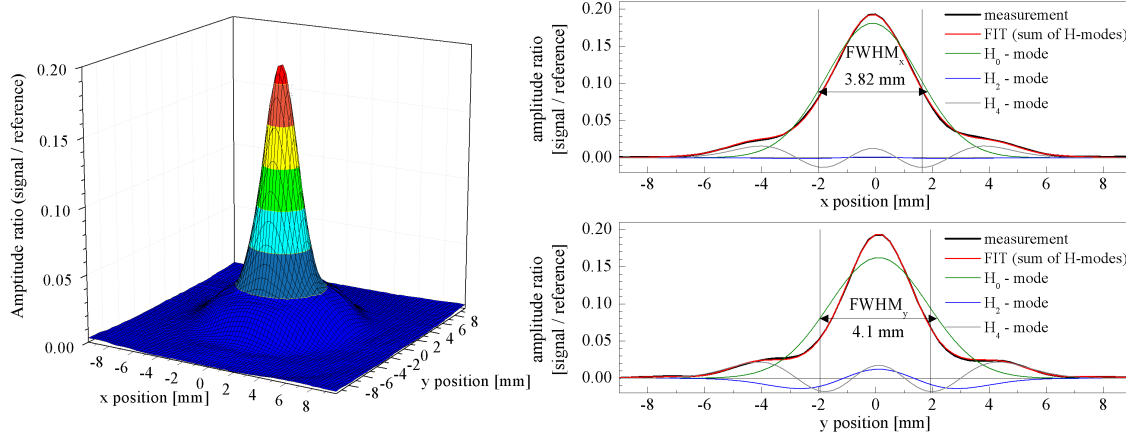


Figure A-10: Focused GAUSSIAN beam. (left) Two-dimensional measurement of the interferometer beam in focus. (right) Beam profile in the x direction at y=0 and profile in the y direction at x=0. The determined profiles are the superposition of the HERMITE-GAUSSIAN beam modes, while the fundamental H₀ mode dominates.

For the applied interferometer, accuracy is limited due to the statistical error of the measurement. As the electron density deviates from the phase shift due to the plasma, the effective phase error has to be quantified. The phase error depends on the phase noise of the analog interferometer setup and the additional phase noise produced by phase detection. The analog phase noise is caused by the time domain instabilities (jitter) of the interferometer. The analyzed signals are the mixed signals of two not ideal oscillators (stabilized gun diodes). Both have phase noise, which may be different. In addition, phase noise is added due to mechanical instabilities and vibrations, which lead to tiny fluctuations of the path lengths. Typically, mechanical vibrations are at the millisecond timescale. Therefore, at the microsecond timescale, the phase noise of the oscillators dominates. In Figure A-11 (left), the spectrum of the test signal is given. The bandwidth is about 1 MHz, which corresponds to a Q factor of about $7.5 \cdot 10^4$ for an oscillator operating at 75 GHz. The phase noise depends on the sideband power. At an offset frequency of 5 MHz from the carrier, the relative sideband power is about -96 dB at a normalized detection bandwidth of 1 Hz²⁴.

²³ The corrugated feed horn antennas have to transform a rectangular wave-guide mode into a GAUSSIAN beam. Of course, the transformation of real antennas is not ideal, meaning that a perfectly cylindrical symmetric beam cannot be achieved.

²⁴ The power of the carrier is -36 dBm and the sideband power at an offset frequency of 5 MHz from the carrier is about -96 dBm at a 5 kHz resolution bandwidth and -132 dBm at a resolution bandwidth of 1 Hz. Accordingly, the sideband power at an offset frequency of 5 MHz is 96 dB smaller than the power of the carrier.

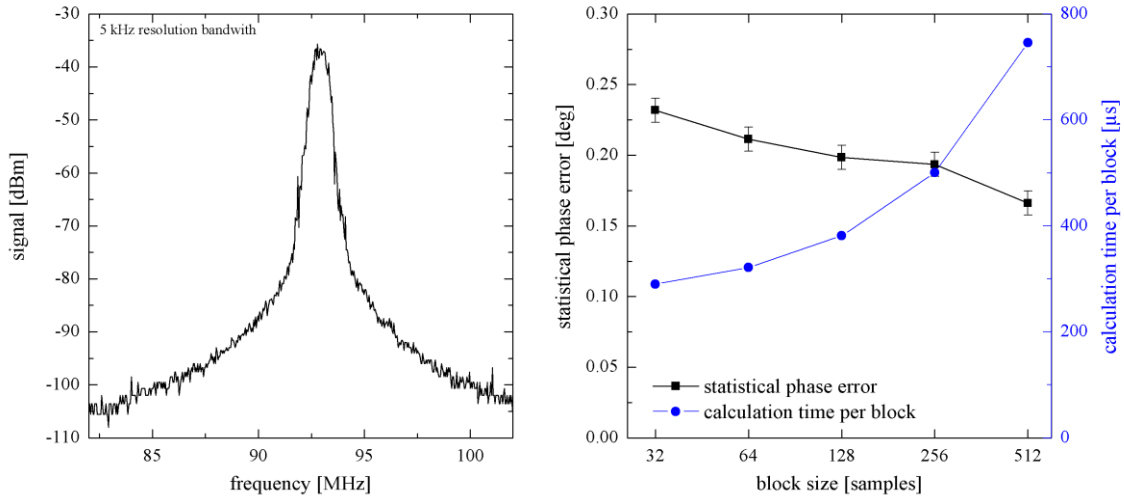


Figure A-11: Noise of an interferometry measurement. (left) Spectrum of the down-mixed test signal measured by a spectrum analyzer with a spectral resolution of 5 kHz. (right) Statistical error of phase measurement and calculation time per single point for different block sizes (length of the analyzed sequences).

The effective statistical phase error including the analog error and phase detection error is given in Figure A-11 (right) for different block sizes (length in the samples of the analyzed sequences). The phase detection error is caused by sampling the analog signals, leading to quantization noise and the error of the phase detection algorithm. By increasing the block size, the phase error decreases but the computation time increases. At the used sampling frequency of 500 MHz, a block size of 32 samples corresponds to a block length of 64 ns, which is the maximum temporal resolution. However, the statistical phase noise is in the region of about 0.2 degrees and it decreases only a small amount by significantly increasing the block size. As a good compromise between calculation times, temporal resolution and noise, a standard block size of 64 samples (temporal resolution of 128 ns) is chosen. In general, in this work periodic electron densities are measured. Thus, the phase error can be reduced by averaging several measurements, while the statistical phase noise will be reduced by the square root of the number of averages.

Application of microwave interferometry on fluorescent lamps

The typical inner diameter of the investigated T8 fluorescent lamps is about 25.4 mm. By assuming a constant electron density across the whole diameter, the path-averaged electron density $\langle n_e \rangle_{\text{path}}$ can be calculated from the measured phase shift $\Delta\varphi$ according to equation (A-16):

$$\langle n_e \rangle_{\text{path}} = 1.22 \cdot 10^{17} \text{ m}^{-3} \cdot \frac{\Delta\varphi}{\text{deg}} \pm 0.24 \cdot 10^{17} \text{ m}^{-3}. \quad (\text{A-23})$$

The given error is the statistical error for a single measurement (0.2 degrees). For an electron density measurement, the phase difference between the plasma on and off has to be determined. In practice, the time between the reference measurement and electron density determination should be as short as possible as long as time phase drifts occur. To avoid such problems, the lamp is switched off during measurement. The electrical setup is given in Figure A-12. An IGBT⁹-shorting circuit is placed parallel to the lamp. At the zero crossing of the lamp current ($t = 0$ ms), a trigger pulse activates the IGBT-shortening circuit. The current is bypassed and the lamp voltage collapses; then, the lamp is switched off. After a few milliseconds (typically 5 ms), the shorting circuit is deactivated, the lamp voltage builds up and the lamp is switched on again. This so-called blanking is only a short interruption of the normal lamp operation. To prevent the used power supply from damage, a resistor is placed in line with the lamp. The chosen resistance of 220Ω corresponds to typical lamp resistances.

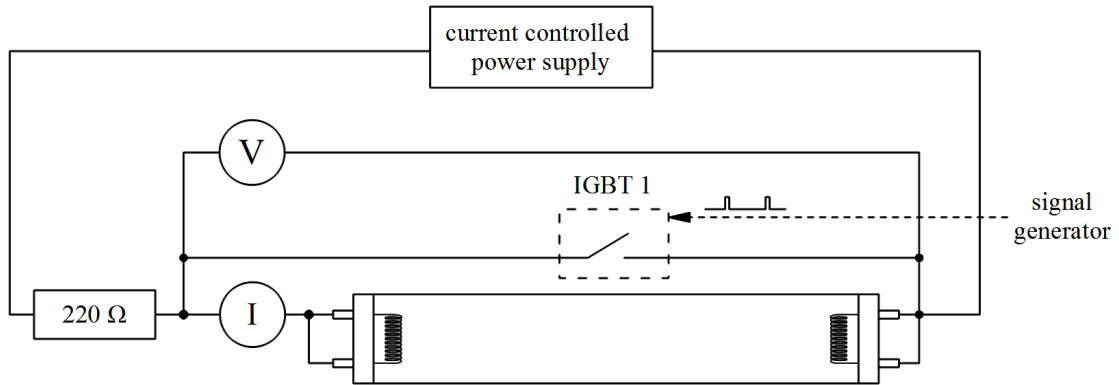


Figure A-12: Electrical setup for measuring the electron densities of a fluorescent lamp with microwave interferometry.

In Figure A-13, a typical measurement with the interferometer at the electrode region (red) and the positive column (blue) is given. The lamp is switched off at $t = 0$ ms with the IGBT-shortening circuit, whereas a small current of approximately 10 mA still appears during the first 100 μs . The cathode fall decreases immediately after the shut off and high energetic electrons (so-called beam electrons) are no longer present in the electrode region. The remaining electrons relax in a 100 μs timescale due to ambipolar diffusion. Thus, the

phase at 5 ms can be used as a reference for the lamp being off. In addition, the diffusion constant, characterizing the buffer gas and pressure, can be deduced from the decay. The electron densities both in the positive column and in the electrode region are significantly higher than the detection limit.

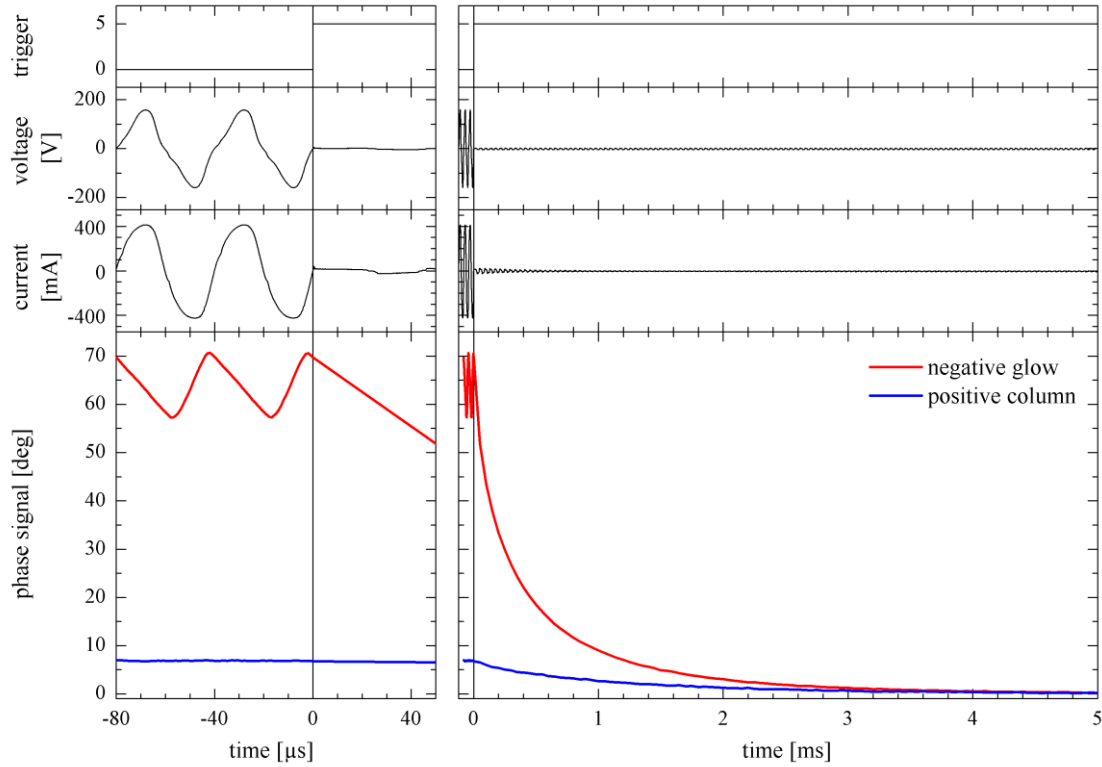


Figure A-13: Typical measurement with the interferometer at the electrode region (red) and the positive column (blue) of a fluorescent lamp. The lamp is switched off at $t = 0$ ms.

A.4 Determination of absolute particle densities by using LIF

If an ensemble of similar atomic particles (such as metal vapors) is illuminated by white light, Rayleigh scattering is observable. In addition, there is another wavelength in which selective and more intensive scattering is present (so-called fluorescence). In the first approximation, wavelength-selected fluorescence can be interpreted as the absorption of a photon followed by the re-emission of another. During this, the atom changes from a starting energy level to a second and finally a third one. The wavelengths involved depend on the energy differences of the corresponding levels.

If a laser is used instead of white light, the method is called LIF. The wavelength is adjusted to the excitation wavelength. In contrast to white light excitation, only one energy level is excited. Therefore, the resulting fluorescent light corresponds only to this level. After excitation by short laser pulses, fluorescent radiation decays exponentially due to spontaneous emission. This depends on the fact that isolated atoms stay at an excited energetic level for a typical time before they decay spontaneously by emitting a photon. The length of stay is statistically distributed. The mean value of this distribution is called the natural lifetime or *radiation lifetime*. The lifetime of species varies in a wide range, although a typical value for atoms is 10 ns for transitions in the visible range.

In general, the intensity of fluorescent radiation is directly proportional to the particle density in the excitation volume, but for higher laser intensity, this is affected by saturation effects. For the determination of absolute particle densities, a suitable calibration and knowledge of the spectroscopic data of the involved transitions are needed. In Figure A-14, the typical setup for a LIF experiment is given. The spatial resolution depends on the dimension of the laser pulse, whereas the temporal resolution is limited by the pulse duration and relaxation time of the excited state.

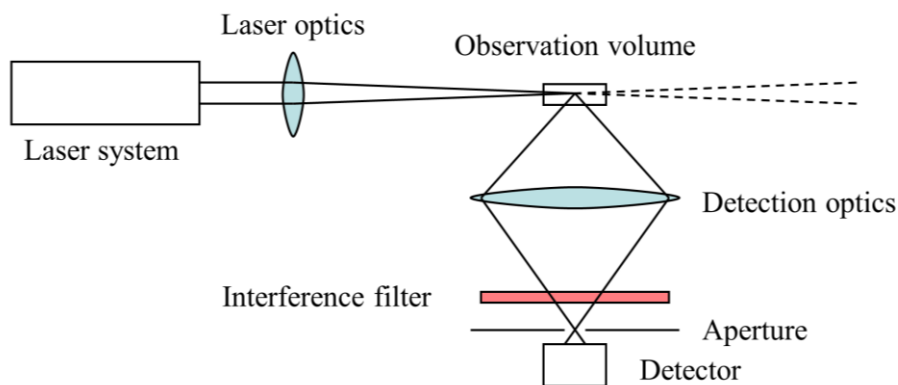


Figure A-14: Schematic setup for the LIF experiments

The theoretical fundamentals of LIF spectroscopy are discussed in detail in several textbooks such as [DEMTRÖDER 2007] as well as in a few theses such as [KRAMES 2000;

[NIEMI 2003; SCHNABEL 1999]. Therefore, a summary of the fundamentals of LIF is presented including all the relevant parts necessary for this work.

In general, the radiation theory of EINSTEIN is used, which is a phenomenological theory [NIEMI 2003]. This theory can be deduced from density matrix formalism in the approximation of the optical BLOCH equations by the use of an explicit formulation of the optical excitation cross sections [NIEMI 2003].

The validity of this theory is limited by the suppression of coherence effects such as RABI oscillations by phase-degrading mechanisms such as spontaneous emissions, elastic collisions, photoionization and broadband excitation. For the experiments realized in this work, the excitation bandwidth $\Delta\nu_L$ of the used laser system is higher than the corresponding RABI frequency ν_R ²⁵. Thus, broadband excitation (in comparison to the RABI frequency) is the dominant phase-degrading mechanism for [NIEMI 2003] and the theory can be applied.

A.4.1 Rate equation model

Consider an atom with a simplified three-level diagram (such as that in Figure A-15), where $|1\rangle$ is the ground state (or a thermally populated metastable level) with energy E_1 . The laser-excited state should be $|2\rangle$ with energy E_2 and $|3\rangle$ is the state with energy E_3 populated from the upper state by emitting a fluorescent photon. The third level should be assumed to be a metastable level. E_{ion} is the ionization energy.

If the energy of the laser photons is equal to the energy difference of $|1\rangle$ and $|2\rangle$ ($h\nu_L = h\nu_{12} = E_2 - E_1$), these photons can induce a transition between these levels. The corresponding processes are called induced absorption and induced emission. The probabilities per second for such a process are the so-called rate coefficients. The induced excitation rate R_{12} is connected to the induced emission rate R_{21} by the statistical weights g_1 and g_2 and they depend on the EINSTEIN transition probability B_{21} for induced emission as well as on the local spectral energy density $\rho(r, t)$ produced by the excitation laser:

$$R_{21} = \frac{g_1}{g_2} R_{12} = B_{21} \cdot \rho(r, t). \quad (\text{A-24})$$

²⁵ The RABI frequency depends on the intensity of the excitation radiation I and the excitation cross-section σ : $(\pi^2/3) \nu_R^2 = \sigma (I/h\nu)$.

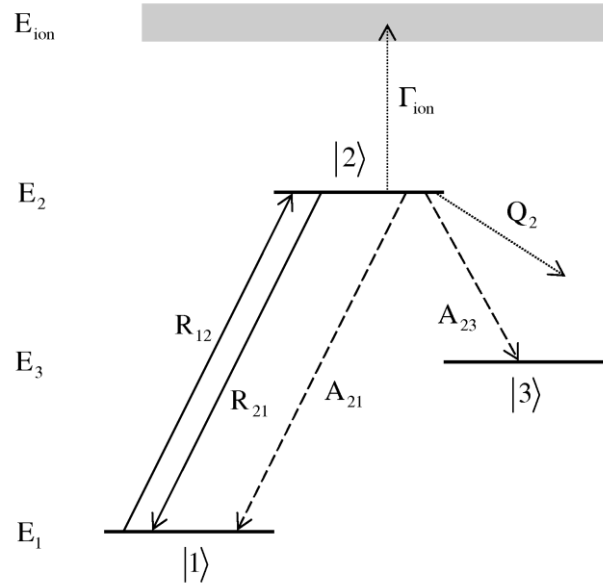


Figure A-15: Three-level energy diagram with rate coefficients. The ground state $|1\rangle$ of energy E_1 , the excited state $|2\rangle$ of energy E_2 and a metastable state $|3\rangle$ of energy E_3 are marked. The following possible processes are symbolized by arrows: induced absorption R_{12} , induced emission R_{21} , spontaneous emission A_{21} and A_{23} , collision depopulation Q_2 and ionization Γ_{ion} .

The EINSTEIN transition probability for induced emission B_{21} is directly connected to the EINSTEIN transition probability for spontaneous emission A_{21} (the probability per second for a spontaneous emission by transition from $|2\rangle$ to $|1\rangle$):

$$B_{21} = \frac{c^3}{8\pi \cdot h \nu_{21}^3} \cdot A_{21}. \quad (\text{A-25})$$

The local spectral energy density $\rho(r, t)$ produced by the excitation laser can be calculated from the laser intensity $I(r, t)$ in W/m^2 :

$$\rho(r, t) = g(\Delta\nu) \cdot \frac{I(r, t)}{c}, \quad (\text{A-26})$$

where the spectral line profile of excitation $g(\Delta\nu = \nu_L - \nu_{21})$ is the convolution of the absorption profile of the transition $g_{12}(\nu - \nu_{21})$ with the spectral profile of the laser $g_L(\nu - \nu_L)$:

$$g(\Delta\nu) = g_{12} * g_L = \int g_{12}(\Delta\nu - \nu) \cdot g_L(\nu) d\nu. \quad (\text{A-27})$$

In the first approximation, the absorption profile is a convolution of the profile of the natural line width (a LORENTZ profile) with the homogeneous DOPPLER profile (GAUSSIAN profile). For the conditions relevant to this work, DOPPLER broadening can be assumed to be the dominant effect. Therefore, the absorption profile is in general the GAUSSIAN-shaped DOPPLER profile with the line width $\Delta\nu_D = (\nu_{21}/c) \cdot \sqrt{8kT \ln(2)/m}$. By assuming a

GAUSSIAN-shaped spectral profile of the laser with a line width $\Delta\nu_L$, the resulting spectral line profile of excitation is also a GAUSSIAN profile with the line width $\Delta\nu_{\text{Ex}} = \sqrt{\Delta\nu_D^2 + \Delta\nu_L^2}$. The resulting line profile of excitation $g(\Delta\nu = \nu_L - \nu_{21})$ can be calculated as follows:

$$g(\Delta\nu) = \sqrt{\frac{4\ln 2}{\pi}} \cdot \frac{1}{\Delta\nu_{\text{Ex}}} \exp\left(-4\ln 2 \left(\frac{\nu_L - \nu_{21}}{\Delta\nu_{\text{Ex}}}\right)^2\right). \quad (\text{A-28})$$

Sometimes, it is useful to introduce the excitation cross section σ_{LIF} :

$$\sigma_{\text{LIF}} = \frac{g_2}{g_1} \frac{c^2}{8\pi\nu_{21}^2} A_{21} = \frac{g_2}{g_1} \frac{h\nu_{21}}{c} B_{21}, \quad (\text{A-29})$$

which allows formulating the induced excitation rate R_{12} more comprehensibly:

$$R_{12} = \sigma_{\text{LIF}} \cdot g(\Delta\nu) \cdot \frac{I(\vec{r}, t)}{h\nu_{21}}. \quad (\text{A-30})$$

The EINSTEIN transition probability A_{23} depends on the observed transition from $|2\rangle$ to $|3\rangle$, which emits the measured fluorescent radiation. Furthermore, the natural lifetime of an excited state can be derived by the sum of the EINSTEIN transition probability:

$$\tau_i = \frac{1}{\sum_j A_{ij}}. \quad (\text{A-31})$$

$$\tau_2 = \frac{1}{A_{21} + A_{23}}$$

The photoionization rate Γ_{ion} is proportional to the photoionization cross section σ_i and the laser intensity:

$$\Gamma_{\text{ion}} = \int \sigma_i(\nu + E_e/h) \cdot g_L(\nu) d\nu \cdot \frac{I(\vec{r}, t)}{h\nu_L} \approx \sigma_i(E_e/h) \cdot \frac{I(\vec{r}, t)}{h\nu_L}, \quad (\text{A-32})$$

where E_e is the average photo electron energy. The ionization cross section increases by increasing the main quantum number of the bonded state and decreases by increasing the photoelectron energy [NIEMI 2003]. In general, photoionization has a non-resonant character (except in the spectral near of auto-ionizing states) and is negligible, meaning $R_{12}, R_{21} \gg \Gamma_{\text{ion}}$ [SCHNABEL 1999].

The collision depopulation rate Q_2 describes the radiation less the depopulation of the excited state $|2\rangle$ induced by collision. In the normal case of a two-species collision, a phenomenological formula is found:

$$Q_2 = \sum_q k_{2,q} \cdot n_q, \quad (\text{A-33})$$

where n_q is the density of the collision partner and $k_{2,q}$ is the corresponding collision depopulation coefficient. For normal conditions $A_{23} \gg Q_2$, collision depopulation is often neglected. By taking into account all these processes, a rate equation can be found for the population density n_i of each level $|i\rangle$. The complete set of these equations are the rate equations:

$$\begin{aligned}
 \frac{d}{dt}n_1 &= -R_{12}(t) \cdot n_1 + R_{21}(t) \cdot n_2 + A_{21} \cdot n_2 \\
 \frac{d}{dt}n_2 &= R_{12}(t) \cdot n_1 - R_{21}(t) \cdot n_2 - (A_{21} + A_{23} + Q_2 + \Gamma_{\text{ion}}(t)) \cdot n_2 \\
 \frac{d}{dt}n_3 &= A_{23} \cdot n_2 \\
 \frac{d}{dt}n_{\text{ion}} &= \Gamma_{\text{ion}}(t) \cdot n_2 \\
 \frac{d}{dt}n_Q &= Q_2 \cdot n_2
 \end{aligned} \tag{A-34}$$

with the additional conditions:

$$\begin{aligned}
 n_{\text{total}}(t) &= n_1(0) = n_1(t) + n_2(t) + n_3(t) + n_{\text{ion}}(t) + n_Q(t) \\
 &\Rightarrow n_2(0) = n_3(0) = n_{\text{ion}}(0) = n_Q(0) = 0
 \end{aligned} \tag{A-35}$$

The population densities n_{ion} and n_Q are auxiliary densities to satisfy particle conservation by summarizing species that are ionized or collisions depopulated into other levels. These auxiliary densities can also be used to consider additional levels.

The additional conditions include the particle conservation as well as the starting condition. Before the laser starts its excitation, all atoms are in the ground state $|1\rangle$. Time-dependent fluorescent radiation is the amount of spontaneous transition from excited level $|2\rangle$ to $|3\rangle$ and, according to equation (A-34), it is directly proportional to the population of level $|2\rangle$.

The saturation parameter

Owing to saturation effects, LIF can be divided into the regimes of *weak excitation* and *intense excitation*. For the typical laser powers applied, LIF experiments are somewhere between these regimes. To take this fact into account, [DEMTRÖDER 2007] introduced the saturation parameter, which is used in a few other works [HADRATH 2007; KRAMES 2000; SCHNABEL 1999].

The saturation parameter describes the static relation between the population densities of the pumped system of level $|1\rangle \Leftrightarrow |2\rangle$ and it is defined as the ratio of the sum of the pump and relaxation rates:

$$\begin{aligned}
 S &= \frac{R_{12} + R_{21}}{\sum_i A_{2i}} = \left(\frac{g_1 + g_2}{g_1} \right) \cdot \frac{c^2}{8\pi \cdot h \nu_{21}^3} \cdot A_{21} \cdot g(\Delta\nu) \cdot I(r, t) \cdot \tau_2 \\
 &= \left(\frac{g_1 + g_2}{g_1} \right) \cdot \frac{c^2}{8\pi \cdot h \nu_{21}^3} \cdot b_{21} \cdot g(\Delta\nu) \cdot I(r, t)
 \end{aligned} \tag{A-36}$$

The used branching ratio (also called the relative transition probability) b_{21} is the probability that the transition $|2\rangle \Rightarrow |1\rangle$ is used for a spontaneous emission and it is defined as follows:

$$\begin{aligned}
 b_{21} &= \frac{A_{21}}{\sum_i A_{2i}} = A_{21} \cdot \tau_2, \\
 &\Rightarrow \sum_i b_{2i} = 1
 \end{aligned} \tag{A-37}$$

Thus, the saturation parameter depends only on the laser intensity and branching ratio. It describes the static equilibrium of the population ratio of $|1\rangle$ and $|2\rangle$, whereas the timescale for reaching the equilibrium (see equation (B-92)) is determined by the absolute transition probability. The spectral laser intensity yielding to a saturation parameter of $S = 1$ is called *saturation laser intensity* I_ν^S :

$$I_\nu^S = \left(\frac{g_1}{g_1 + g_2} \right) \cdot \frac{8\pi h}{c^2} \cdot \frac{1}{b_{21} \cdot g(\Delta\nu)} \cdot \nu_{21}^3. \tag{A-38}$$

Owing to the ν_{21}^3 dependence, a transition with high excitation energy can be saturated only by relatively high laser energies.

By replacing the term of laser intensity, the rate equations can be written as a function of the saturation parameter S , allowing a more general formulation. Figure A-16 shows the calculated temporal population of the excited upper level $|2\rangle$ for a barium atom for different saturation parameters. For excitation, a temporal square laser pulse with a duration of 10 ns is assumed. In the regime of intense excitation ($S \gg 1$), the static equilibrium of the population ratio of the pumped system $|1\rangle \Leftrightarrow |2\rangle$ is reached with a time constant of $1/\lambda_1$ while the pumped system is depopulated (transitions to other level) with a time constant of $1/\lambda_2$. After excitation, the density of the excited level $|2\rangle$ decays with a time constant of $1/\lambda_3$, the natural lifetime of this level. The corresponding population densities of the ground state and level $|3\rangle$ are given in Figure A-17.

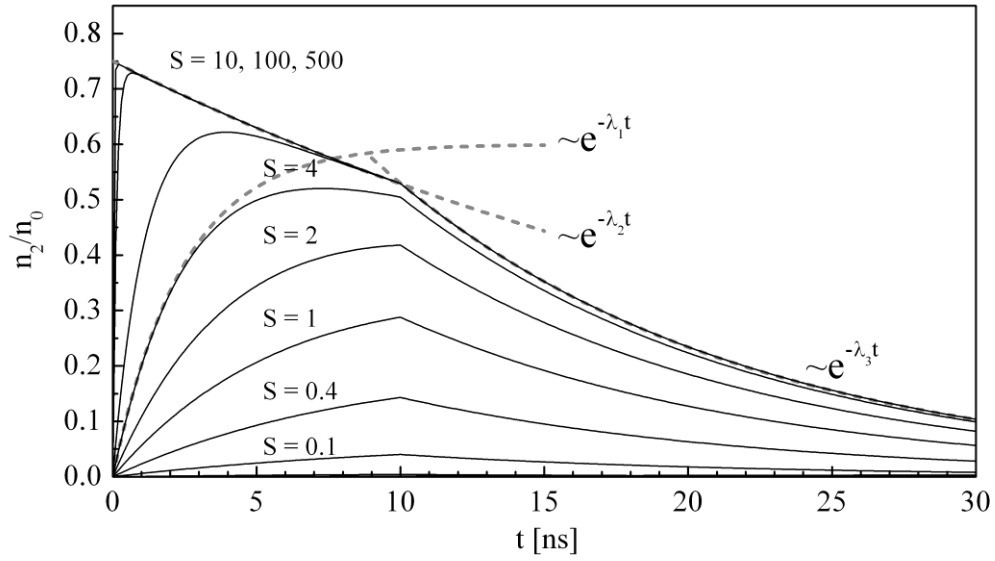


Figure A-16: Temporal dependence of the density n_2 of the upper level $|2\rangle$ during and after excitation by a temporal rectangular laser pulse for different saturation parameters S . For the calculation, the parameters of barium atoms are used and a laser pulse duration of 10 ns is assumed.

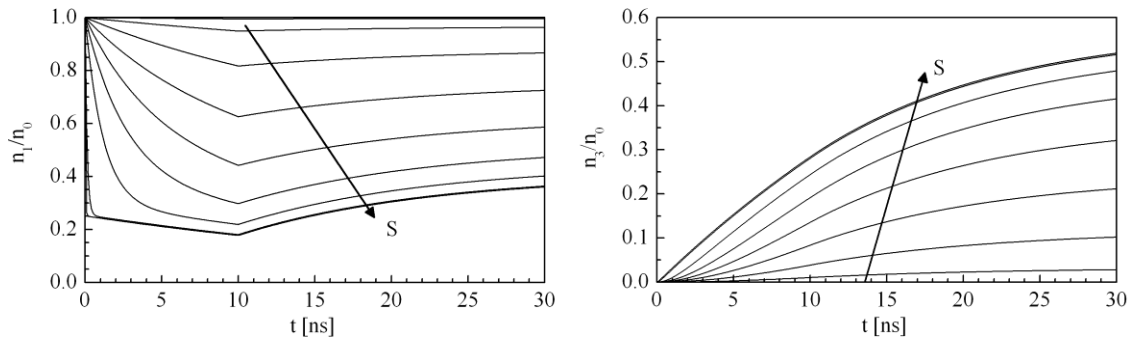


Figure A-17: Temporal dependence of the densities n_1 of the ground state $|1\rangle$ and the fluorescent level $|3\rangle$ (n_3) during and after excitation by a temporal square laser pulse for different saturation parameters S . For the calculation, the parameters of barium atoms are used and a laser pulse duration of 10 ns is assumed.

A.4.2 Fluorescent radiation

As fluorescent radiation is the amount of spontaneous transition from the excited level $|2\rangle$ to $|3\rangle$, it is directly proportional to the population of level $|2\rangle$ (equation (A-34)). Therefore, time-dependent fluorescent radiation is directly connected by the EINSTEIN factor A_{23} with the time-dependent population density given in Figure A-16:

$$n_{\text{LIF}}(t) = A_{23}n_2(t). \quad (\text{A-39})$$

Regime of weak excitation

In the case of weak excitation and sufficiently short laser pulses, the induced emission, photoionization and lost population of the ground state can be neglected ($R_{21}(t)=0$, $\Gamma_{\text{ion}}(t)=0$, $n_1(t) \approx n_1(0)=n_0$), simplifying the rate equation system (A-34) to a single differential equation for the density in the excited state:

$$\frac{d}{dt}n_2 = R_{12}(t) \cdot n_0 - (A_{21} + A_{23} + Q_2) \cdot n_2. \quad (\text{A-40})$$

After introducing the unit step function $H(t)$, the solution can be written as a convolution of the time-dependent excitation rate and the fluorescent answer [BRONSTEIN et al. 2001; DEMMIG and DEMMIG 1990; SCHNABEL 1999]:

$$n_2(t) = n_0 \cdot \int_{-\infty}^{\infty} R_{12}(t-\tau) \cdot H(\tau) e^{-(A_{21}+A_{23}+Q_2)\tau} d\tau$$

with

$$H(\tau) = \begin{cases} 0 & \tau < 0 \\ 1 & \tau > 0 \end{cases} \quad (\text{A-41})$$

The total number of fluorescent photons $N_{\text{LIF}}^{\text{total}}$ emitted in a volume V with the length of the laser beam l can be calculated by the temporal and spatial integration of this solution by taking (A-34) into account:

$$\begin{aligned} N_{\text{LIF}}^{\text{total}} &= A_{23} \cdot \int_V \int_{-\infty}^{\infty} n_2(t) dt dV \\ &= \frac{A_{23}}{A_{21} + A_{23} + Q_2} \cdot n_0 \cdot \int_V \int_{-\infty}^{\infty} R_{12}(t) dt dV \\ &= \frac{A_{23}}{A_{21} + A_{23} + Q_2} \cdot n_0 \cdot \sigma_{\text{LIF}} \cdot g(\Delta\nu) \cdot \int_V \int_{-\infty}^{\infty} \frac{I(r,t)}{h\nu_L} dt dV \\ &= \frac{A_{23}}{A_{21} + A_{23} + Q_2} \cdot n_0 \cdot \sigma_{\text{LIF}} \cdot g(\Delta\nu) \cdot l \cdot N_L \end{aligned} \quad (\text{A-42})$$

The advantage of this regime is that the total number of fluorescent photons is linear to the total number of laser photons N_L and does not depend on their temporal distribution $I(t)$. As the total number of laser photons (the laser energy) can be measured more exactly, this is the ideal regime for the quantitative determination of the absolute ground state population.

Regime of intense excitation

In the case of intense excitation and sufficiently short laser pulses $t_1 = 1/\lambda_1 \ll T_{\text{laser}} \ll t_2 = 1/\lambda_2$, the pumped system of $|1\rangle$ and $|2\rangle$ is in equilibrium according to their statistical weights ($n_1/n_2 = g_2/g_1$). By neglecting the lost in the pumped system during excitation, the population of the excited state after excitation can be calculated according to (B-92):

$$n_2(T_{\text{laser}}) = n_0 \frac{g_2}{g_1 + g_2}. \quad (\text{A-43})$$

After excitation ($t > T_{\text{laser}}$), the density decays exponentially (B-86) with the effective lifetime of the state $\tau_{2,\text{effective}}$, meaning that the total number of fluorescent photons is given by:

$$\begin{aligned} N_{\text{LIF}}^{\text{total}} &= A_{23} \cdot \int_V \int_{T_{\text{laser}}}^{\infty} n_2(t) dt dV \\ &= \frac{A_{23}}{A_{21} + A_{23} + Q_2} \cdot \frac{g_2}{g_1 + g_2} \cdot \int_V n_0 dV \end{aligned} \quad (\text{A-44})$$

In principal, the total number of fluorescent photons is independent of the laser energy and higher than the weak excitation. It is useful to introduce *fluorescent efficacy* as the ratio of the total number of emitted fluorescent photons and the total number of atoms in the initial number of atoms in the lower state before excitation:

$$\begin{aligned} \eta_{\text{LIF}} &= \frac{N_{\text{LIF}}}{N_0} = \frac{n_{\text{LIF}}}{n_0} \\ &= \frac{A_{23}}{A_{21} + A_{23} + Q_2} \cdot \frac{g_2}{g_1 + g_2}. \end{aligned} \quad (\text{A-45})$$

This allows formulating (A-44) much simpler:

$$N_{\text{LIF}}^{\text{total}} = \eta_{\text{LIF}} \cdot \int_V n_0 dV = \eta_{\text{LIF}} \cdot N_0 \quad (\text{A-46})$$

However, the assumption made such as short laser pulses $t_1 = 1/\lambda_1 \ll T_{\text{laser}} \ll t_2 = 1/\lambda_2$ can be fulfilled in practical applications. The fact that there also exist spectral-, temporal- and spatial-dependent saturation [DAILY 1977] makes exact quantitative measurement more complicated. To solve this shortcoming, my own approach for the determination of corrected fluorescent efficacy $\eta_{\text{LIF,cor}}$ is presented in Appendix A.5.

Directional characteristic of fluorescence

In the case of collision-less LIF, the anisotropic excitation of atomic transitions with a linear polarized laser leads to anisotropic-polarized fluorescent radiation. For quantitative measurements, this characteristic has to be taken into account [NIEMI 2003].

By excitation with linear-polarized laser radiation, according to the selection rule of possible transitions [DEMTRÖDER 2005], only transitions between states with the same magnetic quantum number can be excited ($m_{|1\rangle} = m_{|2\rangle}$). Therefore, the excited state has a defined population of magnetic states. Usually, this leads to the partial polarization of fluorescent radiation. By the spontaneous transition of the excited state, the change in the magnetic quantum number can be $m_{|2\rangle} - m_{|3\rangle} = 0, \pm 1$. As a result, fluorescent radiation consists of π -polarized and σ_{\pm} -polarized components. π -polarized radiation has the characteristic of an electric dipole swinging parallel to the polarization of the laser. σ_{\pm} -polarized radiation has the characteristic of an electric dipole rotating on a plane perpendicular to the polarization of the laser. By introducing the observation angle θ between the polarization direction of the laser and the observation direction, π -polarized radiation has an intensity proportional to $\sin^2(\theta)$ and σ_{\pm} -polarized radiation is proportional to $1 + \cos^2(\theta)$. Total fluorescent intensity as a function of the observation angle can be formulated as the sum of the intensity of π - and σ_{\pm} -polarized radiation:

$$I(\theta) = I_{\perp}^{\pi} \sin^2(\theta) + I_{\perp}^{\sigma} (1 + \cos^2(\theta)) \quad (\text{A-47})$$

where I_{\perp}^{π} and I_{\perp}^{σ} are the intensity of the π - and σ_{\pm} -polarized radiation perpendicular to the laser polarization ($\theta = 90^\circ$).

For further consideration, it is useful to define the degree of polarization as a function of I_{\perp}^{π} and I_{\perp}^{σ} :

$$P_{\perp} = \frac{I_{\perp}^{\pi} - I_{\perp}^{\sigma}}{I_{\perp}^{\pi} + I_{\perp}^{\sigma}} \quad (\text{A-48})$$

Finally, the directional characteristic [NIEMI 2003] of fluorescent radiation can be formulated as:

$$K(\theta) = \frac{I(\theta)}{\int I(\theta) d\Omega} = \frac{1}{4\pi} \cdot \frac{3}{3 - P_{\perp}} \cdot (1 - P_{\perp} \cos^2(\theta)). \quad (\text{A-49})$$

For an observation angle of $\theta = 54.7^\circ$ the directional characteristic and thus the intensity of fluorescent radiation is independent of the degree of polarization. Therefore, this angle is called the “magic angle” and it should be used if several different transitions are observed. If the experiment is focused on specific transitions, it is useful to choose the observation angle with the maximum intensity.

For the calculation of the degree of polarization, the relative transition probabilities of the relevant transitions have to be taken into account. A detailed description is given in [FEOFILOV 1961; NIEMI 2003; SOBELMAN 1979]. Therefore, only a summary of the calculation by laser excitation from $|1\rangle$ to $|2\rangle$ and emission to $|3\rangle$ is given in table A-1 as a parameter of the total angular momentum quantum number J_1 , J_2 and J_3 of the corresponding states.

J_2	J_3	$P_{\perp}(J_1, J_2, J_3)$
$J_1 - 1$	$J_1 - 2$	$\frac{1}{7}$
$J_1 - 1$	$J_1 - 1$	$-\frac{2J_1 - 3}{6J_1 + 1}$
$J_1 - 1$	J_1	$\frac{(J_1 - 1)(2J_1 - 3)}{14J_1^2 + 5J_1 + 1}$
J_1	$J_1 - 1$	$-\frac{2J_1 + 3}{6J_1 - 1}$
J_1	J_1	$\frac{(2J_1 + 3)(2J_1 - 1)}{8J_1^2 + 8J_1 - 1}$
J_1	$J_1 + 1$	$-\frac{2J_1 - 1}{6J_1 + 7}$
$J_1 + 1$	J_1	$\frac{(J_1 + 2)(2J_1 + 5)}{14J_1^2 + 23J_1 - 10}$
$J_1 + 1$	$J_1 + 1$	$-\frac{2J_1 + 5}{6J_1 + 5}$
$J_1 + 1$	$J_1 + 2$	$\frac{1}{7}$

Table A-1: Degree of polarization of emitted fluorescent radiation by excitation from $|1\rangle$ to $|2\rangle$ with a linear polarized laser and spontaneous emission to $|3\rangle$ as a function of the total angular momentum quantum number J_1 , J_2 and J_3 of the corresponding states [NIEMI 2003].

A.4.3 LIF experimental setup

For the laser excitation of the interesting transitions, a powerful and tunable laser system is required. A pulsed dye laser [DEMTRÖDER 2007] in combination with a second harmonic generator (SHG) fulfill these requirements in the needed spectral range (300 nm – VIS). An Nd:YAG laser is used for the excitation of the dye laser. The used solid-state Nd:YAG laser QUANTA RAY PRO-230 (from SPECTRA PHYSICS) is pumped by flash-lamps. The laser produces a pulse at 1064 nm with an energy of approx. 1250 mJ. The repetition rate is 10 Hz and it has a typical pulse length between 8 and 12 ns [SPECTRA-PHYSICS 1999]. Depending on the requirements of the used dye, either the second harmonic at 532 nm or the third harmonic at 355 nm produced by KDP¹⁰ crystals is used to pump the dye laser.

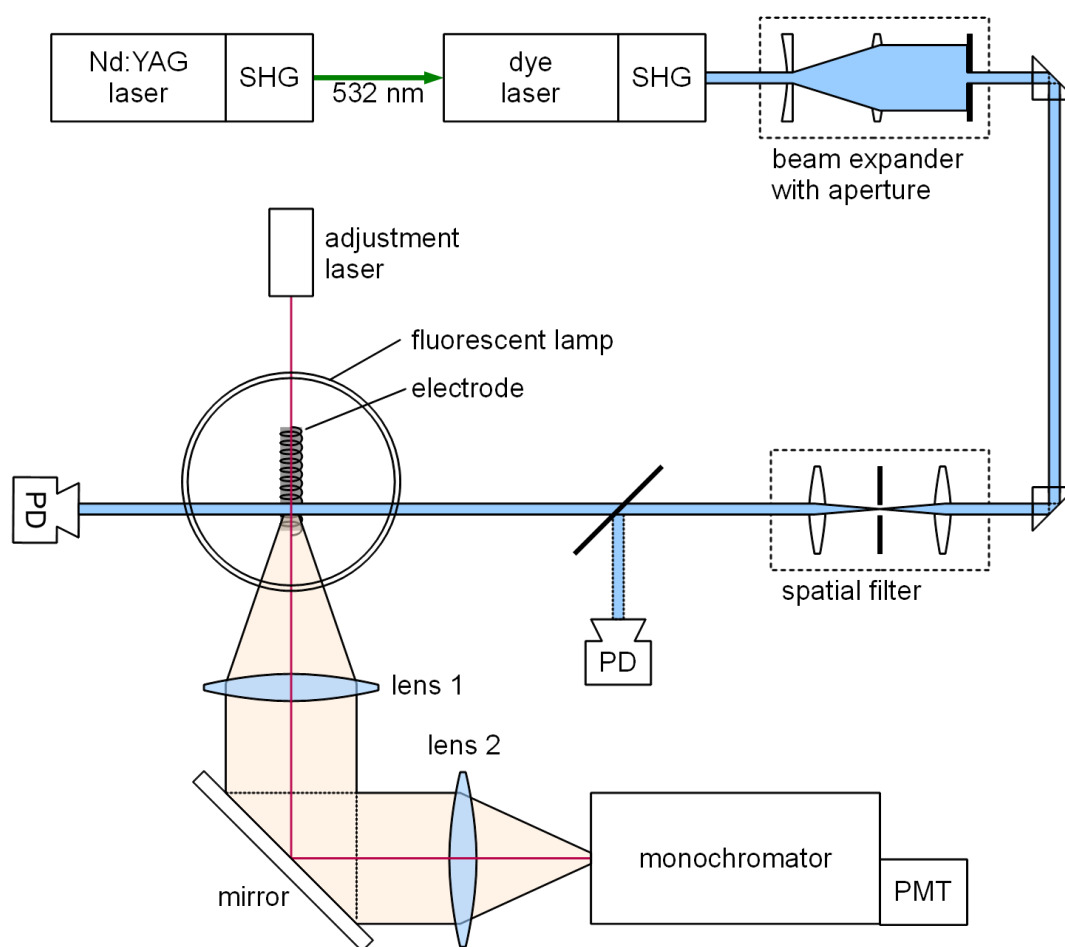


Figure A-18: The experimental setup used for LIF experiments. The Nd:YAG pumped dye laser is frequency doubled by a second harmonic generator (SHG). A beam expander and a spatial filter optimize the laser beam profile. The laser excites the barium or barium ions in front of the electrode of a fluorescent lamp. Fluorescent radiation is imaged to a monochromator and detected by a photomultiplier (PMT). The laser intensity is monitored by two photo diodes. For adjustment, a red adjustment laser is used.

As dye laser, the commercially available PRECISIONSCAN - D1800 (from SIRAH) [SIRAH-GMBH 1998] is used. The resonator consists of two gratings (each with 1800 grooves/mm) in a LITTMANN configuration. The wavelength can be tuned depending on the chosen dye solution by the rotation of one of the gratings. The laser beam produced by the resonator is amplified by two amplifying stages and, depending on the needed wavelength, frequency doubled by a KDP crystal. The typical line width is 1.34 pm (value given for 350 nm, see Figure A-19).

For the laser-induced excitation of the barium ions at a wavelength of 455.4 nm, Coumarin 460 (also known as Coumarin 1 or Coumarin 47) [EXCITON] in ethanol is used as the dye solution. This is pumped by the third harmonic of the Nd:YAG laser at 355 nm and it has a maximum efficacy of 14% at 460 nm.

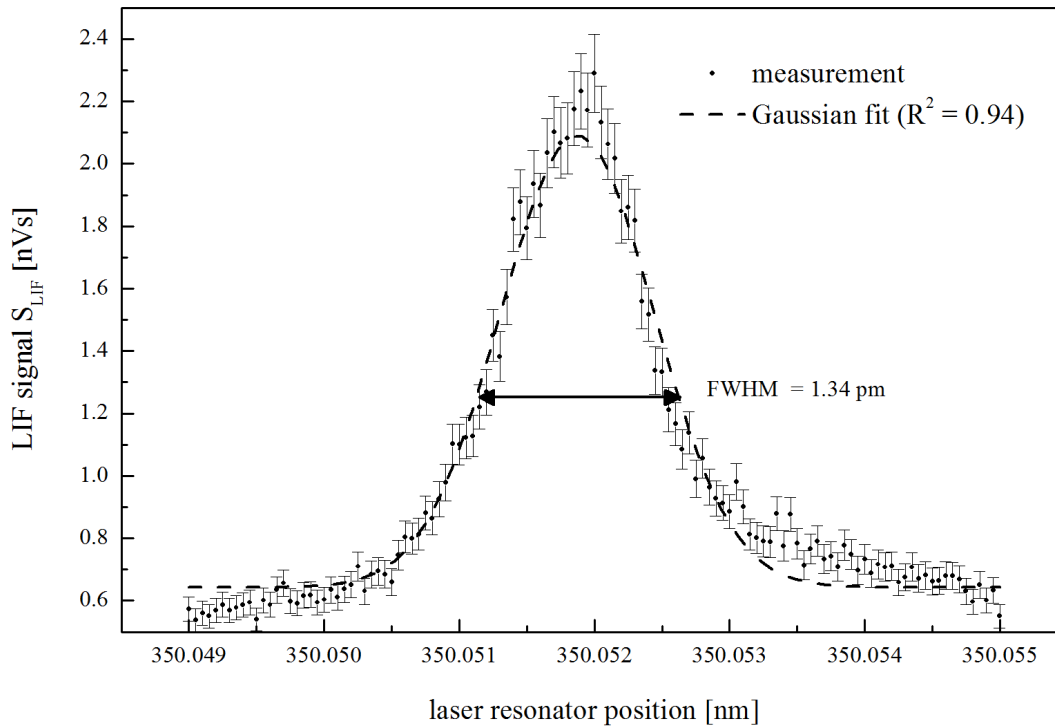


Figure A-19: Detection of the line width of the used dye laser. For the measurement, the fluorescent signal by exciting the ground state of the barium atoms is detected while tuning the dye laser wavelength. The laser power is attenuated by filters to operate in the regime of weak excitation. A GAUSSIAN beam is fitted to the measurements. The FWHM of the spectral laser profile is approx. 1.34 pm.

In the case of the excitation of the barium atoms at 350.1 nm, LDS 698 (also known as Pyridine 1) [EXCITON] in ethanol is used as the dye solution. This is pumped with the second harmonic of the Nd:YAG at 532 nm and it has a maximum efficacy of 20% at 692 nm. The resonator is tuned to 700.2 nm and the laser radiation is then frequency doubled by the KDP crystal to the desired 350.1 nm.

For beam quality optimization, the laser beam of the dye laser is broadened by using a GALILEO telescope. This consists of two lenses with $f_1 = -50$ mm and $f_2 = 200$ mm and it expands the beam diameter by a factor of four, whereas the beam power density is reduced by a factor of $4^2 = 16$. An aperture with a diameter of 1 mm is used to select the most homogeneous region of the expanded beam. For further beam optimization, a spatial filter is then placed onto the aperture. The first lens with $f_1 = 100$ mm is used to focus the beam. An aperture with a diameter of 50 μ m is placed on the focal point and a second lens with $f_2 = f_1 = 100$ mm is placed at a distance of 100 mm to produce a parallel beam. The optimized laser beam has a GAUSSIAN beam profile (see Figure A-20) with an FWHM of approx. 0.72 mm.

To monitor the laser energy permanently, a small amount of laser energy (approx. 4%) is coupled out by inserting a glass pane into the beam. The resulting laser reflex hits a white pane working as a diffuse reflector and a part of the reflected light is observed by a photodiode. In contrast to giving the laser reflex directly to the diode, the setup allows selecting the amount of laser light detected by the diode by changing the distance between the diode

and the white pane. Another advantage is, that the measured signal is not affected by small movements of the laser beam.

Antireflective-coated prisms are used to direct the laser beam through the electrode region of a fluorescent lamp. For additional control of the laser beam, especially of the amount passing through the fluorescent lamp, a second photo diode is placed afterwards.

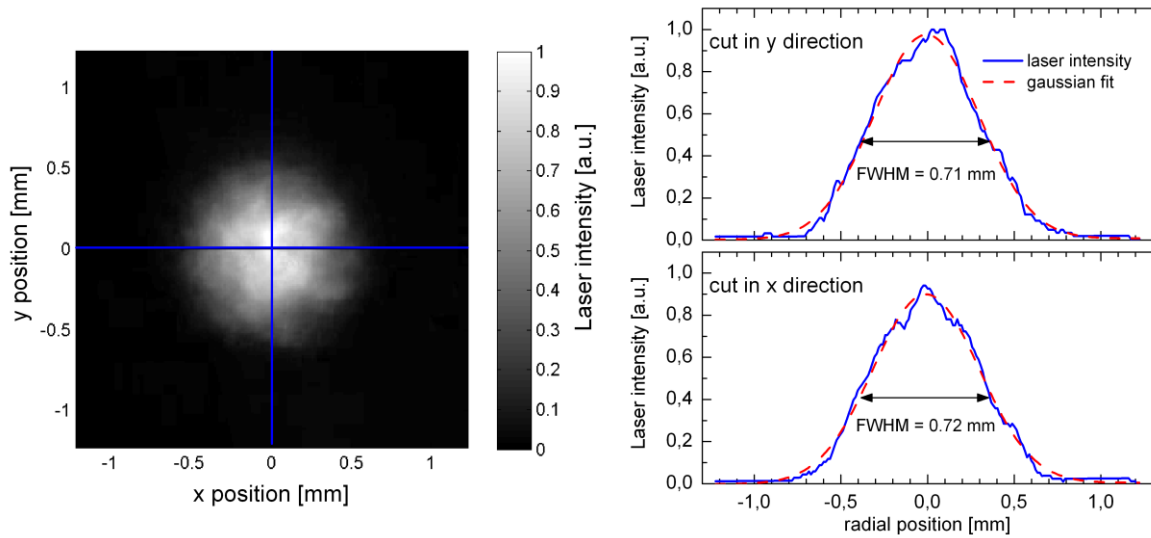


Figure A-20: (left) Spatial intensity at the position of the LIF measurement of a single laser pulse measured by using a CCD camera. (right) Beam profile of a single laser pulse in the y direction (top left) and in the x direction (bottom left). The used 1 mm aperture in combination with the spatial filter produces a GAUSSIAN beam profile with an FWHM of approx. 0.72 mm.

Fluorescent radiation detection system

Fluorescent radiation is observed perpendicular to the laser beam. The region of interest is imaged by using a system of two lenses and a mirror at the entrance slit of a 0.5 m monochromator (ACTON RESEARCH – SPECTRA PRO-500i). To collect as much light as possible, the first lens with $f_1 = 65$ mm and a diameter of $d = 50$ mm is placed at a distance of 65 mm from the observed volume. The second one, placed in front of the monochromator lens, has a focal length of $f_2 = 200$ mm and a diameter of $d = 50$ mm. This configuration expands the region of interest by a factor of three and reduces the aperture angle to the acceptance angle of the monochromator, which allows collecting enough light for a sensitive detection.

The monochromator is used as a wavelength separator to suppress scattering laser light as well as the background light emitted by the plasma in the lamp. A grating with 1800 grooves/mm and a blazing wavelength of 500 nm is used. To increase sensitivity, the entrance and exit slits of the monochromator are set to 2 mm. These relatively wide slits reduce the effective wavelength resolution to approx. 1.5 nm, which is enough for the suppression of background light. The height of the slit is limited to 2 mm so that the effective entrance area of the monochromator is $2 \times 2 \text{ mm}^2$. By taking the magnification of

3 produced by the lens system into account, the observed region of interest has a size of $0.67 \times 0.67 = 0.44 \text{ mm}^2$.

For light detection, a photomultiplier (HAMAMATSU D1477-06) is mounted behind the exit slit. The photomultiplier is connected to a gated socket (HAMAMATSU C1392-56). The gating option allows switching the first dynode so that the photomultiplier can be set to be active for a short time (a few μs). This avoids the saturation of the photo cathode by continuous parasitic light.

For signal detection, a four-channel digital storage oscilloscope (LeCroy WavePro 7300) with a maximum sample rate of 20 Gs/s and a maximum analog bandwidth of 3 GHz is used. The oscilloscope is triggered by a synchronization signal of the Nd:YAG laser, and the signals of the photomultiplier and of the photodiodes are recorded simultaneously. For further analyses, the waveforms are transferred to a PC.

Detected Signal

As discussed before, for quantitative measurements it is useful to measure the time integration of the LIF signal I_{LIF} . Therefore, intensified CCD cameras in combination with an interference filter or a monochromator are used. For the detection of very low intensity or if a good time resolution is necessary, photomultipliers are typically used. A time-integrated signal can be described as follows:

$$\begin{aligned} S_{\text{LIF}} &= \int I_{\text{LIF}}(t) dt \\ &= G(\nu_{\text{LIF}}) \cdot \int_{\Delta\theta_{\text{LIF}}} K(\theta) d\Omega \cdot N_{\text{LIF}}^{\text{total}} \end{aligned} \quad (\text{A-50})$$

where $G(\lambda_{\text{LIF}})$ is the sensitivity of the detection system at the wavelength of the fluorescence radiation including the transmission of the detection path, quantum efficacy of the detector and amplification of the signal, $\Delta\theta_{\text{LIF}}$ is the angle of aperture used for detection and $N_{\text{LIF}}^{\text{total}}$ is the total number of fluorescent photons emitted in the observed volume. For small angles of aperture or small degrees of polarization ($|P_{\perp}| \ll 1 \rightarrow K(\theta) \approx \text{const.}$), the angular integral of the directional characteristic can be replaced by the product of the solid angle of observation $\Delta\Omega = 2\pi \sin(\Delta\theta_{\text{LIF}}/2)$ and the directional characteristic of the angle of observation θ_{LIF} . By assuming the regime of weak excitation (see equation (A-42)), we obtain for the time-integrated signal:

$$\begin{aligned} S_{\text{LIF}} &= \int I_{\text{LIF}}(t) dt \\ &= G(\lambda_{\text{LIF}}) \cdot \Delta\Omega \cdot K(\theta_{\text{LIF}}) \cdot \frac{A_{23}}{A_2 + Q_2} \cdot n_0 \cdot \sigma_{\text{LIF}} \cdot g(\Delta\nu) \cdot l \cdot N_{\text{laser,LIF}}, \end{aligned} \quad (\text{A-51})$$

where $N_{\text{laser,LIF}}$ represents the total numbers of laser photons used for the excitation and l represents the length of the overlap volume V of the observation volume and laser beam. In the regime of intense excitation (see equation (A-44)), the signal can be described as similar:

$$S_{\text{LIF}} = G(\lambda_{\text{LIF}}) \cdot \Delta\Omega \cdot K(\theta_{\text{LIF}}) \cdot \eta_{\text{LIF}} \cdot n_0 \cdot V, \quad (\text{A-52})$$

where $\eta_{\text{LIF,cor}}$ represents the fluorescent efficacy (see equation (A-46)) in the case of saturation.

A.4.4 Absolute calibration by Rayleigh scattering

The measured signal depends on the constants of the investigated species as well as on the parameters of the specific experimental setup. For quantitative measurements, the main difficulties are the exact determination of the geometry as well as the spectral response of the optical setup. The easiest method to overcome these issues is to measure the LIF signal for a known density. Typically, LIF as a complex diagnostic is used if other methods are not applicable and the exact absolute density is of special interest. In that case, a precise determination of the sensitivity of the detection system $G(\nu_{\text{LIF}})$, the solid angle of observation and the observation volume V can be avoided by taking a RAYLEIGH scattering calibration measurement.

Rayleigh scattering

For RAYLEIGH calibration, the RAYLEIGH scattering measured at a reference gas, usually a rare gas, of known density is detected under the same experimental conditions. The scattered light is compared with the LIF signal, allowing a characterization of the detection conditions. This technique is well known and described in several papers [AMORIM et al. 2000; BOGEN 1983; HAMAMOTO et al. 1981; JAUERNIK et al. 1987; KRAMES 2000; RECKERS et al. 1997]. The technique is suitable if the fluorescence and excitation wavelength (as well as the wavelength of the scattered light) are in the same spectral region. If this condition is not fulfilled, the relative calibration of the spectral sensitivity $G(\lambda)$ of the detection system is required.

The time-integrated RAYLEIGH signal can be described by

$$\begin{aligned} S_{\text{Ray}} &= \int I_{\text{Ray}}(t) dt \\ &= G(\lambda_{\text{Ray}}) \cdot \frac{\Delta\Omega}{4\pi} \cdot \sigma_{\text{Ray}} \cdot L \cdot n_{\text{Gas}} \cdot N_{\text{laser,Ray}} \end{aligned} \quad (\text{A-53})$$

where σ_{Ray} denotes the RAYLEIGH scattering cross section, λ_{Ray} the responding wavelength, n_{Gas} the density of the used reference gas and $N_{\text{laser,Ray}}$ the total number of laser photons.

The RAYLEIGH scattering cross section is given by:

$$\sigma_{\text{Ray}} = \frac{128\pi^5 \alpha^2}{3\lambda_{\text{Ray}}^4}$$

with

$$\alpha^2 = \frac{1}{5} \alpha_0^2 \cdot \left(3\kappa^2 + (5 + \kappa^2) \cdot \cos(\theta_{\text{Ray}}) \right) \quad (\text{A-54})$$

where α is the dipole polarizability, κ the anisotropy of the used gas and $\theta_{\text{Ray}} = \theta_{\text{LIF}}$ the angle between the vector of the electric field strength of the laser radiation and the RAYLEIGH scattering light. In contrast to molecular gases, the anisotropy of rare gases is negligible. Note that the scattering cross section and RAYLEIGH scattering signal are proportional to $S_{\text{Ray}} \propto \lambda^{-4}$. Therefore, RAYLEIGH scattering is intense for short wavelengths and decreases very strongly for longer wavelengths.

By dividing equation (A-51) by (A-53), the ground state density before laser excitation n_0 can be determined in the regime of weak excitation:

$$n_0 = \frac{G(\lambda_{\text{Ray}})}{G(\lambda_{\text{LIF}})} \cdot \frac{A_2 + Q_2}{A_{23}} \cdot \frac{\sigma_{\text{Ray}}}{4\pi \cdot K(\theta_{\text{LIF}}) \cdot \sigma_{\text{LIF}} \cdot g(\Delta\nu)} \cdot \frac{n_{\text{Gas}} \cdot N_{\text{laser, Ray}}}{S_{\text{Ray}}} \cdot \frac{S_{\text{LIF}}}{N_{\text{laser, LIF}}} \quad (\text{A-55})$$

Thus, the solid angle of observation and geometric parameters (volume, length, cross section) of the observation volume can be eliminated. Only the ratio of the spectral sensitivities $G(\lambda_{\text{Ray}})/G(\lambda_{\text{LIF}})$ has to be known. If the wavelengths are close, the ratio is equal to one and no relative calibration is needed. The absolute density of the ground state depends only on known constants, a RAYLEIGH correction term and the ratio of the measured LIF signal S_{LIF} and the laser energy/number of laser photons.

By dividing (A-52) by (A-53), the ground state density can be determined in the case of intense excitation:

$$n_0 = \frac{G(\lambda_{\text{Ray}})}{G(\lambda_{\text{LIF}})} \cdot \frac{1}{\eta_{\text{LIF}}} \cdot \frac{1}{4\pi \cdot K(\theta_{\text{LIF}})} \cdot \frac{\sigma_{\text{Ray}}}{A_{\text{beam}}} \cdot \frac{n_{\text{Gas}} \cdot N_{\text{laser, Ray}}}{S_{\text{Ray}}} \cdot S_{\text{LIF}} \quad (\text{A-56})$$

where $A_{\text{beam}} = V/l$ represents the cross section area of the observed volume, which can be interpreted as the effective laser beam cross section area. In this case, the solid angle of observation can be eliminated but the laser beam cross section has to be known. Typical for intense excitation, the determination of the ground state density is independent of the laser energy used for excitation.

Determination of the experimental Rayleigh correction term

For the absolute calibration of the experiment, the RAYLEIGH correction term has to be determined:

$$C_{\text{Ray}} = \frac{n_{\text{Gas}} \cdot N_{\text{laser, Ray}}}{S_{\text{Ray}}} \quad (\text{A-57})$$

In general, the RAYLEIGH scattering cross section (A-54) is much smaller than the LIF cross section. In addition, RAYLEIGH scattering is observed at the laser wavelength. Such parasitic scattered laser light is a problem for the determination of RAYLEIGH scattering. Therefore, RAYLEIGH scattering is measured as a function of the particle density of the used gas, which allows determining the parasitic scattered laser light for a particle density $n_{\text{gas}} = 0$. For the measurement, a special vacuum vessel (see Figure A-21) is used. To suppress parasitic scattered laser light in the vessel, the inner walls are blackened. The gas filling as well as the pressure can be controlled by the connected pumping system.

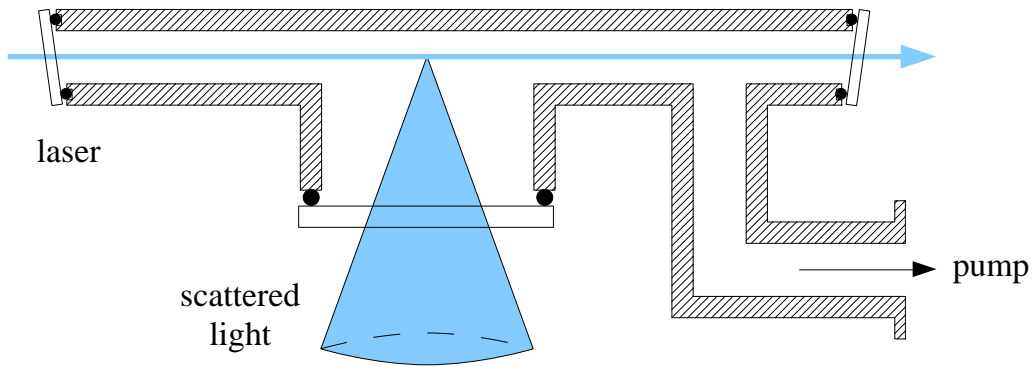


Figure A-21: Vacuum vessel for the determination of RAYLEIGH scattering for the absolute calibration of the LIF experiment. To suppress parasitic scattered laser light in the vessel, the inner walls are blackened. The gas filling as well as the pressure can be controlled by the connected pumping system.

As Xenon has $\alpha_0 = 4.044 \text{ \AA}^3$ [LIDE 2001], the highest dipole polarizability of the noble gases, it has been used for the determination of RAYLEIGH scattering. In contrast, Argon as a cheap alternative has a much smaller dipole polarizability of $\alpha_0 = 1.6411 \text{ \AA}^3$ [LIDE 2001; RECKERS et al. 1997].

In Figure A-22, the measured RAYLEIGH signal as a function of the Xenon pressure is given. The slope of the fitted line (linear regression) represents the RAYLEIGH signal normalized to the laser power per pressure interval $S_{\text{Ray}} / (E_{\text{laser}} p_{\text{Xenon}}) = 0.102 \text{ pVs} \mu\text{J}^{-1} \text{ mbar}^{-1}$

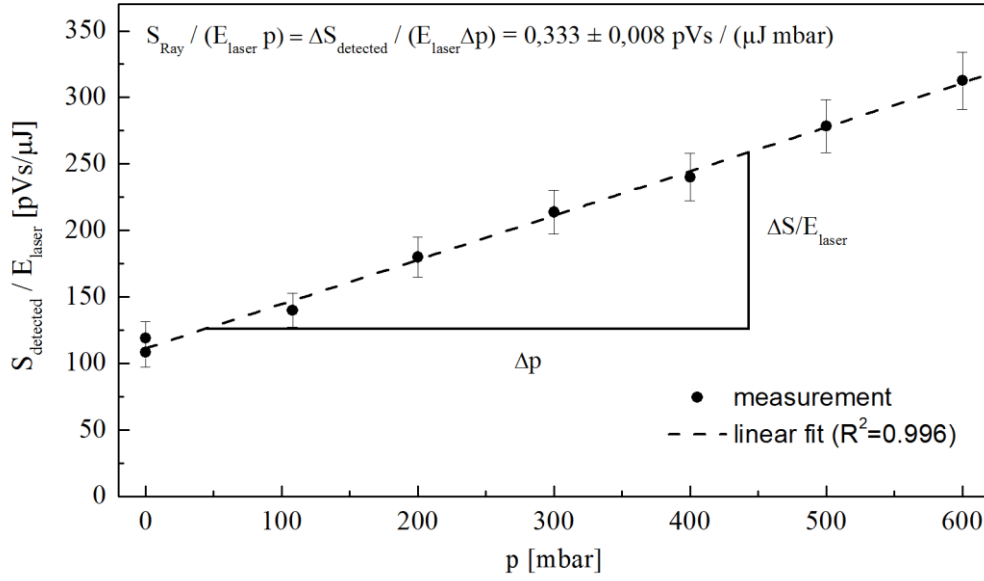


Figure A-22: Measured RAYLEIGH signal normalized to a laser power of $E_{\text{laser}} = 3.4 \mu\text{J}$ as a function of the Xenon pressure. For the separation of parasitic scattered laser light, pressure-dependent RAYLEIGH scattering can be determined from the slope of the curve.

In the case of the saturated LIF excitation applied in the work, the absolute calibrated barium atom sensitivity can be calculated according to equation (A-56):

$$n_0 = 2.98 \cdot 10^{15} \frac{1}{\text{m}^3 \text{nVs}} \cdot S_{\text{LIF}}. \quad (\text{A-58})$$

For the calculation, a fluorescent efficacy according to equation (A-45) of $\eta_{\text{LIF}} = 0.414$ is used.

A.4.5 Saturation correction

For absolute density calibration, a fluorescent efficacy according to equation (A-45) of $\eta_{\text{LIF}} = 0.414$ is used. This value is only valid for the assumption of a spatially homogeneous laser beam profile. The energy density of real laser beams decreases from the center towards the edge (ideally, a laser has a GAUSSIAN beam profile). With increasing laser energies (increasing saturation parameter), the saturated area of the beam profile extends, leading to an increased effective laser beam cross section area A_{beam} . This effect is called power broadening [DAILY 1977] and it has to be considered for absolute calibrated experiments. My model for solving the temporal- and spatial-dependent rate equations in the case of the barium atoms is given in appendix A.5. It includes the measured laser beam characteristics and the characteristics of the observation optics.

For saturation correction, the saturation characteristic obtained from the model (see Section A.5) has to be compared to the real saturation characteristic measured. This procedure allows determining the saturation parameter for the laser power used in the experiment.

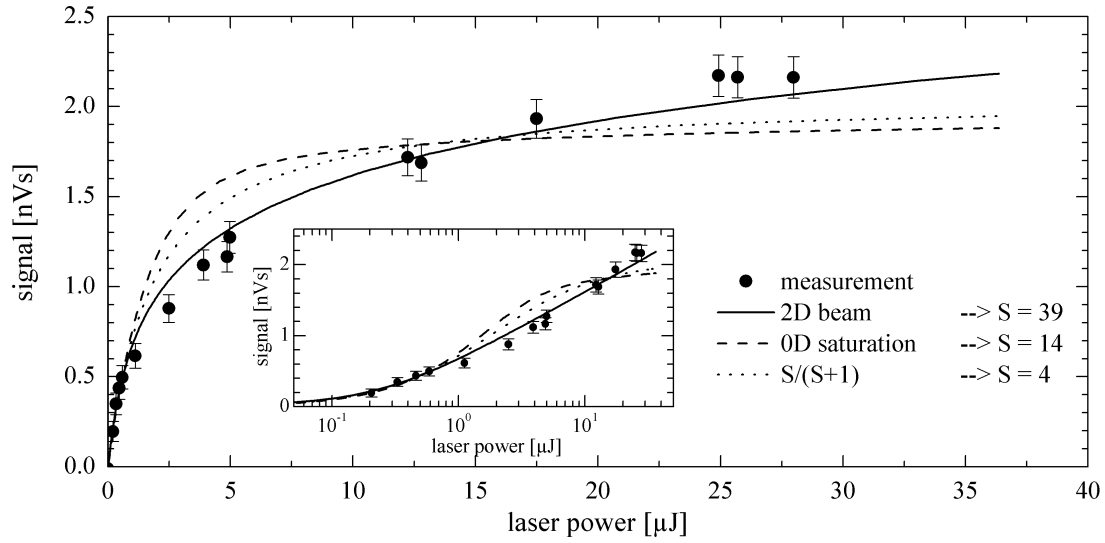


Figure A-23: Experimentally determined saturation characteristic. The fluorescent signal as a function of the laser power (dots) for the excitation of the barium atom ground state 5 mm in front of a heated electrode. By fitting the saturation characteristics (straight line – computed by considering a 2D Gaussian laser beam profile, dashed line – computed by considering a homogeneous beam, dotted line – simplified model) to the measured values, the saturation parameter for the laser power used in the experiment of 8 μJ can be determined.

In the case of the barium atoms, the saturation characteristic is measured by the variation of the laser power and detection of the fluorescent signal. To be as close as possible to the measurements of the lamps, the saturation characteristic is measured in a fluorescent lamp. The lamp is not ignited and a constant current is applied through one electrode (about 420 mA). Thus, the electrode is heated to a constant temperature, while barium is produced and diffused through the electrode region. Hence, a constant barium density is built up, as indicated by a constant LIF signal. To have a homogeneous barium density, the measurement is placed 5 mm in front of the center of the heated electrode. The laser power is varied by placing a neutral density filter in the laser beam.

The measured saturation characteristic is given in Figure A-23. The LIF signal is the time-integrated signal of the photomultiplier. To determine the saturation parameter for the laser power used in the experiment (8 μJ), the saturation characteristics computed in Appendix A.5 are fitted to the measurements²⁶ by the use of the least squares method [HELMERT 1907]. In addition, the simplified model of equation (A-64) [DEMTRÖDER 2007] is fitted. This simplified model, as well as by assuming a round, homogeneous beam (identical to 0D saturation in Figure A-23), describes the measured characteristic insufficiently. It overestimates the fluorescent signal for a laser power of $1\mu\text{J} < P_{\text{laser}} < 15\mu\text{J}$ and

²⁶ The previously determined saturation characteristics $N_{\text{LIF}}(S)$ are fitted by scaling: $I(P_{\text{laser}}) = a N_{\text{LIF}}(b \cdot P_{\text{laser}})$. The fitting is done in MatLab by the use of the least squares method [HELMERT 1907].

underestimates it for higher laser power. In particular, it does not represent the further increase in the fluorescent signal in the case of high saturation. This effect can only be represented by considering *power broadening*. Thus, the saturation characteristic computed in Appendix A.5, by considering the 2D laser beam profile, represents the measured characteristic well.

For the laser power used in the experiment of $8 \mu\text{J}$, a saturation parameter of $S_a = S(P_{\text{laser},a} = 8 \mu\text{J}) = 39$ is found. Hence, the effective beam size in the y direction is about 1.5 mm (see Figure A-28b) and corrected fluorescent efficacy is $\eta_{\text{LIF},\text{cor}} = N_{\text{LIF}} / N_0 = 0.83$ (see Figure A-28a). The value of corrected fluorescent efficacy is significantly higher than the theoretical value for saturated LIF of $\eta_{\text{LIF}} = 0.414$ (given in equation (A-45)), and this leads to a correction of about a factor of two. By considering the correction for the absolute density calibration (see Section A.4.4), the saturation-corrected absolute barium atom density can be calculated according to:

$$n_0 = 1.49 \cdot 10^{15} \frac{1}{\text{m}^3 \text{nVs}} \cdot S_{\text{LIF}}. \quad (\text{A-59})$$

Correction of laser power fluctuations

To reduce the errors in the LIF experiment due to fluctuations in the laser power, an additional correction is applied. For each LIF measurement, the fluorescent signal and actual laser power are detected. In the experiments, the typically applied laser power is about $P_{\text{laser},a} = 8 \mu\text{J}$, leading to a saturation parameter of about $S_a = 39$ (see Appendix A.4.5). At this power level, the laser (the Nd:YAG laser as well as the dye laser) works at a very stable and reproducible regime. However, small power fluctuations lead to fluctuations in the fluorescent signal that can be corrected. For the correction, the calculated saturation characteristic $N_{\text{LIF}}(S)$, representing the dependence of the fluorescent signal on the laser power, is used.

In a first step, the Taylor series (first degree) of the saturation characteristic $N_{\text{LIF}}(S)$ at the typical laser power S_a is calculated:

$$N_{\text{LIF}}(S) \approx N_{\text{LIF}}(S_a) + N'_{\text{LIF}}(S_a) \cdot (S - S_a). \quad (\text{A-60})$$

As the saturation parameter is proportional to the laser power:

$$S = \frac{S_a}{P_{\text{laser},a}} \cdot P_{\text{laser}} \quad (\text{A-61})$$

and the measured fluorescent signal $I_{\text{LIF}}(P_{\text{laser}})$ is proportional to the saturation characteristic $N_{\text{LIF}}(S)$:

$$I_{\text{LIF}}(P_{\text{laser}}) \propto N_{\text{LIF}}\left(S = \frac{S_a}{P_{\text{laser},a}} \cdot P_{\text{laser}}\right), \quad (\text{A-62})$$

a correction of the fluorescent signal can be made for small power fluctuations:

$$\begin{aligned}
 I_{LIF, corrected} &= I_{LIF}(P_{laser, a}) \\
 &= \frac{N_{LIF}(S_a)}{N_{LIF}(S)} \cdot I_{LIF}(P_{laser}) \\
 &\approx \frac{N_{LIF}(S_a)}{N_{LIF}(S_a) + N'_{LIF}(S_a) \cdot (S - S_a)} \cdot I_{LIF}(P_{laser}) \\
 &\approx \frac{1}{1 + \frac{N'_{LIF}(S_a)}{N_{LIF}(S_a)} \cdot (S - S_a)} \cdot I_{LIF}(P_{laser}) \\
 &\approx \frac{1}{1 + \frac{N'_{LIF}(S_a)}{N_{LIF}(S_a)} \cdot S_a \cdot \left(\frac{P_{laser}}{P_{laser, a}} - 1 \right)} \cdot I_{LIF}(P_{laser})
 \end{aligned} \tag{A-63}$$

Here, P_{laser} is the actual laser power and $P_{laser, a} = 8\mu J$ is the standard laser power, while the saturation parameter $S_a = 39$ is also known.

A.5 Model for the correction of saturation effects by the application of LIF

LIF can be described by a system of rate equations (equation (A-34)). In Section 0, the system is discussed and a more general solution presented that includes several assumptions such as a temporal rectangular laser pulse. In the regime of weak excitation, fluorescent radiation is proportional to the laser pulse energy (linear regime). For high laser intensities, saturation occurs and fluorescent radiation is independent of the laser pulse energy (intense excitation).

In general, the regime of weak excitation is preferred for LIF experiments due to the linear dependency of the fluorescent signal on the laser power. However, for low densities of the investigated species, the regime of intense excitation has to be used, as the fluorescent signals are at least two orders of magnitude higher.

In this work, very low densities of barium (low densities in a small volume) are investigated. Thus, the regime of intense excitation is used. For absolute density determination in this regime, the process of saturation, especially the transition from the regime of weak excitation to that of an intense one, has to be treated more in detail. The amount of saturation is described by the saturation parameter S (see page 119 and equation (A-36) for details). A simplified model describing the number of emitted fluorescence photons as a function of the saturation parameter $N_{LIF}(S)$ is given by [DEMTRÖDER 2007]:

$$\frac{N_{LIF}(S)}{N_{LIF}(S \rightarrow \infty)} = \frac{S}{1 + S}. \tag{A-64}$$

This empirically found model is valid for a temporal rectangular laser pulse with a homogeneous laser beam profile but it does not consider the pump-over effect (see page 150). For absolute density determination, a saturation correction has to be performed.

Therefore, the

laser power is varied (typically by attenuating with filters) and the fluorescent signal is measured. By fitting equation (A-64), the saturation parameter S at the applied laser power can be determined. For saturation correction, the measured fluorescent signal has to be multiplied by $(1 + S)/S$.

In this work, the barium level Ba ($5d6p^1P_1$) with a natural lifetime of 12.17 ns is investigated. The lifetime is of the order of the length of the laser pulse of approx. 5 ns. Hence, for saturation correction, the pump-over effect and the temporal shape of the laser pulse has to be considered. Thus, the simplified model of equation (A-64) cannot be applied, as this leads to a significant systematic error.

To perform a sufficient saturation correction, an own model is applied. In the first step, the rate equation system (equation (A-34)) is solved for the investigated transitions of barium (Section A.5.1). In the second step, the spatial beam profile is considered, allowing the correction of spatial saturation broadening. Finally, the obtained saturation characteristic is compared to a measured saturation characteristic to determine the saturation parameter at the applied laser power and perform a saturation correction (Section A.4.5).

A.5.1 Solving the rate equation system for real laser pulses

The rate equation system given in equation (A-34) is solved numerically for real laser pulses. For the computation, the *ode45 solver* of the commercially available software MATLAB [MATHWORKSINC.] is used. The solver implements the 4th/5th-order RUNGE-KUTTA method.

For a more general treatment of the LIF process the temporal-dependent excitation rate $R_{12}(t)$ and induced emission rate $R_{21}(t)$ are expressed by the temporal-dependent saturation parameter $S(t)$ according to equations (A-36) and (A-24):

$$\begin{aligned} R_{21}(t) &= \frac{g_1}{g_1 + g_2} \cdot \sum_i A_{2i} \cdot S(t) \propto I_{\text{laser}}(t) \\ R_{12}(t) &= \frac{g_2}{g_1 + g_2} \cdot \sum_i A_{2i} \cdot S(t) \propto I_{\text{laser}}(t) \end{aligned} \quad (\text{A-65})$$

Defining temporal excitation

The temporal-dependent saturation parameter is proportional to the laser power. Thus, it is deduced from the temporal evolution of real laser pulses. In Figure A-24, the temporal behavior of laser intensity averaged over 1200 pulses is shown.

To find an analytical expression for the temporal excitation, a so-called bell function

$$I_{\text{bell}}(t) = A \cdot \begin{cases} 0 & t < -\tau \\ 0.5 + 0.5 \cos\left(\pi \cdot \frac{t}{\tau}\right) & \text{for } -\tau \leq t \leq \tau \\ 0 & t > \tau \end{cases} \quad (\text{A-66})$$

is fitted to the measured curve, whereas A denotes the amplitude and τ the FWHM. In contrast to other curves that can be assumed, such as a GAUSSIAN function, a bell function is equal to zero for $t < -\tau$ or $t > \tau$. This provides stability and plausibility by solving the rate equation system, especially for high saturation parameters. As an example, the use of a GAUSSIAN function leads to an increase in the effective duration of excitation for increasing saturation parameters. In the case of very high saturation parameters, the slopes would produce excitation before the laser pulse appears, which is not plausible.

By fitting a bell function to the measured curve (see Figure A-24), an FWHM of $\tau = 4.85$ ns is found. This value corresponds to the manufacturer's specification of the dye laser system used [SIRAH-GMBH 1998].

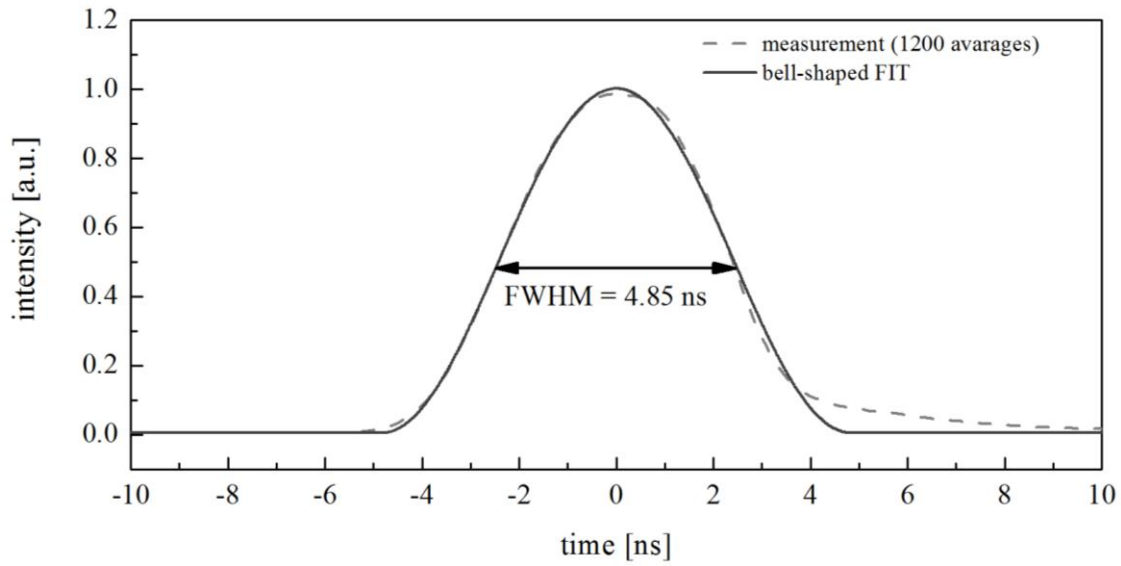


Figure A-24: Average of the temporal evolution of 1200 laser pulses at 350 nm produced by a frequency doubled dye laser. The temporal evolution can be fitted well by a bell-shaped curve with a duration of 4.85 ns (FWHM).

The temporal-dependent saturation parameter $S(t)$ is defined as a bell function with the amplitude S and duration τ :

$$S(t) = S \cdot \begin{cases} 0 & t < -\tau \\ 0.5 + 0.5 \cos\left(\pi \cdot \frac{t}{\tau}\right) & -\tau \leq t \leq \tau \\ 0 & t > \tau \end{cases} \quad (\text{A-67})$$

To be consistent, the integral of the time-dependent saturation parameter (which is proportional to the laser pulse energy) $\int S(t) dt = S\tau$ is the same as that for a rectangular

pulse with the intensity S and duration τ . In the following, both temporal excitations are compared to illustrate the limitation of the commonly used assumption of a rectangular pulse.

Having defined the temporal saturation parameter, the excitation rate $R_{12}(t)$ and induced emission rate $R_{21}(t)$ can be calculated and used as input parameters for solving the rate equation system. To simplify the computation, the effect of photoionization and collision depopulation is neglected. Thus, the photoionization rate is $\Gamma_{\text{ion}}(t)=0$ and the collision depopulation rate is $Q_2(t)=0$. The validation of neglecting the collision depopulation is proven in Section 5.1.

Solution of the rate equation system

The numerical solution of the rate equation system provides the temporal density of the three states $|1\rangle$ (ground state), $|2\rangle$ (excited barium level $5d6p^1P_1$) and $|3\rangle$ (metastable state). The temporal solution for the population density of the excited barium level $|2\rangle$ normalized to the ground state population density before excitation is given in Figure A-25. As discussed in Section A.4.2, fluorescent radiation is directly proportional to the population densities of this state. As a comparison, bell-shaped and rectangular temporal excitations are assumed for different values of the saturation parameter.

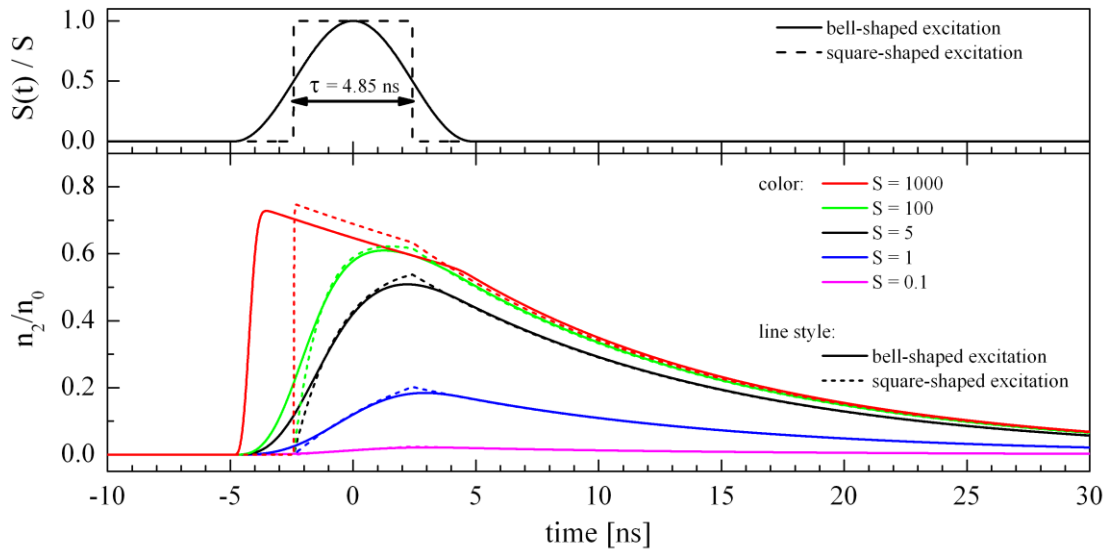


Figure A-25: Numerical solution of the rate equation system. (Top) Assumed temporal excitation $S(t)$ in the case of a bell-shaped (full line) and a rectangular (dotted line) excitation pulse with a duration of 4.85 ns, normalized on the saturation parameter S . (Bottom) Temporal population of the excited barium level ($5d6p^1P_1$) during and after excitation by a bell-shaped (full line) and a rectangular (dotted line) pulse for different saturation parameters, normalized to the ground state population density before excitation.

For low saturation parameters ($S \leq 0.1$, weak excitation), the population densities of the excited level are similar for both temporal excitations. The population densities are the convolutions of the temporal excitation and the exponential decay of the excited state $|2\rangle$. By increasing the saturation parameter ($0.1 < S < 100$), the saturation of the excited level

can be observed. During excitation, the population densities increase exponentially and reach a maximum. In comparison to the rectangular excitation, the bell-shaped excitation produces a smoother increase of the population densities.

For very high saturation ($S > 100$, intense excitation), the pump-over effect can be observed directly. During the whole laser pulse, the pumped system is saturated and it decays exponentially by emitting fluorescent photons. In spite of the same FWHM of the bell-shaped and the square temporal excitations, the time span during which excitation occurs is twice as long for the bell-shaped excitation. Thus, the duration of the pump-over effect is twice as long for the bell-shaped excitation.

During saturation, the excited system (level $|1\rangle \leftrightarrow |2\rangle$) is depopulated into the other levels. The number of fluorescent photons is determined by the branching ratio b_{23} . As the photons that spontaneously emitted from the excited state to the ground state are re-excited and therefore not lost, the branching ratio is higher during saturation:

$$\begin{aligned} b_{23} &= \frac{A_{23}}{\sum_i A_{2i}} = A_{23} \cdot \tau_2 \\ b_{23, \text{saturated}} &= \frac{A_{23}}{\sum_i A_{2i} - A_{21}} = \frac{A_{23}}{\frac{1}{\tau_2} - A_{21}} \end{aligned} \quad (\text{A-68})$$

In addition, the effective live time of the excited system during saturation is longer than that without saturation (see equations (2-1) and (B-91)). Thus, the total number of emitted fluorescent photons increase with the saturation parameter as well as with the duration of saturated excitation and this depends on the temporal characteristic of the laser pulse. As this duration of the excitation pulse is longer for the bell-shaped excitation for high saturation, the total number of emitted fluorescent photons is higher, as shown in Figure A-26. Importantly, the total number of emitted fluorescent photons is computed by the temporal integration of the fluorescent photon emission rate:

$$\begin{aligned} N_{\text{LIF}} &= A_{23} \int n_2(t) dt \\ \frac{N_{\text{LIF}}}{N_0} &= A_{23} \int \frac{n_2(t)}{n_0} dt \end{aligned} \quad (\text{A-69})$$

For low saturation, the total number of emitted fluorescent photons is the same for both the bell-shaped and the square excitations²⁷, and this amount is proportional to the saturation parameter. This linear dependence starts to saturate for $S \approx 0.1$. For the saturation parameter $S > 10$, the total number of emitted fluorescent photons starts to differ for both

²⁷ The same amount of fluorescent photons in the case of low saturation occurs for different temporal excitations/laser pulse shapes only if the temporal integral is the same. The saturation parameter represents a kind of normalized power density. By comparing different temporal pulses, the energy (the temporal integral) should be the same.

investigated temporal excitations. Owing to the longer duration of saturated excitation, the bell-shaped excitation produces more fluorescent photons. As the slopes are smooth, the effective duration of saturated excitation increases slightly with an increasing saturation parameter. Full saturation by bell-shaped excitation can thus be observed only for very high saturation parameters $S \approx 10^4 \dots 10^5$.

Thus, the total number of emitted fluorescent photons normally measured depends on the saturation parameter, especially on the temporal saturation parameter. For LIF experiments, the laser pulse energy and its duration determine the saturation effects. If the laser pulse is significantly shorter than the natural lifetime of the excited level, its duration may be neglected. Otherwise, the pump-over effect occurs for high energetic pulses and this has to be considered for the calculation of absolute densities. As this effect strongly depends on the excited species and levels, a general description of this phenomenon is not useful. Therefore, it has to be examined for each LIF experiment separately.

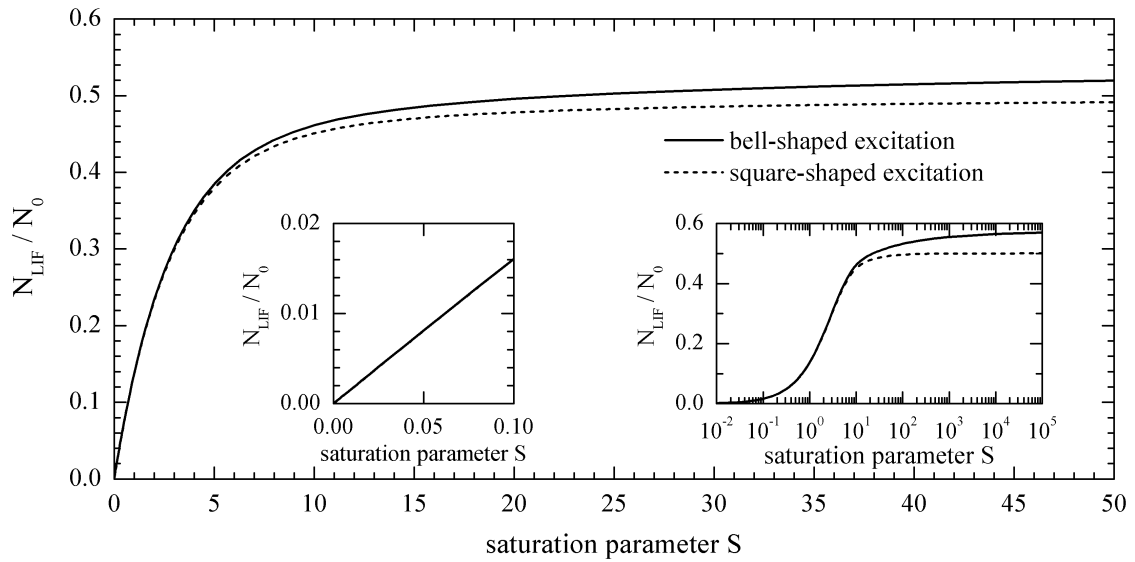


Figure A-26: Fluorescent efficient $\eta_{\text{LIF}} = N_{\text{LIF}} / N_0$ in the case of a bell-shaped (full line) and a square (dotted line) excitation with a duration of 4.85 ns.

A.5.2 Correction for a Gaussian-shaped laser profile

So far, the local saturation effect has been characterized as a function of laser power density. This assumption is sufficient as long as the laser beam profile can be approximated as spatially homogeneous. In contrast, real laser pulses have a spatially distributed power density, whereas a good configured laser system has a GAUSSIAN-shaped profile.

Thus, the saturation parameter is spatially distributed $S(r)$ according to the laser beam power density:

$$S(r) \propto I_{\text{beam}}(r) \quad (\text{A-70})$$

In the case of a GAUSSIAN-shaped beam profile, the excited state at the center of the laser beam is first saturated, while the outer region is not or only partly saturated. By increasing the laser power, additional fluorescent photons can be produced in the outer region but not in the saturated beam center. Thus, by increasing the laser power, the saturated region expands from the beam center to the outer region, leading to a broadening of the effective excited region (effective excitation cross section). This effect is called *power broadening* [DAILY 1977].

For the precise determination of absolute particle densities in a saturated LIF experiment, the effect has to be corrected. Therefore, in the following a correction is presented by considering *power broadening* and the correction of the previous section in the case of the investigated barium atoms.

Spatial saturation parameter

The applied excitation laser beam has a GAUSSIAN-shaped beam profile with an FWHM of $d_{\text{FWHM}} = 0.71 \text{ mm}$ (see Figure A-20). As the spatial-dependent saturation parameter is proportional to the beam power density (see equation (A-70)), it can be described by the GAUSSIAN function:

$$S_{\text{Gauss}}(r) = S \cdot e^{-\frac{1}{2} \frac{r^2}{\sigma^2}}, \quad (\text{A-71})$$

whereas $d_{\text{FWHM}} = 2 \cdot \sqrt{\ln(4)} \cdot \sigma = 0.71 \text{ mm}$.

To compare the results with the commonly used approach of a round homogeneous laser beam, a homogeneous profile is also assumed:

$$S_{\text{homogenous}}(r) = \begin{cases} S & , \text{ for } r < R_{\text{homogenous}} \\ 0 & \text{otherwise} \end{cases} \quad (\text{A-72})$$

The radius $R_{\text{homogenous}}$ is set in such a way that the spatial integral of the saturation parameter (equivalent to the laser power) is the same for both profiles:

$$R_{\text{homogenous}} = \sqrt{2} \cdot \sigma = \frac{1}{\sqrt{2 \cdot \ln(4)}} \cdot d_{\text{FWHM}} = 0.43 \text{ mm}. \quad (\text{A-73})$$

Both assumed beam profiles are shown in Figure A-27b. In the following, the saturation parameter S (spatial independent) defines the maximum of the spatial-dependent saturation parameter profiles and is identical to the saturation parameter in the laser beam center:

$$S = \text{MAX}(S(r)) = S_{\text{Gauss}}(r=0) = S_{\text{homogenous}}(r=0). \quad (\text{A-74})$$

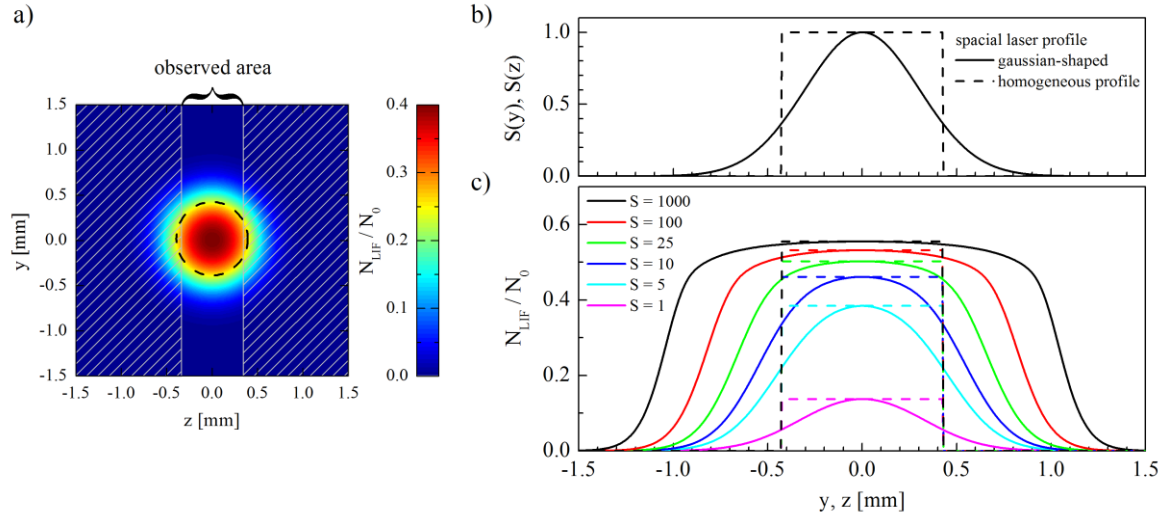


Figure A-27: Spatial dependence of the saturation effect on the laser beam profile.

- Emission of fluorescent photons in the plane perpendicular to the laser beam according to the assumption of a **GAUSSIAN**-shaped beam profile for a saturation parameter of $S = 1$. The dashed circle indicates the cross section area under the assumption of a homogeneous circular beam profile generating the same number of fluorescent photons in the case of unsaturated excitation.
- Spatial (radial)-dependent saturation parameter (equivalent to the excitation laser beam profile) by assuming a Gaussian-shaped beam profile (solid line) and a homogeneous circular beam profile (dashed line) for a saturation parameter of $S = 1$.
- Resulting spatial-dependent emission of fluorescent photons normalized to the particle density of the ground state before excitation for various saturation parameters.

By neglecting the movement of particles during excitation²⁸, the spatial-dependent fluorescent emission can be determined according to the saturation correction calculated in Section A.5.1. Therefore, the global fluorescent photon emission N_{LIF} has to be transformed into a local fluorescent photon emission $n_{LIF}(r)$:

$$\frac{n_{LIF}(S(r))}{n_0} = \frac{n_{LIF}(r)}{n_0(r)} = \frac{N_{LIF}}{N_0}(r) = \frac{N_{LIF}}{N_0}(S(r)), \quad (\text{A-75})$$

while the ground state density before excitation is assumed to be spatially homogeneous $n_0(r) = n_0$.

By the use of the spatial-dependent saturation parameter of equations (A-71) and (A-72), the local fluorescent photon emission can be calculated. In Figure A-27a), the emission of fluorescent photons in the plane perpendicular to the laser beam (beam cross section) is given for a GAUSSIAN-shaped beam profile at a saturation parameter of $S = 1$. The shaded area in the Figure indicates the region that is not observed by the fluorescent detection

²⁸ Significant particle movement such as diffusion processes occur in a timescale of milliseconds. The states investigated in this work (barium atom and ion) have a lifetime of a few nanoseconds. Thus, the effect of particle movement during excitation can be neglected.

system²⁹. In Figure A-27c, the spatial-dependent emission of fluorescent photons is given for different saturation parameters. In the case of the homogeneous beam profile (dashed line), the spatial distribution is constant, whereas the emission of fluorescent photons corresponds to the saturation characteristic calculated in Section A.5.1. In the case of the GAUSSIAN-shaped beam profile (solid line), the fluorescent profile is broadened (so-called *power broadening*) for high saturation parameters ($S > 1$). Hence, a saturation parameter of $S = 100$ doubles the profile width (FWHM).

Observed fluorescent photons

For saturation correction, the number of observed fluorescent photons has to be considered by using the integration equation (A-75) over the observation volume:

$$N_{LIF} = \int_{V, observation} n_{LIF}(r) d^3r = \iint n_{LIF}(r) dydz \cdot l, \quad (A-76)$$

where l is the length of the observation volume in the x direction. For the determination of fluorescent efficacy η_{LIF} , the quotient of observed fluorescent photons and number of atoms in the ground state before excitation is calculated. In the case of the homogenous beam profile, the number of atoms in the ground state before excitation in the homogenous beam profile is given by:

$$\begin{aligned} N_{0, homogenous} &= \int_{V, homogenous} n_0(r) d^3r = 2\pi \int_0^{R_{homogenous}} r n_0(r) dr \cdot l \\ &= n_0 \cdot \pi \cdot R_{homogenous}^2 \cdot l \end{aligned} \quad (A-77)$$

Accordingly, fluorescent efficacy η_{LIF} is given by:

$$\begin{aligned} \eta_{LIF} &= \frac{N_{LIF}}{N_{0, homogenous}} = \frac{\iint n_{LIF}(r) dydz \cdot l}{n_0 \cdot \pi \cdot R_{homogenous}^2 \cdot l} \\ &= \frac{\iint n_{LIF}(r) dydz}{n_0 \cdot \pi \cdot R_{homogenous}^2} \end{aligned} \quad (A-78)$$

In the case of a GAUSSIAN-shaped beam profile, the normalization of the number of atoms in the ground state before excitation in the excited and observed volumes is not useful, as the GAUSSIAN beam profile is in principal infinitely large. Thus, in both cases fluorescent efficacy η_{LIF} is calculated according to equation (A-78) by normalizing the observed fluorescent photons on $N_{0, homogenous}$ (the atoms in the ground state before excitation in the homogeneous beam profile). For both profiles, the spatial integral of the saturation parameter (equal to the laser power) is the same. Thus, in the unsaturated regime, the

²⁹ To ascertain a sufficient and well-defined spatial resolution, the observed volume is limited in the x and z directions. See Section A.4.3 for further details.

number of fluorescent photons and therefore fluorescent efficacy η_{LIF} is the same. The integral of equation (A-78) is solved with MatLab [MATHEWORKS 2011] by using its implemented numerical integration algorithm.

In Figure A-28a), the calculated fluorescent efficacies η_{LIF} are given for both beam profiles as a function of the saturation parameter. The fluorescent efficacy η_{LIF} of the homogeneous beam profile is equal to the saturation characteristic of the local solution determined in Section A.5.1. For low saturation parameters $S \ll 1$, fluorescent efficacy for the GAUSSIAN-shaped beam profile is proportional to the efficacies of the homogeneous profile. This proportionality can be observed more directly in the logarithmic plot of Figure A-28b, where the ratio of both fluorescent efficacies $\eta_{LIF, Gauss} / \eta_{LIF, homogenous}$ is given. The proportionality constant of 0.84 occurs due to the limitation of the observed volume in the z direction (see footnote 29 and Section A.4.3 for further details). In contrast to the round homogeneous profile, the slopes of the GAUSSIAN beam profile excites atoms in the outer region $r > R_{homogenous}$. Thus, a significant number of fluorescent photons (about 14%) come from the unobserved region not observed and are undetected.

For higher saturation parameters $S > 5$, power broadening leads to additional fluorescent photons in comparison to the homogeneous profile. By excitation with the homogeneous profile, the full beam cross section is saturated. An increase in the laser (or saturation parameter) leads to only a small number of additional fluorescent photons. In contrast, the slope of the Gaussian beam profile is not saturated. Therefore, an increase in the laser power and saturation parameter leads to additional fluorescent photons from this region. Thus, the effective excitation cross section increases. In the first approximation for intense saturation $S \gg 1$, the number of fluorescent photons is proportional to the saturated region that corresponds to the effective excitation cross section. Thus, dependence $N_{LIF} \propto \ln(S)$ would be expected (see Appendix B.7). The observed volume is limited in the z direction. Hence, by an increase in the *effective excitation cross section* above the observed length in the z direction, only additional fluorescent photons due to broadening in the y direction are observed. Thus, for high saturation parameters, fluorescent efficacy η_{LIF} depends on:

$$\eta_{LIF} = \frac{N_{LIF}}{N_{0, homogenous}} \propto \sqrt{\ln(S)}, \text{ for } S \gg 1. \quad (\text{A-79})$$

In addition, the spatial broadening of the saturated region allows determining an effective beam size in the y direction (see Figure A-28b) – right ordinate). This is defined as the length in the y direction of a round homogeneous profile producing the same number of fluorescent photons. In the case of high saturation, the effective beam size in the y direction may be significantly higher than the FWHM of the applied Gaussian beam. In conclusion, this defines the spatial resolution in the y direction. As an example, for a saturation parameter of $S=50$ and an increase in the effective beam size in the y direction of 0.71 mm in the case of low saturation, up to 1.6 mm has been found.

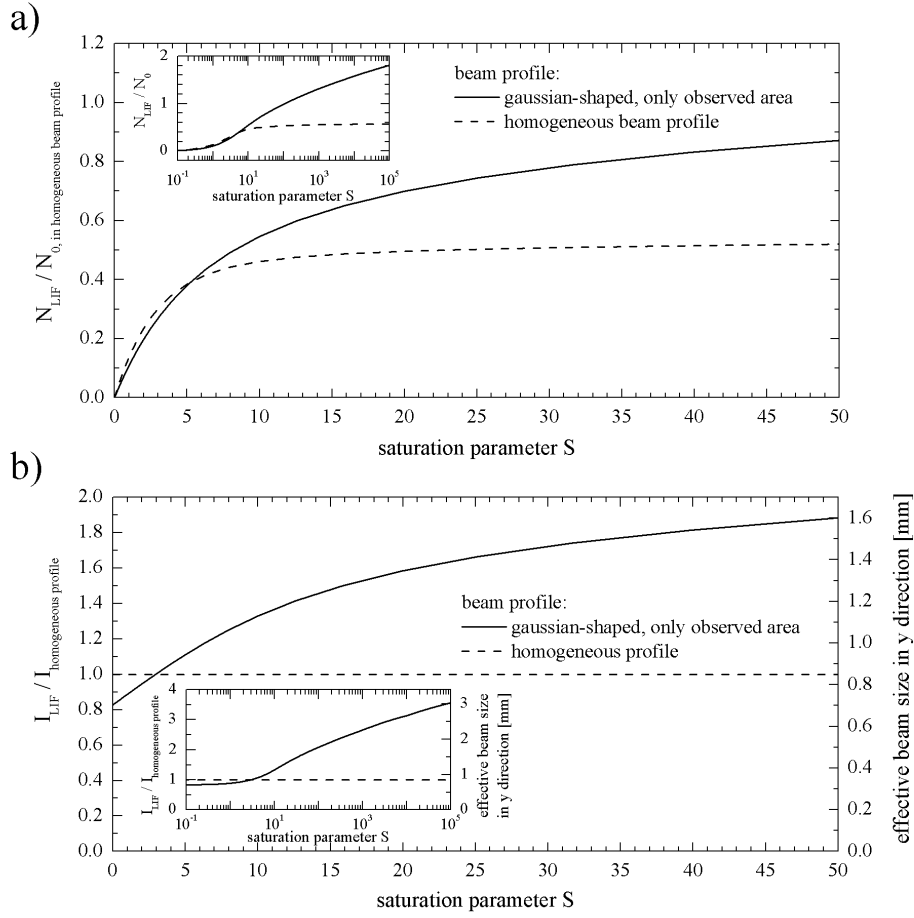


Figure A-28: Dependence of fluorescent efficacies on the saturation parameter by considering the spatial laser beam profile.

- Fluorescent efficacies as a function of the saturation parameter by assuming a round, homogeneous and a **GAUSSIAN**-shaped laser beam profile.
- Ratio of the fluorescent efficacies of a **GAUSSIAN**-shaped and a round, homogeneous laser beam profile. In addition, the effective beam size in the y direction is given.

B Additional calculations

B.1 Estimation of the averaged barium loss flux for typical electrode lifetimes

The typically emitted mass of the investigated stick coil electrodes is 10 mg. Assuming a pure barium carbonate is emitted, the total amount of barium is $N_{\text{Barium}} = 5.06 \cdot 10^{-5} \text{ mol}$. During lamp production, the barium carbonate is converted into barium oxide (see equation (2-1)). During lamp operation, the oxide is reduced by tungsten (see equation (2-7)). The produced barium tungstate Ba_3WO_6 is further reduced by tungsten to BaWO_4 (see equation (2-9)). Thus, about 75% of the barium is lost during the electrode lifetime. Assuming a typical lamp lifetime of 20000 hours, the average barium flux is about:

$$\begin{aligned} \langle \Gamma_{\text{Barium}} \rangle_{\text{lifetime}} &= \frac{75\% \cdot N_{\text{Barium}}}{t_{\text{lifetime}}}, \\ &= 3.17 \cdot 10^{11} \text{ s}^{-1} \end{aligned} \quad (\text{B-1})$$

B.2 Temperature-dependent coefficient of the thermal conductivity of Argon

The thermal conductivity of gases depends on the temperature. [YOUNGLOVE and HANLEY 1986] present a formula for this calculation:

$$\kappa(T) = \sum_{i=1}^9 g_i \cdot T^{\frac{i-2}{3}}, \quad (\text{B-2})$$

where g_i is the gas-dependent coefficients. The unit of κ is $\text{mW}/(\text{m} \cdot \text{K})$ and the temperature T has to be in Kelvin. In the case of Argon, the coefficients are:

$$\begin{aligned}
 g_1 &= -0.6700976192 \cdot 10^5 \\
 g_2 &= 0.6153355283 \cdot 10^5 \\
 g_3 &= -0.2049218286 \cdot 10^5 \\
 g_4 &= 0.2216966254 \cdot 10^4 \\
 g_5 &= 0.3579189325 \cdot 10^3 \\
 g_6 &= -0.136465891 \cdot 10^3 \\
 g_7 &= 0.1718671649 \cdot 10^2 \\
 g_8 &= -0.1018933154 \cdot 10^1 \\
 g_9 &= 0.2397996932 \cdot 10^{-1}
 \end{aligned}$$

The given formula is valid for a temperature range of $50\text{K} < T < 3273\text{K}$ and for pressures equal to or less than 100 kPa.

B.3 Analytical solution of the rate equations

In general, the system of the coupled differential equation needs to be solved numerically. However, by assuming a rectangular temporal laser intensity $I(t)$ with the duration T_{laser} , an analytical solution exists:

$$I(t) = \begin{cases} I_0 & \text{for } 0 < t < T_{\text{laser}} \\ 0 & \text{else} \end{cases} \quad (\text{B-82})$$

With the starting condition:

$$n_2(0) = n_3(0) = n_{\text{ion}}(0) = n_Q(0) = 0, \quad n_1(0) = n_{\text{total}}, \quad (\text{B-83})$$

the population densities during the excitation phase $0 < t < T_{\text{laser}}$ are given by the nontrivial solution

$$\begin{aligned}
 n_2(t) &= n_{\text{total}} \cdot \frac{R_{12}}{\lambda_1 - \lambda_2} \cdot (e^{-\lambda_2 t} - e^{-\lambda_1 t}) \\
 n_1(t) &= \frac{(\lambda_1 - R_{12})e^{-\lambda_2 t} - (\lambda_2 - R_{12})e^{-\lambda_1 t}}{\lambda_1 - \lambda_2} \cdot n_{\text{total}} \\
 n_3(t) &= \frac{A_{23}}{\Gamma_2 + Q_2 + A_{23}} \cdot \left(1 - \frac{1}{\lambda_1 - \lambda_2} \cdot (\lambda_1 e^{-\lambda_2 t} - \lambda_2 e^{-\lambda_1 t}) \right) \cdot n_{\text{total}} \\
 n_{\text{ion}}(t) &= \frac{\Gamma_2}{\Gamma_2 + Q_2 + A_{23}} \cdot \left(1 - \frac{1}{\lambda_1 - \lambda_2} \cdot (\lambda_1 e^{-\lambda_2 t} - \lambda_2 e^{-\lambda_1 t}) \right) \cdot n_{\text{total}}
 \end{aligned} \quad (\text{B-84})$$

with the characteristic rates

$$\lambda_{1/2} = \frac{R_{12} + R_{21} + \Gamma_{\text{ion}} + A_{21} + A_{23} + Q_2}{2} \pm \sqrt{\left(\frac{R_{12} + R_{21} + \Gamma_{\text{ion}} + A_{21} + A_{23} + Q_2}{2}\right)^2 - R_{12}(A_{23} + \Gamma_{\text{ion}} + Q_2)}. \quad (\text{B-85})$$

For the relaxation phase $t > T_{\text{laser}}$, there exists the trivial solution

$$\begin{aligned} n_2(t) &= n_2(T_{\text{laser}}) \cdot \exp(-\lambda_3(t - T_{\text{laser}})) \\ n_1(t) &= n_1(T_{\text{laser}}) + \frac{A_{21}}{\lambda_3} \cdot n_2(T_{\text{laser}}) \cdot [1 - \exp(-\lambda_3(t - T_{\text{laser}}))] \\ n_3(t) &= n_3(T_{\text{laser}}) + \frac{A_{23}}{\lambda_3} \cdot n_2(T_{\text{laser}}) \cdot [1 - \exp(-\lambda_3(t - T_{\text{laser}}))] \\ n_{\text{ion}}(t) &= n_{\text{ion}}(T_{\text{laser}}) \end{aligned} \quad (\text{B-86})$$

The formulas show a depopulation of level $|2\rangle$ by an exponential decay, whereas levels $|1\rangle$ and $|3\rangle$ (as well as the auxiliary level $|Q\rangle$) are populated by optical transition in the ratio of their EINSTEIN coefficients. The characteristic decay rate is the reciprocal effective lifetime of the excited state, which in principal is the natural lifetime complemented by the effect of collision depopulation:

$$\lambda_3 = \frac{1}{\tau_{2,\text{effective}}} = \frac{1}{\tau_2} + Q_2 = A_{21} + A_{23} + Q_2. \quad (\text{B-87})$$

As the solution (especially in the excitation phase) is not quite transparent, this should be discussed in the case of weak and intense excitation.

Regime of weak excitation

The weak excitation regime can be estimated for low laser intensity, resulting in small induced excitation and emission rates: $R_{12}, R_{21} \ll A_{21}, A_{23} + \Gamma_2 + Q_2$. For this estimation, the characteristic rates can be approximated as follows:

$$\lambda_1 \approx A_{21} + A_{23} + \Gamma_2 + Q_2 \gg \lambda_2 \approx R_{12} \frac{(A_{23} + \Gamma_2 + Q_2)}{A_{21} + A_{23} + \Gamma_2 + Q_2}. \quad (\text{B-88})$$

Within the time scale $t_1 = 1/\lambda_1 \ll t_2 = 1/\lambda_2$, a dynamic equilibration between induced excitation and spontaneous emission builds up:

$$n_2(t) = n_{\text{total}} \cdot \frac{R_{12}}{\lambda_1} \cdot (1 - e^{-\lambda_1 t}) \ll n_1(t). \quad (\text{B-89})$$

For short excitation ($T_{\text{laser}} \ll t_2 = 1/\lambda_2$), the population of the excited state depends only on the laser intensity. Therefore, the transition is called unsaturated. For long laser excitation $T_{\text{laser}} \approx t_2 = 1/\lambda_2$, the pumped system of levels $|1\rangle$ and $|2\rangle$ is depopulated into the metastable level $|3\rangle$ by photoionization and collision depopulation:

$$n_1(t) + n_2(t) = n_{\text{total}} \cdot e^{-\lambda_2 t} \quad (\text{B-90})$$

Regime of intense excitation

The regime of weak excitation has the most important disadvantage that only a very small number of ground state atoms are excited $n_2(t) \ll n_1(t)$, which of course degrades the detection limit significantly. Therefore, the regime of intense excitation $R_{12}, R_{21} \gg A_{21}, A_{23} + \Gamma_2 + Q_2$ is mostly intended to be used. For this estimation, the characteristic rates can be approximated as follows:

$$\lambda_1 = \frac{g_1 + g_2}{g_2} \cdot R_{12} \gg \lambda_2 = \frac{g_2}{g_1 + g_2} \cdot (A_{23} + \Gamma_2 + Q_2). \quad (\text{B-91})$$

The higher rate λ_1 determines the timescale at which an equilibration between induced excitation and induced emission builds up:

$$n_2(t) = n_{\text{total}} \frac{g_2}{g_1 + g_2} (e^{-\lambda_2 t} - e^{-\lambda_1 t}). \quad (\text{B-92})$$

In the equilibration, the corresponding levels are populated according to their statistical weights ($n_1/n_2 = g_2/g_1$). For higher laser intensities, the population ratio stays the same. Therefore, this is called complete saturation. The lower rate λ_2 determines the timescale of depopulating the pumped system of levels $|1\rangle$ and $|2\rangle$ into the metastable level $|3\rangle$ by photoionization and collision depopulation. This effect is the so-called pump-over effect [LIEDER 1989; MATSUDA et al. 1994; SCHNABEL 1999]. For LIF diagnostic, this regime of intense excitation has the advantages of high signals and the independence of the signal of the fluctuation of the laser pulse intensities.

B.4 Estimation of the statistical error by applying the resistive method for the determination of the averaged electrode temperature

The error from applying the resistive method is determined by the error from resistance determination. Cold resistances (about $R_{\text{cold}} \approx 2\Omega$) are measured at a current of $I_{\text{cold}} = 1\text{mA}$, whereas hot resistances (about $R_{\text{hot}} \approx 9\Omega$) are measured at currents of about $I_{\text{hot}} = 500\text{mA}$.

By taking into account the precision of the applied current source with integrated high precision current measuring KEITHLEY 238 and the voltage measuring unit KEITHLEY 2001 and an additional fluctuation of the contact resistance of $R_{\text{contacterror}} = \pm 0.025\Omega$, the error of resistance measuring can be calculated (see table B-2).

	cold resistance, R_{cold}	hot resistance, R_{hot}
Typical values	$R_{\text{cold}} = 2\Omega$ $I_{\text{cold}} = 1\text{mA}$ $U_{\text{cold}} = 2\text{mV}$	$R_{\text{hot}} = 9\Omega$ $I_{\text{hot}} = 500\text{mA}$ $U_{\text{hot}} = 4.5\text{V}$
precision of current measurement by KEITHLEY 238	$I_{\text{range}} = 10\text{mA}$ $I_{\text{error}} = 2\mu\text{A} \pm 0.05\%$ $I_{\text{measured}} = 1\text{mA} \pm 2.5\mu\text{A}$	$I_{\text{range}} = 1000\text{mA}$ $I_{\text{error}} = 700\mu\text{A} \pm 0.12\%$ $I_{\text{measured}} = 500\text{mA} \pm 1.3\text{mA}$
precision of voltage measurement by KEITHLEY 2001	$U_{\text{range}} = 10\text{mV}$ $U_{\text{error}} = \pm 1.3\mu\text{V}$ $U_{\text{measured}} = 2\text{mV} \pm 1.3\mu\text{V}$	$U_{\text{range}} = 10\text{V}$ $U_{\text{error}} = \pm 0.25\text{mV}$ $U_{\text{measured}} = 4.5\text{V} \pm 0.25\text{mV}$
precision of R_{measured}	$R_{\text{measured}} = 2\Omega \pm 0.63\text{m}\Omega$	$R_{\text{measured}} = 9\Omega \pm 23.9\text{m}\Omega$
precision of R_{cold}	$R_{\text{cold}} = R_{\text{measured}} \pm R_{\text{contact error}}$ $R_{\text{cold}} = R_{\text{measured}} \pm 0.025\Omega$ $R_{\text{cold}} = 2\Omega \pm 25.63\text{m}\Omega$	$R_{\text{hot}} = R_{\text{measured}} \pm R_{\text{contact error}}$ $R_{\text{hot}} = R_{\text{measured}} \pm 0.025\Omega$ $R_{\text{hot}} = 9\Omega \pm 48.9\text{m}\Omega$
error	1.28%	0.54%

Table B-2: Calculation of the error in resistance measurement.

The error in resistance measurement is about 1.28% for cold resistances and 0.54% for hot resistances. Accordingly, the resulting resistance ratio has an error of about 1.82%. By considering this error in the formula for the estimation of the hot temperature from the resistance ratio (see equation (3-1)), we obtain this from the Taylor expansion:

$$\begin{aligned}
 T_h &= T_c \cdot \left(\frac{R_h}{R_c} \pm 1.82\% \right)^{0.814} \\
 &\approx T_c \cdot \left(\frac{R_h}{R_c} \right)^{0.814} \cdot (1 \pm 0.0148) = T_c \cdot \left(\frac{R_h}{R_c} \right)^{0.814} \pm 1.5\%
 \end{aligned} \tag{B-14}$$

Thus, the statistical error resulting from the measurement can be estimated to be about 1.5% of the obtained temperature.

B.5 Calculation of the collision frequency

In general, the effective electron collision frequency for a momentum transfer ν_m is given by:

$$\nu_m = (n_{gas}Q_{ea} + n_e Q_{ei}) \cdot v_{th}^e, \quad (B-15)$$

where n_{gas} is the particle density of the buffer gas, n_e the electron density and v_{th}^e the mean thermal velocity of the electrons.

In the case of Argon, the cross section for the collisions of electrons with atoms Q_{ea} and ions Q_{ei} , respectively, is given by [DRESVIN and DONSKOI 1977; MITCHNER and KRUGER 1973]:

$$Q_{ea} = (3.6 \cdot 10^{-4} T_e - 0.1) \cdot 10^{-20} [m^2], \quad (B-16)$$

and

$$Q_{ei} = \frac{e^4}{24\pi(k_b \epsilon_0)} \ln \left(1.2384 \cdot 10^7 \sqrt{\frac{T_e^3}{n_e}} \right) \frac{1}{T_e^2} [m^2], \quad (B-17)$$

where T_e is the electron temperature in Kelvin.

For the typical discharge condition in this work, namely an Argon gas pressure of 3 mbar and electron energy of about 3 eV, the electron collision frequency for momentum transfer is about $\nu_m = 12.5 \cdot 10^9$. As the interferometer operates at 150 GHz, the quotient of electron collision frequency and angular microwave frequency is $\nu_m/\omega = 0.0133$. Therefore, the assumption of $\nu_m/\omega \ll 1$ is fulfilled.

B.6 Microwave interferometry by known electron density profile

In general, microwave interferometry is applied for plasmas where the electron density is much lower than the critical density $n_e \ll n_c$. This allows approximating equation (A-15) by the TAYLOR expansion of the integral to:

$$\Delta\varphi = \frac{1}{2} \cdot \frac{\omega}{c} \cdot \int \frac{n_e(r)}{n_c} dr. \quad (B-18)$$

From a known spatial electron density distribution along the path, which can be described as:

$$n_e(r) = n_{e,0} \cdot f(r), \quad (B-19)$$

the integral of the distribution function has to be solved. Thus, the amplitude of the electron density distribution can be determined from the phase difference:

$$n_{e,0} = 2 \cdot \frac{c}{\omega} \cdot n_c \cdot \frac{\Delta\varphi}{\int f(r) dr}. \quad (B-20)$$

In the simplest approximation, a constant electron density along the whole plasma with the observed length l can be assumed:

$$n_e(r) = n_{e,0} \cdot f(r) = n_{e,0} \cdot \begin{cases} 0, & \text{for } r < 0 \\ 1, & \text{for } 0 \leq r \leq l \\ 0, & \text{for } r > l \end{cases} \quad (\text{B-21})$$

The corresponding solution of equation (B-20) defines the path-averaged electron density:

$$n_{e,0} = \langle n_e \rangle_{\text{path}} = 2 \cdot \frac{c}{\omega} \cdot n_c \cdot \frac{\Delta\varphi}{l}. \quad (\text{B-22})$$

B.7 High power broadening for a Gaussian-shaped laser profile

For high laser power (intense saturation), so-called power broadening can be observed. The number of emitted fluorescent photons is no longer proportional to the laser power and the spatial dependence of the laser profile gains in importance. By increasing the laser power, the unsaturated areas of the laser profile emit additional fluorescent photons, whereas saturated areas do not. In addition, the saturated areas grow. For further increased laser powers, a linear increase in the number of emitted fluorescent photons proportional to the cross section area of the laser profile where the intense saturation exists can be observed. In the first approximation, the number of emitted fluorescent photons is proportional to the cross section area A of the laser profile where the saturation parameter $S(r)$ is higher than 1:

$$N_{LIF} \propto A(S(r) > 1) \quad (\text{B-23})$$

For a rotation symmetric laser profile, an effective saturation radius r_{sat} can be defined:

$$\begin{aligned} S(r \leq r_{sat}) &\geq 1 \\ N_{LIF} &\propto A(r \leq r_{sat}). \\ N_{LIF} &\propto r_{sat}^2 \end{aligned} \quad (\text{B-24})$$

For radial decreasing laser profiles, the effective saturation radius r_{sat} can be defined as:

$$S(r_{sat}) = 1 \quad (\text{B-25})$$

For a GAUSSIAN laser profile, as considered in this work, the saturation radius r_{sat} can be deduced from equation (A-71) as follows:

$$\begin{aligned} S_{\text{Gauss}}(r_{sat}) &= S \cdot e^{-\frac{1}{2} \frac{r_{sat}^2}{\sigma^2}} = 1 \\ \ln(1) &= \ln(S) - \frac{1}{2} \cdot \frac{r_{sat}^2}{\sigma^2} \\ r_{sat}^2 &= 2\sigma^2 \cdot \ln(S) \end{aligned} \quad (\text{B-26})$$

In combination with equation (B-24), the dependence of the number of emitted fluorescent photons on the saturation parameter S is given by:

$$\begin{aligned} N_{LIF} &\propto A(r \leq r_{sat}) \propto r_{sat}^2 \\ N_{LIF} &\propto \ln(S) \end{aligned} \quad (B-27)$$

In this work, the observation volume is limited in one direction perpendicular to the laser beam by an aperture. Thus, the observed excitation volume is not proportional to the saturation radius r_{sat} . If the width of the observed volume $b_{observed}$ is smaller than twice the saturation radius $2 \cdot r_{sat} > b_{observed}$, the observed saturated cross section $A_{observed}$ is no longer proportional to r_{sat}^2 as a growth in the limited direction would not be observed. In this case, the observed saturated cross section can be approximated by:

$$A_{observed} \approx b \cdot 2r_{sat} \quad (B-28)$$

The dependence of the observed fluorescent photons $N_{LIF,observed}$ on the saturation parameter S is now given by:

$$\begin{aligned} N_{LIF,observed} &\propto A_{observed} \propto r_{sat} \propto \sqrt{N_{LIF}} \\ N_{LIF,observed} &\propto \sqrt{\ln(S)} \end{aligned} \quad (B-29)$$

B.8 Estimation of the capacitance of the band probe diagnostic

By the application of the band probe diagnostic (see Figure A-4), the inner wall potential is capacitively coupled to the outer band probe. The band capacitance C_b can be estimated according to the formula for a cylindrical capacitance:

$$C = 2\pi\epsilon_0\epsilon_r \frac{l}{\ln\left(\frac{r_1}{r_2}\right)}, \quad (B-30)$$

where ϵ_0 is the vacuum permittivity, ϵ_r is the relative permittivity of the glass tube (a typical value of 6 is assumed), l is the length of the cylinder or the width of the band probe $l = 2.4\text{cm}$, r_1 is the outer radius of the glass tube $r_1 = 2.54\text{cm}/2$ and r_2 is the inner radius of the glass tube $r_2 = 2.34\text{cm}/2$. If the inner wall sheath is assumed to be ideal for conducting the electrode, the resulting wall capacitance is approximately $C_b \approx 100\text{pF}$.

C Indices

C.1 Bibliography

- [ABEYWICKRAMA 1997] **Abeywickrama, M. G.** Fluorescent lamps. in *Lamps and lighting*, London [u.a.], Arnold: pp. 194 - 215, ISBN: 0340646187 (1997)
- [AMIRAN 1970] **Amiran, R.** *Ancient pottery of the Holy Land; from its beginnings in the neolithic period to the end of the iron age*. New Brunswick, N.J., Rutgers University Press, ISBN: 0813506344 (1970)
- [AMORIM et al. 2000] **Amorim, J., G. Baravian, et al.** Laser-induced resonance fluorescence as a diagnostic technique in non-thermal equilibrium plasmas. *Journal of Physics D-Applied Physics* 33(9), R51-R65 (2000)
- [ANDRASCH et al. 2014] **Andrasch, M., J. Ehlbeck, et al.** Influence of the dielectric surrounding of plasma on the electron density measurement by microwave interferometer. *Measurement Science and Technology* 25(7), 075004 (2014)
- [ARNDT 1976] **Arndt, R.** Electrode investigations on Ar-Hg alternating current discharges in fluorescent lamps. I. Electrode voltage drops. *Beiträge aus der Plasmaphysik* 16(1), 11-22 (1976)
- [BECKER 1935] **Becker, J. A.** *Rev. Mod. Phys.* 7, pp. 95 (1935)
- [BHATTACHARYA 1989a] **Bhattacharya, A. K.** Measurement of Barium Ion Density in the Vicinity of Fluorescent Lamp Electrodes. *Journal of Applied Physics* 65(12), 4603-4607 (1989a)
- [BHATTACHARYA 1989b] **Bhattacharya, A. K.** Measurement of Barium Loss from a Fluorescent Lamp Electrode by Laser-Induced Fluorescence. *Journal of Applied Physics* 65(12), 4595-4602 (1989b)
- [BITTENCOURT 2004] **Bittencourt, J. A.** *Fundamentals of plasma physics*. New York ; London, Springer, ISBN: 0387209751 : No price (2004)
- [BLEWETT et al. 1939] **Blewett, J. P., H. A. Liebhafsky, et al.** The Vapor Pressure and Rate of Evaporation of Barium Oxide. *J. Chem. Phys.* 7, pp. 478 - 484 (1939)

- [BOGEN 1983] **Bogen, P.** Application of Fluorescence Spectroscopy to the Diagnostic of Plasma Close to the Wall. *XVI International Conference on Phenomena in Ionized Gases*, Düsseldorf (1983)
- [BORN et al. 2000] **Born, M., P. Lilie, et al.** Measurement of tungsten densities by means of laser-induced fluorescence during ignition of a pulsed low-pressure argon discharge. *Journal of Physics D-Applied Physics* 33(13), 1576-1580 (2000)
- [BRONSTEIN et al. 2001] **Bronstein, I. N., K. A. Semendjajew, et al.** *Taschenbuch der Mathematik*. Thun [u.a.], Deutsch, ISBN: 3817120052 (2001)
- [BUSO et al. 2009] **Buso, D., S. Bhosle, et al.** Predictive evaluation of fluorescent lamp lifetime. *2009 Ieee Industry Applications Society Annual Meeting*, 251-257 (2009)
- [BUSO et al. 2012] **Buso, D., M. Mayrhofer, et al.** Influence of Auxiliary Heating on the Degradation of Fluorescent Lamp Electrodes Under Dimming Operation. *Ieee Transactions on Industrial Electronics* 59(4), 1889-1897 (2012)
- [CHEN and LABORATORY 1964] **Chen, F. F. and P. U. P. P. Laboratory** *The Behavior of Langmuir Probes in Time-varying Situations*, Princeton University Plasma Physics Laboratory (1964)
- [CHITTKA et al. 1997] **Chittka, U., P. Postma, et al.** Electrodes for gas discharge lamps. *Applied Surface Science* 111, 302-310 (1997)
- [CLAASSEN and VEENEMANS 1932] **Claassen, A. and C. F. Veenemans** Dampfdruckbestimmungen von BaO, SrO, CaO und deren Mischungen aus Verdampfungsgeschwindigkeitsmessungen. *Zeitschrift für Physik A Hadrons and Nuclei* 5-6, pp. 342-351 (1932)
- [CURRY 2004] **Curry, J. J.** Compilation of wavelengths, energy levels, and transition probabilities for BaI and BaII. *Journal of Physical and Chemical Reference Data* 33(3), 725-746 (2004)
- [DAILY 1977] **Daily, J. W.** Saturation Effects in Laser-Induced Fluorescence Spectroscopy. *Applied Optics* 16(3), 568-571 (1977)
- [DEMMIG and DEMMIG 1990] **Demmig, R. and G. Demmig** *Repetitorium höhere Mathematik Teil 3 Differentialgleichungen*. Nauheim, Demmig, ISBN: 3921092647 (1990)
- [DEMTRÖDER 2005] **Demtröder, W.** *Experimentalphysik 3 Atome, Moleküle und Festkörper*. Berlin, Heidelberg, Springer-Verlag Berlin Heidelberg, ISBN: 9783540274117 (2005)

- [DEMTRÖDER 2007] **Demtröder, W.** *Laserspektroskopie: Grundlagen und Techniken*. Berlin, Heidelberg, Springer-Verlag Berlin Heidelberg, ISBN: 9783540337935 (2007)
- [DORLEIJN and GOUD 2002] **Dorleijn, J. W. F. and L. H. Goud** Standardisation of the static resistances of fluorescent lampcathodes and new data for preheating. *Conference Record of the Industry Applications Conference, 2002. 37th IAS Annual Meeting*, pp. 665 - 672 (2002)
- [DRESVIN and DONSKOI 1977] **Dresvin, S. V. and A. V. Donskoi** *Physics and technology of low-temperature plasmas*. Ames, Iowa State University Press, ISBN: 0813819504 (1977)
- [DWIVEDI and SINGH 2010] **Dwivedi, V. and D. Singh** Electric Power Quality Monitoring (PQM) using Virtual Instrumentation. *International Symposium on Power Electronics Electrical Drives Automation and Motion (SPEEDAM)* (2010)
- [EDISON 1880] **Edison, T. A.** U.S. Patent 223.898 (1880)
- [EHLBECK et al. 2011] **Ehlbeck, J., K. Rackow, et al.** Electron Density Determination by Means of Tuneable 50 GHz and 150 GHz Interferometers. *Contributions to Plasma Physics 51(2-3)*, 131-136 (2011)
- [EXCITON 2011] Retrieved 26.08.2011 from <http://www.exciton.com> (2011)
- [FEOFILOV 1961] **Feofilov, P. P.** *The physical Basis of polarized emission*. New York, Consultants Bureau (1961)
- [FROST and SULLIVAN 2011] **Frost and Sullivan** The LED Revolution and Key Opportunities for Lighting Companies in the Global Market (2011)
- [GARNER 1998] **Garner, R.** conference proceeding. *8th International Symposium on the Science and Technology of Light Sources*, Greifswald, Germany (1998)
- [GARNER 2008a] **Garner, R.** Application of a 150 GHz interferomter to fluorescent lamps. *35th IEEE International Conference on Plasma Science*, Karlsruhe, Germany (2008a)
- [GARNER 2008b] **Garner, R.** Dynamics of plasma-electrode coupling in fluorescent lamp discharges. *Journal of Physics D-Applied Physics 41(14)* (2008b)
- [GARNER 2008c] **Garner, R.** Interpretation of the external band technique for cathode fall measurements of fluorescent lamps. *Journal of Physics D-Applied Physics 41(14)* (2008c)
- [GOLDSTON and RUTHERFORD 1995] **Goldston, R. J. and P. H. Rutherford** *Introduction to plasma physics*. Bristol, UK ; Philadelphia, PA, Institute of Physics Pub., ISBN: 0750303255 (1995)

- [GOLUBOVSKII et al. 2006] **Golubovskii, Y. B., S. Hadrath, et al.** Investigations of the diffuse and spot modes in a low-pressure dc argon discharge with coiled-coil cathodes. *Journal of Physics D-Applied Physics* 39(21), 4601-4610 (2006)
- [GOREN-INBAR et al. 2004] **Goren-Inbar, N., N. Alpers, et al.** Evidence of Hominin Control of Fire at Gesher Benot Ya'aqov, Israel. *Science* 304(5671), 725-727 (2004)
- [GOUD and DORLEIJN 2002] **Goud, L. H. and J. W. F. Dorleijn** Standardized data for dimming of fluorescent lamps. *Conference Record of the Industry Applications Conference, 2002. 37th IAS Annual Meeting.*, pp. 673 - 679 (2002)
- [GREENBERG and HEBNER 1993] **Greenberg, K. E. and G. A. Hebner** Electron and Metastable Densities in Parallel-Plate Radiofrequency Discharges. *Journal of Applied Physics* 73(12), 8126-8133 (1993)
- [HADRATH 2007] **Hadrath, S.** On electrode erosion in fluorescent lamps during instant start. Universität Greifswald, Mathematisch- Naturwissenschaftliche Fakultät. Greifswald, Universität Greifswald. Dr. rer. nat. (2007)
- [HADRATH and GARNER 2010] **Hadrath, S. and R. Garner** Fabry-Perot measurements of barium temperature in fluorescent lamps. *Journal of Physics D-Applied Physics* 43(16), 165203 (2010)
- [HADRATH et al. 2007] **Hadrath, S., R. C. Garner, et al.** Time resolved measurements of cathode fall in high frequency fluorescent lamps. *Journal of Physics D-Applied Physics* 40(22), 6975-6981 (2007)
- [HAMAMOTO et al. 1981] **Hamamoto, M., M. Maeda, et al.** Absolute Density-Measurement of Metal Atoms by Laser Resonance Scattering with the Aid of Rayleigh-Scattering. *Japanese Journal of Applied Physics* 20(9), 1709-1713 (1981)
- [HAMMER 1989] **Hammer, E. E.** Comparative starting-operating of typical F40-systems. *Journal of the Illuminating Engineering Society* 18(1), 63-69 (1989)
- [HAMMER 1995] **Hammer, E. E.** Cathode fall voltage relationship with fluorescent lamps. *Journal of the Illuminating Engineering Society* 24(1), 116-& (1995)
- [HANNAFORD and LOWE 1983] **Hannaford, P. and R. M. Lowe** Determination of Atomic Lifetimes Using Laser-Induced Fluorescence from Sputtered Metal Vapor. *Optical Engineering* 22(5), 532-544 (1983)
- [HAVERLAG et al. 2002] **Haverlag, M., A. Kraus, et al.** High-frequency cold ignition of fluorescent lamps. *Journal of Physics D-Applied Physics* 35(14), 1695-1701 (2002)
- [HELMERT 1907] **Helmert, F. R.** *Die Ausgleichungsrechnung nach der Methode der kleinsten Quadrate, mit Anwendungen auf die Geodäsie, die Physik und die Theorie der Messinstrumente.* Leipzig ; Berlin, B. G. Teubner (1907)

- [HERRMANN 1958] **Herrmann, R.** Über den Verlust der Emissionsmasse von Oxydkathoden in der Niederdruckgasentladung. in *Technisch-wissenschaftliche Abhandlung der Osram-Gesellschaft*, vol. 7, Heidelberg, Springer-Verlag: p95 - p102(1958)
- [HEWITT 1901] **Hewitt, P. C.** U.S. Patent 682.692 (1901)
- [HILSCHER et al. 2004] **Hilscher, A., R. Garner, et al.** Improvement of Fluorescent Lamp Cold Start. 10rd International Symposium on the Science and Technology of Light Sources. G. Zissis. Toulouse, France, Institute of Physics: pp. 147-148 (2004)
- [HODGSON and WEBER 1992] **Hodgson, N. and H. Weber** *Optische Resonatoren Grundlagen, Eigenschaften, Optimierung*. Berlin [u.a.], Springer, ISBN: 3540544046 (1992)
- [JAUERNIK et al. 1987] **Jauernik, P., H. Kempkens, et al.** Simultaneous Detection of Rayleigh and Thomson Scattering Signals from a Hollow Cathode Arc Plasma. *Plasma Physics and Controlled Fusion* 29(11), 1615-1630 (1987)
- [JENKINS 1969] **Jenkins, R. O.** A review of thermionic cathodes. *Vacuum* 19(8), p353-359 (1969)
- [KOBAYASHI et al. 2010] **Kobayashi, I., R. Bruckshaw, et al.** Modeling of Emitter Loss in Fluorescent Lamps. *Proc. 12th International Symposium on the Science and Technology of Light Sources and the 3rd International Conference on White LEDs and Solid State Lighting*, Eindhoven, Netherlands, FAST-LS Ltd. (2010)
- [KÖNIG et al. 2013] **König, N., G. Lieder, et al.** personal communication: determination of density and temperature of released Barium. to K. Rackow Greifswald (2013)
- [KRAMES 2000] **Krames, B.** Räumliche Konzentrationsverteilungen von N₂-Triplett-Zuständen im elektrodennahen Plasma einer RF-Niederdruckentladung. TU Chemnitz, Fakultät für Naturwissenschaften. Chemnitz, TU Chemnitz. doctor rerum naturalium: 128 (2000)
- [KÜHL 1958] **Kühl, B.** Über das Verhalten von Oxydkathoden in der Niederdruckentladung. in *Technisch-wissenschaftliche Abhandlung der Osram-Gesellschaft*, vol. 7, Heidelberg, Springer-Verlag: 84 - 94(1958)
- [LAKATOS and BITO 1964] **Lakatos, G. and J. Bito** Evaporation Rate of Oxide Coated Cathode. *British Journal of Applied Physics* 15(2), 189 (1964)
- [LANKHORST and NIEMANN 2000] **Lankhorst, M. H. R. and U. Niemann** Amalgams for fluorescent lamps Part I: Thermodynamic design rules and limitations. *Journal of Alloys and Compounds* 308, 280-289 (2000)

- [LEBON 1799] **Lebon, P.** Patent: Nouveaux moyens d'employer les combustibles plus utilement, soit pour la chaleur, soit pour la lumière, et d'en recueillir les divers produits (1799)
- [LIDE 2001] **Lide, D. R.** *CRC-Handbook of Chemistry and Physics* Boca Raton, Florida, CRC Press LLC (2001)
- [LIEBERER et al. 2011] **Lieberer, M., G. Lieder, et al.** personal communication: application of optical emission spectroscopy for determination of emitter losses. to K. Rackow Greifswald (2011)
- [LIEDER 1989] **Lieder, G.** Laserinduzierte Fluoreszenz zur Bestimmung der absoluten Dichte und der Anregungstemperatur von atomaren Eisendampf. Greifswald, Ernst-Moritz-Arndt-Universität Greifswald. PhD: 126 p. (1989)
- [LU et al. 2005] **Lu, D. L., L. X. Zhong, et al.** Investigation of electrical parameters in compact fluorescent lamps. *Conference Record of the 2005 IEEE Industry Applications Conference, Vols 1-4*, 2335-2339 (2005)
- [MANABE et al. 2007] **Manabe, Y., T. Ueda, et al.** Characterization of Ba atom emission from fluorescent lamp filament by Laser-Induced Fluorescence technique, CP005. *11th International Symposium on the Science and Technology of Light Sources*, Shanghai, China (2007)
- [MARTIN and BOWEN 1993] **Martin, D. H. and J. W. Bowen** Long-wave optics. *Microwave Theory and Techniques, IEEE Transactions on* 41(10), 1676-1690 (1993)
- [MATHWORKS 2011] R2010b Documentation - pdepe from <http://www.mathworks.com/help/techdoc/ref/pdepe.html> (2011)
- [MATHWORKSINC.] **MathWorksInc.** MATLAB. Natick, MA., USA
- [MATSUDA et al. 1994] **Matsuda, Y., T. Kido, et al.** Laser-Induced Fluorescence Observation of in-Atoms Produced by Dc Reactive Sputtering of Indium-Tin-Oxide Target. *Japanese Journal of Applied Physics Part 1-Regular Papers Short Notes & Review Papers* 33(7B), 4469-4472 (1994)
- [MCKINSEY 2012] **McKinsey** Lighting the way: Perspectives on the global lighting market, second edition (2012)
- [MELISSINOS 1966] **Melissinos, A. C.** Chapter 8. in *Experiments In Modern Physics*, New York, Academic Press: pp. 65-71(1966)
- [MICHAEL 2001] **Michael, J. D.** Measurement of Barium Evaporation Rates for F-Lamp Cathodes using Laser Induced Fluorescence. *9th International Symposia on the Science and Technology of Light Sources*, Ithaca, NY, USA (2001)

- [MISHRA et al. 2004] **Mishra, K. C., R. Garner, et al.** Model of work function of tungsten cathodes with barium oxide coating. *Journal of Applied Physics* 95(6), p3069-3074 (2004)
- [MISONO 1992] **Misono, K.** The Cathode Fall Voltage of Low Current Fluorescent Lamps. *Journal of Light & Visual Environment* 16(2), 53-60 (1992)
- [MITCHNER and KRUGER 1973] **Mitchner, M. and C. H. Kruger** *Partially ionized gases*. New York, Wiley, ISBN: 0471611727 (1973)
- [MOSKOWITZ 1992] **Moskowitz, P. E.** Fluorescent lamp electrode diagnostics by laser-induced fluorescence. 6rd International Symposium on the Science and Technology of Light Sources. Budapest, Hungary (1992)
- [MOTT-SMITH and LANGMUIR 1926] **Mott-Smith, H. M. and I. Langmuir** The Theory of Collectors in Gaseous Discharges. *Physical Review* 28(4), 727-763 (1926)
- [MYOJO 2010] **Myojo, M.** Thermionic Emission Properties of Emissive Oxides. *Journal of Light & Visual Environment* 34(1), 24-34 (2010)
- [NACHTRIEB et al. 2005] **Nachtrieb, R., F. Khan, et al.** Cathode fall measurements in fluorescent lamps. *Journal of Physics D-Applied Physics* 38(17), 3226-3236 (2005)
- [NAMIoTKA et al. 1996] **Namiotka, R. K., E. Ehrlacher, et al.** Diffusion of barium atoms in the 6s5d D-3(J) metastable levels and the 6s(2) S-1(0) ground state through noble-gas perturbers. *Physical Review A* 54(1), 449-461 (1996)
- [NATIONAL 2012] How Does the Buneman Frequency Estimator VI Work?
Retrieved 22.12.2012 from
<http://digital.ni.com/public.nsf/allkb/4D01B90DCBAD81C0862570FC005A914E>
(2012)
- [NIEMI 2003] **Niemi, K.** *Nachweis leichter Atome in reaktiven Plasmen mittels Zweiphotonen laserinduzierter Fluoreszenzspektroskopie unter besonderer Berücksichtigung der Absolutkalibrierung*. Göttingen, Cuvillier, ISBN: 3898738329 (Kt.) (2003)
- [NIGGLI and HUBER 1987] **Niggli, S. and M. C. E. Huber** Transition-Probabilities in Neutral Barium. *Physical Review A* 35(7), 2908-2918 (1987)
- [NOTTINGHAM 1936] **Nottingham, W. B.** *Phys. Rev.* 49, pp. 78 (1936)
- [OSRAM 2010] Osram GmbH from <http://www.osram.com> (2010)
- [PROUD 1983] **Proud, J. M.** Compact Fluorescent Lamps. *3rd International Symposium on the Science and Technology of Light Sources*, Toulouse, France (1983)
- [QIN and GUO 1998] **Qin, Y. and Q. Guo** Quasi optic lens antenna with corrugated feed horns. 382-386 (1998)

- [RACKOW et al. 2011] **Rackow, K., J. Ehlbeck, et al.** Microwave-based characterization of an atmospheric pressure microwave-driven plasma source for surface treatment. *Plasma Sources Science and Technology* 20(3), 035019 (2011)
- [RACKOW et al. 2010] **Rackow, K., F. Sigeneger, et al.** Emitter erosion in fluorescent lamps. *Proc. 12th International Symposium on the Science and Technology of Light Sources and the 3rd International Conference on White LEDs and Solid State Lighting*, Eindhoven, Netherlands, FAST-LS Ltd. (2010)
- [RAIZER 1991] **Raizer, Y. P.** *Gas discharge physics*. Berlin ; New York, Springer-Verlag, ISBN: 3540194622 (1991)
- [RECKERS et al. 1997] **Reckers, W., Y. W. Gu, et al.** Rayleigh scattering of excimer laser light from some simple molecules at 193 nm and 248 nm: The effect of polarization upon imaging diagnostics. *Applied Spectroscopy* 51(7), 1012-1016 (1997)
- [RICHARDSON 1965] **Richardson, O. W.** Thermionic phenomena and the laws which govern them (Nobel Lecture 1928). in *Nobel Lectures, Physics 1922-1941*, Amsterdam(1965)
- [RITTNER et al. 1957] **Rittner, E. S., R. H. Ahlert, et al.** Studies on the Mechanism of Operation of the L Cathode .1. *Journal of Applied Physics* 28(2), 156-166 (1957)
- [ROSILLO and CHIVELET 2009] **Rosillo, F. G. and N. M. Chivelet** Lifetime prediction of fluorescent lamps used in photovoltaic systems. *Lighting Research & Technology* 41(2), 183-197 (2009)
- [ROZENBOOM 1983] **Rozenboom, J.** Electronic Ballast for Gas Discharge Lamps. *3rd International Symposium on the Science and Technology of Light Sources*, Toulouse, France (1983)
- [RUTLEDGE and RITTNER 1957] **Rutledge, W. C. and E. S. Rittner** Studies on the Mechanism of Operation of the L Cathode .2. *Journal of Applied Physics* 28(2), p167-173 (1957)
- [RUTSCHER and DEUTSCH 1984] **Rutscher, A. and H. Deutsch** *Plasmatechnik: Grundlagen und Anwendungen*, Hanser, ISBN: 9783446136274 (1984)
- [SAMIR et al. 2007] **Samir, A., G. Yamashita, et al.** Loss of Ba Atom from the Electrode of Fluorescent Lamp Operating under AC and DC Discharges. *IEEJ Transactions on Fundamentals and Materials* 127(9), 543-548 (2007)
- [SAMIR et al. 2005] **Samir, A., G. Yamashita, et al.** Temporal and Spatial Distributions of Ba Atoms in a Fluorescent Lamp Discharge Using Laser-induced Fluorescence. *66(3)*, 981 (2005)

- [SCHNABEL 1999] **Schnabel, R.** *Zeitaufgelöste, nichtlineare laserinduzierte Fluoreszenz zur Messung von Lebensdauern, Übergangswahrscheinlichkeiten und Besetzungsdichten*. Berlin, Wiss.-und-Technik-Verl., ISBN: 3896853260 (brosch.) (1999)
- [SIGENEGER et al. 2010] **Sigeneger, F., K. Rackow, et al.** Barium transport in the hot spot region of fluorescent lamps. *Journal of Physics D-Applied Physics* 43(38) (2010)
- [SINGAL et al. 2005] **Singal, J., E. Wollack, et al.** Design and performance of sliced-aperture corrugated feed horn antennas. *Rev. Sci. Instrum.* 76(12), 124703 (2005)
- [SIRAH-GMBH 1998] **Sirah-GmbH** *PrecisionScan Service Manual*. Kaarst, Sirah GmbH (1998)
- [SOBELMAN 1979] **Sobelman, I. I.** *Atomic spectra and radiative transitions*. Berlin, Springer, ISBN: 3540090827 (1979)
- [SOULES et al. 1989] **Soules, T. F., J. H. Ingold, et al.** Thermal-Model of the Fluorescent Lamp Electrode. *Journal of the Illuminating Engineering Society* 18(2), 81-92 (1989)
- [SPECTRA-PHYSICS 1999] **Spectra-Physics** *Quanta-Ray PRO-Series: User's Manual*. Mountain View, CA, Spectra-Physics (1999)
- [STECKELMACHER 1986] **Steckelmacher, W.** Knudsen flow 75 years on: the current state of the art for flow of rarefied gases in tubes and systems. *Reports on Progress in Physics* 49(10), 1083 (1986)
- [STERN and VOLMER 1919] **Stern, O. and M. Volmer** Über die Abklingungszeit der Fluoreszenz. *Physikalische Zeitschrift* 20, 183-188 (1919)
- [STUART and WEHNER 1962] **Stuart, R. V. and G. K. Wehner** Sputtering Yields at Very Low Bombarding Ion Energies. *Journal of Applied Physics* 33(7), 2345-2352 (1962)
- [TONKS and LANGMUIR 1929] **Tonks, L. and I. Langmuir** Oscillations in Ionized Gases. *Physical Review* 33(2), 195-210 (1929)
- [TORRES et al. 2007] **Torres, J., J. M. Palomares, et al.** A Stark broadening method to determine simultaneously the electron temperature and density in high-pressure microwave plasmas. *Journal of Physics D: Applied Physics* 40(19), 5929 (2007)
- [VAN DEN HOEK 2003] **van den Hoek, W. J.** Electrode aspects of fluorescent lamps. *IEEE Industry Applications Society 38th Annual Meeting*, Salt Lake City, Utah USA (2003)
- [VAN DEN HOEK et al. 2002] **van den Hoek, W. J., T. L. G. Thijssen, et al.** Emitter depletion studies on electrodes of 50 Hz mercury/noble gas discharge lamps during ignition. *Journal of Physics D-Applied Physics* 35(14), 1716-1726 (2002)

- [WALKER et al. 1987] **Walker, T. G., K. D. Bonin, et al.** Modulation Technique for Measuring Diffusion-Coefficients of Ba in Noble-Gases. *Journal of Chemical Physics* 87(1), 660-663 (1987)
- [WAYMOUTH 1971] **Waymouth, J. F.** *Electric discharge lamps*. Cambridge Mass., M.I.T. Press, ISBN: 0262230488 (1971)
- [WAYMOUTH 2003] **Waymouth, J. F.** Chemistry and physics of electron emitting cathodes for fluorescent lamps. *IEEE Industry Applications Society 38th Annual Meeting*, Salt Lake City, Utah USA (2003)
- [WHARMBY 2004] **Wharmby, D. O.** Cathode heating rate and life prediction in fluorescent lamps. *Light Sources 2004*(182), 235-236 (2004)
- [WINTER et al. 2008] **Winter, J., H. Lange, et al.** Gas temperature in the cathode region of a dc glow discharge with a thermionic cathode. *Journal of Physics D-Applied Physics* 41(8), - (2008)
- [WYLDE 1984] **Wylde, R. J.** Millimetre-wave Gaussian beam-mode optics and corrugated feed horns. *Microwaves, Optics and Antennas, IEE Proceedings H* 131(4), 258-262 (1984)
- [WYLDE and MARTIN 1993] **Wylde, R. J. and D. H. Martin** Gaussian Beam-Mode Analysis and Phase-Centers of Corrugated Feed Horns. *Ieee Transactions on Microwave Theory and Techniques* 41(10), 1691-1699 (1993)
- [YOUNGLOVE and HANLEY 1986] **Younglove, B. A. and H. J. M. Hanley** THE VISCOSITY AND THERMAL-CONDUCTIVITY COEFFICIENTS OF GASEOUS AND LIQUID ARGON. *Journal of Physical and Chemical Reference Data* 15(4), 1323-1337 (1986)
- [ZISSIS and KITSINELIS 2009] **Zissis, G. and S. Kitsinelis** State of art on the science and technology of electrical light sources: from the past to the future. *Journal of Physics D-Applied Physics* 42(17) (2009)

C.2 Glossary

C.2.1 Used symbols

$T_n, T_i, T_e,$	neutral particle, ion temperature and electron temperature	eV, K
$W(E)$	work function	eV
E	energy	eV
E_F	Fermi energy	eV
T	temperature	K
k_B	Boltzmann constant	$1.380648813 \cdot 10^{-23} \text{ J K}^{-1}$
J	current density	A m^{-2}
A	RICHARDSON constant	$1.20173 \cdot 10^6 \text{ A m}^{-2} \text{ K}^{-2}$
Φ	work function	eV
Φ_0	original work function	eV
$\Delta\Phi$	the drop of the potential barrier	eV
e	electron charge	$1.60217656535 \cdot 10^{-19} \text{ C}$
ϵ_0	vacuum permittivity	$8.854187817 \cdot 10^{-12} \text{ F m}^{-1}$
π	pi	
r	position	m
P	pressure	Pa, bar
Γ_{Ba}	barium flux	$\text{atoms m}^{-2} \text{ s}^{-1}$
n_{Ba}	barium density	m^{-3}
D_{Ba}	barium diffusion coefficient	$\text{cm}^2 \text{ s}^{-1}$
R, R_c, R_h	ohmic, cold and hot resistance	Ω
T_c, T_h	cold and hot electrode temperature	K
$L(\lambda, T)$	temperature dependent spectral radiance	$\text{W sr}^{-1} \text{ m}^{-2} \text{ Hz}^{-1}$
h	PLANCK constant	$6.6260695729 \cdot 10^{-34} \text{ J s}$
c	speed of light	$299792458 \text{ m s}^{-1}$
λ	wavelength	nm
C	capacitance	F
U	voltage	V
t	time	s
V	electric potential	V
f	frequency	Hz, s^{-1}
c_{band}	correction factor for the capacitively coupled band diagnostic	
f_c	cutoff frequency	Hz, s^{-1}

\vec{E}	electric field vector	V m^{-1}
\vec{k}	wave vector	m^{-1}
ω	angular frequency	s^{-1}
ω_p	plasma frequency introduced by Tonks and Langmuir [1929]	s^{-1}
ν_m	effective electron collision frequency for momentum transfer	s^{-1}
n_e	electron density	m^{-3}
m_e	electron mass	kg
ϵ_r	relative permittivity	
n_c	cutoff electron density	m^{-3}
$\langle n_e \rangle_{\text{path}}$	path-averaged electron density	m^{-3}
$\varphi, \Delta\varphi$	phase and phase different	
l	length	m
$\Delta\nu_L$	excitation bandwidth	s^{-1}
ν_L	laser frequency	s^{-1}
E_n	energy of atomic level n	eV
E_{ion}	ionization energy	eV
R_{12}	induced excitation-rate	s^{-1}
R_{21}	induced emission-rate	s^{-1}
B_{ik}	EINSTEIN-transition probability for induced emission from state $ i\rangle$ to $ k\rangle$	
A_{ik}	EINSTEIN-transition probability for spontaneous emission from state $ i\rangle$ to $ k\rangle$	
g_i	statistical weight of level i	
τ, τ_0, τ_i	lifetime, natural lifetime, life time of the stated i	s
$I(r, t)$	laser intensity	W m^{-2}
$g(\Delta\nu)$	the spectral line profile of excitation	
Γ_{ion}	photo ionization rate	s^{-1}
Q	collision depopulation rate	s^{-1}
n_i	density of species or level i	m^{-3}
S	saturation parameter	
I_v^S	saturation laser intensity	W m^{-2}
$N_L, N_{LIF}^{\text{total}}$	total number of laser and fluorescent photons	
V	Volume	m^3

T_{laser}	laser pulse length	s
ν_{ik}	frequency of the light emitted by the transition from state $ k\rangle$ to $ i\rangle$	s^{-1}
η_{LIF}	fluorescent efficacy	
I_{LIF}	measured fluorescent signal	V
S_{LIF}	time-integrated fluorescent signal	sV
σ_{LIF}	laser induced fluorescent cross section	m^2
$G(\lambda_{\text{LIF}})$	spectral sensitivity of the detection system	
σ_{Ray}	Rayleigh scattering cross section	m^2
$\nu_{\text{Ba}}^{\text{io}}, \nu_{i \rightarrow 0}$	barium ionization and excitation frequency	s^{-1}
x, y, z, r	coordinates	m
P, P_{laser}	power and laser power	W
A	area	m^2
ε	emissivity of a material	
$I, I_{\text{lamp}}, I_{\text{heat}}$	current, lamp and heating current	A

C.2.2 Abbreviations used

AC	alternating current
CRI	color-rendering index
DC	direct current
FWHM	full wide at half maximum
HID	high intensify discharge
LIF	laser induced fluorescents
OES	optical emission spectroscopy
TTL	transistor–transistor logic compatible level

C.2.3 List of figures

Figure 2-1	Schematic of a tubular fluorescent lamp with stick electrodes	10
Figure 2-2	Regions and potential of a fluorescent lamps	11
Figure 2-3	Selection of different commercial available fluorescent	13
Figure 2-4	Standard circuits for operation of fluorescent lamps	14
Figure 2-5	Standard electrodes of fluorescent lamps	15
Figure 2-6	Processes during activation of emitter	17
Figure 2-7	Reduction of work function by electric fields	20
Figure 2-8	Production of free barium at the surface of tungsten wires during operation in spot mode	21
Figure 2-9	SEM image of a new electrode and an electrode at about 75% of its lifetime	24
Figure 3-1	Setup for heating and determination of the of averaged electrode temperature by the resistive method	28
Figure 3-5	Photos of the electrode region of the investigated T8-lamps	35
Figure 3-6	Standard Electrical setup	36
Figure 3-7	Experimental arrangement of the LIF and interferometry experiment	37
Figure 3-8	Positioning of the electrode for the LIF experiment	38
Figure 4-1	Geometry and triangular mesh grid of the model	41
Figure 4-2	Schematic of the model	43
Figure 4-3	Temperature distribution computed by the model	44
Figure 4-4	Spatial and time dependent evolution of barium densities computed by the model	45
Figure 4-5	Temperature dependence of the solution	47
Figure 4-6	Comparison of two different boundary conditions at the electrode surface	48
Figure 4-7	Spatial resolved rise time of the densities	49
Figure 4-8	Measurements while blanking (switching off) the lamp	51
Figure 4-9	Barium density during shutting-off the lamp	52
Figure 4-10	Determined barium diffusion coefficient for different Argon pressures	53
Figure 5-1	Time resolved fluorescent signal of the excited barium Ba level	56
Figure 5-2	Determination of quenching rates by Stern-Volmer-plots	57
Figure 5-3	Barium evaporation of a heated electrode	58
Figure 5-4	Absolute density of the evaporated barium 1 mm in front of the electrode as function on the averaged electrode temperature	60

Figure 5-5	Barium densities decay in front of the electrode	61
Figure 5-6	Heating power-temperature characteristic	62
Figure 5-7	The 25 kHz operation mode	64
Figure 5-8	Typical results for the 25 kHz operation mode for a lamp current of 320 mA	66
Figure 5-9	Spatial dependents of the measured quantities for the 25 kHz operation mode	68
Figure 5-10	Temperature profile of the electrode for different lamp currents	70
Figure 5-11	Variation of lamp current by operating at 25 kHz	71
Figure 5-12	Applied electrical setup for variation of lamp and heat currents	73
Figure 5-13	Electrode temperature profiles by application of additional heat currents	74
Figure 5-14	Influence of additional applied heat currents on electrode processes	75
Figure 5-15	Electrical setup used for frequency variation	77
Figure 5-16	Anode oscillation illustrated by the path-averaged electron densities in the electrode region	78
Figure 5-17	Modulation of the barium ground state density due to anode oscillations	79
Figure 5-18	Time dependent behavior by variation of the operation frequency	81
Figure 5-19	Dependence on the operation frequency	83
Figure 5-20	Characteristically behavior at conventional net frequency operation	84
Figure 5-21	Modified net frequency operation with defined off-times during transitions between anode and cathode phases	86
Figure A-1	Basic configuration for spatial resolved electrode temperature measuring system	94
Figure A-2	Calibration of the online electrode temperature measuring system	95
Figure A-3	Experimental setup for the band diagnostic method	96
Figure A-4	Cross section of the lamp in the electrode region by application of the band method	97
Figure A-5	Typical signals and calibration of the external circuit by application of the band method	101
Figure A-6	Dispersion relation of high frequency electromagnetic waves in non-magnetized plasmas	104
Figure 6-7	Dependence of the measured phase difference on the path averaged electron density and the operation frequency of the applied interferometer	106
Figure A-8	Configuration of the 150 GHz heterodyne microwave interferometer	108
Figure A-9	Numerical method for phase detection	109

Figure A-10	Two dimensional measurement of the interferometer beam in focus	111
Figure A-11	Noise and statistical error of phase measurement	112
Figure A-12	Electrical setup for measuring electron densities of a fluorescent lamp with microwave interferometry	113
Figure A-13	Typical measurement with the interferometer at the electrode region	114
Figure A-14	Schematic setup for the LIF experiments	115
Figure A-15	Three level energy diagram with rate coefficient	117
Figure A-16	Temporal dependence of the density n_2 of the upper level	121
Figure A-17	Temporal dependence of the densities of the ground state and the fluorescent level	121
Figure A-18	The experimental setup used for LIF experiments	126
Figure A-19	line width of the used dye laser	127
Figure A-20	Spatial intensity of the laser pulse	128
Figure A-21	Vacuum vessel for determination of RAYLEIGH-scattering	132
Figure A-22	Measured RAYLEIGH-signal	133
Figure A-23	Experimental determined saturation characteristic	134
Figure A-24	The temporal evolution of laser pulses	138
Figure A-25	Numerical solution of the rate equation system	139
Figure A-26	Fluorescent efficient in case of a bell-shaped and a square-shaped excitation	141
Figure A-27	Spatial dependence of the saturation effect on the laser beam profile	143
Figure A-28	Dependence of the fluorescent efficacies on the saturation parameter by considering the spatial laser beam profile	146

C.2.4 List of tables

Table A-1	Degree of polarization of emitted fluorescent radiation by excitation with a linear polarized laser	125
Table B-2	Calculation of the error of the resistance measurement	151

Eigenständigkeitserklärung

Hiermit erkläre ich, dass diese Arbeit bisher von mir weder an der Mathematisch-Naturwissenschaftlichen Fakultät der Ernst-Moritz-Arndt-Universität Greifswald noch einer anderen wissenschaftlichen Einrichtung zum Zwecke der Promotion eingereicht wurde.

Ferner erkläre ich, dass ich diese Arbeit selbstständig verfasst und keine anderen als die darin angegebenen Hilfsmittel und Hilfen benutzt und keine Textabschnitte eines Dritten ohne Kennzeichnung übernommen habe.

Danksagung

An dieser Stelle möchte ich mich bei allen bedanken, die zum Gelingen dieser Dissertation beigetragen haben.

Dem Leibnitz-Institut für Plasmaforschung und Technologie möchte ich für die Möglichkeit diese Arbeit anfertigen zu können danken. Einen besonderen Dank möchte ich dem Direktor Prof. Dr. Klaus-Dieter Weltmann aussprechen, der meine Betreuung übernahm und mich auf Zielkurs hielt.

Dr. Jörg Ehlbeck möchte ich für interessante Themenstellungen und die Möglichkeit dieses Thema mit seiner Unterstützung in seiner Abteilung bearbeiten zu können, einen besonderen Dank aussprechen. Er hat das Thema erst ermöglicht und war immer ein hilfreicher Ansprechpartner zum Thema Diagnostik.

Für die immer fruchtbare Zusammenarbeit bedanke ich mich recht herzlich bei Dr. Gerd Lieder. Er hat das Thema in der Osram AG begleitet und immer die nötigen Voraussetzungen geschaffen (unter anderem die benötigten Lampen organisiert). Durch viele Diskussionen hat er diese Arbeit mitgestaltet.

Für die Unterstützung bei Aufbau und Durchführung der Diagnostiken bedanke ich mich bei Alfred Scholz und für die Erstellung von Testlampen und diversen anderen Glasarbeiten bei Udo Nehmzow.

Bei Dr. Mathias Andrasch bedanke ich mich für seine Zusammenarbeit bei Schaffung aller Voraussetzungen für diese Arbeit. Wir sind einen langen Weg gegangen.

Für die detaillierte Erklärung der Elektrodenphysik und die Zusammenarbeit danke ich Dr. Richard Garner.

Für die detaillierten Vorarbeiten und die Unterstützung möchte ich Dr. Stefan Hadrath meinen Dank aussprechen. Bei Markus Lieberer möchte ich mich für die Zusammenarbeit innerhalb der gemeinsamen Projekte bedanken, hierbei kamen viele zielführende Ideen zustande. Bei Dr. Andrei Pipa möchte ich mich für die Einführung in die Optische Emissionsspektroskopie bedanken.

Für die Unterstützung innerhalb des INP's danke ich Dr. Dirk Uhrland, Liane Kanz und Dr. André Bösel.

Meiner Familie gilt ein ganz besonderer Dank. Ihr hattet viel Geduld und habt mich immer unterstützt.

Danke, dass es euch gibt.

List of publications and contributions

- [1] Rackow, K., F. Sigeneger, et al. "Emitter erosion in fluorescent lamps" *Proc. 12th International Symposium on the Science and Technology of Light Sources and the 3rd International Conference on White LEDs and Solid State Lighting, Eindhoven, Netherlands, FAST-LS Ltd.*, 2010
- [2] Rackow, K., J. Ehlbeck, et al. "Microwave-based characterization of an atmospheric pressure microwave-driven plasma source for surface treatment", *Plasma Sources Science and Technology* 20(3): 035019, 2011
- [3] Rackow, K., S. Hadrath, et al. "Determination of Barium Loss in Fluorescent Lamps", *Poster at the 11th International Symposium on the Science and Technology of Light Sources*, 2007
- [4] Sigeneger, F., K. Rackow, et al. "Barium transport in the hot spot region of fluorescent lamps", *Journal of Physics D-Applied Physics* 43(38), 2010
- [5] Ehlbeck, J., K. Rackow, et al. "Electron density determination by means of tunable 50 GHz and 150 GHz interferometers", *Contributions to Plasma Physics Vol. 2-3/2011: page 131-136*, 2011
- [6] Ehlbeck, J., K. Rackow, et al., "Laser induced fluorescence measurements on W- and Ba atoms eroded from fluorescent lamp electrodes", *Journal of Physics: Conference Series* 227(1 (2010)): 4, 2010
- [7] Baeva, M., K. Rackow, et al. "Characterization of atmospheric pressure microwave plasma in N₂/O₂/H₂O gas mixtures", *Proc. 30th ICPIG. Belfast, Northern Ireland, UK*, 2011
- [8] Pipa, A. V., Andrasch, M., Rackow, K., Ehlbeck, J., Weltmann, K. D., "Observation of microwave volume plasma ignition in ambient air", *Plasma Sources Science and Technology* 21(3): 035009, 2012
- [9] Ehlbeck, J., M. Andrasch, et al. "Dekontamination von Primärverpackungen mittels Atmosphärendruckplasmen", *Vakuum in Forschung und Praxis*, 2010
- [10] Siegmund, K., Hübner, N., Heidecke, C.-D., Brandenburg, R., Rackow, K., Benkhail, H., Schnaak, V., Below, H., Dornquast, T., Assadian, O., Kramer, A , "Are laptop ventilation-blowers a potential source of nosocomial infections for patients?", *GMS Krankenhaushygiene Interdisziplinär* 2010 5(2): 6, 2010

Patents

- [11] Krohmann, U., Neumann, T., Ehlbeck, J., Rackow, K., “Method and Device for Igniting and Generating an Expanding Diffuse Microwave Plasma and Method and Device for Plasma Treating Surfaces and Substances by Using This Plasma”, *United States patent: US 2010/0001647*, 2010

Talks (international)

- [12] Rackow, K., F. Sigeneger, et al. “Emitter erosion in fluorescent lamps”, *Invited talk at the 12th International Symposium on the Science and Technology of Light Sources and the 3rd International Conference on White LEDs and Solid State Lighting, Eindhoven, Netherlands*, 2010
- [13] Rackow, K., F. Sigeneger, et al. “Investigation of Barium evaporation and diffusion in fluorescent lamps”, *Talk at the 36th International Conference on Plasma Science and 23rd Symposium on Fusion Engineering, San Diego, USA*, 2009
- [14] Rackow, K., Ehlbeck, J., et al. “Electron density determination by means of tunable 50 GHz and 150 GHz interferometers”, *Talk at the 18th Int. Conf. Gas Discharges and their Applications, Greifswald/Germany 2010*, 2010
- [15] Rackow, K., “Emitter erosion in fluorescent lamps”, *Talk at the colloquium of the International Helmholtz Graduate School for Plasma Physics (HEPP)*, 2012
- [16] Rackow, K., “Erosion of thermionic electrodes in fluorescent lamps”, *Talk at the colloquium of the International Helmholtz Graduate School for Plasma Physics (HEPP)*, 2013